Accurate Profile Measurement of the low Intensity Secondary Beams in the CERN Experimental Areas

THÈSE N^O 8278 (2018)

ÉCOLE POLYTECHNIQUE FÉDÉRALE DE LAUSANNE

POUR L'OBTENTION DU GRADE DE DOCTEUR ÈS SCIENCES

PAR

Inaki ORTEGA RUIZ

EPFL

ÉCOLE POLYTECHNIQUE
FÉDÉRALE DE LAUSANNE

Suisse
2018

To my loving parents and wife,
I don't shine if you don't shine.

Acknowledgements

First, I would like to thank my two supervisors, Gerard Tranquille and Aurelio Bay, for supporting me and giving me the opportunity to undertake this PhD project. Doing a PhD is not easy, particularly at the beginning, as you need to develop some autonomy and a certain degree of self-confidence, necessary to face the many "unknowns" that you find in research. If this project has reached such degree of progress, and if I have become an expert on my research field, is thanks to their smart and subtle guidance.

My special gratitude to Guido Haefeli and Jens Spanggaard for their invaluable advice and the many interesting chats that we have had. Guido has been, in some way, a mentor on scintillating fibres and silicon photomultipliers. From Jens, I have learned a myriad of things about the CERN Experimental Areas and their beam instrumentation.

J'aimerais remercier Wilfried Devauchelle et Alexandre Frassier d'une manière spéciale, car tout ce travail ne serait pas possible sans ses excellentes compétences techniques et sa généreuse volonté de toujours m'aider.

Any experimental work is full of technical challenges and, very often, the path to follow looks blurry. In my case, Christian Joram, Thomas Schneider, Sune Jakobsen, and Raphael Dumps were generous and patient to throw the necessary light on me. Thanks to them, I solved many technical issues and my gratitude towards them is only exceeded by their generosity.

My appreciation and esteem also goes to Lau Gatignon, for being so supportive since the beginning of my PhD. He has always been eager to share his clear insight with me and to help me with many academical matters.

The day-to-day support is vital, no matter the enterprise we undertake. I owe this support to my section colleagues: Philippe Carriere, Stephane Deschamps, Jocelyn Tan, Jean Cenede, Pierre Grandemange, Adriana Rossi, Bruno Galante, and Lars Joergensen. Sometimes we are absorbed by work and we resist to stop until we have solved a particular task that is troubling us. In that moment, a coffee break can the best remedy to all your problems. After a friendly chat about things unrelated to work, it is sure that any problem will seem easier and the chances of success will be higher.

Acknowledgements

Abstract

The CERN accelerators deliver a wide spectrum of secondary beams to the Experimental Areas. These beams are composed of hadrons, leptons, and heavy ions that can vary greatly in momentum ($1\,\mathrm{GeV/c}$ to $400\,\mathrm{GeV/c}$) and intensity (10^2 to 10^8 particles per second). The profile, position, and intensity of these beams are measured using particle detectors. However, the current systems show several problems that limit the quality of this kind of monitoring.

The aim of this doctoral thesis is to investigate the best detector technology that could replace the existing monitors and build a first prototype of it. A review of the existing detection techniques has led to the choice of Scintillating Fibres (SciFi) read-out with Silicon Photomultipliers (SiPM). This detection technology has the potential to perform better in terms of material budget, range of intensities measured, and active area size. In addition, it has particle counting capabilities, which could extend its application to momentum spectrometry or Time-of-Flight (ToF) measurements. Its resistance to radiation damage offers good potential for longevity of use.

A first prototype of a SciFi-SiPM monitor has been successfully tested with different particle beams at CERN, giving accurate profile measurements over a wide range of energies and intensities. It has only shown problems during use with lead ion beams, whose origin is believed to be crosstalk between the fibres.

A Geant4 simulation of a single scintillating fibre has been performed to estimate its signal generation. This simulation is verified by real measurements of the light yield of scintillating fibres. Similarly, another Geant4 simulation of a full SciFi monitor has been developed to characterise the perturbation of the beam by the monitor.

The future beam instrumentation for the Neutrino Platform at CERN is also described here, which is being developed as a continuation of the work conducted during this thesis.

Key words: *CERN, Experimental areas, Secondary beam, Beam Instrumentation, Profile monitor, Charged-particle tracking, Scintillating fibres (SciFi), Silicon photomultipliers (SiPM), Momentum spectrometer, Time-of-Flight (ToF), Neutrino Platform.*

Résumé

Les accélérateurs du CERN délivrent une grande variété de faisceaux secondaires aux Zones Expérimentales. Ces faisceaux sont composés de hadrons, de leptons et d'ions lourds, présentant de grandes variations tant en quantités de mouvement (de $1\,\mathrm{GeV/c}$ à $400\,\mathrm{GeV/c}$) et qu'en intensité (de 10^2 à 10^8 particules par seconde). Le profil, la position et l'intensité de ces faisceaux sont mesurés en utilisant des détecteurs de particules. Cependant, les systèmes actuels présentent plusieurs inconvénients qui limitent la qualité de mesure.

Le but de ce travail de recherche est d'étudier la meilleure technologie de détection qui pourrait remplacer les capteurs existants et d'en construire un premier prototype. L'examen des techniques de détection actuelles et récentes a conduit au choix des Fibres Scintillantes (SciFi) lues avec des Photomultiplicateurs en Silicium (SiPM). Cette technologie de détection offre de nombreux avantages en termes de 'material budget', de gamme d'intensités mesurées et de taille de la zone active. En outre, elle permet la détection de particules individuelles, ce qui pourrait étendre le champ d'application à la spectrométrie et la mesure de temps de vol (ToF). Sa bonne résistance aux radiations est une garantie pour des années de fonctionnement.

Un premier prototype d'un moniteur SciFi-SiPM a été testé avec succès sur différents faisceaux au CERN, ce qui a permis d'obtenir des mesures de profil précises sur une large gamme d'énergies et d'intensités. Seuls des problèmes attribués à la diaphonie entre les fibres ont été rencontrés avec des faisceaux d'ions plomb.

Une simulation sur Geant4 d'une seule fibre scintillante a été réalisée pour estimer le signal généré par celle-ci, dont le résultat a été confirmé par une mesure réelle de la lumière produite par des fibres scintillantes. De la même manière, une autre simulation sur Geant4 d'un moniteur SciFi intégral a été effectuée pour caractériser la perturbation des faisceaux due au moniteur.

La future instrumentation pour les faisceaux de la Neutrino Platform au CERN y est également décrite, laquelle sera développée comme une prolongation de ce travail.

Mots clefs : *CERN, Zones expérimentales, Faisceaux secondaires, Instrumentation pour accélérateurs de particules, Moniteurs de profil, Traçage de particules chargées, Fibres scintillantes (SciFi), Photomultiplicateurs en silicium (SiPM), Spectrométrie de faisceaux secondaires, Mesure de temps de vol (ToF), Neutrino Platform.*

Contents

Contents

Contents

Chapter 1

Introduction

This chapter introduces the CERN experimental areas and the secondary beams. It serves as background for the objective of this research work: the development of a new profile monitor for those secondary beams. An overview of the CERN accelerator complex is outlined, which helps to understand some of the characteristics of these particle beams. A brief description of the monitors currently used is also given.

1.1 The CERN Accelerators

The European Organisation for Nuclear Research (CERN) is one of the largest particle physics laboratories in the world and has as main mission to provide the necessary infrastructure for research on high-energy physics. Among other facilities, the laboratory counts with several particle accelerators that deliver beams of diverse types of particles over a wide range of energies and intensities. As can be seen in fig. 1.1, the major active accelerators are the Proton Synchrotron (PS), the Super Proton Synchrotron (SPS), and the Large Hadron Collider (LHC); these machines have a broad history and have paved the road for significant discoveries in particle physics.
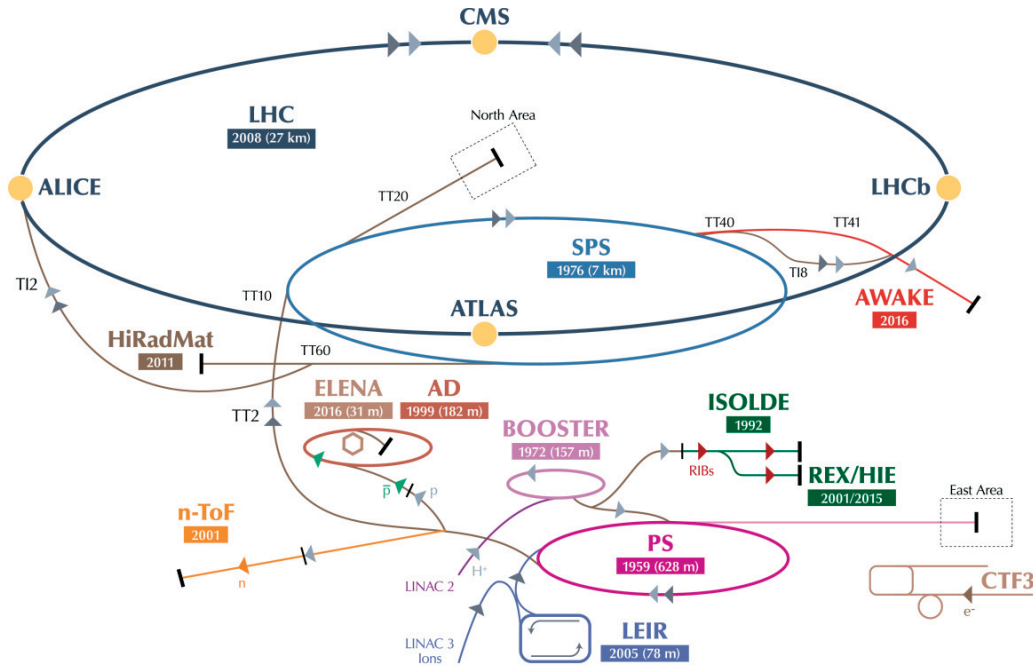
Figure 1.1 – Diagram of the CERN accelerator complex in 2017. (Copyright: CERN).

1.1.1 The Accelerator Complex

In the present configuration, the PS, the SPS, and the LHC form an accelerating chain where the beam is injected from one machine into the next one, in order to increase its energy. The PS is the first and oldest accelerator in this chain, dating from 1959. It is composed of almost three hundred conventional electromagnets forming a circumference of 628 metres. It receives protons from the Proton Synchrotron Booster (PSB) or heavy ions from the Low Energy Ion Ring (LEIR), for the purpose of accelerating them to $25\,\mathrm{GeV/c/Z}$. Once the particles reach that momentum, they can be injected into the SPS or be extracted to several experimental facilities. Among these facilities, there are the Antiproton Decelerator (AD), the Neutron Time-Of-Flight installation (n-TOF), and the *East Area Experimental Hall.*

The SPS is a circular accelerator of $6.9\,\mathrm{km}$ length that accelerates the particles received from the PS up to $450\,\mathrm{GeV/c/Z}$. In the past, this machine has worked as a collider, but now its beams are injected into the LHC or extracted to experimental installations, like the High Radiation to Materials facility (HiRadMat), the Proton Driven Plasma Wakefield Experiment (AWAKE), and the *North Area.*

The LHC is the last and largest accelerator, designed to serve as a collider. Its $27\,\mathrm{km}$ long circumference is mainly composed of superconducting magnets, allowing a maximum design energy of $7\,\mathrm{TeV/c/Z}$ per circulating beam, thus making it the most powerful particle accelerator in the world.

1.2 The East and North Experimental Areas

This manuscript is focused on the East and North Experimental Areas (EA) [1], since the main objective of this research project is to develop a new beam profile monitor for these installations. These facilities host a multitude of fixed-target experiments and test beams used for research on high-energy physics, detectors R&D, education, and the study of the effects of radiation on materials and electronics, among others.

The most common type of beam delivered to these facilities are *secondary beams*. A secondary beam is composed of particles produced in the collision of high-energy protons with certain special targets, principally beryllium. As a result, diverse hadron and lepton species are created with lower energy and a wider momentum spread. Thereupon, they can be selected by systems of magnets and filters, and be sent to the experiments (fig. 1.2).

Depending on the requirements of the experiment, a second target can be added to the beam line in order to create *tertiary beams*, which have lower energy and intensity than the secondary beams.

Under some special conditions, attenuated *primary beams* formed by particles directly extracted from the accelerator can be also delivered, such as protons, lead ions, or other ion species.
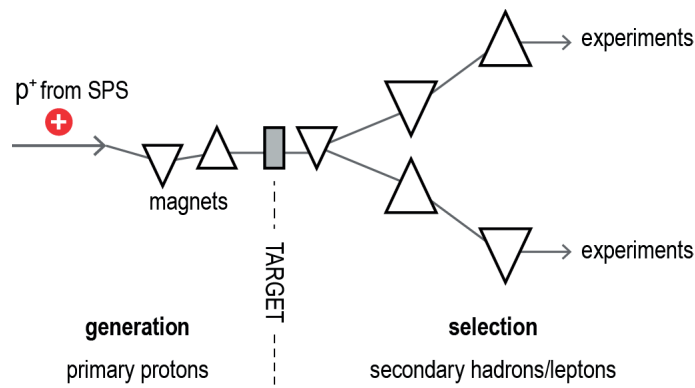
Figure 1.2 – Schematic of the creation of a secondary beam in the EA.

To produce a secondary beam, around 10^{13} high-energy primary protons are collided with the target during an extraction. However, the creation of secondary beams is not very efficient and only a maximum of approximately 10^8 secondary particles can be harnessed. The final energy and intensity of the beam can be selected by the users, making these beam lines very versatile.

1.2.1 The East Area

The *East Area Hall* comprises four beam lines making a total length of $300\,\mathrm{m}$ (fig. 1.3) that are used by ~ 300 scientists in a year, working in many different experiments (fig. 1.4). Its secondary beams have a range of momenta from $1\,\mathrm{GeV/c}$ to $15\,\mathrm{GeV/c}$ and intensities between 10^3 to 10^6 particles/extraction. The extractions last $400\,\mathrm{ms}$ and there is typically one every $33.6\,\mathrm{s}$.
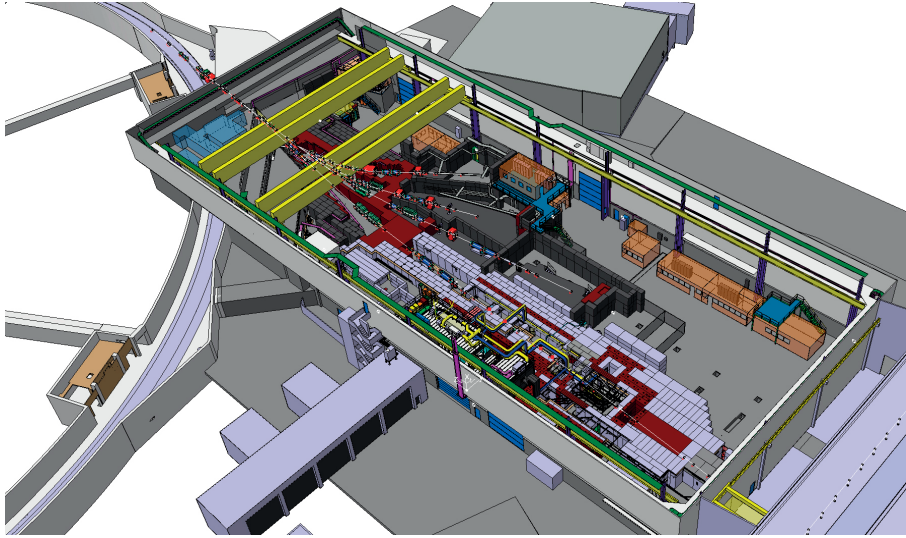
Figure 1.3 – Aerial 3D image of the East Area Hall showing the PS extraction on the left-upper part.
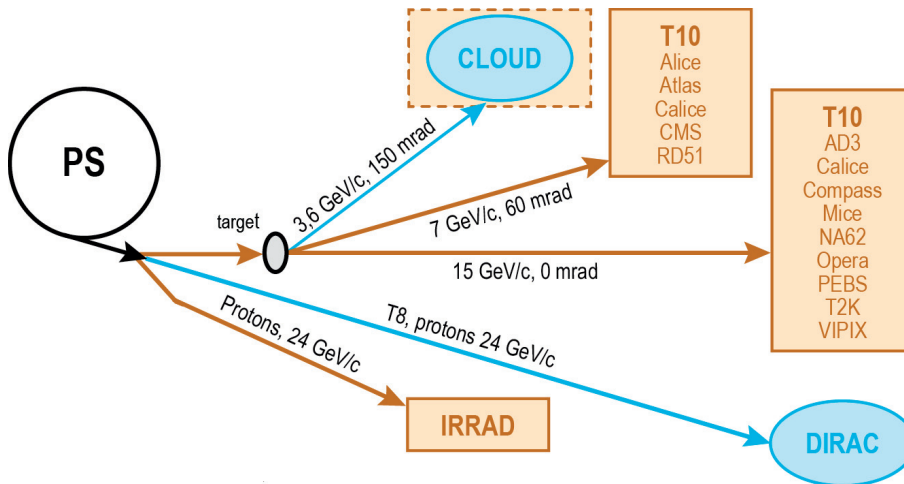
Figure 1.4 – Experimental layout of the East Area in 2009.

1.2.2 The North Area

The *North Area* is the largest experimental area at CERN with six beam lines that make a total length of 5.8 km. It dates from 1978 (fig. 1.5) and nowadays it accommodates numerous experiments where more than 2,000 visitor scientists work throughout a year.

Figure 1.5 – General view of the Experimental Hall EHN1 in the SPS North Area, 1978. Photograph kindly offered by CERN (copyright CERN).

The North Area is divided into three experimental halls, as shown in fig. 1.6: EHN1, EHN2, and ECN3 (respectively, Experimental Halls North 1 and 2, and Experimental Cave North 3). Three primary targets, called T2, T4, and T6, provide secondary beams in addition to protons and ions directly extracted from the SPS (fig. 1.7).
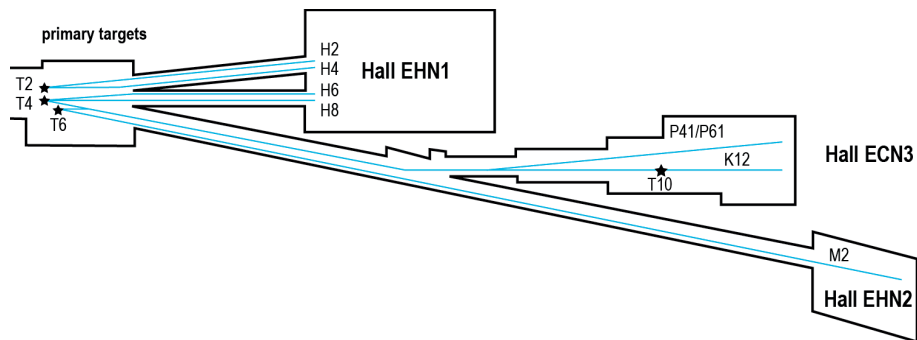
Figure 1.6 – Experimental layout of the SPS North Area experimental facility.

EHN2 is the experimental hall of the M2 beam line, which provides ultra-high intensity muon and hadron beams. At present it hosts the COMPASS experiment [2].

Figure 1.7 – View of the target hall showing the targets stations, in brown at the back, and the secondary beams towards North Area experimental halls at the front. Photograph kindly offered by CERN (copyright CERN).

Two beam lines end in ECN3, the K12 beam line that provides high-intensity beams of kaons or muons, and P41 with attenuated primary protons.

EHN1 is the largest hall with four beam lines (H2, H4, H6, and H8) and several permanent experiments and test zones (fig. 1.8). The beam lines of EHN1 have a general purpose and are highly configurable by the users.
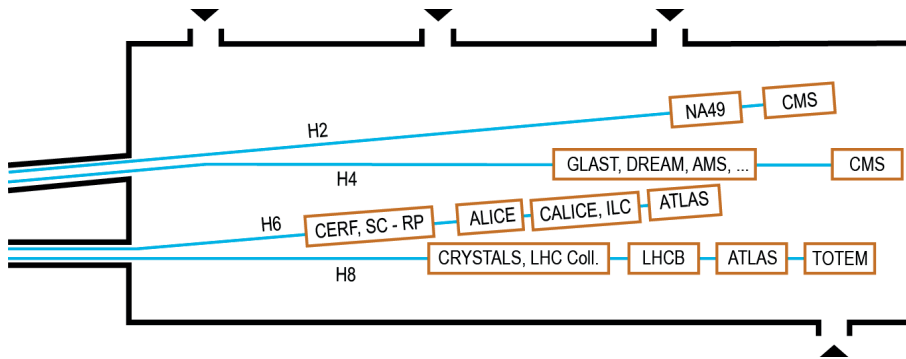
Figure 1.8 – Layout of the EHN1 hall in 2009.

1.2.3 Description of the EHN1 Beams

The beam lines of EHN1 (H2, H4, H6, and H8) have a general-purpose, serving from detector R&D to physics research. They provide high-resolution secondary and tertiary beams of charged particles, with a range of momenta within $10\,\text{GeV/c}$ to $400\,\text{GeV/c}$, and intensities from 10^3 to 10^8 particles per extraction.

Some of these beam lines can also provide lead ion beams ($^{208}\text{Pb}^{+82}$) directly extracted from the SPS, with a maximum momentum of $400\,\text{GeV/c/Z}$, and a maximum intensity of 10^6 Pb ions/burst. In a similar way, under certain conditions they can also provide attenuated proton beams, up to $450\,\text{GeV/c}$, directly extracted from the SPS.

Table 1.1 summarises the different particle species found in the EHN1 beams, along with their typical momenta and intensities.

Table 1.1 – Common types of particles in the EHN1 beams, their ranges of momenta, and intensities.

Beam type	Particle	Momentum (GeV/c/Z)	Max. Intensity (part/second)
Primary	p^+	400 - 450	10^7
	$^{208}\text{Pb}^{+82}$	32 - 380	10^7
Secondary	π^+/π^-	20 - 360	10^7
	e^+/e^-	10 - 350	10^6
	μ^+/μ^-	12 - 200	10^5
	other hadrons at lower I (K, p^-, ...)		
Tertiary	π^+/π^-	0.5 - 200	10^4
	e^+/e^-	0.5 - 100	10^4

The production of particles in proton-beryllium collisions at $400\,\text{GeV/c}$ is very well documented [3], which allows to predict the composition of the secondary beams. For example, fig. 1.9 shows the fraction of different hadron species in secondary beams as a function of the momentum.

The users of the beam line can tune some beam line elements (magnets, collimators, and secondary targets among others) in order to get a beam with the sought particle composition and characteristics. By introducing secondary targets in the beam line, it is possible to further change the beam composition, filtering particles to produce purer beams, or by creating new particle species. For example, almost pure hadron beams can be obtained using polyethylene and copper targets, and pure electron/positron beams can be produced by means of a Pb target.
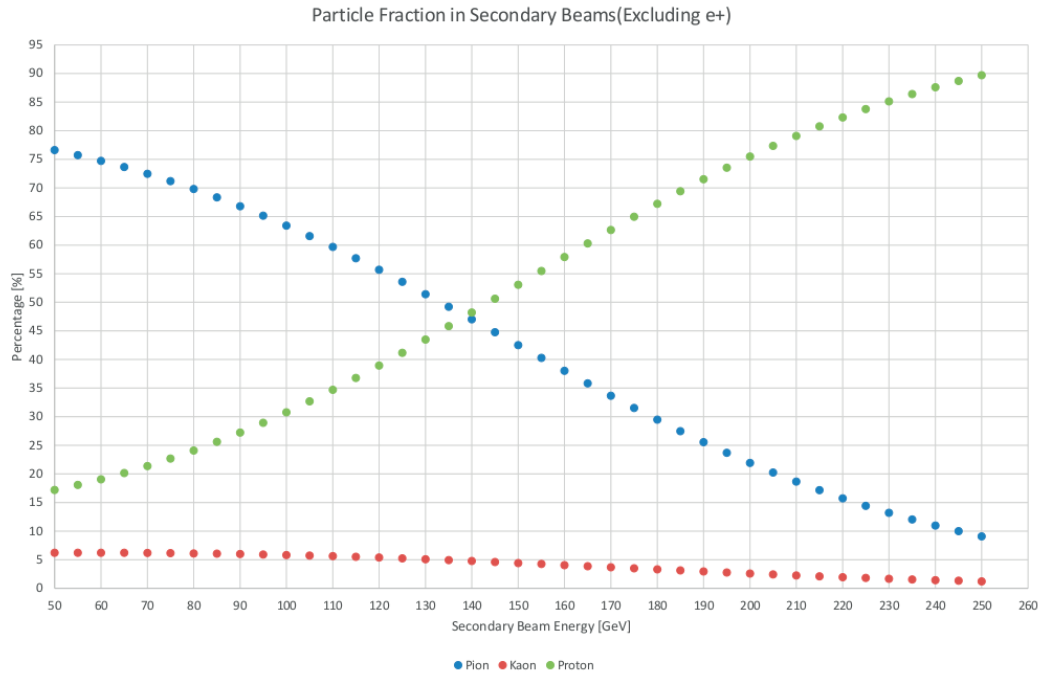
Figure 1.9 – Calculation of the hadron fraction of secondary beams as a function of the beam energy. Source: [3].

Slow Extraction

The delivery of beams to the North Area is done slowly, in a process that commonly lasts 4.8 or 9.6 seconds. Such *slow extraction* is achieved by inducing high-order resonances in the SPS which provoke that only a small number of particles per turn exit the accelerator; thus, a slow extraction requires 200,000 or 400,000 turns to empty the machine.

There is typically one or two extractions every 40.8 s, although this number is determined by the organisation of the SPS super-cycle (number of experiments requiring beams and injection to the LHC). Hereinafter, a beam extracted to the experimental areas will be referred indifferently to as a *burst* or *spill*.

1.2.4 EHN1 Extension: The CERN Neutrino Platform

The experimental hall EHN1 is being extended to host a new test facility within the framework of the CERN Neutrino Platform programme. This programme gathers an international collaboration on neutrino research that is materialised at CERN, among other projects, with protoDUNE: the construction of two large-scale prototypes of neutrino detectors for the Deep Underground Neutrino Experiment (DUNE) [4] [5].

The objective of protoDUNE is to investigate the feasibility of two different technologies for large liquid-argon time-projection chambers (fig. 1.10). For that purpose, two detectors (NP-02 and NP-04) filled with ~ 700 tons of liquid argon will be characterised with charged particle beams at CERN. The characterisation requires low energy and low intensity beams: $1\,\text{GeV}$ to $15\,\text{GeV}$ and a maximum of 100 particles/s, which requires an adaptation of the existing beam lines. In consequence, H2 and H4 are being extended to provide tertiary beams to NP-02 and NP-04, respectively (fig. 1.11 and fig. 1.12).

Figure 1.10 – Assembly works carried on the external frame that will host the liquid-argon chamber of NP-04.

Figure 1.11 – Layout of the EHN1 extension showing the future location of the neutrino detectors and the beam line extensions.
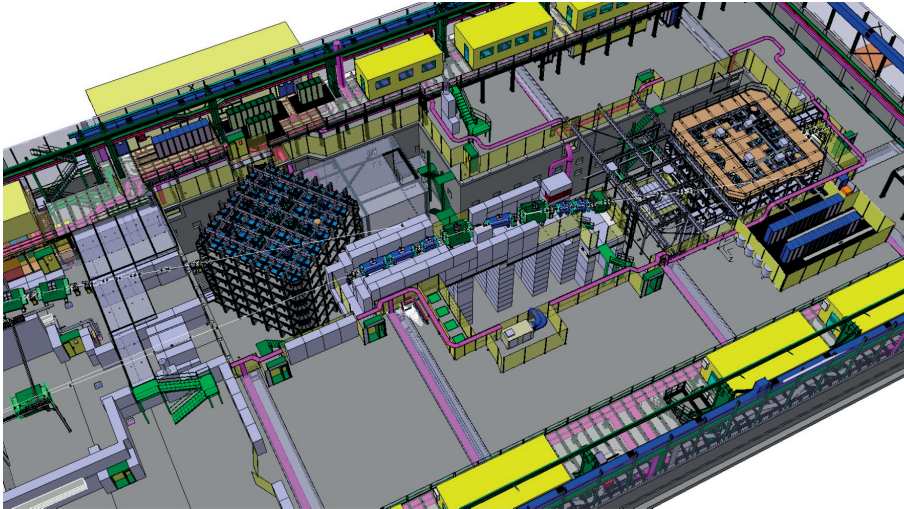
Figure 1.12 – Another view of the EHN1 extension. The beam trajectory is shown as a thin white line that crosses the different beam line elements and reaches the liquid argon tanks.

1.3 Instrumentation of the CERN Experimental Areas

The quality of the beams in the EA is monitored by several types of particle detectors. Some of them are specialised in measuring the position, profile, and intensity, which are the objective of this thesis work; others can provide particle identification or measure the beam energy.

There is a substantial difference between the monitors used in the EA and the monitors for circular accelerators. In circular machines, the beam turns thousands of times per second and, therefore, it is necessary to avoid any material standing in the beam trajectory. If not, the integrity of both the detector and the beam are seriously compromised. In the EA, however, the beam crosses only once and with an intensity several orders of magnitude lower than the circular machines, which allows a monitor to stay in front of the beam and recover information from a direct interaction. In consequence, the monitors of the EA employ technologies closer to the particle detectors of high-energy physics experiments.

1.3.1 Present EA Monitors

The following detectors have been monitoring the EA beam lines for several decades:

- Scintillator paddles (fig. 1.14): these detectors consist in a large scintillator tile coupled to a light-guide and a photomultiplier tube. They count the passage of

every individual particle and they are used for beam intensity measurement and the generation of trigger signals for other detectors.

- Multi-Wire Proportional Chambers (MWPC) [6] (fig. 1.15): this type of gaseous detector is composed of layers of micro-metric metallic wires that are alternated with layers of ultra-thin conductive foils (fig. 1.13). Wires and foils are biased differently with a high voltage (larger than $1\,\text{kV}$), which produces a strong electric field that allows to detect the ionisation of the gas by an impinging particle . By integrating the charge collected by every wire over a spill, the beam profile is reconstructed with a resolution of $1\,\text{mm}$. These chambers do not work properly with beams of intensity lower than $\sim 10^3$ part/s.

- Delay Wire Chambers (DWC) [7] (fig. 1.16): they are similar to MWPC, with the difference that the conductive foils are replaced by another layer of transverse wires, as can be seen in fig. 1.13. Instead of integrating the charge on the wires, the readout of the DWC employs the combination of a Signal Delay Line and a Time-to-Digital Converter (TDC) that is able to infer the place where the ionisation occurred. As a result, individual particle tracks are registered with a resolution better than $200\,\mu\text{m}$. On the negative side, the delay line imposes a dead time on the detector that prevents it from working efficiently above particle rates of some kHz.

- Filament Scintillators (FISC) (fig. 1.17): these detectors consist in a thin scintillator filament that scans the beam thanks to a motor system. Two photomultiplier tubes detect the scintillation light produced and the beam profile is reconstructed by correlating the position of the filament with the signals from the photomultipliers. It can work on a fast or slow mode: in the fast mode, a full scan of the beam is done in one spill by moving the sheet rapidly; in the slow mode, the scan is done through several spills by slowly moving the sheet one step every spill. The larger the number of steps, the higher the profile resolution, with a limitation of $200\,\mu\text{m}$. A disadvantage of these detectors is that they need a long time (several minutes) to produce a profile at low intensities ($<10^3$ part/s) or with high resolution.

- Threshold Cherenkov Counters (CET) (fig. 1.18): these monitors do not measure the profile, but identify particles by counting the number of Cherenkov photons created by a particle in a gas (the Cherenkov process is described in appendix A.2.4). By changing the pressure and the gas type it is possible to identify several particle species over a wide range of momenta.

- CEDAR Counters (fig. 1.18): these detectors, based also on the emission of Cherenkov radiation, have a complex optical system that processes the light, allowing to recognise the characteristic Cherenkov ring pattern. This allows particle identification at high momenta.
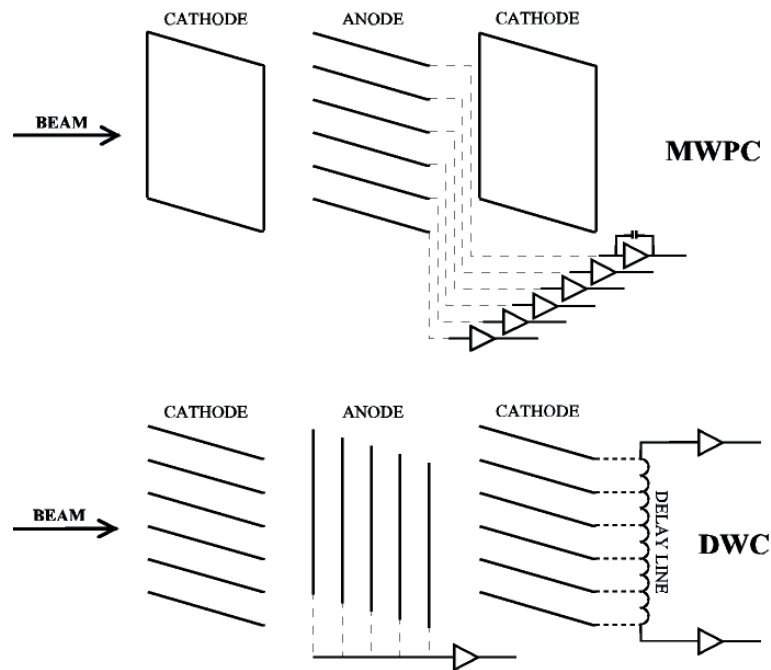
Figure 1.13 – Operating diagram of a MWPC and a DWC.
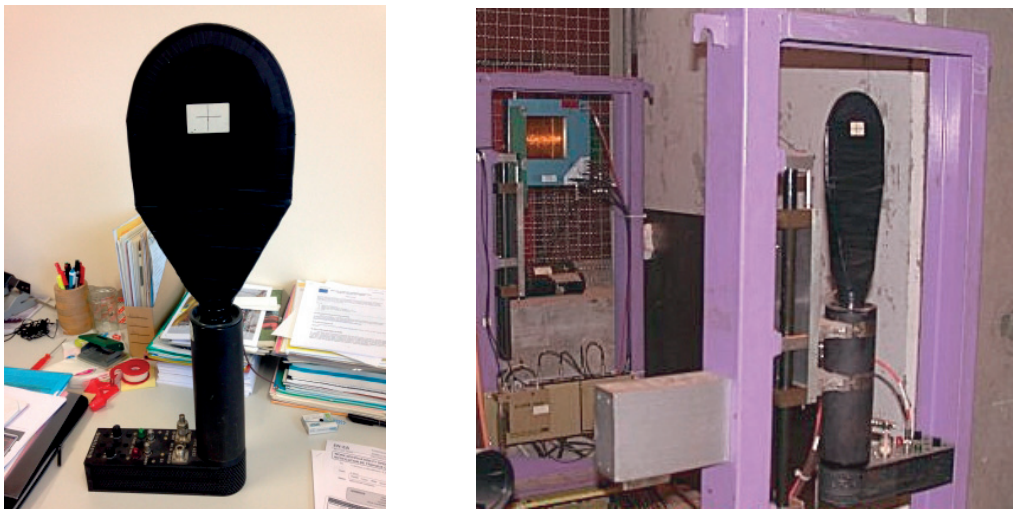
Figure 1.14 – Scintillator paddle with attached photomultiplier tube at the laboratory (left) and installed in the North Area (right). *Note: a DWC can be noticed at the back of the right picture.*

1.3.2 Need for New Monitors

The current profile monitors have worked satisfactorily for decades, however there is a need to renovate some of them, particularly the MWPC and the DWC, since they are showing symptoms of ageing. The production of these chambers is cumbersome, especially
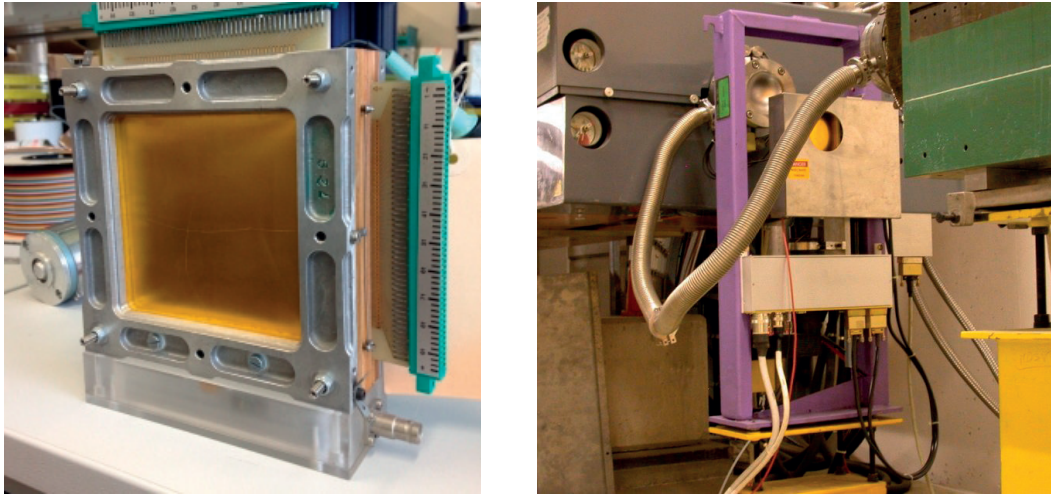
Figure 1.15 – MWPC at the laboratory (left) and in a beam line (right). The monitor is equipped with a motor system that allows removing it from the line when is not being used.
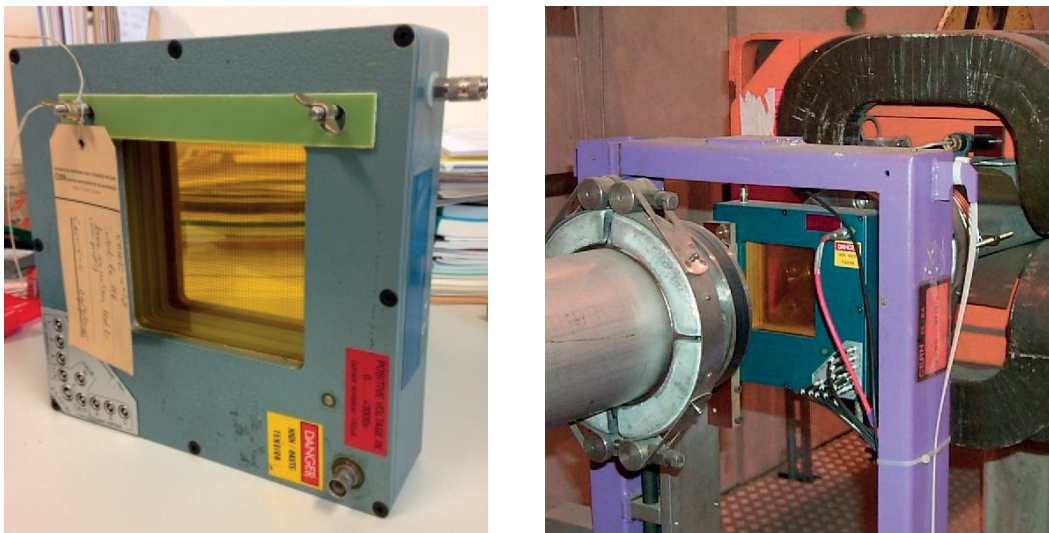
Figure 1.16 – DWC at the laboratory (left) and placed in front of a dipole magnet (right).

regarding the positioning of the thin wires, and the expertise on their assembly techniques has gradually been lost. Additionally, the present monitors have design limitations that make them unsuitable for the upcoming extension of the North Area. The new beam lines need an instrumentation with a large active area of $200\,\text{mm} \times 200\,\text{mm}$ and capable of detecting individual particle tracks (more information in section 7.1). The DWC is the only monitor that can detect individual particles, however is limited in size to $100\,\text{mm} \times 100\,\text{mm}$.

Hence, the motivation of this PhD work is to investigate a new profile monitor that
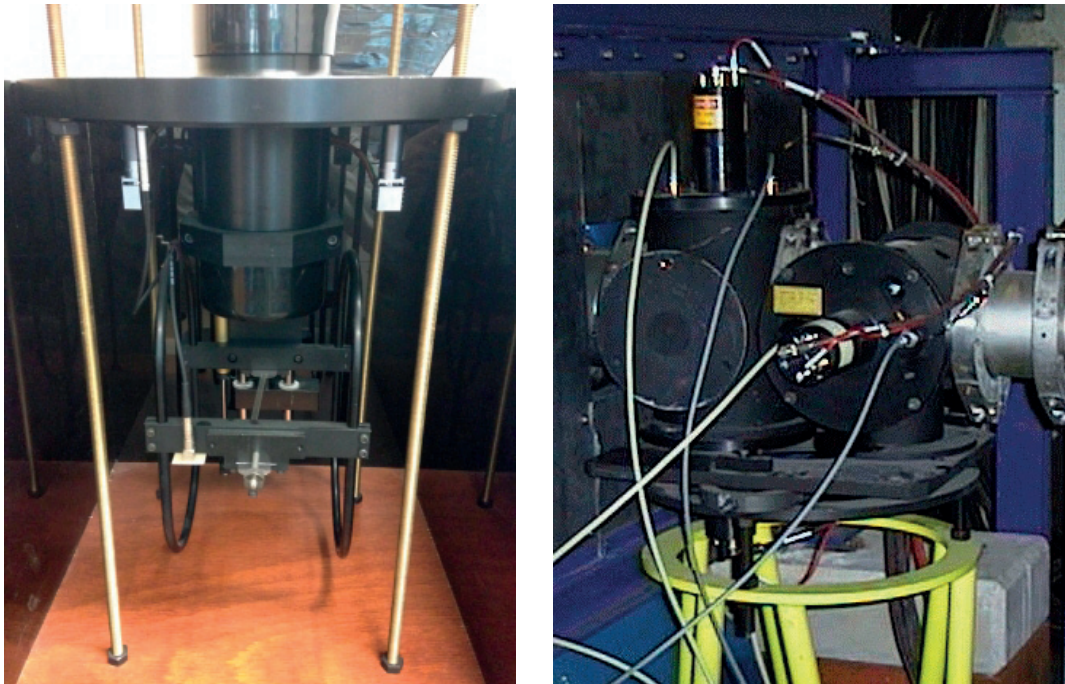
Figure 1.17 – Interior of a FISC (left); the thin scintillator filament can be noticed in the middle (transparent white), held by the motorisation system (the detector shown has an educational purpose and only equips one photomultiplier tube). A complete system of FISC on a beam line (two tanks, for horizontal and vertical profile) can be seen on the right image.

Figure 1.18 – Left image: CET monitor with gas pressure control system. Right image: CEDAR installed in a North Area beam.

can fulfil the requirements of the EA and the EHN1 extension, and improve whether is possible the performance of the present monitors.

Chapter 2

Review of Detection Techniques

This chapter defines the required performance and characteristics of the new beam monitor. Thereupon, the most common type of particle detectors meeting those requirements are reviewed, which finally leads to the choice of one of them for a first prototype of the monitor.

2.1   Requirements of the new Beam Profile Monitor

The specific requirements of the new monitor, according the characteristics of the EA beams (section 1.2), are summarised hereafter:

- Sensitivity and efficiency: the detector should be sensitive to all types of charged particles. A large detection efficiency is not needed when only a reconstruction of the beam profile is sought. Nevertheless, if the monitor is used for other applications, such as spectrometry or time-of-flight, an efficiency close to 100% is desirable.

- Spatial resolution: it should be fine enough to resolve the beam size; a value of 1 mm is typically sufficient.

- Maximum operating frequency: it is determined by the intensity of the secondary beams, which can be as high as 7.5×10^8 particles/s.

- Dynamic range: the detector should have a constant response over a wide energy region of $1\,\text{GeV}$ to $400\,\text{GeV}$.

- Material budget: it has to be minimised to avoid beam scattering and energy dispersion. Therefore, materials with low density and high radiation length are favoured (further explained in appendix A.6).

- Active area: the EA monitors typically exist in two formats, $10\,\text{cm} \times 10\,\text{cm}$ and $20\,\text{cm} \times 20\,\text{cm}$.

- Radiation hardness: the monitor has to withstand the passage of high fluxes of diverse types of particles at different energies. A detector moderately radiation-hard that could work uninterruptedly for several years is preferred.

- Robustness and maintenance: the monitors are expected to work without assistance for months. Because the access to them is rare during beam line operation, they should be reliable and have a low failure rate. The maintenance should be also simple and not require a profound knowledge of the detector. A modular design with easily replaceable parts would facilitate the maintenance and would also be more cost-efficient.

- Cost: typically, the higher the performance, the higher the cost. An optimum compromise between performance and cost must be found.

2.2 Review of the most common Tracker Detectors

The new beam profile monitor has to register the tracks of individual particles, whilst minimising the perturbation on its energy and trajectory. Therefore, it resembles what in high-energy physics is commonly called a *tracker detector*.

The most widely used tracker detectors in high-energy physics are founded on three technologies: *gaseous chambers*, *semiconductors*, and *scintillators*.

2.2.1 Gaseous Detectors

The principle of detection of gaseous detectors is the ionisation of gas molecules inside a chamber subjected to a high voltage. As a result of the ionisation, pairs of electrons and ions are created and transported by electric fields to the readout electrodes.

Gaseous detectors for tracking applications can be divided in two categories: *Wire Chambers* and *Micro-Pattern Gaseous Detectors*. The MWPC and the DWC currently installed in the EA belong to the wire chamber classification. Among the micro-pattern detectors, the major exponents are *Micromegas* and *Gas Electron Multipliers* (GEM).

GEM

The basis of a GEM detector is a thin foil of metal-coated polymer with a high density of micro pierced holes (fig. 2.1) [8]. The two sides of the foil are biased in order to create a strong electric field within the holes (fig. 2.2). With such arrangement, the electrons from the primary ionisations are attracted towards the holes, where the strong fields produce an avalanche that greatly multiplies the strength of the signal. Multiple GEM foil can be stacked, to further increase the multiplicative effect.
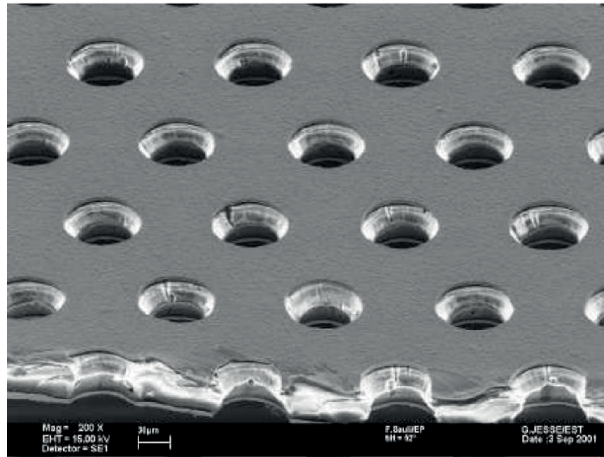
Figure 2.1 – Electron microscope image of a GEM foil. The holes pitch and diameter are $140\,\mu$m and $70\,\mu$m, respectively. Image from: [8].

The avalanche electrons are finally collected by the readout electrode anodes, typically strips or pixels (fig. 2.3). Their size and pitch greatly determine the spatial resolution of the detector.

The main advantages of GEM are their high gain, stability, robustness, and low-cost production techniques.

The COMPASS experiment, installed in the North Area, is a pioneer in the use of large area GEM ($31\,\text{cm} \times 31\,\text{cm}$), for the tracking of high rate secondary beams (up to $10^5\,\text{part/s/mm}^2$) [9]. Its performance strongly depends on the type of gas mixture and the operating voltage, with typical values of $40\,\mu$m to $100\,\mu$m for the spatial resolution and 90% to 99% for the detection efficiency. The material budget of one detector, comprising the GEM foils, gas windows, and support structure is kept around 0.7% x/X_0. This detector is relatively radiation-hard, being able to withstand accumulated fluxes of $\sim 10^{13}$ MIP/cm^2 before showing damage.
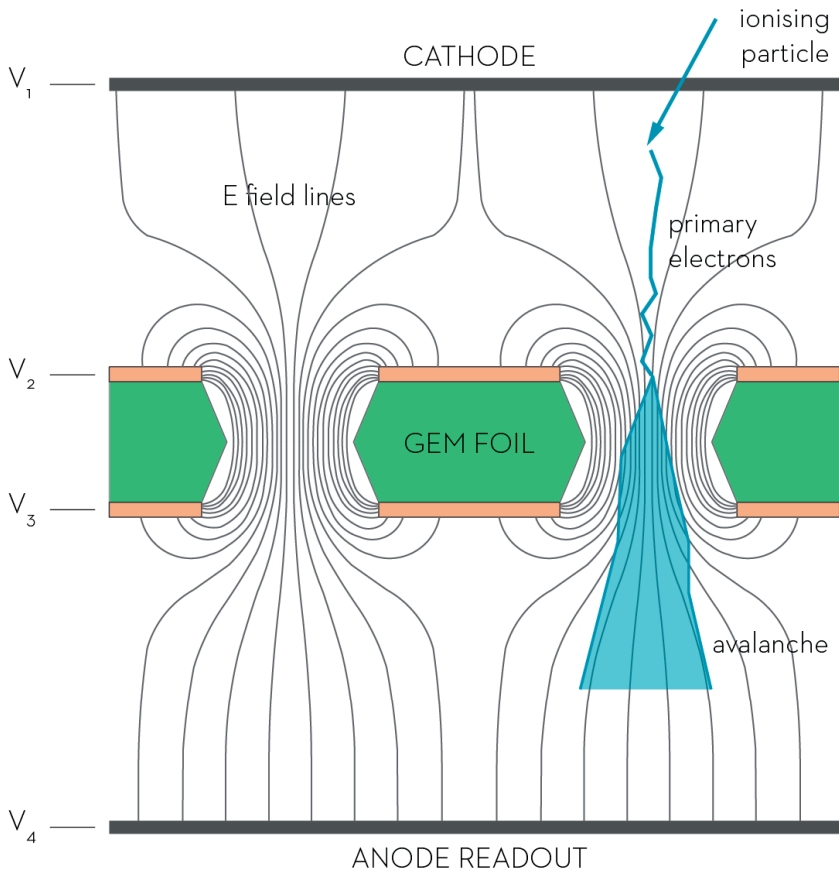
Figure 2.2 – Electric field lines in a GEM and multiplication of a primary ionisation.
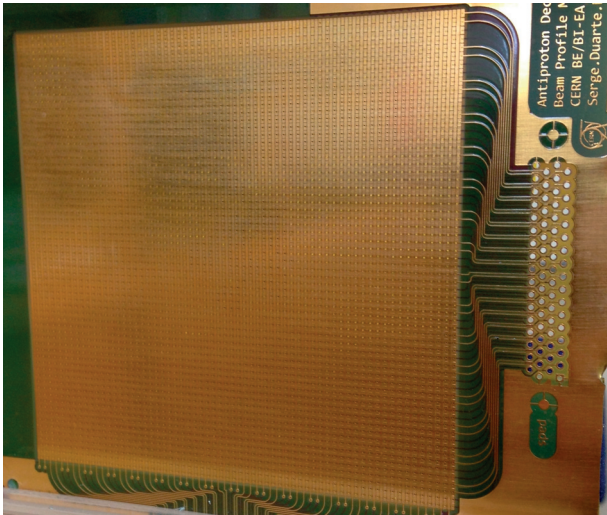
Figure 2.3 – Pixelated readout of a GEM detector.

Micromegas

The distinctive feature of Micromegas is a fine micro-mesh that divides the gas volume into two regions: a large one where the primary ionisation occurs and another one, micrometric, where a strong avalanche multiplies the ionisation electrons (fig. 2.4). The micro-mesh can be a physical metal layer sustained by tiny pillars (bulk Micromegas, fig. 2.5) or be based on Kapton etching technology (microbulk Micromegas).

Similarly to GEM, the avalanche electrons are collected by a set of readout electrodes, pixels or strips, that determine the spatial resolution of the detector. Micromegas also show high internal gain, are stable and robust.
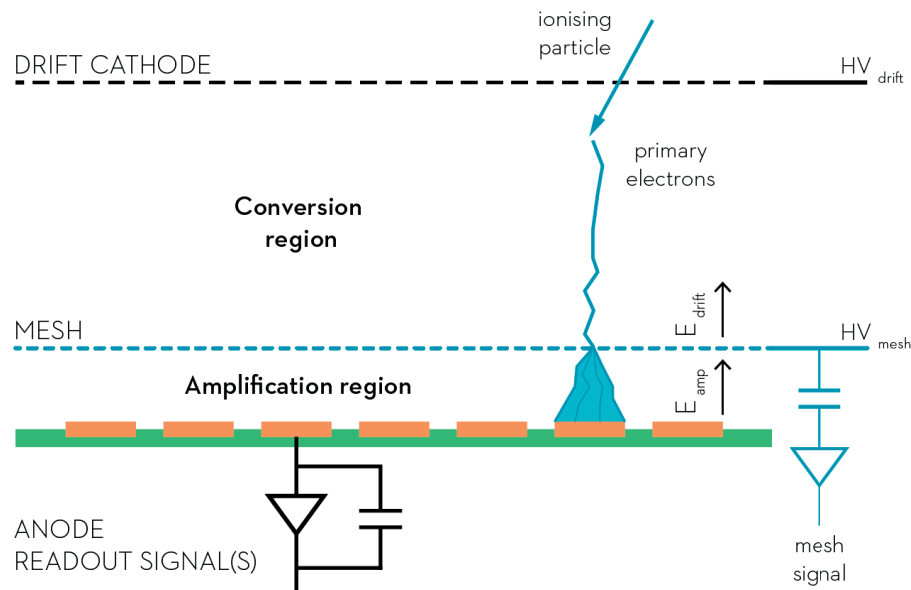
Figure 2.4 – Signal creation in a Micromegas detector. The image is not to scale for illustrative purposes: the distance between the mesh and the anode readout is typically micrometric.

A large area Micromegas of $26\,\text{cm} \times 36\,\text{cm}$ has been also developed by the COMPASS experiment for the tracking of secondary beams up to 3×10^5 part/s/mm^2 [10]. Like the GEM, its performance is highly dependent on the operating voltage and the gas mixture. Resolutions of $50\,\mu\text{m}$ and efficiencies above 95% are reported [10]. The material budget is greatly reduced to 0.45% x/X_0, thanks to the design of a sophisticated epoxy support and honey-comb structure to hold the detector. Its radiation hardness is similar to that of the GEM.

A common problem of both GEM and Micromegas is the random occurrence of discharges that can harm permanently the detector and shorten its lifespan. These sparks produce microscopic breakdowns in the dielectric materials, making unusable that area of the detector. The damage is almost impossible to repair.
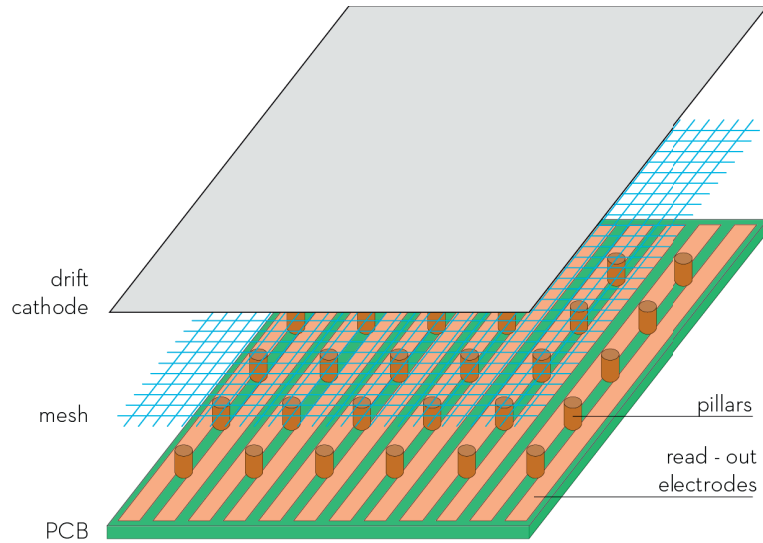
Figure 2.5 – Structure of a bulk Micromegas and its main components.

The phenomenon of discharges can be reduced by operating the detector at lower voltages, although in exchange for detector performance. The probability of sparks also increases with the particle flux and for heavy, highly ionising particles.

2.2.2   Semiconductor Detectors

The working principle of semiconductor detectors is similar to gaseous chambers, with the difference that the ionisation medium is a semiconductor instead of a gas. Therefore, a crossing particle ionises the semiconductor, typically silicon, creating electron-hole pairs that are transported by electric fields to the corresponding readout electrodes (fig. 2.6). Compared to gaseous detectors, the average energy required to create electron-hole pairs is lower, resulting in an increased number of carriers per same amount of energy deposited. Additionally, semiconductors have larger stopping power than gases due to their higher densities (more on the stopping power in appendix A.3), which means that the particles deposit more energy in comparison.

Despite the high number of primary carriers, these detectors have little internal gain and low-noise preamplifiers are required to process the weak currents produced by the electron-hole flow. These electronics are thus a critical part of the detector and must be placed very close to it.
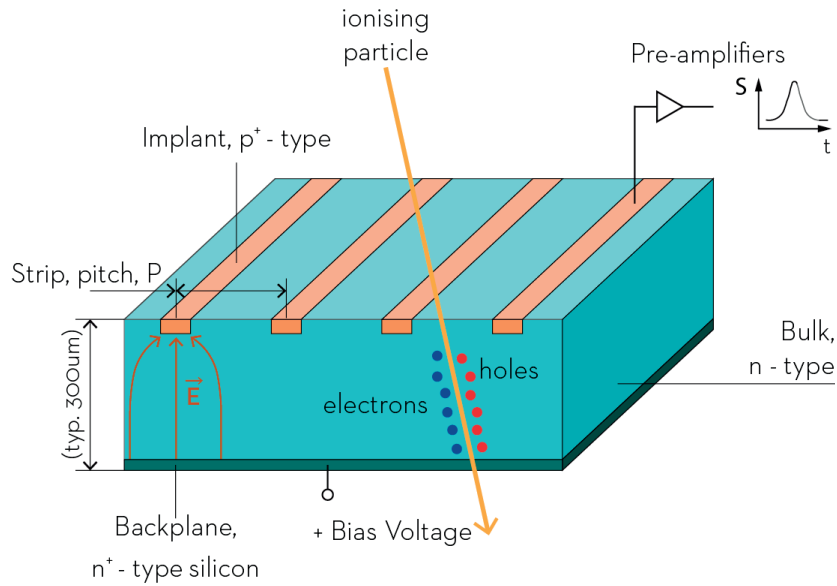
Figure 2.6 – Illustration of the working principle of a silicon detector with strip readout electrodes.

Performance

The detection efficiency of semiconductor detectors is mainly determined by the capability of the electronics to discriminate signal currents from noise currents, the so-called signal-to-noise ratio. The number of signal carriers can be augmented by increasing the operating voltage, but at the expense of a higher leakage current in the semiconductor junction, which is the major source of noise. The signal-to-noise ratio can be greatly improved by cooling-down the detector; this, in fact, is necessary for most of the applications.

One of the major advantages of these detectors is their fine spatial resolution, of typically a few microns for both micro-strip and pixel detectors.

Regarding the material budget, the thickness of the silicon substrate usually ranges between 200 and 500 microns, although the total detector ensemble must include mechanical support structures or even sometimes coupled electronics. For example, the FE-I4 telescope [11], frequently used in the North Area beams by users that need a high precision tracking, is composed of $350\,\mu\text{m}$ of Si, plus a support structure of $100\,\mu\text{m}$ of aluminium and a certain quantity of ABS plastic to enclose the detector. This ensemble yields a material budget around 0.5% x/X_0.

The hit efficiency of the FE-I4 is close to 100% and its spatial resolution can achieve $10\,\mu\text{m}$. It has been successfully tested at rates of $10^4\,\text{Hz/mm}^2$, although its maximum design intensity is $10^6\,\text{Hz/mm}^2$. Its active area is $2\,\text{cm} \times 1.7\,\text{cm}$, which needs to be cooled down to $-75\,^\circ\text{C}$ by means of an oil cooling system.

Semiconductor detectors are sensitive to radiation damage, being the main effect an accumulative increase in the leakage current that debilitates the signal-to-noise ratio. LHC experiments typically require these detectors to work until integrated fluxes of 10^{14} hadrons/cm^2 have been reached.

To increase the radiation hardness, diamond can be used as ionisation medium in substitution of semiconductors. However, diamond is a very costly material which makes these type of detectors non feasible for large area applications.

Since preamplifiers are often placed close to the detector, under the influx of radiation, they are also required to be radiation-hard.

2.2.3 Scintillators

Scintillator detectors have been extensively used in physics since the beginning of the 20$^{\text{th}}$ century. Their working principle is the emission of light as a result of the interaction with an ionising particle and the detection of that light by a *photodetector*. There exist several types of scintillating materials with different properties that make them more suited to a specific application. Due to their versatility, scintillators are largely utilised outside high-energy physics.

In the recent years, a format of scintillator especially adapted to high resolution tracking is attracting wide attention: plastic scintillating fibres (SciFi). This product has properties of both optical fibres and scintillators: the core of the fibre is made of a plastic scintillator, covered by a thin cladding of acrylic material with lower refractive index. This design allows a fraction of the scintillation light created in the core to be captured and transported to the end of the fibre by total internal reflection.

Plastic scintillating fibres can be manufactured in diverse lengths, thicknesses, cross-section shapes, and with specific optical and radiation-hardness properties depending on the chemicals used. The versatility of the fibres, and the large variety of photodetectors available, allow for many various designs of SciFi detectors.

Performance

Scintillating fibre trackers are typically composed of two or more planes of fibres, positioned perpendicularly, or with a certain degree of rotation, in order to collect enough information to reconstruct the track of the particles.

A common strategy to improve the performance of SciFi detectors is to stagger several layers of fibres within a plane (fig. 2.7). This technique can increase the efficiency of the

detector and its granularity (and therefore improve the spatial resolution). For example, the ATLAS ALFA experiment [12] arranges square fibres of 500 μm width in 10 staggered layers that are shifted 50 μm to each other. With this design, resolutions of 30 μm and efficiencies higher than 90% are achieved.
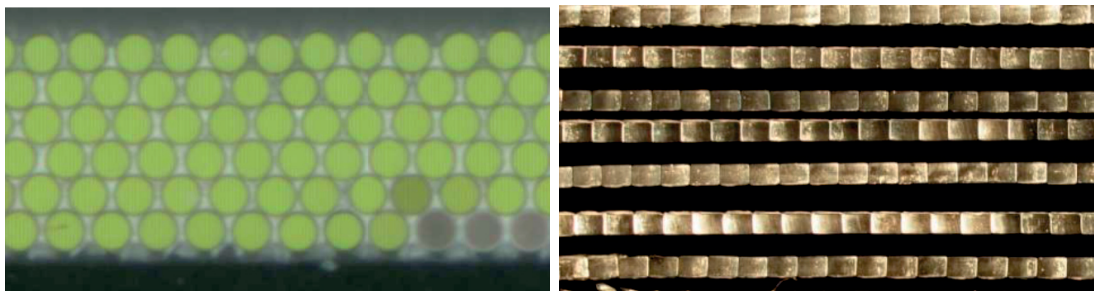
Figure 2.7 – Left image: prototype of a fibre mat for the LHCb SciFi Tracker (image from: [13]). Right image: staggered layers of fibres of an ATLAS ALFA module (image from: [14]).

If the planes are formed by only one layer of fibres, the profile reconstruction resolution would be equal to the thickness of the fibre employed (typically 0.5 mm or 1 mm), and the detection efficiency would be around 90% (being the main limitation the cladding of the fibre, which represents a dead area of the detector). However, fibre planes made of one layer of fibres are notably less complex to build than staggered layers of fibres.

Plastic scintillating fibres have fast rise and decay times of a few nanoseconds, hence, they can potentially handle particle rates up to $\sim 10^8$ particles/second/fibre. However, a limitation in the maximum rate would be due to the photodetector and the associated electronics. The COMPASS experiment has a SciFi hodoscope for beam tracking and timing measurements, composed of 0.5 mm fibres read-out by Multi-Anode Photomultipliers; its maximum operating rate by design is 10^{12} Hz/mm^2 [15] [16].

Scintillating fibres are moderately radiation-hard, showing evident damage from accumulated doses of 10 kGy (which translates into fluencies of $\sim 10^{13}$ MIP/cm^2). The main effect of damage in fibres is manifested as a decrease in the light yield and a worse transmission of light. Photodetectors can also be affected to a lesser extent by stray radiation from the accelerators, since they do not need to stand in front of the beam flux.

The material budget of plastic scintillating fibres is low because they have low density and long X_0. The analytical calculation of the x/X_0 of a scintillating fibre monitor is done in appendix D.1. It shows that a fibre monitor with a total thickness of 1 mm represents 0.24%, and a monitor of 2 mm thickness, 0.48%.

ATLAS ALFA features a gluing technique that allows the fibres to stay inside a primary vacuum while the photodetectors are placed outside, at atmospheric pressure. A similar design for the EA would allow an integration with the vacuum beam pipe in which only

the fibres stand in front of the particle beam. In such case, the use vacuum windows to interrupt the line could be avoided; such windows, and the air in between, increment the material budget of the beam line by $\sim 0.19\%$ (calculated in appendix D.1).

2.3   Choice of a Detection Technique

The four type of detectors reviewed: GEM, Micromegas, semiconductors, and scintillating fibres are suitable candidates for a beam profile monitor. All of them potentially have an excellent performance, can handle high rates, and are radiation-hard enough for the EA. However, the choice of one of them has to be optimised in base of the specific requirements of the EA (section 2.1).

Silicon detectors show a superior performance, but their price per mm^2 is excessively high to produce dozens of detectors with an active area of $100\,mm \times 100\,mm$ and $200\,mm \times 200\,mm$. In consequence, this technology can be discarded from an economic point of view.

There has been a previous attempt to use robust versions of triple-foil GEM detectors for the EA [17] (fig. 2.8). Despite of having a good performance, the material budget of this detector was excessive, which finally forced its disuse. Since Micromegas have a similar material budget, they would show a similar disadvantage.
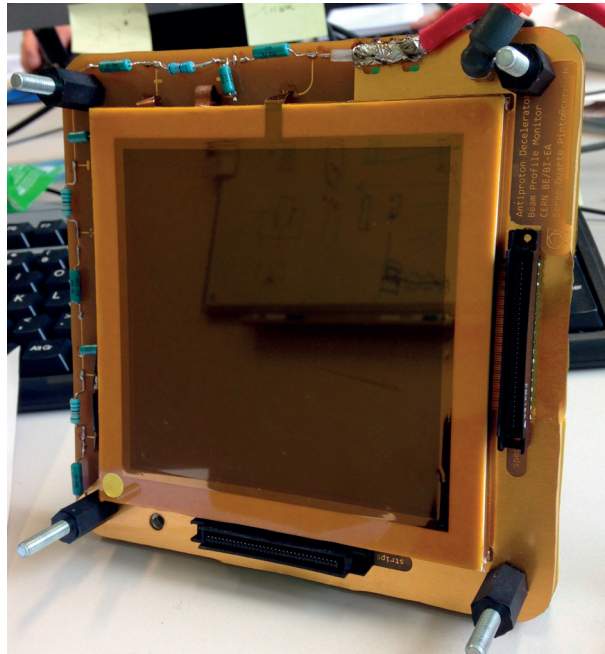
Figure 2.8 – GEM detector developed for the EA, currently used in the Antiproton Decelerator at CERN.

A low material budget version of GEM or Micromegas could be investigated, probably by integrating these detectors in vacuum. However, this solution would require extensive R&D, which favours other detection techniques, such as scintillating fibres, as they can be easily integrated in vacuum by following a similar design to ATLAS ALFA.

Scintillating fibres seem to offer several advantages that encourage their choice for a new beam profile monitor of the EA. A detector based on single layers of fibres would fulfil the requirements of performance, present a low complexity of construction, be easily integrated in vacuum, and have a low cost.

The aforementioned performance of the GEM and Micromegas monitors of COMPASS (section 2.2.1), the FE-I4 silicon telescope (section 2.2.2), and the ATLAS ALFA detector (section 2.2.3) has been used to build the table shown in fig. 2.9, which compares qualitatively these detection techniques. It highlights the points in which they stand out and their negative features:

- In terms of detection efficiency and spatial resolution, silicon detectors clearly offer the best performance.

- Due to the easy integration into vacuum, scintillating fibres have an advantage in terms of material budget.

- GEM, Micromegas, and SciFi are easily scalable to large areas, while semiconductors are not.

- The maintenance of a SciFi monitor would be the simplest, since no gas installation is needed, neither cooling.

	Efficiency & Resolution	Material budget	Active area	Vacuum integration	Maintenance & Cost
GEM			✓	✗	
µMegas			✓	✗	
Silicon	✓		✗	✗	✗
SciFi		✓	✓	✓	✓

Figure 2.9 – Qualitative comparison between the reviewed detection techniques, in terms of the most interesting features for a beam profile monitor of the EA.

A preliminary study with small setups of scintillating fibres (described in appendix C) served to learn the assembly techniques of fibres, and lead the way to a first prototype of

a SciFi beam profile monitor. The construction of this prototype is completely described in chapter 5, and its test in the beam lines is presented in chapter 6.

The main advantages of a SciFi monitor are summarised hereafter:

- It could be completely produced and maintained in a workshop of the Beam Instrumentation group at CERN. Compared to gaseous detectors and semiconductors, which usually require ultra-clean rooms to avoid microscopic dust that can harm the detectors, scintillating fibres can be easily handled in a common workshop with the due attention to cleanliness. Its assembly do not require specialised machinery, or skills, and could be learned by a technician.

- The production cost of such simple fibre detector would probably be the lowest from the reviewed detectors. Scintillating fibres are relatively inexpensive, with prices of a few thousands of CHF per kilometre of fibre. On the contrary, photodetectors can represent an important cost, specially if a large number of channels is required. Nevertheless, the new generation of photodetectors, Silicon Photomultipliers, are undergoing constant developments and reducing their production costs; at present, devices with a price of a few tens of CHF per channel are available.

- Scintillating fibres would easily allow a modular design of the detector in which fibres, photodetectors, and readout electronics are separate units. Such detector would be easier to maintain and more cost-effective on the long term.

- Scintillating fibres do not require gas installations, cooling, or high-voltages, reducing therefore the cost and simplifying the design and maintenance of the monitor.

- The material budget of a fibre monitor could be similar, or slightly better, than the current monitors. The x/X_0 of the MWPC, the DWC, and a SciFi monitor are calculated analytically in appendix D.1. Such calculation yields 0.36% and 0.28% for the MWPC and the DWC, respectively. A fibre monitor made of two planes of fibres would have 0.24%, if it is made of 0.5 mm fibres, and 0.48% for 1 mm fibres.

- A fibre plane made of only one layer of fibres would have a detection efficiency around 90%, and the beam profile reconstruction resolution would be equal to the thickness of the fibre used (typically 0.5 mm or 1 mm). Nevertheless, in special applications where a higher efficiency and a finer resolution are needed, an upgrade to several layers of staggered fibres could be investigated.

Chapter 3

Plastic Scintillating Fibres

This chapter describes plastic scintillating fibres and the physics behind their operating principle. Some of their issues, such as optical crosstalk and radiation damage, are also presented. Finally, two different models of fibres particularly suited for a SciFi beam monitor are reviewed.

3.1   Introduction

The first *scintillating fibres* were used in particle physics as early as the decade of 1950. However, early after their discovery, they were abandoned in favour of other detection mechanisms, principally *bubble chambers* and *wire chambers*. The interest for them flourished again in the decades of 1980-90, at the same time that the development of solid-state photodetectors, being adopted by major high-energy physics experiments like UA2 [18], CHORUS [19] or DØ [20].

At present, scintillating fibres are employed, or will be employed, in many experiments, among others ATLAS ALFA [12], LHCb [12] or Mu3e [21]; they are also used in instrumentation for particle accelerators, like the new spectrometer at the Mainz Microtron [22], and there are ongoing investigations for their application in beam loss monitoring at the J-PARC LINAC [23]; other various applications include nuclear waste management [24], dosimetry [25], or cosmic rays balloon experiments [26].

Scintillating fibres are based on two principles: the production of light via *scintillation* and its transportation trough the fibre by means of *total internal reflection*. They can be based on different type of scintillators: inorganic crystals [27] (fig. 3.1), organic liquids [28], and organic plastics [29]. Nevertheless, the most widely used and developed are *plastic scintillating fibres* (fig. 3.1).
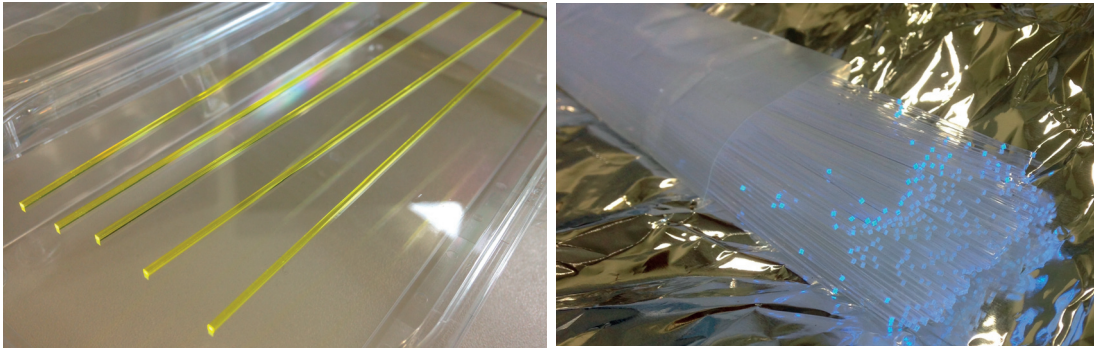
Figure 3.1 – Left: inorganic fibres of YAG:Ce. Right: plastic scintillating fibres.

3.2 Scintillation Mechanism

The core represents the bulk of the fibre and is made of a polymeric material, typically Polystyrene (PS[1]). When a particle interacts with the fibre, the energy from the ionisation excites free valence electrons of PS from ground state, S_0, to higher electronic and vibrational levels (fig. 3.2). Thermal equilibrium to a lower state (S_1) is rapidly reached within 10^{-11} s, however without the emission of radiation. Thereupon, radiative transitions from this state to ground states occur with a typical lifetime of 10^{-8} s to 10^{-9} s. Triplet states can be also populated (T_1 and T_2), which have delayed transitions to S_0, although their contribution is practically negligible.

However, polystyrene is a bad scintillator, having very poor light yield (Table 3.1) and showing a high attenuation of its own emitted light. In fact, PS is practically opaque for wavelengths below 350 nm as can be seen in fig. 3.3, which shows its attenuation length (defined in appendix A.7.5).

3.3 Fluorescent Dyes

The dilution of a fluorescent dye in the PS matrix can enhance the scintillating properties of the fibre. Such dyes must have an absorption spectrum that matches the emission of PS and a *Stokes shift* (the difference between the maxima of the absorption and emission

---

[1]Hereinafter, PS will denote Polystyrene instead of Proton Synchrotron (employed in section 1.1)
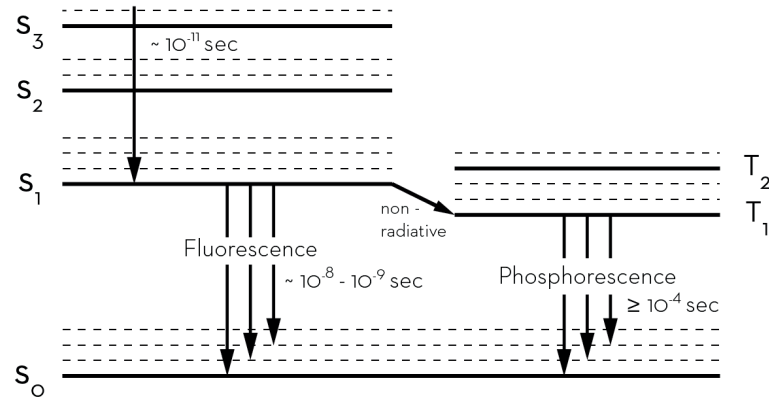
Figure 3.2 – Energy levels of PS and electronic transitions caused by the interaction with an ionising particle that lead to scintillation.
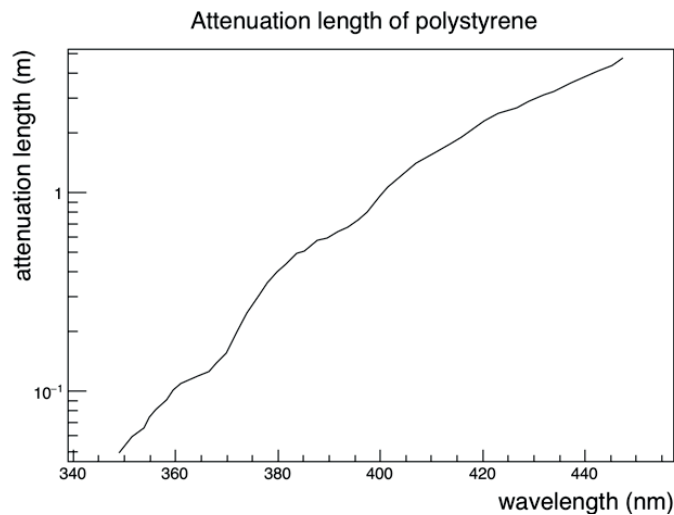
Figure 3.3 – Attenuation length of polystyrene as a function of the light wavelength. Source: [30].

spectra) that re-emits the light in larger wavelengths, far from the attenuation of PS; the shift also helps matching the quantum efficiency of the photodetector. A high light yield and a fast response are also sought properties of these dopants. The characteristics of several common fluorescent dyes are presented in Table 3.1, and the absorption and emission spectra of some of them are illustrated in fig. 3.4.

When the concentration of the fluorescent dye is high enough, the molecules of both PS and dye can be sufficiently close (1 nm to 2 nm) to allow a special transfer of energy from the PS to the dye known as *Förster transfer*. This energy transfer is mediated through a non-radiative dipole-dipole coupling of the molecules, making it fast, in the order of ns, and very efficient. However, its efficiency strongly decreases with the distance between molecules.

Table 3.1 – Fluorescent properties of polystyrene and some common dopants employed in plastic scintillating fibres. Source: [30]

Compound	Maxima Abs. (nm)	Maxima Emiss. (nm)	Decay time (ns)	Quantum efficiency	Stokes shift (eV)
Polystyrene	265	330		0.03	0.62
3HF [1] [3]	340	530	8.0	0.4	1.27
PMP420 [1]	300	415	3.0	0.88	1.11
PMP450 [1]	305	435	3.6	0.74	1.24
PBBO [1]	330	395	2.1	0.79	0.62
p-terphenyl [2]	275	340	0.95	0.93	0.86
PBD [2]	300	360	1.0	0.83	0.69
POPOP [3]	360	420	1.5	0.93	0.49
BBOT [3]	370	425	1.1	0.74	0.43
TPBD [3]	345	450	1.8	0.6	0.84

[1] Typically used in one-component formulations.
[2] Typically used as primary dye in two-component formulations.
[3] Typically used as wavelength-shifter in two-component formulations.

The light yield of a fibre increases with the dye concentration, due to a more efficient Förster transfer, until a saturation point is reached in which phenomena of self-absorption begin to occur [31] [32]. Common concentrations are around 1%-2% by weight.

Some formulations use a secondary dye as a wavelength shifter to emit the light at larger wavelengths, resulting in a higher light yield of the fibre. However, due to the low concentration of the dyes, the transfer of energy from the primary dopant to the secondary is done via a radiative process, instead of a Förster transfer. As a result of this radiation, the phenomenon of *optical crosstalk* between fibres can occur, which will be further discussed in section 3.5.

Most of the commercial fibres are based on two-component formulations (such as p-Terphenyl plus POPOP or TPBD), due to their high light yield, short decay times, long attenuation lengths, and their emission in the blue (in fact, the exact combination of dopants and their concentrations are kept secret by the manufacturers). For example, the DØ experiment used a formulation of p-Terphenyl (1%) plus 3HF (0.1%), specially investigated for radiation hard environments [33].
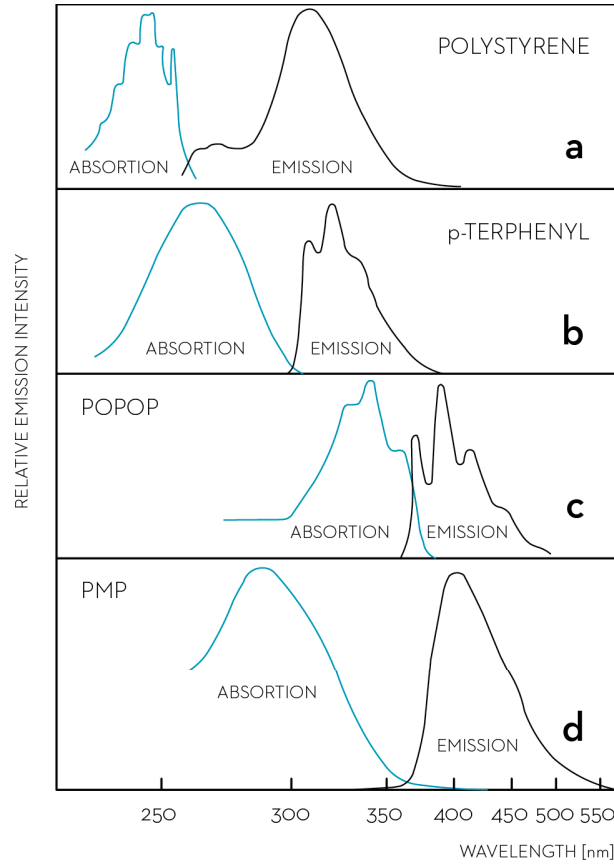
Figure 3.4 – Absorption and emission spectra of common scintillators employed in plastic scintillating fibres. Source: [30].

3.4 Timing Properties

The conversion of ionisation energy into scintillation light is very fast, with rise and decay times of a few nanoseconds (Table 3.2). Therefore, plastic scintillating fibres are *fast scintillators*. The distribution of the fast light pulses from scintillating fibres is well described by the convolution of a Gaussian with an exponential [34]:

$$N\left(t\right) = N_0 f\left(\sigma, t\right) e^{-\frac{t}{\tau}}, \tag{3.1}$$

being $N\left(t\right)$ the number of photons created at a moment t, τ the decay time of the scintillator, and $f\left(\sigma, t\right)$ a Gaussian function characterised by a standard deviation σ.

A complete and exhaustive description of the physics of scintillation can be found in [35].

3.5 Optical Crosstalk

In fibres using two-component formulations, part of the photons emitted isotropically by the primary dye can escape the fibre without interacting with the secondary dye. If those photons are instead converted inside a neighbouring fibre, a phenomenon of *optical crosstalk* between fibres can occur. This results in the production of false signals that can smear the resolution of a tracker detector.

There are several techniques to suppress the crosstalk. In the case of fibres using p-Terphenyl (the most common), the primary photons are emitted in the ultra-violet (UV) and the following treatments are effective:

- Deposition of an ultra-thin aluminium coating over the fibres that reflects the primary photons. Such technique is applied by the ATLAS ALFA experiment [12], which has fibres with a 100 nm aluminium coating (fig. 3.5).

- Painting the fibre with thin Extra Mural Absorber (EMA) that absorbs the UV light. Some companies, such as Saint-Gobain, offer the possibility of delivering the fibres with a 10 µm to 15 µm layer of EMA paint [36].

- When the fibres are grouped in bundles, a UV absorbing powder, such as TiO_2, can be mixed with the structural glue that lies between the fibres. This is the method followed by the LHCb SciFi tracker [13].

Figure 3.5 – Plastic scintillating fibres coated with a 100 nm aluminium layer. *Note: it can be appreciated how the coated fibres do not scintillate in the presence of ambient UV light, in contrast with the uncoated fibres of fig. 3.1.*

Due to the short absorption length of UV light of polystyrene (fig. 3.3), primary photons have a higher probability of escaping thin fibres than thicker ones. Therefore, crosstalk is more intense for thin fibres, particularly below 500 µm.

3.6 Fibre Fabrication

The mechanical layout of plastic scintillating fibres typically consists in a PS matrix covered by a thin cladding of Poly-Methyl Methacrylate (PMMA, also known commercially as Plexiglas), which has a thickness of 2% or 4% of the fibre width. The exact thickness can vary depending on the fibre model, as can be seen in Table 3.2.

Scintillating fibres are fabricated from the extrusion of a highly purified PS+dye rod that is enclosed in a PMMA tube. The ensemble is heated to the temperature in which both materials soften and, thereupon, it is slowly pulled out as shown in fig. 3.6. The complete process requires a multitude of steps not described here to ensure the good quality of the product and, in total, the fabrication of a batch can take several weeks. Further details can be found in [37].
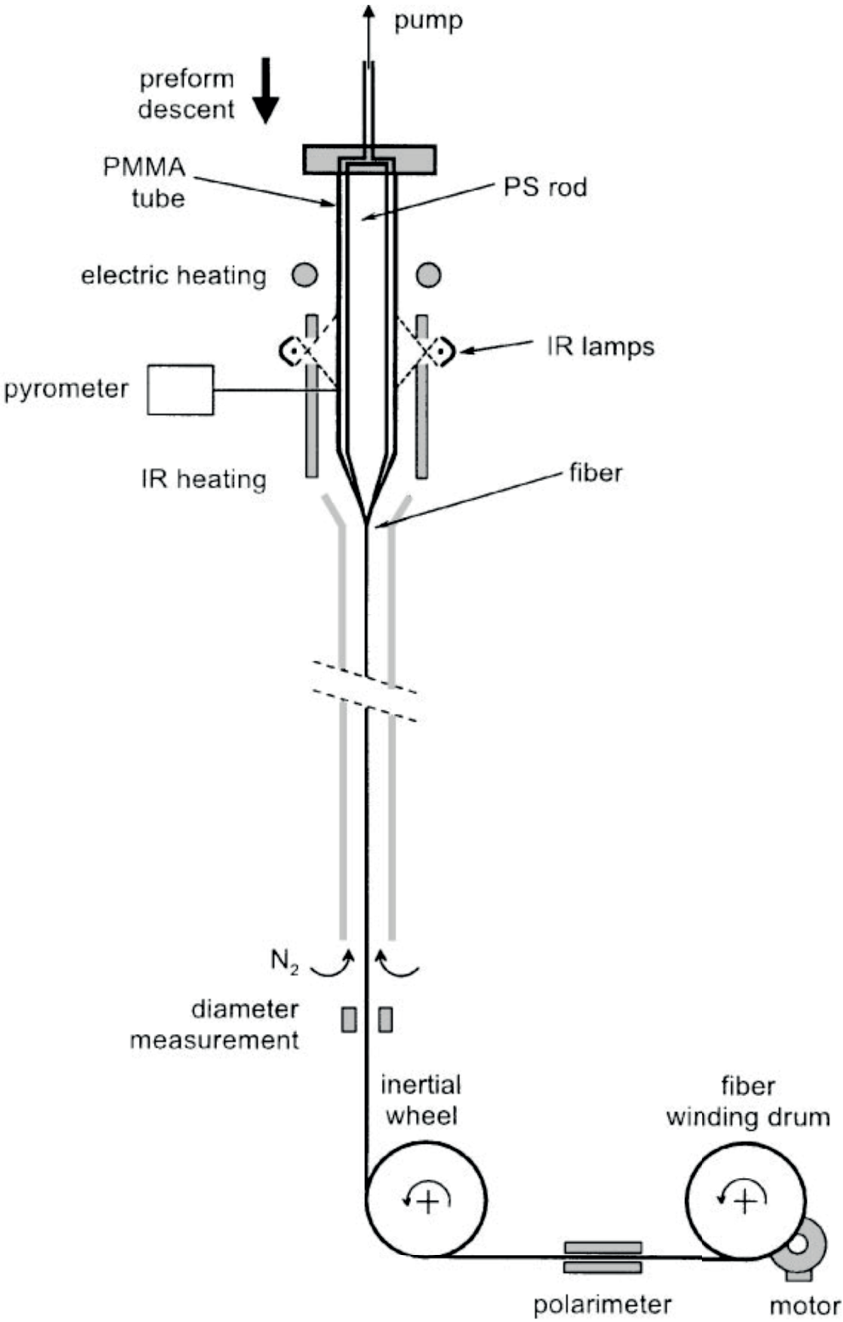
Figure 3.6 – Fabrication of scintillating fibres by extrusion. Image from: [37].

3.7 Light Capture and Transmission

Light can be trapped inside a scintillating fibre by *total internal reflection* at the core-cladding boundary. Scintillation photons are emitted isotropically, however, only those emitted within the *critical angle* are trapped inside the fibre and can travel to its end (fig. 3.7). The critical angle can be easily calculated from Snell's law:

$$n_{core} \sin(\theta_i) = n_{clad} \sin(\theta_f),\tag{3.2}$$

under the condition of total internal reflection: $\sin(\theta_f) = 1$,

$$\implies \cos(\theta_{crit}) = \frac{n_{clad}}{n_{core}}.\tag{3.3}$$

As can be seen from eq. (3.3), $n_{core} > n_{clad}$ is required for the total internal reflection to occur, and the larger the difference between them, the wider is the critical angle. In the case of PS and PMMA, the refraction indexes are $n_{PS} = 1.6$ and $n_{PMMA} = 1.49$, which yield a critical angle of $\sim 21°$.
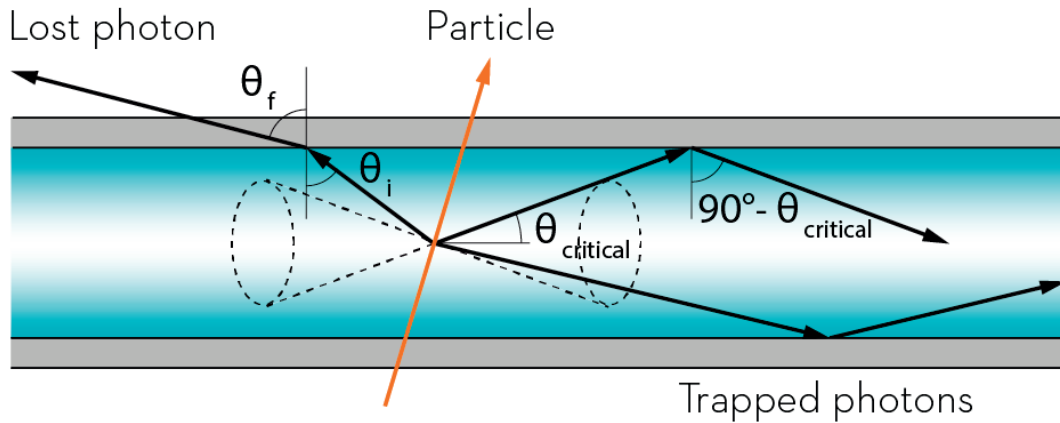
Figure 3.7 – Total internal reflection in plastic scintillating fibres.

Similarly to multimode optical fibres, light can propagate in two modes in scintillating fibres: meridionally and helicoidally [38]. Meridional rays follow pathways that can be drawn on a single plane, while helical rays follow skew pathways near the boundaries of total reflection, turning completely around the fibre axis after several reflections (fig. 3.8).
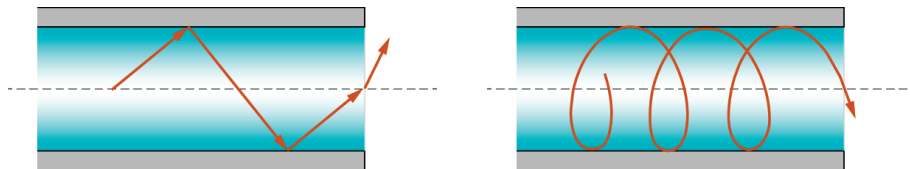
Figure 3.8 – The two modes of light propagation in plastic scintillating fibres: meridionally (left) and helicoidally (right).

The *trapping efficiency* in one hemisphere of a round scintillating fibre can be analytically calculated for meridional and helical rays [39]:

$$\varepsilon_{merid} = \frac{1}{2} \left[1 - \sin\left(\theta_{crit}\right) \right], \tag{3.4}$$

$$\varepsilon_{helic} = \frac{1}{2} \left[1 - \sin\left(\theta_{crit}\right) \right] \theta_{crit}, \tag{3.5}$$

which yield a total trapping efficiency:

$$\varepsilon_{trap} = \varepsilon_{merid} + \varepsilon_{helic} = \frac{1}{2} \left[1 - \cos^2\left(\theta_{crit}\right) \right] = \frac{1}{2} \left[1 - \left(\frac{n_{clad}}{n_{core}}\right)^2 \right]. \tag{3.6}$$

This efficiency is calculated for round fibres; an analytical solution for square fibres is more difficult to find, although real measurements and simulations show that square fibres have a higher trapping efficiency than round fibres [39].

3.8 Multi-clad fibres

A second cladding layer can be added over the PMMA to further increase the light capture. This outer cladding is typically made of a fluorinated polymer (FP) with a lower refractive index than PMMA. In this configuration, the PMMA just serves as an interface between the PS and the fluoro-acrylic, which are mechanically incompatible. These multi-clad fibres are superior mechanically and optically, trapping around 60% more photons than single-clad fibres.

Equation 3.6 shows why multi-clad fibres are superior to single-clad in light capture, since the refractive index of the fluorinated polymer is smaller than that of PMMA ($n_{FP} = 1.42$ vs $n_{PMMA} = 1.49$).

3.9 Core and Cladding Light

Hitherto, only the light trapped at the core-cladding boundary, or *core light*, has been considered. In fact, light trapped at the external surface, or *cladding light*, has a larger trapping efficiency:

$$\varepsilon_{trap}^{core} = \frac{1}{2} \left[1 - \left(\frac{n_{clad}}{n_{core}}\right)^2 \right] = \frac{1}{2} \left[1 - \left(\frac{1.49}{1.6}\right)^2 \right] = 6.6\%, \tag{3.7}$$

$$\varepsilon_{trap}^{clad} = \frac{1}{2} \left[1 - \left(\frac{n_{air}}{n_{clad}}\right)^2 \right] = \frac{1}{2} \left[1 - \left(\frac{1}{1.49}\right)^2 \right] = 27\%, \tag{3.8}$$

Unfortunately, cladding light is highly attenuated due to mechanical imperfections in the waveguide structure of the fibre at the level of the external surface. These imperfections can be caused by surface irregularities, such as bumps, dust, scratches, and fingerprints, among others. The total internal reflection at the surface can be also suppressed if the fibre is in contact with a material with higher refractive index, for example a glue.

3.10   Attenuation Length

Core and cladding light experience a different attenuation length, as can be appreciated in fig. 3.9: core rays travels longer distances due to the better quality of the core-cladding interface.

Several studies show also that the attenuation can be divided in two regimes, for short and long distances [40] [41]. In the short distance regime ($\Delta x <\sim 40\,\mathrm{cm}$), helical and cladding rays strongly contribute to the total light yield of the fibre (helical rays are highly attenuated due to the longer net pathways that they follow). The long regime ($\Delta x \geq\sim 40\,\mathrm{cm}$) is dominated by meridional rays travelling in the core.

The total attenuation length in the short region is small, less than $50\,\mathrm{cm}$, while in the long regime is in the order of $2\,\mathrm{m}$ to $4\,\mathrm{m}$, depending on the fibre characteristics.
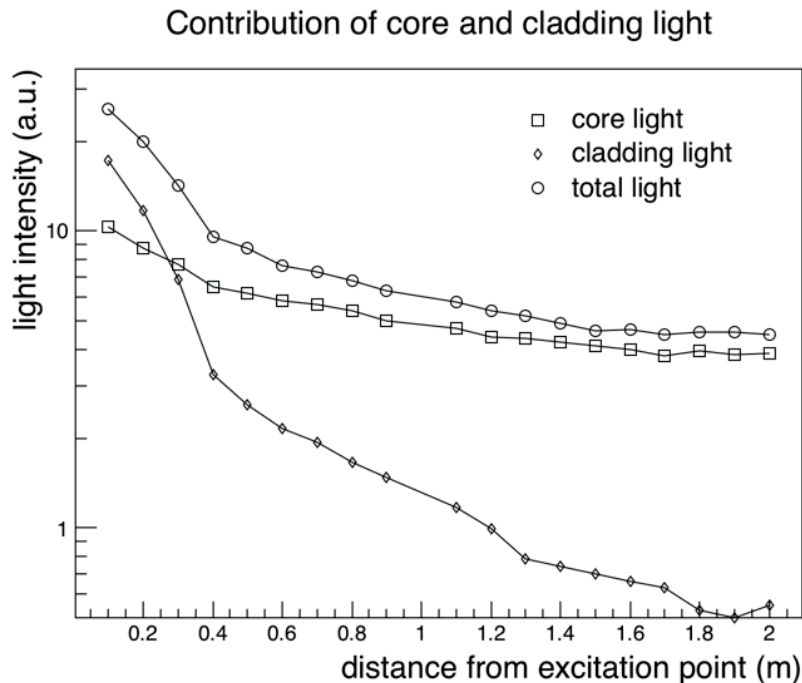
Figure 3.9 – Contribution of core and cladding light to the total light yield, as a function of the distance. Measured for a Kuraray SCSF-81 fibre. Source: [41].

There are two fundamental processes contributing to the attenuation of light in scintillating fibres: absorption and scattering [42]. The self-absorption of light by the fibre is mostly due to the excitation of certain electronic and vibrational energy levels of the dyes and the PS, resulting in an absorption dependent on the wavelength. The scattering of a photon from its trajectory can cause the lost of the total internal reflection condition, thus provoking its exit from the fibre. This effect is mainly due to Rayleigh scattering in the PS and fabrication imperfections at the core-cladding boundary, such as an incomplete adherence of the PMMA to the PS, or microscopic fluctuations of the fibre size.

The spectral attenuation length measured for a Kuraray SCSF-78 round fibre of 250 µm is shown in fig. 3.10. It should be noted that, because its attenuation is larger for shorter wavelengths, the output of long fibres tends to shift towards higher wavelengths (fig. 3.11).
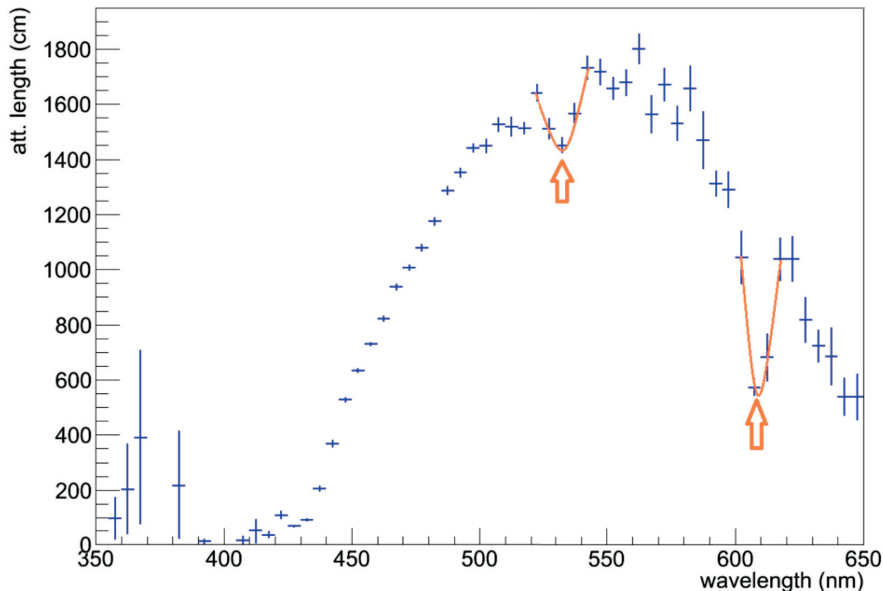
Figure 3.10 – Measured spectral attenuation length of a Kuraray SCSF-78 round fibre of 250 µm diameter. The orange arrows indicate two pronounced absorption peaks of PS. Image from: [13].

3.11 Radiation Damage

Scintillating fibres are sensitive to radiation damage in a dose-dependent manner. It worsens the transparency of the PS bulk and damages the fluorescent dyes, reducing both the attenuation length and the light yield. Another effect is the appearance of colour-centres that absorb shorter wavelengths, favouring larger wavelengths.

A review of the literature shows that radiation damage in plastic scintillating fibres is
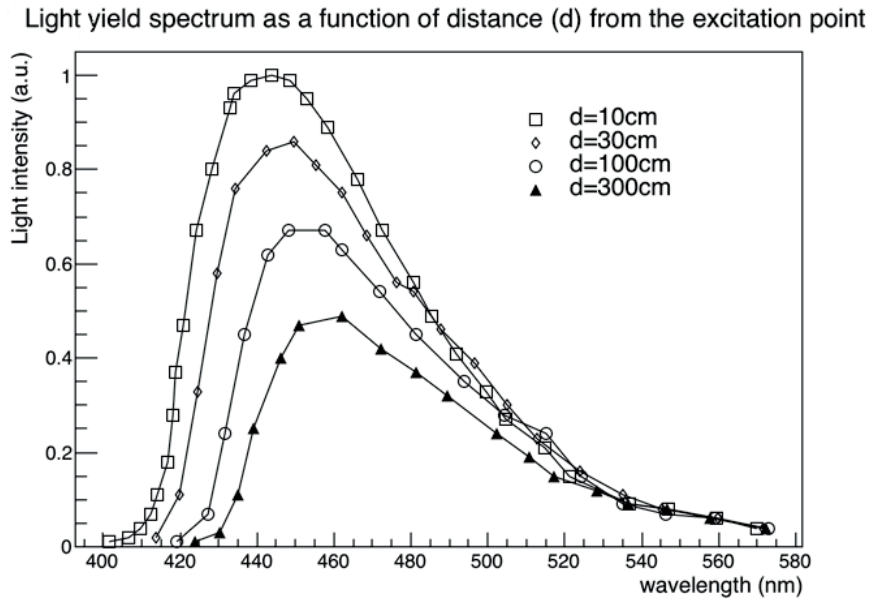
Figure 3.11 – Spectral light yield of a Kuraray SCSF-78 fibre as a function of the distance that light has travelled along the fibre since the excitation. Source: [43].

a complex topic with inconsistencies between similar studies [44]. The origin of these differences has been related to several factors:

- Dependency on both dose rate and total accumulated dose.

- Fibre temperature during irradiation.

- Time passed after the irradiation, since fibres can recover from radiation damage under certain conditions (annealing processes).

- Exposure of fibres to certain gases that can accelerate the recovery processes.

- Mechanical stress and bending of the fibres.

- Characteristics of the fibre: content of dopants and oxygen, polymerisation time during production.

- Storage conditions after irradiation: temperature, atmosphere, and darkness.

- Age of the fibres.

A conclusion drawn from the variance of irradiation studies is that radiation damage strongly depends on the measurement conditions. Despite this complexity, most of the commercial fibres retain around 70% of their detection efficiency for accumulated doses of 10 kGy [45]. Figure 3.12 shows the results of a study of irradiation done with several

models of square fibres of 0.5 mm width: Kuraray SCSF-78, BCF-12 single-clad, and Kuraray SCSF-3HF.
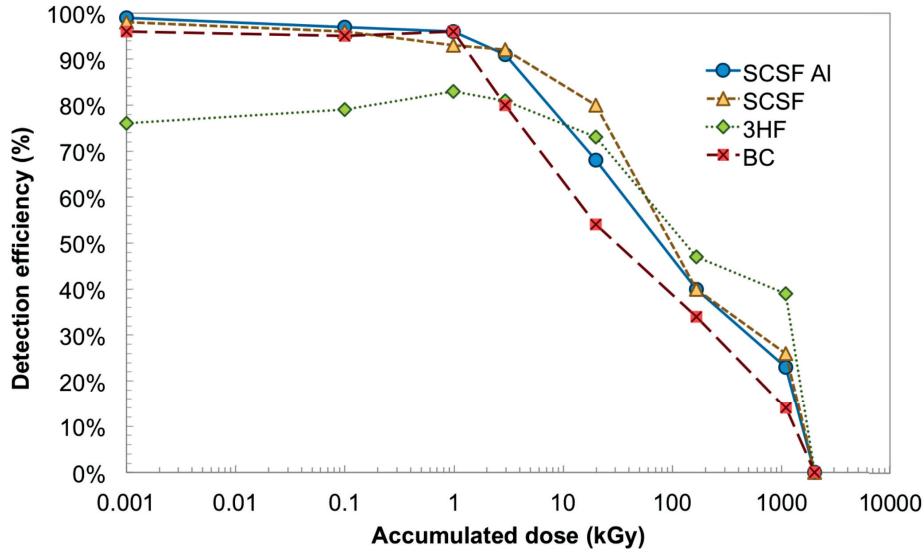
Figure 3.12 – Detection efficiency of different models of plastic scintillating fibres as a function of the accumulated dose. Image from: [45].

3.12   Outlook for Improvement

Plastic scintillating fibres still have potential for improvement. Claddings with a lower refractive index would increase the trapping efficiency, although they present the challenge of guaranteeing a good mechanical contact between the materials. There is also active research on new fluorescent dopants that could improve the conversion efficiency of ionisation energy to scintillation light, which at present is very low, about a 4%. Nanostructured Organosilicon Luminosphores (NOLs) are very promising, as they show a higher quantum efficiency and would produce fibres with a larger attenuation length [46] [47].

3.13   Fibres for the Beam Monitor

There are two major manufacturers of plastic scintillating fibres: Kuraray in Japan and Saint-Gobain in USA (previously known as Bicron before its purchase by the latter in the nineties). Their product catalogues are very similar ([43], [36]), both producing fibres with round and square cross sections, thicknesses from 0.25 mm to 2 mm and lengths that range from straight canes of a few metres to spools of several kilometres. Depending

on the dye formulation, which is kept secret by both companies, they offer several models suited for diverse applications, such as blue emitting fibres, fibres optimised for long lengths, and radiation hardened fibres.

Two different models of blue emitting square fibres are considered for the development of the beam profile monitor: the SCSF-78 produced by Kuraray and the BCF-12 from Saint-Gobain. Some of the characteristics of the fibres are presented in Table 3.2.

Both fibres have a similar scintillation yield (about 8,000 photons per MeV deposited by a MIP), although their trapping efficiencies and attenuation lengths are different. Kuraray has made a great effort producing fibres with a large attenuation length, while Saint-Gobain has developed a technique to produce multi-clad square fibres, which represents a great advantage in terms of trapping efficiency. There is a study reporting a better geometric finishing of Kuraray fibres over Saint-Gobain [48].

The square shape is preferred because it offers a more homogeneous coverage of the beam in a detector equipped with a single fibre plane. In such case, it is also important to consider the size of the cladding, since it does not scintillate and represents a dead zone of the detector.

Table 3.2 – Properties of SCSF-78 and BCF-12 square fibres. Source: products catalogue.

Fibre model	Emiss. peak (nm)	Decay time (ns)	Att. length (m)	Trapping efficiency (%)	Cladding thickness (% fibre)
SCSF-78 [1]	450	2.8	4.0	4.2	4
BCF-12 SC [1]	435	3.2	2.7	4.4	8
BCF-12 MC [2]	435	3.2	2.7	7.3	12

[1] Single-clad.
[2] Multi-clad.

3.14   Estimation of Light Signal

A simple estimation of the signal created by a scintillating fibre can be done with a few calculations. Assuming a square fibre of 1 mm thickness and a MIP impinging perpendicularly to it, the stopping-power curve of Polystyrene (fig. A.3) predicts a mean energy deposition of 120 keV. For a scintillation efficiency of $\sim 8,000$ photons/MeV, about $\sim 1,000$ scintillation photons are created. Thereupon, considering a trapping efficiency of 5%, the number of travelling photons inside the fibre in one direction is ~ 50. The next loss is due to the attenuation of light in the fibre; for an attenuation length of 2.5 m and a fibre length of 50 cm (realistic for a fibre monitor), about 20%

of the light is lost, which means a total of ~ 40 photons arriving to the photodetector. Depending on the photo detection efficiency of the photodetector and the quality of its coupling with the fibre, another 50% to 70% of the photons are lost; thus, about 15-20 photoelectrons are detected and form a signal. If a mirror is coupled to one side of the fibre, this quantity can be increased by $\sim 70\%$ by reflecting part of the photons that otherwise would escape the fibre.

The goodness of this estimation is verified with a special fibre setup described in appendix C.

Chapter 4

Photodetectors and Readout Electronics

This chapter presents a review of the most common photodetectors for scintillating fibres. From all of these detectors, the Silicon Photomultiplier is favoured and the reason of this choice is justified. Some of the different available ASIC for Silicon Photomultiplier read-out are also reviewed.

4.1   Photodetectors for Scintillating Fibres

A photodetector for scintillating fibre read-out must be sensitive to ultra-low levels of light (around 10 photons or less, as shown in section 3.14). Several detectors have been employed in the past, such as Charge-Couple Devices (CCD), Photomultiplier Tubes (PMT), Hybrid Photodiodes (HPD), Avalanche Photodiodes (APD) or Position Sensitive Photomultipliers. Nowadays, Multi-Anode Photomultiplier Tubes (MA-PMT) and Silicon Photomultipliers (SiPM) are the most common options, since these detectors offer a good performance and integrate a high density of channels in a compact size and for an affordable price.

4.1.1 Multi-Anode Photomultipliers

The operating principle of a *MA-PMT* is similar to a common PMT, with the main difference that the dynodes are formed by a stack of perforated metal sheets configuring vertical independent channels (fig. 4.1). The anode of every channel is independent, which allows for a segmented readout integrated in a small volume of typically some centimetres. The photocathode, however, is common and shared by all the anodes.
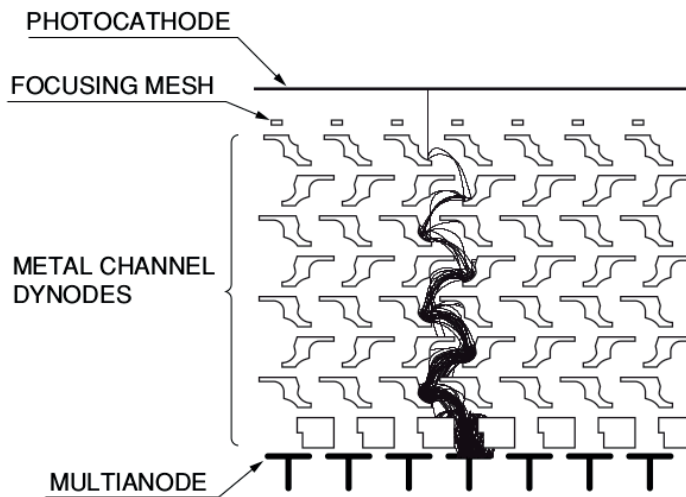
Figure 4.1 – Layout of a MA-PMT showing the dynode channels structure and the avalanche multiplication of a photoelectron. Image from: [49].

MA-PMT share many ***advantages*** with PMT:

- High gain: typically 10^6.

- High quantum efficiency: between 25% to 35% for blue light at 420 nm, determined by the composition of the photocathode. There is normally a trade-off between cost and efficiency.

- Low dark current: the count of events in a dark state is very low, typically some Hz.

- Fast signals: rise times and decay times of a few ns.

Nevertheless, this type of device has also some ***drawbacks***:

- Gain uniformity between channels: as large as a factor 4 between channels of a same detector.

- Channel crosstalk: due to leaks in the dynode structure, some current is measured in the adjacent anodes of a channel. Its value is typically a few percent.

- High voltage: these devices require high-voltage, usually $\sim 1\,\mathrm{kV}$.

- They are sensitive to magnetic fields.

For example, the model H7546 from Hamamatsu features 8×8 channels of $2\,\mathrm{mm} \times 2\,\mathrm{mm}$ each, integrated in a compact volume of $45\,\mathrm{mm} \times 30\,\mathrm{mm} \times 30\,\mathrm{mm}$ (fig. 4.2).

Figure 4.2 – Multi-Anode Photomultiplier H7546 from Hamamatsu.

4.1.2 Silicon Photomultipliers

Silicon Photomultipliers are a new type of semiconductor photodetectors developed in the early 1990s as an upgrade of Geiger-Mode Avalanche Photodiodes (G-APD, or SPAD). They are also known under the name of Solid-State Photomultipliers (SSPM) or Multi-Pixel Photon Counter (MPPC).

The operating principle of a G-APD is a photodiode biased with a reverse voltage above the breakdown of the diode (fig. 4.3). Therefore, when a quantum of light creates an electron-hole pair in the p-n junction, it immediately provokes an avalanche process that multiplies the number of carriers by a factor of 10^5 to 10^6. The avalanche is stopped by means of a quenching resistor in order to make the device useful again for detection.

G-APD are very sensitive devices with a single-photon detection capability, good timing performance, and large internal gain. A characteristic feature of G-APD is that its output signal is not proportional to the number of incident photons, behaving therefore as a "binary" device that measures the mere presence of light.
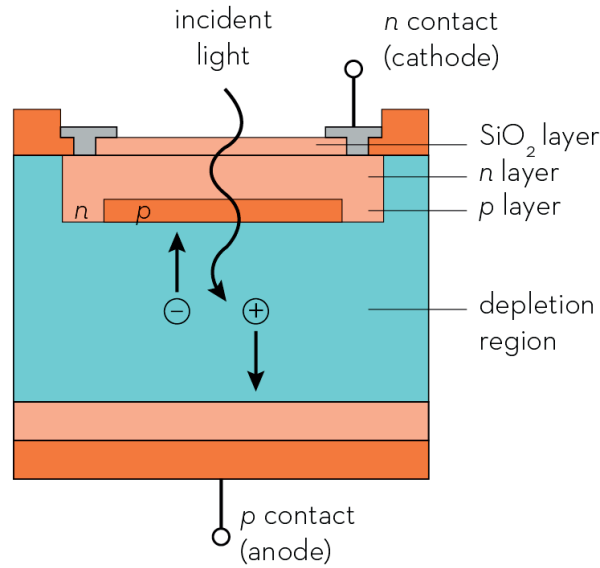
Figure 4.3 – Layout of a Geiger-Mode Avalanche Photodiode.

A SiPM is a matrix of hundreds of G-APD connected in parallel and sharing the same silicon substrate (fig. 4.4 and fig. 4.5). Each G-APD cell, also called a pixel, generates an independent and equal signal. If several photons reach the SiPM simultaneously, the signals from the different activated pixels are added, generating an output signal that is proportional to the number of incident photons (fig. 4.6). Hence, SiPM overcome the binary limitation of G-APD, allowing to count individual photons over a wide dynamic range.
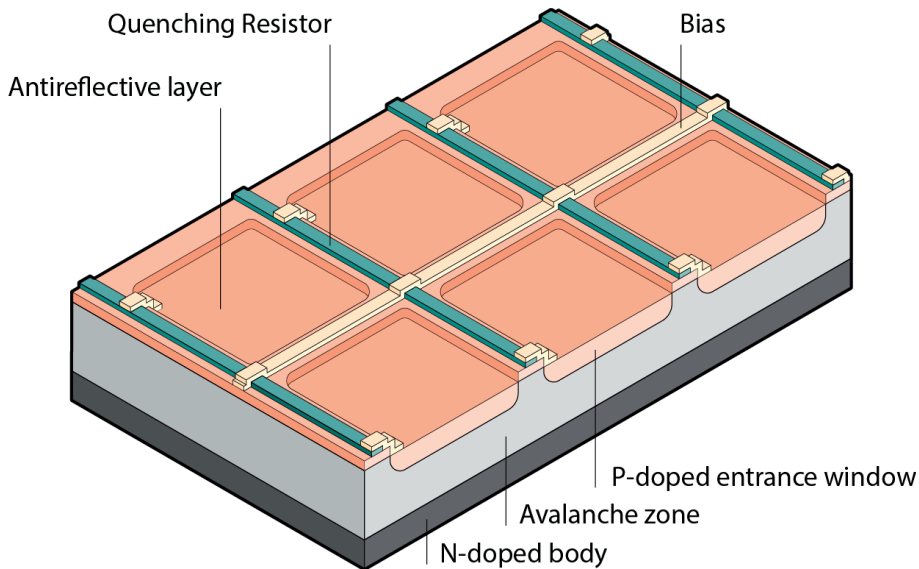
Figure 4.4 – Layout of a SiPM, showing its pixelated G-APD structure.

The following list summarises some advantages and drawbacks of SiPM.
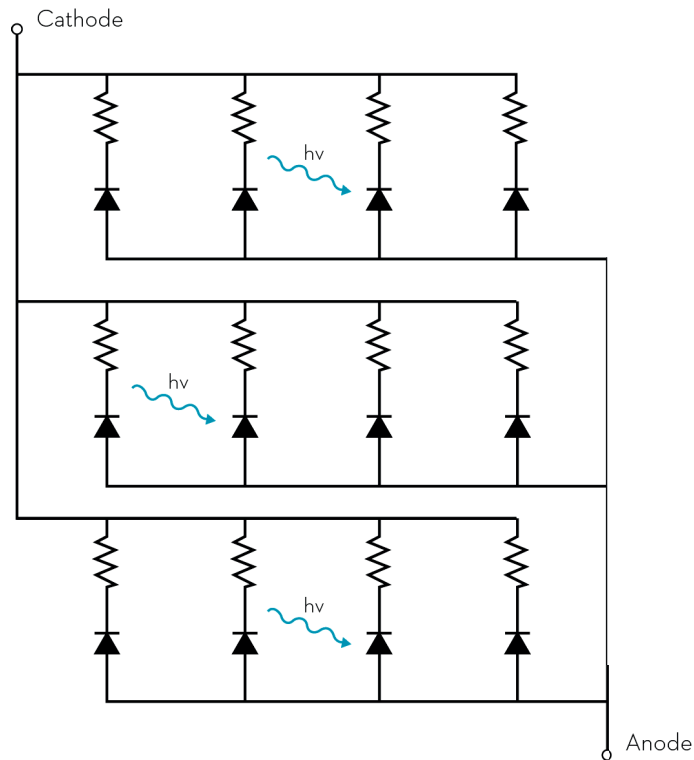
Figure 4.5 – Schematic circuit of a SiPM.
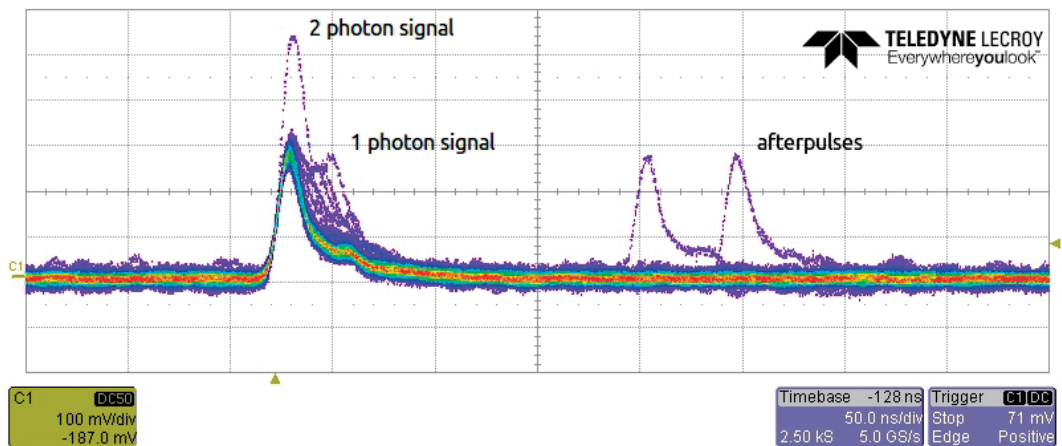
Figure 4.6 – Persistence image of a LeCroy WaveRunner 1 GHz oscilloscope showing dark signals of a SiPM. The two-photon signal is generated by pixel crosstalk.

Advantages:

- High gain: $10^5 - 10^6$.

- High photo detection efficiency: 40% - 50% at 420 nm.

- Fast rise and decay times: <1 ns rise time and 10 ns to 100 ns decay time.

- Low operation voltage: $< 100\,\text{V}$.

- Dimensions: millimetric device.

- Insensitive to magnetic fields up to $15\,\text{T}$.

- New technology still in development: further improvements and price reduction are expected in the coming years.

- Cost: potentially non-expensive.

Drawbacks:

- High dark count rate: depending on the model, from $10\,\text{kHz/mm}^2$ to $1\,\text{MHz/mm}^2$ at room temperature.

- Correlated noise: pixel crosstalk and afterpulsing.

- Temperature dependence on breakdown voltage and dark count rate.

4.1.3   Choice of Photodetector

Both MA-PMT and SiPM are good candidates for the fibre monitor. However, SiPM were favoured for a first prototype due to their potential for future improvements and low cost. Additionally, the main inconvenient of SiPM, its noise, can be greatly diminished by feeding an external trigger signal to the beam monitor (this subject is further elaborated in section 5.5.4).

Nevertheless, the plans for a future monitor include a prototype equipped with MA-PMT, in order to compare both technologies.

4.2   Review of SiPM

4.2.1   Gain

SiPM are characterised by a high gain, which is defined as the charge created by a primary carrier in an avalanche process:

$$Gain = \frac{Q_{created}}{e} = \frac{C_{pixel} \times (V_{bias} - V_{breakdown})}{e},$$
(4.1)

where e is the elementary charge, C_{pixel} is the capacitance of the pixel, V_{bias} is the applied bias voltage, and $V_{breakdown}$ is the breakdown voltage of the detector.

The gain is directly proportional to the magnitude $(V_{bias} - V_{breakdown})$, frequently called *overvoltage (OV)*:

$$V_{ov} = (V_{bias} - V_{breakdown}).$$ (4.2)

Many performance characteristics of SiPM, such as gain, photo detection efficiency, and noise depend on V_{ov}. The manufacturers typically provide a value that optimises the functioning of the device.

4.2.2 Photo Detection Efficiency

The Photo Detection Efficiency (PDE) of the SiPM is determined by three factors: the quantum efficiency (ϵ_Q), the avalanche probability (P_{trig}), and the geometrical fill factor (FF) (eq. (4.3)).

$$PDE = \epsilon_Q \cdot P_{trig} \cdot FF.$$ (4.3)

The quantum efficiency gives the probability that a photon generates an electron-hole pair. It depends on the wavelength of the incoming photon and, by varying the layout of the p-n junction, the SiPM can be optimised for a certain detection spectrum.

The avalanche probability depends on the strength of the electric field in the p-n junction and, therefore, on the bias voltage.

The geometrical fill factor refers to the fraction of sensitive area of the SiPM, which due to the quenching resistor and other necessary connections, it is not the 100% of its surface.

The quantum efficiency and the fill factor are fixed characteristics of a SiPM. However, the avalanche probability increases with the overvoltage, making it an effective way of increasing the PDE of the detector during operation.

The spectral PDE of a Hamamatsu S13360-1350 is shown in fig. 4.7. It conveniently peaks around 450 nm, closely matching the emission spectrum of the SCSF-78 and BCF-12 fibres.

4.2.3 Dark Count Rate

One of the biggest disadvantages of SiPM is their high Dark Count Rate (DCR), from $10\,\mathrm{kHz/mm^2}$ to $1\,\mathrm{MHz/mm^2}$, depending on the model and the operation conditions. These events, produced in the absence of light, are caused by random thermally-generated
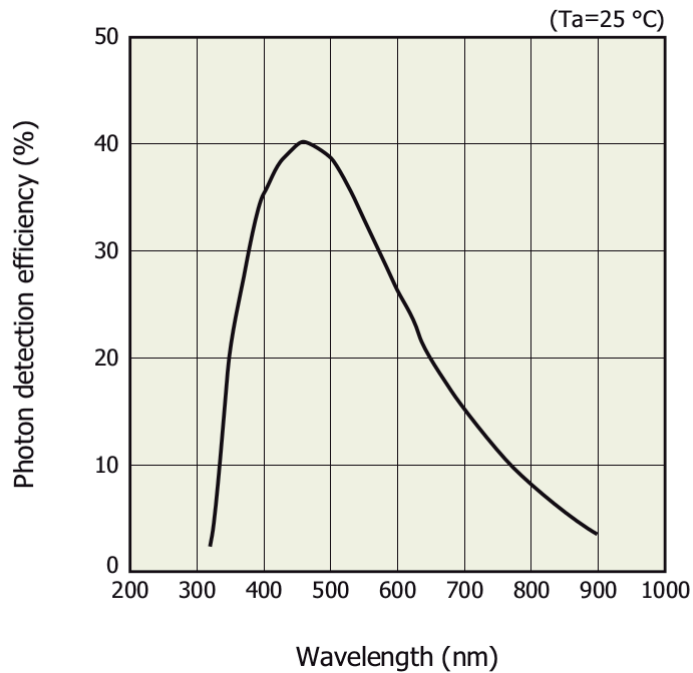
Figure 4.7 – Spectral PDE of a Hamamatsu MPPC S13360-1350 at the recommended overvoltage. Image obtained from the product catalogue: [50].

carriers that can trigger an avalanche in the same way as real photon-generated carriers.

The DCR increases with the overvoltage and the temperature. It can be greatly decreased by cooling down the device.

4.2.4 Correlated Noise

SiPM also suffer from two sources of correlated noised: crosstalk between pixels and afterpulses. The crosstalk between pixels occurs when secondary photons generated in an avalanche escape the pixel and are detected by another cell of the device. As a result, two or more pixels can be fired simultaneously and the output signal is artificially higher (fig. 4.6).

Afterpulses are delayed pulses that appear tens of nanoseconds after a real signal (fig. 4.6). They are caused by trapped carriers in the silicon that are freed after the avalanche has finished, triggering again a new avalanche process.

Both crosstalk and afterpulsing increase with the gain, due to the larger number of carriers, increasing therefore with the overvoltage.

4.2.5 Performance of SiPM

The most recent SiPM have greatly decreased the noise (DCR, crosstalk, and afterpulsing) and further progresses are expected. Afterpulsing probability has been reduced from $\sim 40\%$ of the first devices to less than 1%. This improvement is mainly due to a refinement in the production methods, plus the use of high purity silicon substrates. In the same manner, crosstalk probability has decreased from 10% - 30%, to $\sim 1\%$ in the newest devices. This advance is thanks to the development of the trench technology, which consists in the optical isolation of the pixels by means of opaque trenches.

The typical performance figures of a recent Hamamatsu MPPC S13360-1350 are shown in fig. 4.8.
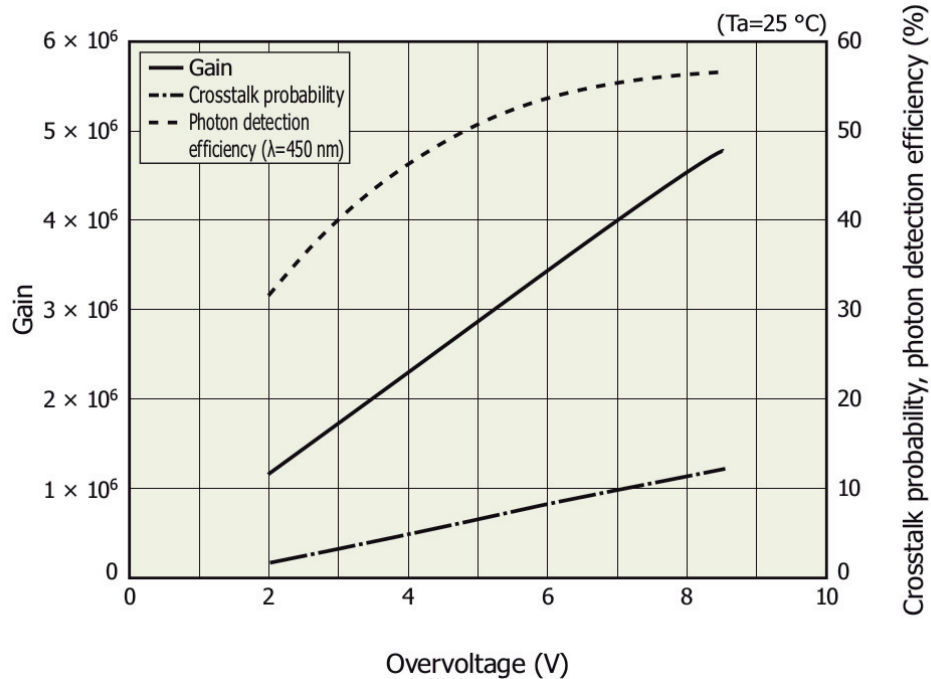
Figure 4.8 – Gain, PDE, and crosstalk of a Hamamatsu MPPC S13360-1350 as a function of the overvoltage. Image obtained from the product catalogue: [50].

4.2.6 Temperature Dependence of SiPM

SiPM have a strong dependency on temperature that primarily affects their breakdown voltage and DCR. Other characteristics, such as PDE, crosstalk, afterpulsing, and gain show negligible dependence on temperature [51].

The change in breakdown voltage with temperature can produce a significant variation in the performance of the SiPM. As previously mentioned, the PDE, crosstalk, afterpulsing,

and gain depend on a great extent on the overvoltage. If the bias voltage is not compensated for a change in breakdown, the overvoltage, $V_{ov} = V_{bias} - V_{breakdown}$, may change with temperature and vary all the aforementioned parameters. The diagram in fig. 4.9, summarises the interdependence of the performance figures of a SiPM with temperature and overvoltage.
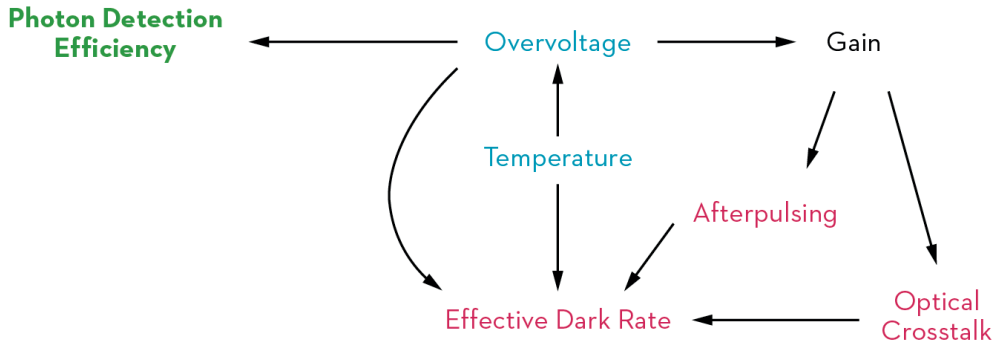
Figure 4.9 – Diagram showing the interdependence of several performance figures of a SiPM with temperature and overvoltage. *Note: for clarity, other dependencies less important are not shown.*

The dependency of the breakdown voltage on temperature is characterised by the manufacturer, who usually provides a temperature correction coefficient. Such correction is applied to the bias voltage in order to maintain a constant performance of the device.

This subject will be further discussed in section 5.7.

4.2.7   Pixel Size

The pixel size plays an important role in the performance of a SiPM. Devices with pixels from 10 µm to 100 µm and densities of 100 to 10,000 pixels/mm^2 are commercially available. However, small pixel devices show several advantages over large pixel SiPM:

- - Larger dynamic range due to the higher number of cells.

- - Lower DCR, crosstalk, and afterpulsing due to lower pixel capacitance.

- - Less dependence of the gain with temperature.

- - Shorter recovery time after an avalanche.

- - Better time resolution.

- - Stronger resistance to radiation damage, due to the lower noise.

The drawbacks of small pixels are:

- Lower gain due to lower pixel capacitance.

- Lower PDE due to a worse fill factor.

The lower gain is not really a drawback, since a high internal gain can be compensated by the electronics readout. The PDE, which is substantially lower compared to high pixel devices, is the major drawback of small pixels.

The research on smaller pixels is very active, especially in micrometric pixels with high fill factor, since they would show a superior performance.

4.2.8 Radiation Damage

As other semiconductor detection devices, SiPM are prone to damage from radiation, which is primarily caused by the displacement of atoms in the lattice. It is manifested as an increase in the DCR and breakdown voltage, and a reduction in the gain; for large accumulated doses, the photo detection efficiency can also be diminished. Most of SiPM can still be employed for detection after neutron equivalent fluencies of $10^{12}\,\mathrm{n/cm^2}$.

It is reported that these devices can recover partially from radiation damage via annealing mechanisms at high temperatures [52] [53].

A frequent solution to counteract radiation damage in SiPM is cooling. It drastically reduces the dark count, allowing the operation at higher operational voltages and thus compensating the losses in gain and PDE. However, it adds a large complexity to the design of a particle detector and significantly raises its cost. Its use is justified in applications where the SiPM are expected to receive a considerable amount of radiation.

4.3 Choice of SiPM

Three models of SiPM have been studied for the beam monitor: Hamamatsu S13360-1350, Ketek PM1150NS, and SensL MicroFC-10050. All the manufacturers provide values of the common performance figures, however, with a simple laboratory setup it is relatively easy to measure some of them. Such characterisation has been done for the DCR and the crosstalk, since they are of special interest for the beam monitor: they are the main source of noise and greatly determine the signal-to-noise ratio of the detector (this subject is further clarified in section 5.5). The PDE is also very important but, unfortunately, it is difficult to measure and requires a rather complex setup.

The SiPM pulses were acquired with an oscilloscope LeCroy WaveRunner with $1\,\mathrm{GHz}$ sampling rate. The DCR was measured by setting a discrimination threshold at 0.5

photoelectrons and subsequently counting the number of signals detected. In a similar way, the crosstalk was measured by counting pulses with levels higher than 1.5 and 2.5 photoelectrons. All the SiPM were in complete darkness and at a similar temperature; they were operated at the V_{ov} recommended by the manufacturer. The results are presented in Table 4.1.

Table 4.1 – DCR and crosstalk measured for different SiPM models.

SiPM model	DCR (kHz)	Crosstalk (%)	V_{ov} (V)
Hamamatsu S13360-1350	26.3 ± 4.2[1]	0.8 ± 0.4	3
Ketek PM1150TS	142.0 ± 6.6[2]	3.9 ± 1.3	2.5
SensL MicroFC-10050	48.5 ± 7.7[3]	6.6 ± 2.0	2.5

[1] Active area: $1.3\,\text{mm} \times 1.3\,\text{mm}$.
[2] Active area: $1.2\,\text{mm} \times 1.2\,\text{mm}$.
[3] Active area: $1\,\text{mm} \times 1\,\text{mm}$.

The three detectors have a similar PDE and gain. However, the Hamamatsu S13360-1350 suits better the requirements of the SciFi beam monitor due to its lower DCR and crosstalk; for this reason, it has been the chosen model. It also has a slightly larger active area, which benefits the coupling with a fibre ('$1.3\,\text{mm} \times 1.3\,\text{mm}$' versus '$1.2\,\text{mm} \times 1.2\,\text{mm}$' of the Ketek and '$1\,\text{mm} \times 1\,\text{mm}$' of the SensL).

4.4   Readout Electronics

In the recent years, several ASIC have been developed in the high-energy physics community for the simple and cost effective read-out of multiple SiPM. These chips typically perform several functions:

- Fine adjustment of every SiPM bias voltage to account for the non-uniformity of breakdown voltage between multiple devices.

- Amplification and shaping of the SiPM signal.

- Charge measurement: done via integration of the pulse or detection its height.

- Discrimination: creation of a fast digital signal when the pulse exceeds a certain amplitude threshold.

Two of such ASIC have been investigated for the fibre monitor: the STiC and the CITIROC:

- The STiC [54] is a 64-channel ASIC developed for Time-Of-Flight systems targeted to Positron Emission Tomography with SiPM (PET scanners). It features a high-performance TDC that can time stamp events with a resolution of 20 ps. The charge of the pulses is measured via a Time-over-Threshold method. Besides medical imaging, it is also used by the Mu3e experiment [21], for example.

- The CITIROC [55] is a 32-channel ASIC for general purpose readout of SiPM. The design of the chip is structured in two "lines" (fig. 4.10): an energy line for the measurement of the charge via pulse height, and a timing line that has several discriminators to produce fast trigger pulses. This chip is used, among other experiments, in the readout of the ASTRI camera for the Cherenkov Telescope Array [56].
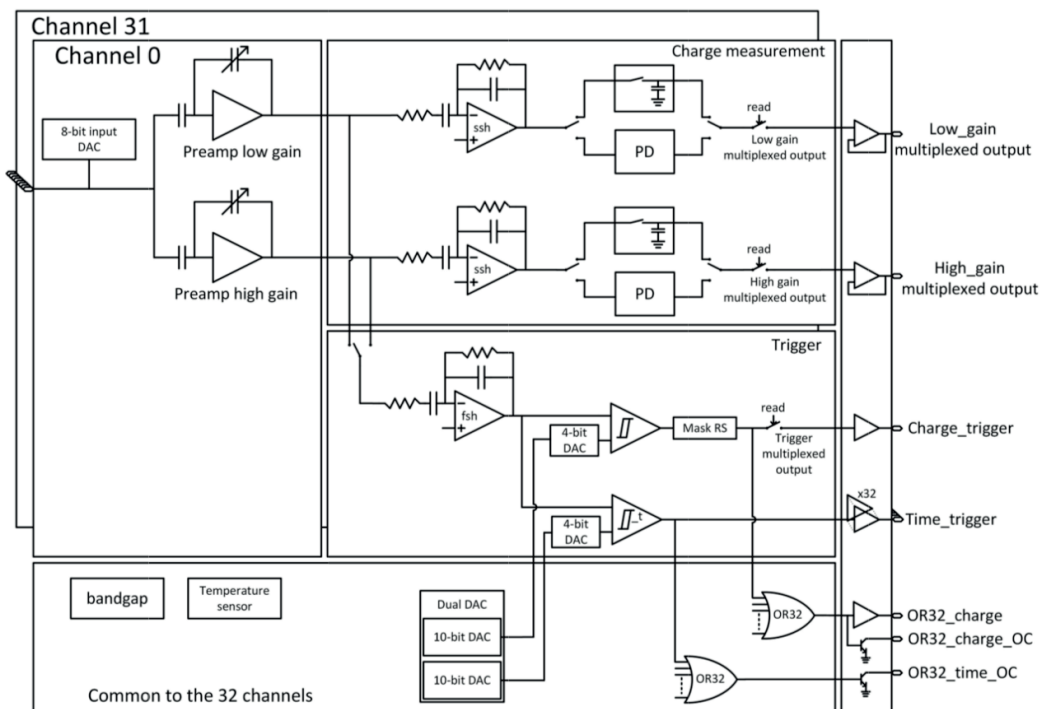
Figure 4.10 – Block diagram of the CITIROC ASIC. Image from: [55].

The CITIROC is a general purpose acquisition ASIC, while the STiC is a highly-specialised chip for timing applications. Due to its higher timing performance, a development with the STiC is substantially more complex. In consequence, the CITIROC has been chosen for a first prototype of the beam monitor, since it provides the required performance, it is simple to use, and also has an affordable price.

Chapter 5

First Prototype

A first prototype of a scintillating fibre detector read-out with silicon photomultipliers has been built and tested in the North Area at CERN. Its mechanic and electronic designs are described hereafter, making emphasis on the issues that have been identified during its construction, along with proposed solutions and improvements. The choice of the threshold of the discriminators, which is a critical parameter of its performance, is also studied in detail. Finally, an estimation of the detection efficiency of the monitor is given based on all the knowledge about it.

5.1   Overview

The active part of the monitor consists in a single plane of scintillating fibres, closely packed together, which is positioned perpendicularly to the particle flux. The fibres have square cross section, $1\,\text{mm}$ of thickness, and there are 64 of them in total forming an active area of $64\,\text{mm} \times 250\,\text{mm}$ (as can be appreciated in fig. 5.2). The employed fibres are Saint-Gobain BCF-12 multi-clad, due to their higher light yield compared to other models (study presented in section 3.13).

In order to simultaneously reconstruct the horizontal and vertical profile of the beam, at least two perpendicular planes of fibres are necessary. However, for reasons of simplicity the prototype has been produced with a single plane of fibres and, therefore, only the horizontal or the vertical profile of the beam can be reconstructed.

A special gluing technique makes the monitor vacuum compatible: the fibres stay inside the vacuum and the photodetectors in air. This represents a great advantage in terms of

material budget, since no additional vacuum windows in the beam line are necessary (as opposed to gaseous chambers).

The monitor features a pixelated fibre read-out in which every scintillating fibre is coupled on one end to an individual SiPM (fig. 5.4). On the opposite end of the fibre a mirror is glued, which increases by $\sim 70\%$ the light detected by the SiPM (according to the measurements described in appendix C.3). The chosen model of SiPM is the Hamamatsu MPPC S13360-1350PE, due to its good performance and its advantages over other models: lower noise and a larger active area (comparison presented in section 4.3).

The signals from the SiPM are processed by a CITIROC evaluation board (the CITIROC ASIC introduced in section 4.4), which allows for an easy acquisition and operation of 32 SiPM simultaneously. Since this board is limited to 32 SiPM, for simplicity it was decided to read-out only every other fibre of the monitor. In consequence, the beam profile can be reconstructed with a spatial resolution of 2 mm.

The CITIROC chip has 32 analogue input channels for the SiPM and 32 corresponding digital output channels; whenever the amplitude of a SiPM pulse exceeds a certain threshold, indicating the presence of a particle signal, the CITIROC generates a fast digital signal. After some digital conversion, these digital signals are processed by a multi-channel Scaler Counter that accumulates the number of hits per channel. The beam profile is reconstructed with the information stored in the Scaler Counter, based on the correspondence of every 'fibre-SiPM' pair with a channel. This acquisition layout allows for a simple and effective reconstruction of the beam profile.

A desktop computer (PC) controls and monitors the operation of the detector and also executes the data acquisition software. A schematic diagram of the prototype is shown in fig. 5.1.
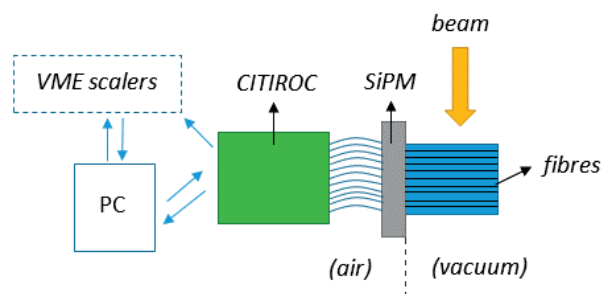
Figure 5.1 – Schematic of the prototype showing its main components.

5.2 Mechanical Description of the Detector

The mechanical design of the detector can be divided in four parts, as presented in fig. 5.2:

- Active area.

- Mirror.

- Vacuum flange.

- Fibre connector.
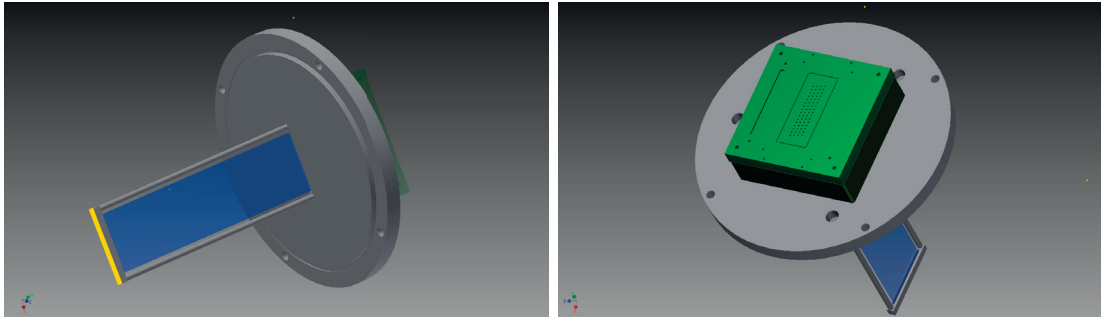
Figure 5.2 – CAD model of the detector showing the active area of the monitor (blue), the supporting frame for the fibres and the vacuum flange (grey), the mirror (yellow), and the fibre connector (green).

5.2.1 Active Area

Within the *active area*, the fibres lay straight and perpendicular to the beam, forming a sort of curtain that is held by a supporting frame. This frame is made of two metallic rods that are fixed to a vacuum flange on one extreme (fig. 5.3) and to a metallic plate on the other. This metallic plate also holds the mirror that is glued on the end of the fibres (fig. 5.7). A small quantity of glue applied on both ends of the frame ensures that the fibres rest in their position with the necessary tension.

5.2.2 Mirror

The *mirror* consists in a high-reflectivity aluminium foil coupled to the fibres with the silicon adhesive Dow Corning 3145RTV [57], which offers a good transparency and an suitable refractive index. It should be noted that there exist alternatives for the reflector and the glue that offer a better performance. As described in [58], the combination of

Figure 5.3 – Picture taken during the assembly of the detector. The flange is resting over the vacuum tank (black), but in the opposite sense to normal operation, showing the active area of the fibres. During the operation of the monitor, the fibres are inserted into the tank.

the EPOTEK H301-2FL epoxy glue with the specialised reflector film ESR, produced by 3M, would increase the mirror reflectivity up to 90%. This will be considered for future development if needed.

5.2.3 Vacuum Flange

An advantage of scintillating fibres is that they can be operated inside the primary vacuum of the CERN experimental areas ($\sim 10^{-3}$ mbar). The prototype is designed in such a way that the scintillating fibres and the SiPM are integrated into a modified *vacuum flange* of a FISC monitor (introduced in section 1.3). This greatly facilitates the integration with the beam line, as the SciFi prototype can be installed in the vacuum tank of an existing FISC (fig. 5.3).

The passage of the fibres from vacuum to ambient pressure is done through a thin slot machined in the flange, which acts as a vacuum feedthrough. Once the fibres are placed in their final position during the assembly, this slot is sealed with a two-phase epoxy resin with commercial name Araldite Standard [59]. This epoxy has a good adherence to plastics and metals and ensures the necessary tightness. Besides, it is widely employed at CERN for its radiation hardness [60].

Note about the epoxy

A common problem of two phase epoxies is the presence of air bubbles trapped in the mix, as can be seen for example in fig. 5.10. This issue can particularly affect applications involving vacuum because air bubbles may escape and debilitate the integrity of the resin. In order to avoid this problem, there are several treatments that can be done to the glue before application [61]. The most common are: centrifugation of the glue, vacuum degassing, and heating.

5.2.4 Fibre Connector

The read-out end of the fibres is arranged in a sort of *fibre connector* onto which a PCB[1] exclusively containing the SiPM is plugged (hereinafter called the SiPM-board). The connector positions the fibres in a pattern that matches the individual SiPM (fig. 5.4), and the alignment of both the fibre connector and the SiPM-board is ensured by a system of precision dowel pins. The ensemble is covered in order to be light-tight and avoid parasitic signals in the SiPM.

The fibre connector and the rest of plastic structures of the monitor are made in Polyoxymethylene (POM), which is a plastic employed in precision parts due to its stiffness and excellent dimensional stability [62]. The use of a plastic is also safer, as the contact with stiffer materials could cause damage to the delicate cladding of the fibres. Another advantage of POM is that it can be produced in black colour, being convenient for applications where light-tightness is required.
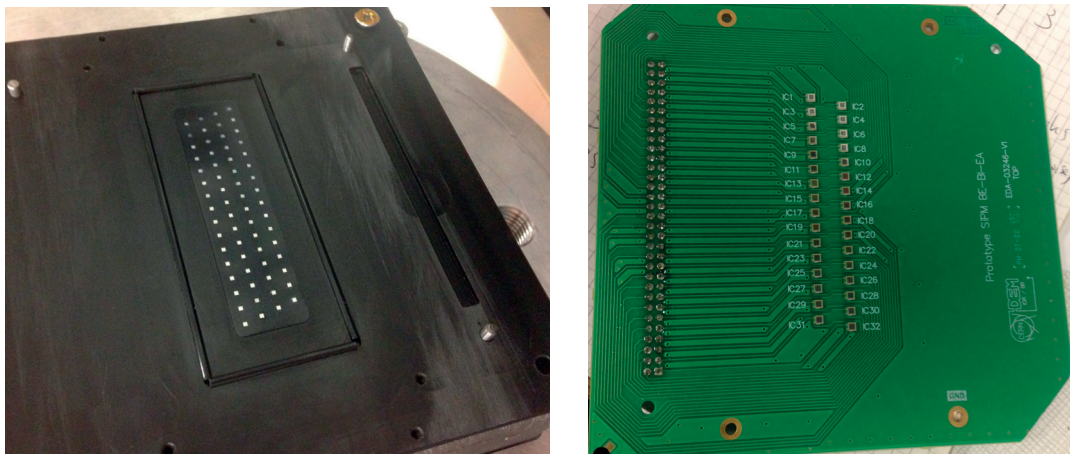
Figure 5.4 – Left: fibre connector in which the 64 fibres are arranged in a pattern that matches the SiPM of the SiPM-board (right image). Right: SiPM-board carrying 32 individual Hamamatsu S13360.

---

[1]Printed Circuit Board

The fibres in the connector are positioned inside circular holes, due to the mechanical difficulty of machining small square shapes. Thus, a small quantity of epoxy glue is deposited inside the gap between the circular holes and the square fibres, in order to guarantee a good mechanical stability (fig. 5.5).

Figure 5.5 – Fibres being glued on the fibre connector.

5.3 Fibre-SiPM Coupling

The *coupling* between the fibres and the SiPM is critical, as it determines the amount of light arriving to the photodetectors. Its quality is affected by the changes in the medium of propagation of light and other phenomena described hereafter:

- Polishing.

- Fresnel reflections.

- Numerical aperture of the fibre.

5.3.1 Polishing

Light losses can occur at the end of the fibres due to the non-uniformity and non-planarity of the surfaces, as illustrated in fig. 5.6. Therefore, it is vital to provide a good smoothness to these surfaces by means of a *polishing treatment*.

The most common polishing methods for plastic scintillators are sanding, hand polishing, and machine polishing [63]. However, the best quality is obtained with diamond milling cutters, which create a surface with an optimum finishing that needs no further treatment.
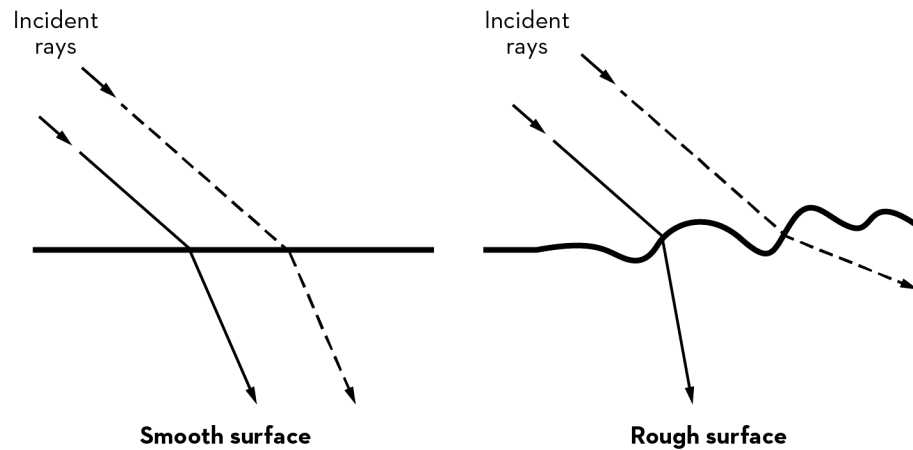
Figure 5.6 – Optical difference between a smooth and a rough surface.

The fibre connector was polished using such diamond cutter, but on the side of the fibres where the mirror is placed this technique could not be employed. The reason is that the structure that holds the fibres on that side is made of aluminium, which is too stiff for the diamond tool. Therefore, that side of the fibres was polished with progressively finer sandpaper (fig. 5.7) and finished with a special polishing paste for acrylic materials [64].

Figure 5.7 – Fibres on the mirror holder during polishing with sandpaper. *Note: there are metallic accessories on the sides of the holder in order to guarantee mechanical stability during the polishing. The orange tape helps avoiding the creation of metallic dust that could harm the fibres.*

5.3.2 Fresnel Reflections

Fresnel reflections occur when light travels between two media with different refractive indexes. The equations for the reflectivity, R, and transmittance, T, were deduced by

Augustin-Jean Fresnel, which for the case of normal incidence have the form:

$$R = \left| \frac{n_1 - n_2}{n_1 + n_2} \right|^2, \tag{5.1}$$

$$T = 1 - R, \tag{5.2}$$

where n_1 and n_2 are the refractive indexes of the two media.

If the mechanical coupling between the fibre and the SiPM is not perfect and there is a small gap of air in between, there will be two possible boundaries where the light will reflect: fibre-air and air-SiPM.

Assuming:

$$n_{fibre} = 1.6 \text{ (light exiting mostly trough the core)}, \tag{5.3}$$

$$n_{SiPM} = 1.55 \text{ (SiPM epoxy window [65])}, \tag{5.4}$$

$$n_{air} = 1, \tag{5.5}$$

the total reflectivity is:

$$R_{total} = R_{fibre-air} + R_{air-SiPM} = 5.3\% + 4.6\% \approx 10\%. \tag{5.6}$$

The losses due to this inhomogeneity can be improved by using an optical coupler in the junction of the fibre and the SiPM. These substances have a refractive index between those of the materials to be coupled, thus favouring a continuous transition. The effect of an optical grease like the Dow Corning Q2-3067 453G, with $n = 1.47$ (at $\lambda = 589\,\text{nm}$), could decrease the reflectivity to:

$$R_{grease} \approx 0.2\%. \tag{5.7}$$

Unfortunately, the prototype does not count with such an optical grease.

A deeper study of Fresnel reflections in scintillators can be found in [66].

5.3.3 Numerical Aperture of the Fibre

Scintillation light is emitted from the fibre within a certain cone described by the *Numerical Aperture* (NA) of the fibre, as illustrated in fig. 5.8. The angle of this cone of light, θ, is given by:

$$NA = n \sin \theta = \sqrt{n_{core}^2 - n_{clad}^2}, \tag{5.8}$$

being n the refractive index of the material coupled to the fibre, n_{core} the refractive index of the core, and n_{clad} the refractive index of the cladding.
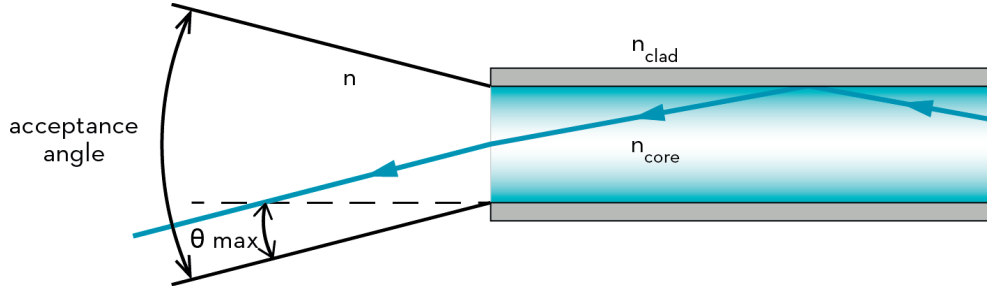
Figure 5.8 – Numerical aperture of a scintillating fibre

In order to collect the maximum of scintillation light, the entire cone should illuminate the active area of the photodetector. However, depending on the refractive index of the SiPM window and its geometry, it may not be the case. The BCF-12 multi-clad fibres have a numerical aperture of 0.74 [36], and the SiPM have a protective epoxy window with $n_{SiPM} = 1.55$ [65]. Hence, the maximum angle for the light exiting the fibre and entering the SiPM is:

$$\theta = 28.5°. \tag{5.9}$$

From the specifications of the manufacturer, the epoxy layer of the S13360-1350PE is 0.3 mm thick. Therefore, when the scintillation light reaches its active area, it covers a surface of:

$$A_{light\ cone} = 1.3\,\text{mm} \times 1.3\,\text{mm}. \tag{5.10}$$

(assuming that the light cone inherits an approximate square shape from the fibre cross section.)

Because the active area of the S13360-1350PE is also 1.3 mm × 1.3 mm, in the case of a perfect alignment of the fibre and the SiPM, the totality of the light is collected, as can be appreciated in fig. 5.9.

Nonetheless, there is an unavoidable uncertainty in the relative position of the fibres and the SiPM. It can have four origins:

1. The precision in the positioning of the alignment pins and other objects in the POM during the machining process. The guaranteed tolerance by the mechanics workshop is 0.1 mm.

2. The uncertainty in the position of the fibres inside the holes of the fibre connector. The round holes have a diameter of 1.5 mm, but the fibres are squares of 1 mm ×
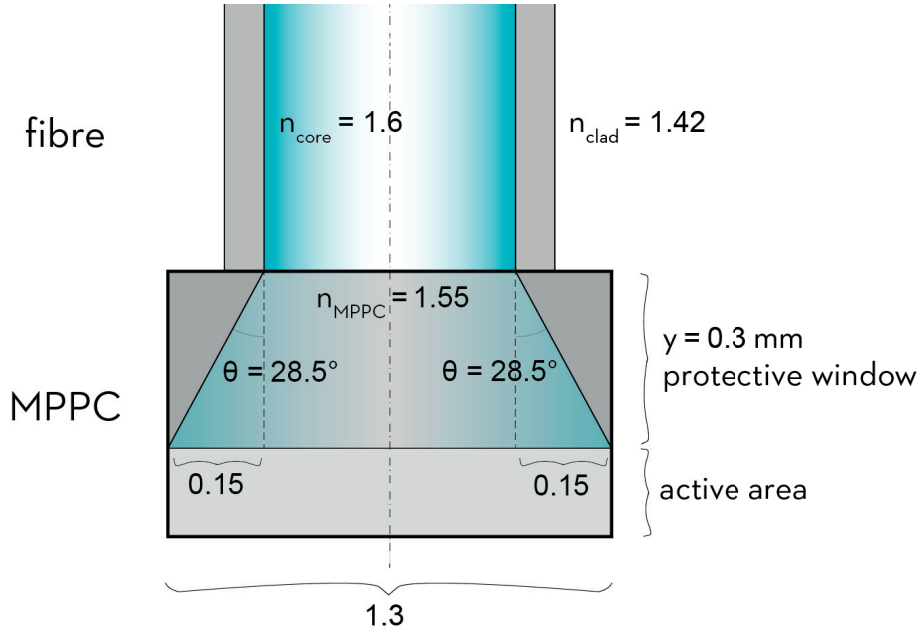
Figure 5.9 – Diagram of a BCF-12 coupled to a MPPC S13360-1350PE, showing the cone of scintillation light reaching the active area of the SiPM.

1 mm, which creates an uncertainty of approximately 0.1 mm in the position within the hole (clearly appreciated in fig. 5.10).

3. The accuracy in the placement of the SiPM during the soldering process on the PCB, which is guaranteed to 0.1 mm by the electronics assembly workshop.

4. The tolerance in the dimensions of the MPPC, which according to the manufacturer [65] is ±0.1 mm.

The addition of these uncertainties yield an upper limit to the misalignment between the SiPM and the fibres of:

$$misalignment \leq 0.4\,\text{mm}. \tag{5.11}$$

Figure 5.11 illustrates the maximum misalignment scenario, in which the centre of the fibre and the centre of the SiPM are shifted by 0.4 mm in any transverse direction. In such case, the illuminated surface of the SiPM is:

$$A_{illuminated} = 0.9\,\text{mm} \times 0.9\,\text{mm}, \tag{5.12}$$

which means that only a fraction of the scintillation light is detected:

$$\frac{A_{illuminated}}{A_{light\ cone}} = \frac{0.9\,\text{mm} \times 0.9\,\text{mm}}{1.3\,\text{mm} \times 1.3\,\text{mm}} \approx 48\%. \tag{5.13}$$
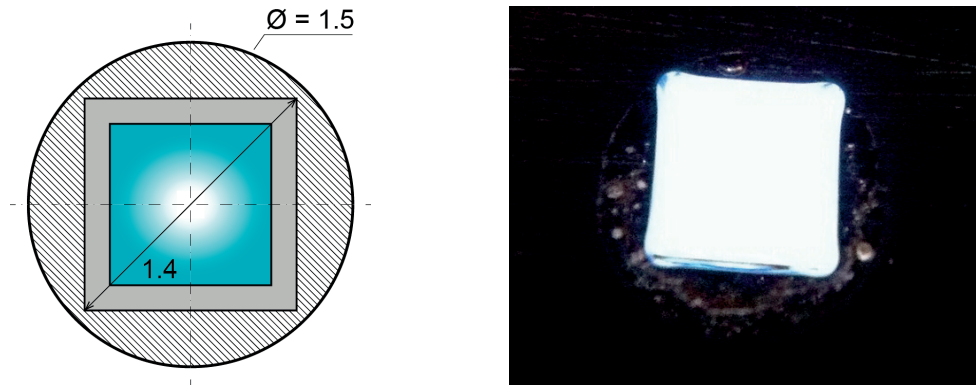
Figure 5.10 – Left: illustration of a 1 mm thickness fibre circumscribed within a 1.5 mm diameter hole. Right: microscope image of a fibre end in the fibre connector. *Note: it can be noticed that the corners of square fibres are not sharp, but instead have a certain curvature. Additionally, as discussed in section 5.2.3, air bubbles can be seen in the epoxy resin.*

Therefore, this value establishes an upper limit to the loss of light due to a possible misalignment between the fibres and the SiPM. It should be noted that the misalignment could be different from fibre to fibre, resulting in an inhomogeneity of the light collection between different channels.

The collection of light could be greatly enhanced using a SiPM with a larger active area and a thinner window, such as the new version of the S13360, the S13360-2050VE [50]. It has an active area of 2 mm × 2 mm and a window of 100 μm, thanks to the adoption of trough-silicon via, eliminating wiring on the photosensitive area side.

5.4 Readout Electronics

The readout electronics are composed of:

- The CITIROC evaluation board (fig. 5.12): receives the SiPM-board, which is plugged into it; provides the bias voltage to the 32 SiPM, acquires their signals, and generates TTL digital signals whenever the SiPM pulses exceed a preset threshold (indicating the detection of a particle).

- CAEN N89 NIM-TTL-NIM converters [67]: used to convert the TTL signals coming from the CITIROC to the NIM standard.

- VME Scalers CAEN V560 [68]: accumulate the number of hits per channel. They work with the NIM standard.

Additionally, a PC is employed to monitor and control the main parts of the detector
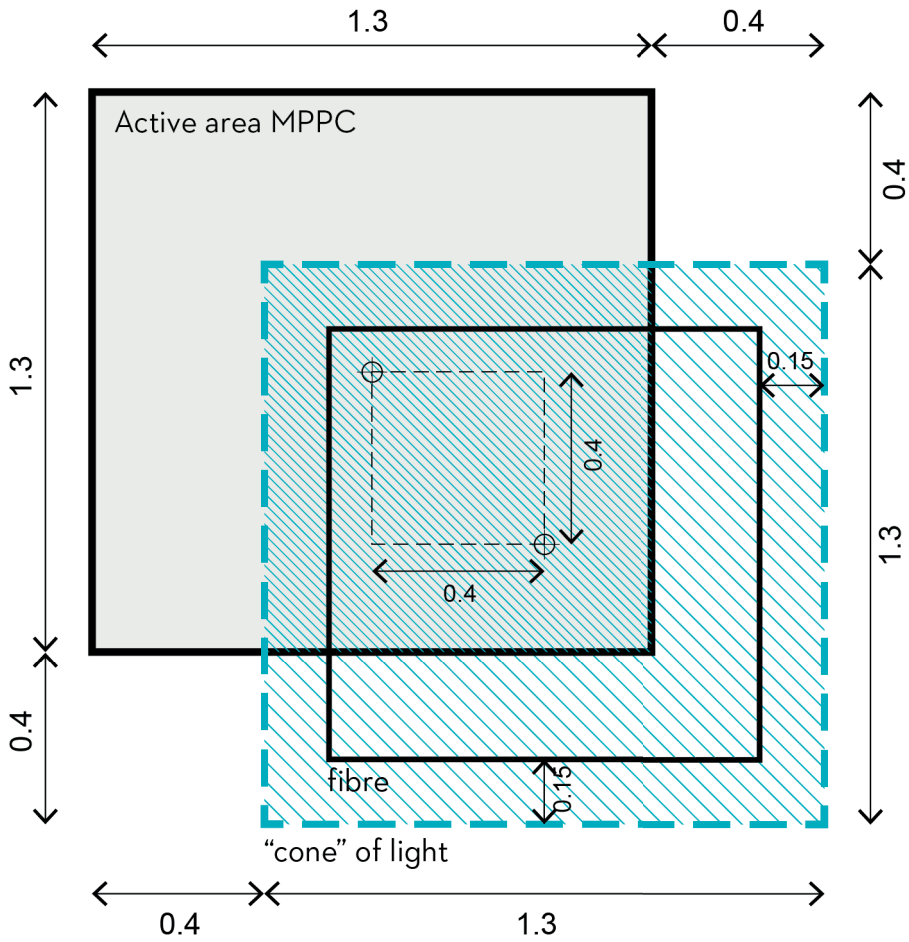
Figure 5.11 – Diagram of the maximal misalignment between the 1 mm BCF-12 and the MPPC S13360-1350PE.

and executes the data acquisition software. All these devices had the advantage of being immediately available in the laboratory and being relatively simple to implement.

5.4.1 SiPM Pulse Acquisition and Processing

In a first stage, the CITIROC preamplifiers and shapes the analogue pulses of the SiPM in order to increase the signal to noise ratio. After this pre-processing phase, the pulses follow the "trigger" line of the ASIC and travel to the discriminators. These generate TTL logic signals whenever the amplitude of the pulses is higher than a preset threshold value.

This threshold value serves to filter the low noise events, such as the dark counts of the SiPM. However, due to the stochastic nature of the particle detection, some real events can have a low amplitude and be rejected by the discriminators. For this reason,
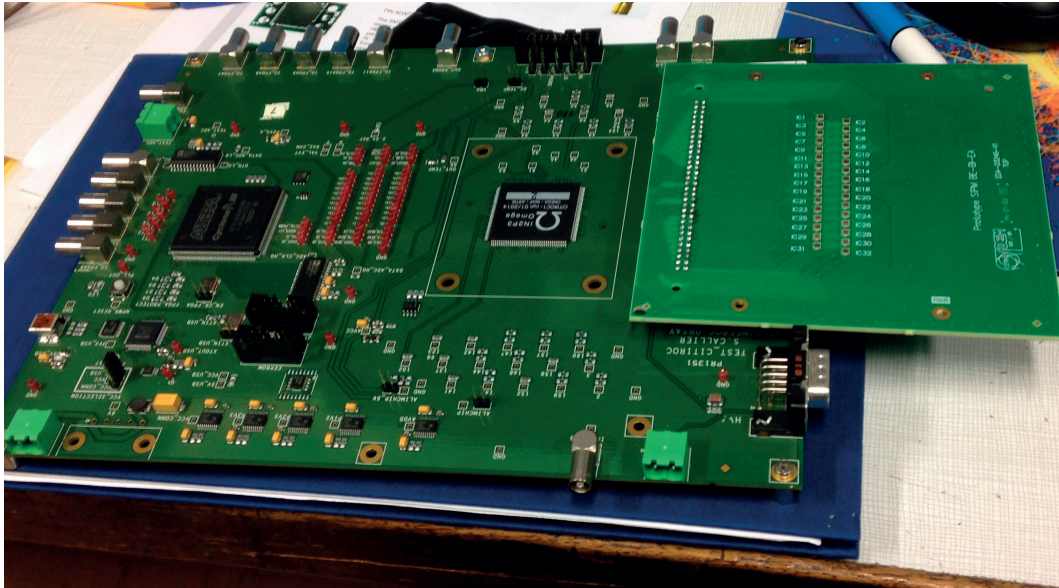
Figure 5.12 – The CITIROC board with the SiPM PCB plugged onto it.

the threshold level of the discriminators has a large impact on the performance of the monitor. This subject is further investigated in detail in section 5.5.

After leaving the CITIROC board, the logic signals travel through coaxial cables to the TTL-NIM converters, where they are transformed into NIM logic signals. This conversion is needed because the next step of the acquisition chain are the VME Scalers that exclusively process NIM signals. The Scalers count and store the number of signals acquired per channel, and finally the PC recovers the data and reconstructs the beam profile.

The Scalers are synchronised with the SPS beam extraction signals, in such a way that their memory buffers are emptied right before the beam extraction begins and read-out immediately after the beam extraction has finished. Therefore, only the events occurring during the 4.8 seconds of the beam extraction are used for the beam profile reconstruction.

In order to keep low the complexity of the prototype readout, only the information of the fibre that has been hit is registered, which is sufficient for the reconstruction of the transverse profile of the beam. The time at which the interaction happened and the energy deposited are not recorded. If the time information were recovered with nanosecond precision, it would be also possible to reconstruct the longitudinal profile of the beam.

5.4.2 SiPM Powering

The SiPM bias voltage is supplied by an external device, an 'iSeg EHS 82 05x high precision power supply' [69]. This module can supply voltages and intensities up to $500\,\text{V}$ and $10\,\text{mA}$, with resolutions of $1\,\text{mV}$ and $30\,\text{nA}$, respectively. The ripple and noise is kept below $5\,\text{mV}$ and it has a stability of $< 0.01\%$ of the nominal voltage, guaranteeing the necessary stability for maintaining a uniform operational voltage of the SiPM. The iSeg module is installed in a MPOD crate [70] that allows remote control from a PC.

The CITIROC has an internal Digital-to-Analogue Converter (DAC) that allows a fine tuning of every individual SiPM voltage by subtracting a certain amount of voltage from its bias voltage (fig. 5.13). This feature is useful to compensate the differences in breakdown voltage that naturally exist between SiPM of the same production lot.
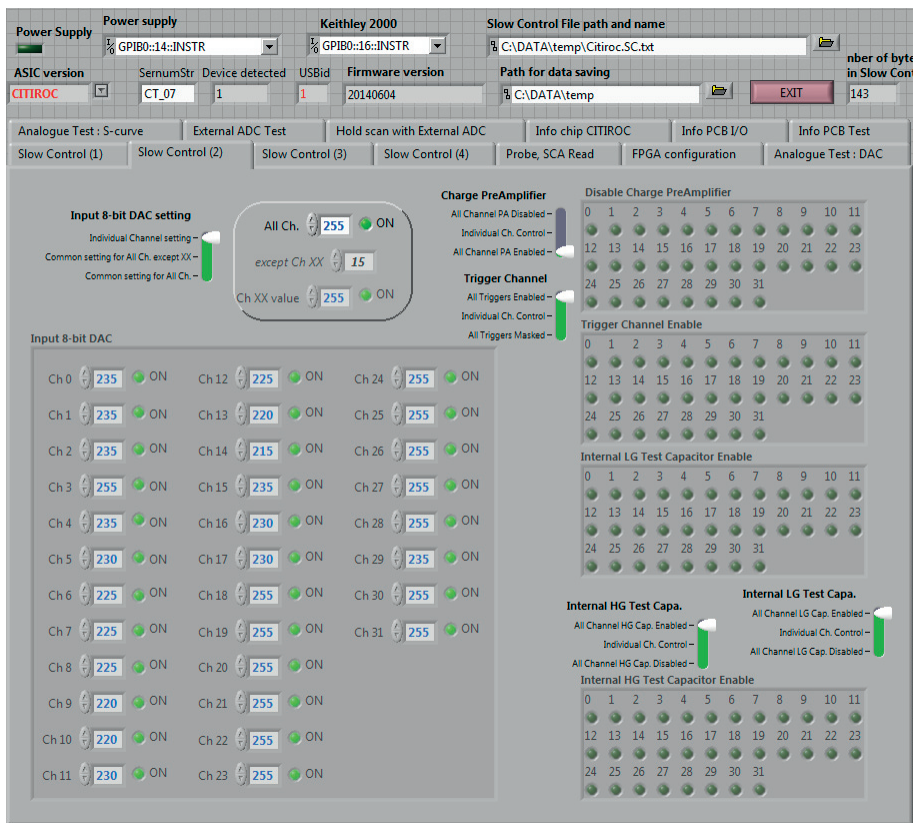
Figure 5.13 – Window of the "Slow Control" of the CITIROC showing the DAC configuration for a refined adjustment of the 32 SiPM bias voltage.

The schematic diagram of one of the 32 input channels of the CITIROC board is shown in fig. 5.14, where x denotes the channel number. The cathodes of the SiPM are connected to the negative high voltage ('HV<x>' in the figure), while the anodes are directly connected to the input channels of the ASIC ('in<x>').
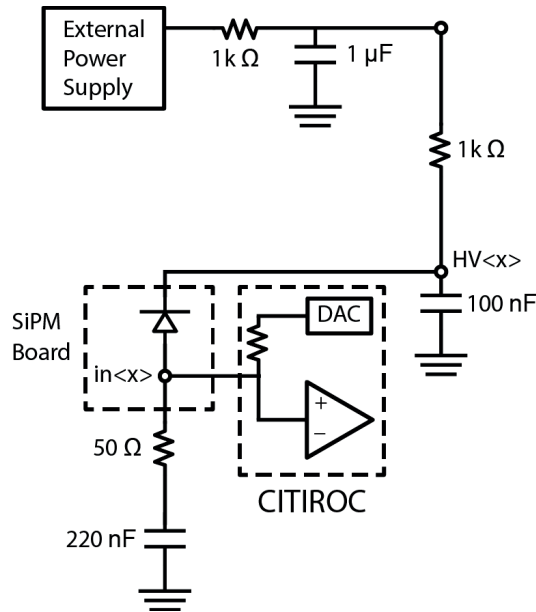
Figure 5.14 – Schematic diagram of the input channels of the CITIROC evaluation board.

SiPM Power Consumption

It is possible to estimate the current consumption of the SiPM-board in the case of maximum absorption. Calling e the elementary charge, $<N>$ the average number of photons detected per event, G the gain of the SiPM, and R the maximum expected particle rate:

$$I_{max} = e \ <N> \ G \ R. \tag{5.14}$$

The leakage current of the SiPM is so low compared to the avalanche current that it can be neglected in this calculation.

If the SiPM are operated at the recommended overvoltage ($G = 1.7 \times 10^6$), assuming an average of 30 detected photons per event, and a maximum event rate of $10\,\text{MHz}$, the maximum consumption of the board is:

$$I_{max} \approx 100\,\text{µA}, \tag{5.15}$$

meaning that the iSeg module can supply enough current to power the SiPM-board, even at higher rates.

5.4.3   Data Acquisition and Control

The data acquisition and the configuration of the prototype is managed by the PC. It mainly performs the following functions:

- Control and reading of the VME scalers.

- Powering of the CITIROC board and Slow Control of the ASIC.

- Control and monitoring of the iSeg HV power supply for the SiPM.

- Execution of the data acquisition software.

The data acquisition software is a custom made program written in LabVIEW [71]. It reads-out the scalers, displays the last measured profile, and stores the data in a safe file system for subsequent analysis (fig. 5.15).
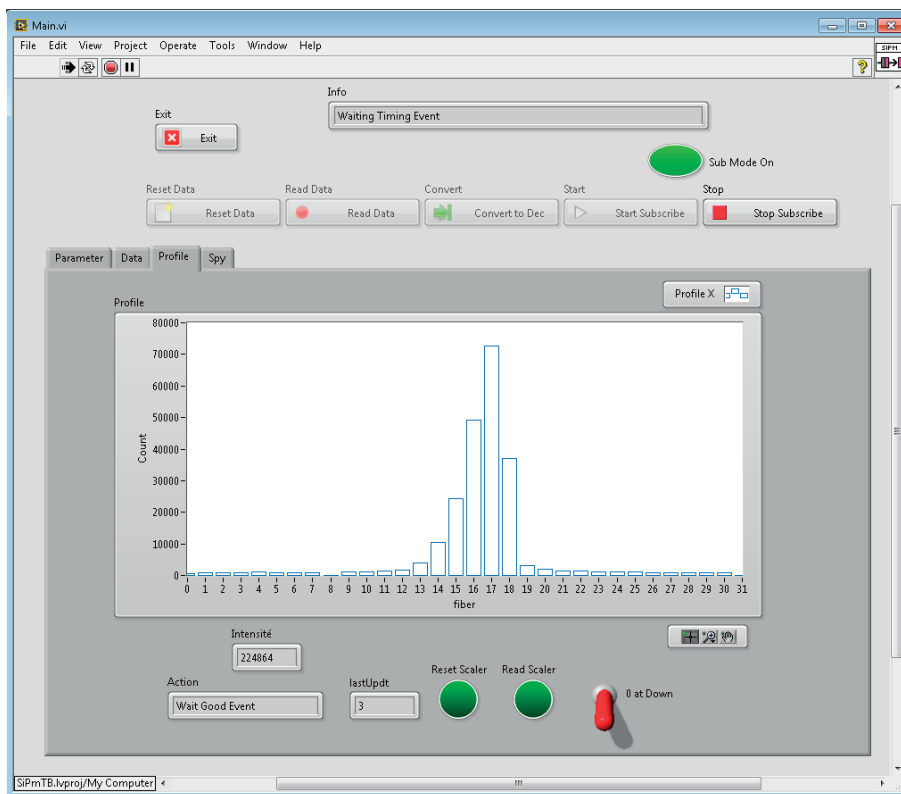
Figure 5.15 – Screen capture of the LabVIEW DAQ software.

All the electronic elements, included the PC, are installed close to the beam line and cannot be accessed during beam line operation (fig. 5.16). However, the PC can be accessed remotely, allowing real-time visualisation of the data acquisition and configuration of the detector systems.
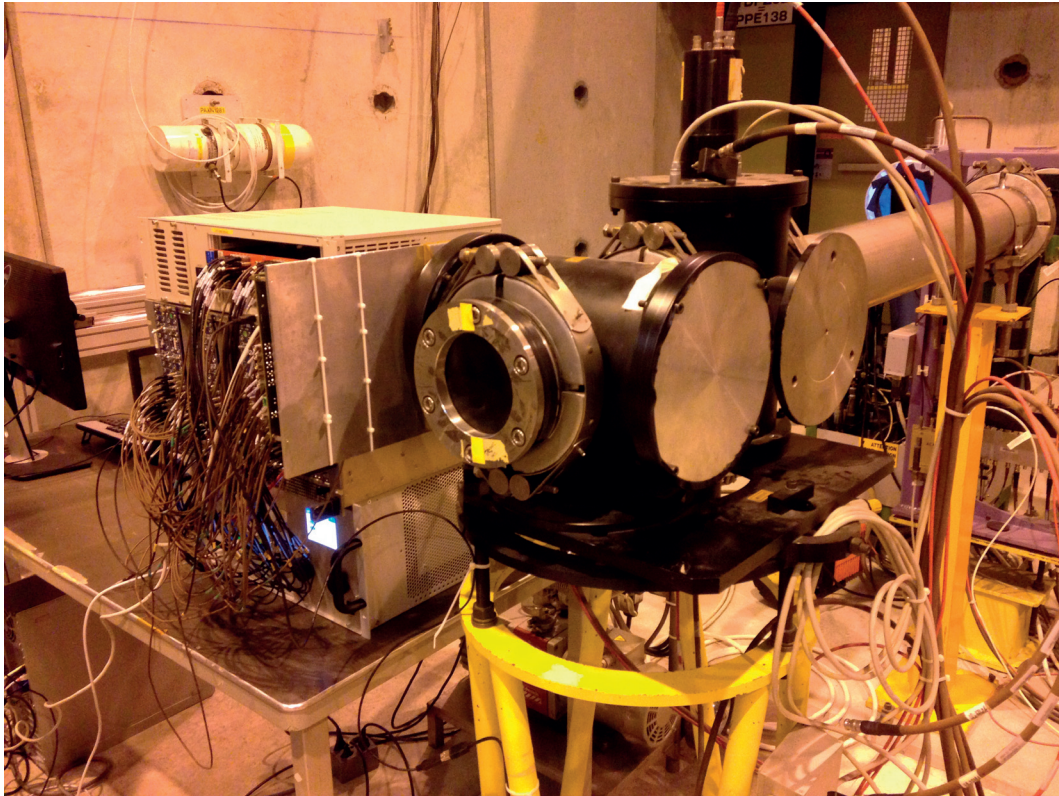
Figure 5.16 – The SciFi prototype installed in the beam line: the FISC vacuum tank in the centre of the picture contains the detector; the CITIROC board is placed very close to the SiPM and is held by a metallic plate (left of the tank); the iSeg power supply, the NIM-TTL converters, the VME Scalers, and the PC stand on the nearby table (left part of the picture).

5.5 Threshold Configuration

As aforementioned in section 5.4, the threshold of the discriminators has a large influence in the detection efficiency of the monitor and, for this reason, its configuration requires careful investigation. The physical processes occurring since a particle hits the scintillating fibre and the light is detected by the SiPM are statistical in nature. This means that for every interacting particle the quantity of light detected, and thus the signal amplitude, fluctuates around a certain value.

If the discriminator threshold is set excessively high, there is a risk of not detecting events that produce few photons. Alternatively, if the threshold is set too low, there is the risk of acquiring non-desirable events, like fluctuations of the electrical noise baseline and dark counts of the SiPM, whose occurrence is also stochastic.

Therefore, setting correctly the threshold requires a characterisation of the number of photons detected, and its fluctuation, during the operation of the monitor with a

particle beam. The light detected typically follows a statistical distribution and once it is characterised, it can be employed to calculate the probability of losing events because the threshold is set to a certain level. In a similar manner, the characterisation of the noise of a SiPM (height of the noise pulses and their frequency of occurrence), provides the probability of acquiring false events because they pass the threshold cut.

5.5.1 Cumulative Distribution Function

The light detected from a scintillating fibre-SiPM ensemble follows a Landau distribution smeared by a resolution function assumed to be Gaussian (more information in appendix C.3). Once that distribution is characterised, making use of statistical tools it is possible to obtain the sought probability of losing events due to setting the threshold to a certain value. The function that gives this probability is called the Cumulative Distribution Function (CDF).

The CDF of a random variable X (fig. 5.17), gives the probability that X will take a value less than or equal to x:

$$CDF(x) = P(X \leq x) = \int_{-\infty}^{x} f(X)dX. \tag{5.16}$$
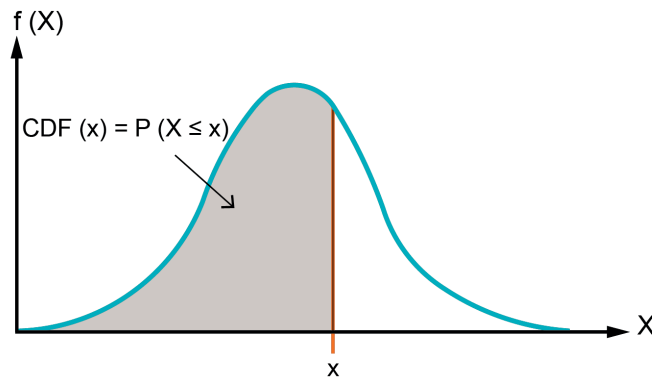
Figure 5.17 – Plot of a statistical distribution f(X) where the shaded area under the curve corresponds to its Cumulative Distribution Function, CDF(x).

Therefore, if the CDF of the detected light distribution is known, it would be possible to estimate the probability of losing events for a given threshold:

$$CDF(threshold) = \; loss \; probability. \tag{5.17}$$

Calculating the CDF of a Landau-Gauss convolution is rather complicated. However, considering the dominating Gaussian character of the distribution would allow using the

well-known standard normal distribution. According to this simplification, the probability of losing events for a given threshold is given by a Z-score value:

$$Z = \frac{threshold - MPV}{\sigma}.$$

(5.18)

Unfortunately, due to a tight schedule on the beam availability, it was not possible to do a dedicated measurement of the collected light distribution in the prototype. Hence, a Geant4 simulation of a scintillating fibre behaviour is employed to estimate such distribution (the simulation is fully described in appendix B.2).

Simulating a beam of MIP (protons of $180\,\mathrm{GeV/c}$), the collected light distribution has the form shown in fig. 5.18. Its best fit yields:

$$MPV = 25.5\ photons,$$

(5.19)

$$\sigma = 10.5\ photons.$$
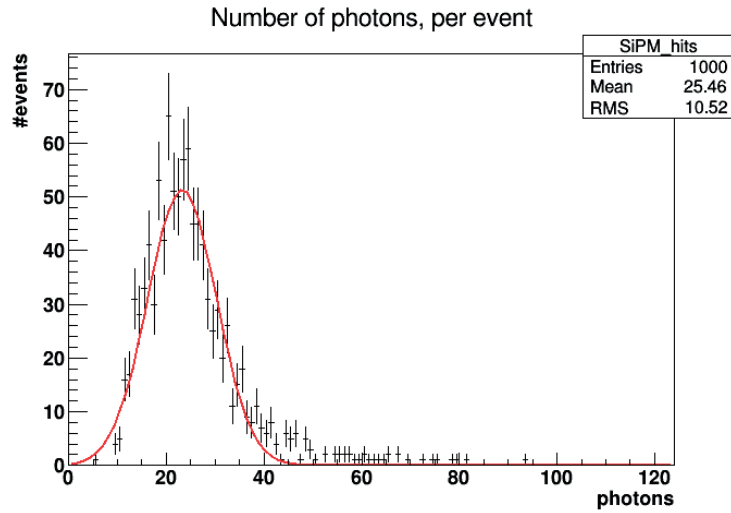
Figure 5.18 – Distribution of detected light of the prototype for a beam of $180\,\mathrm{GeV/c}$ protons. Simulation done with Geant4 for 1,000 particles.

Therefore, using eq. (5.19) in the Z-score equation, eq. (5.18), the probability of losing events as a function of the threshold is calculated and presented in Table 5.1.

It should be noted that, as discussed in section 5.3, the light collection between different channels of the prototype is subject to an uncertainly, due to the alignment and coupling of the SiPM. To correct possible inhomogeneities in the efficiency, the light detection of future versions of the monitor should be properly characterised for every channel.

Table 5.1 – Probability of losing events depending on the threshold level.

Threshold (photons)	Loss probability (%)
0.5	1.0
1.5	1.3
2.5	1.6
3.5	2.0
4.5	2.5
5.5	3.2
6.5	3.9
7.5	4.8

5.5.2 Noise Characterisation

The other factor that needs to be taken into account when setting the threshold level is the noise of the SiPM, which is characterised by counting the number of dark counts for different threshold levels. An example of such characterisation is presented in fig. 5.19, done with the STiC ASIC (introduced in section 4.4), where it is also possible to see the drop in dark rate for 1, 2, and 3 dark photoelectrons.
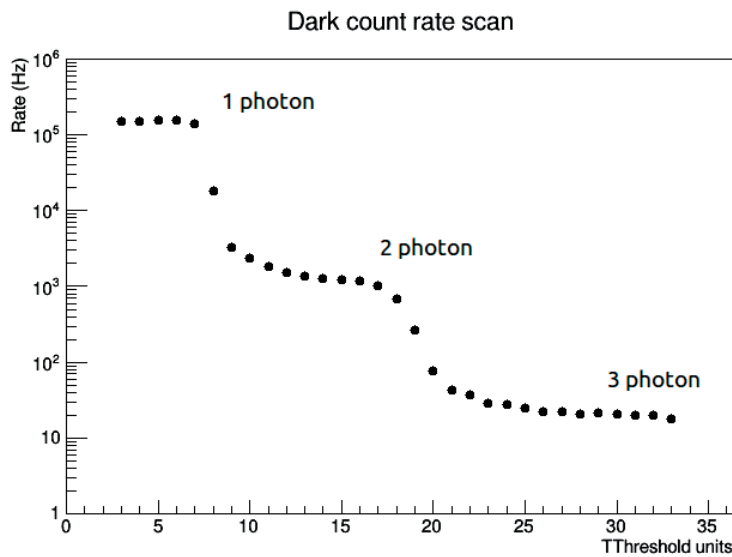
Figure 5.19 – Dark count rate scan of the MPPC S13360-1350 showing the drop in dark rate for a threshold level of 1, 2, and 3 photoelectrons.

The measurement of the noise of a S13360-1350, operated at the recommended operating voltage $V_{op} = 3\,\text{V}$ and a temperature of approximately $25\,°\text{C}$, is presented in Table 5.2.

The existence of dark events with a level higher than 1 photoelectron is related to the pixel crosstalk of the SiPM (more on the crosstalk in section 4.2.4). The 0.8% crosstalk

Table 5.2 – Dark count rate of the MPPC S13360-1350 as a function of the threshold.

Threshold (photons)	Dark count rate (Hz)
0.5	120×10^3
1.5	1.1×10^3
2.5	20
3.5	0.1
4.5	4×10^{-3}

value of the S13360-1350 (Table 4.1) implies that there is a $\sim 1\%$ probability that a pixel activated by a dark count will trigger a neighbouring pixel, thus adding a count to the recorded signal. For this reason the DCR of the S13360-1350 registers less events when the level of the discrimination threshold is increased (a drop of approximately two orders of magnitude in the DCR whenever the threshold is increased by one photoelectron).

5.5.3 Threshold Choice

The combination of the information from Table 5.1 and Table 5.2, allows to choose an optimal value for the threshold. It was decided to operate the detector at a threshold level of *3.5 photons*. This value gives a high probability of detecting approximately 98% of the beam particles, while keeping the acquisition of false-events below 1 event per second. The operation of the system in the beam line supported this choice.

5.5.4 Note About an Auxiliary Trigger Detector

External Sources of Noise

There are other sources of false-events besides the noise of the SiPM. These are principally real particles travelling in the environment, such as cosmic rays, environmental radiation, and stray radiation emanating from the beam lines. They may generate identical signals to the particles in the beam, being effectively detected as true-events.

The prototype is not equipped to differentiate these particles and they are acquired along the rest of events. However, cosmic rays are not expected to have a larger influence than one event per second, due to the size and orientation of the monitor. Stray radiation and radioactive decays are more difficult to predict or measure and they could have a larger influence.

Triggered Acquisition

There is an effective way to suppress the noise, no matter its origin, and greatly improve the signal-to-noise ratio of the monitor. If an auxiliary particle detector is placed upstream in the beam line, it could anticipate the arrival of a particle, and generate a signal that triggers the acquisition of that particle by the SciFi monitor. Thus, the detection threshold could be safely set to the minimum (0.5 photons), without suffering an increase in noise events.

Such auxiliary detector could consist in a thin scintillator tile read-out by a PMT (such as the scintillator paddles described in section 1.3), or even the plane of another fibre profile monitor (for example, the two fibre planes of the horizontal and vertical profiles put in coincidence).

5.6 Efficiency of the Prototype

The SciFi prototype was conceived as a demonstrator to show that the scintillating fibres read-out by SiPM, can successfully reconstruct the beam profile for the energies and intensities of the North Area beams. For this reason, a large detection efficiency was not sought.

5.6.1 Predicted Efficiency

The detection efficiency of the prototype has been estimated from its geometrical acceptance, the threshold level, and the electronics dead time. This calculation yields a value:

$$
\begin{aligned}
\epsilon_{prototype} &= \epsilon_{geometric} \; \epsilon_{threshold} \; \epsilon_{electronics} \\
&= 0.44 \cdot 0.98 \cdot 1 = 0.43 \equiv 43\%.
\end{aligned}
\tag{5.20}
$$

The determination of the three components is given in section 5.6.2, section 5.6.3, and section 5.6.4.

The real efficiency of the prototype was measured from data taken in the beams of the North Area. Its comparison with the estimation is presented in section 6.2.2.

5.6.2 Geometrical Acceptance

If only every other fibre is read-out, the acceptance is already limited to half of the total area covered by the fibres. In addition, because the cladding of the fibres does not scintillate, it represents an inherent loss of geometrical efficiency. The cladding of the BCF-12 multi-clad fibres is the 12% of the fibre width, thus limiting its acceptance to 88%, as can be seen in fig. 5.20. The two effects together yield a geometric efficiency:

$$\epsilon_{geometric} = 0.5 \ \times \ 0.88 = 0.44 \equiv 44\%. \tag{5.21}$$
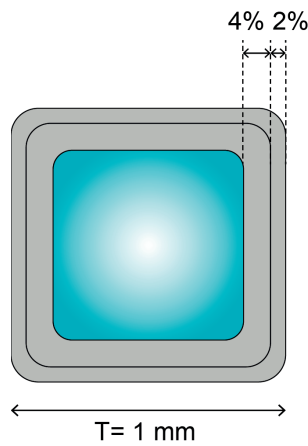
Figure 5.20 – Illustration of the size of the cladding in a BCF-12 multi-clad fibre (image not to scale).

The inefficiency due to the cladding could be avoided if two or more layers of fibres are staggered and shifted by half to each other, hence covering the inactive spaces, as represented in fig. 5.21. Unfortunately, staggering layers of fibres with precision represents a difficult mechanical challenge and, for simplicity, it was decided to remain with one layer.

5.6.3 Threshold Level

Regarding the threshold, the relationship between the discriminators level and the detection efficiency was studied in section 5.5. For the chosen threshold of 3.5 photons, approximately 98% of the incoming particles are detected:

$$\epsilon_{threshold} = 0.98. \tag{5.22}$$
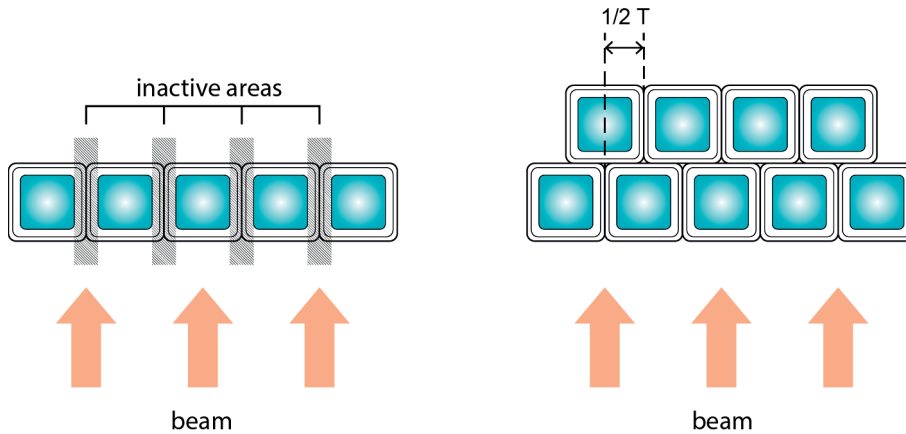
Figure 5.21 – Effect in beam coverage of staggered layers of fibres (cladding exaggerated for an illustrative purpose).

5.6.4 Electronics Dead Time

The dead time of the readout electronics also has an influence in the detection efficiency. The analogue pulses from the SiPM travel to the CITIROC, thereupon go to the logic converters, and finish their journey in the scaler counters, as explained in section 5.4. All the intermediate elements can potentially limit the maximum processing rate, above which a loss of signals cannot be avoided.

The SiPM pixels have a recovery time during which they cannot process new pulses. This recovery time is related to the pixel size, being approximately 100 ns for the S13360-1350, with a pixel size of 50 µm. The CITIROC resolving time is given by the fast shaper, which has a peaking time of 15 ns. The CAEN N89 logic converters and the CAEN V560 scalers have resolving times of 25 ns and 10 ns, respectively. From these four devices, the SiPM is clearly the limiting one, having the largest dead time of 100 ns.

Using Poisson statistics, it is possible to estimate the probability of losing events because multiple events occur within the dead time of one channel. The probability of observing k events during the dead time is:

$$P \left(k \text{ events within dead time } \right) = \frac{\lambda^k e^{-\lambda}}{k!}, \tag{5.23}$$

where λ is the average number of events occurring within the dead time.

Such average is determined by the rate of events in the channel. For a channel rate R, and assuming that the events are uniformly distributed in time, λ is:

$$\lambda = 100 \, \text{ns} \times R, \tag{5.24}$$

due to the 100 ns dead time.

The efficiency of the electronics according to this calculation is presented in Table 5.3 for different channel rates. It worsens noticeably for values above 10^6 Hz.

Table 5.3 – Efficiency of the electronics as a function of the channel rate.

Channel rate (Hz)	$\epsilon_{electronics}$ (%)
10^3	100
10^4	100
10^5	100
10^6	99.5
10^7	73.6

The channel rate is proportional to the intensity of the beam. However, it is difficult to make a precise estimation of the efficiency as a function of the intensity, since the beam spot can have diverse sizes and spread over several fibres. A channel rate of 10^6 Hz has been assumed as a safe value for the total efficiency of the prototype calculated in eq. (5.20).

There are several strategies that could be employed with high intensity beams to guarantee the correct functioning of the monitor:

- Use SiPM with smaller pixel size and a shorter recovery time.

- Use thinner fibres in order to share the beam spot between a larger number of channels.

- Develop a dedicated electronics readout with components that can work at high rates.

5.7 Temperature Effects

Temperature can have an influence in the performance of scintillating fibres and SiPM. The scintillating fibre BCF-12 shows a linear decrease of light output of 0.13% per °C [72]. Thus, the effect can be considered negligible for a beam monitor, as no temperature variations larger enough to be noticeable are expected.

By contrast, SiPM, have a strong dependency on temperature that, for practical purposes, affect their overvoltage and DCR, as explained in detail in section 4.2.6. If the overvoltage is not corrected for the change in temperature, it can vary many performances of the SiPM, such as PDE, crosstalk, gain, and DCR.

5.7.1 Estimation of the Variation in SiPM Performance

The prototype does not have a temperature correction system and, therefore, it was operated at a fixed bias voltage, no matter the changes in ambient temperature. That bias voltage corresponded to the breakdown voltage at $25\,°\text{C}$, provided by Hamamatsu for every individual SiPM, plus the recommended $3\,\text{V}$ overvoltage.

To investigate the impact of ambient temperature variations on the performance of the monitor, a historical of the temperature in the North Area hall was recovered after the data taking from the temperature sensors of the CEDAR detectors (fig. 5.22). The data shows a relatively stable temperature in the hall of around $20\,°\text{C}$ on average, with oscillations of $\pm\,1\,°\text{C}$.
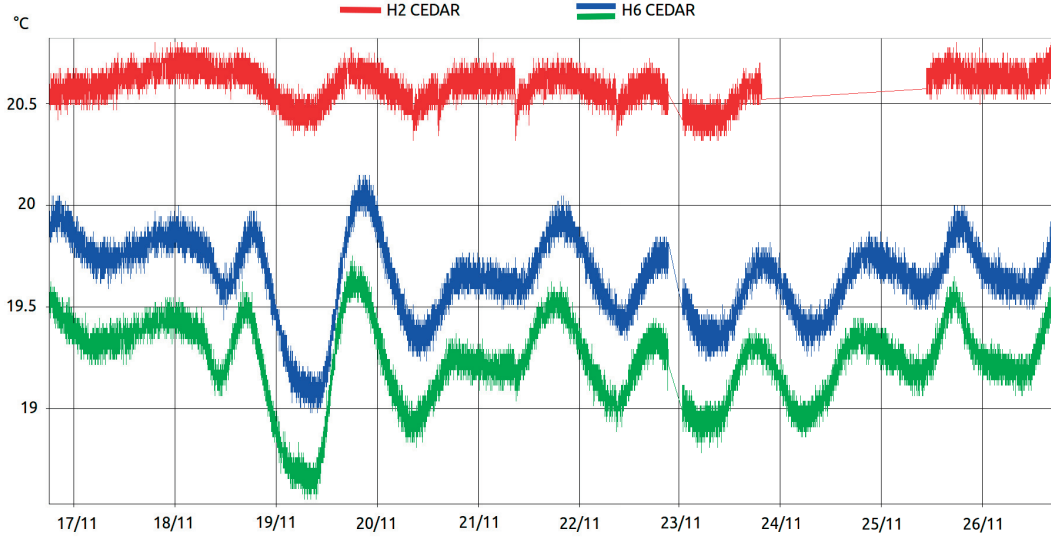
Figure 5.22 – Historical of the temperature in the North Area hall recovered from the temperature sensors of two CEDAR (introduced in section 1.3) installed in the H2 and H6 beam lines.

Because the monitor was operated at approximately $20\,°\text{C}$, instead of $25\,°\text{C}$, the extent of this temperature change is investigated by using analytical models of the SiPM performance. The chosen model for this study is described in [73], which specifically describes the MPPC S13360. According to it, the PDE and the crosstalk can be written as a function of V_{ov}:

$$PDE\left(V_{ov}\right) = C_1 \left[1 - \exp\left(-\frac{V_{ov}}{\alpha}\right)\right], \tag{5.25}$$

$$Cross\left(V_{ov}\right) = C_2 V_{op} \left[1 - \exp\left(-\frac{V_{ov}}{\alpha}\right)\right], \tag{5.26}$$

being C_1 and C_2 proportionality constants, and α a model parameter specifically measured

for the S13360.

The overvoltage at $20\,°\mathrm{C}$ can be calculated with the temperature correction coefficient provided by Hamamatsu, which for the MPPC S13360 is $54\,\mathrm{mV/°C}$:

$$V_{ov}\left(20\,°\mathrm{C}\right) = V_{ov}\left(25\,°\mathrm{C}\right) + 54\,\mathrm{mV/°C} \cdot (20-25) = 3.27\,\mathrm{V}, \tag{5.27}$$

For simplicity, the small oscillations of $2\,°\mathrm{C}$ around the average will be neglected.

Therefore, the sought relative changes in PDE and crosstalk are,

$$\frac{PDE\left[V_{ov}\left(20\,°\mathrm{C}\right)\right]}{PDE\left[V_{ov}\left(25\,°\mathrm{C}\right)\right]} = 1.04,$$
$$\frac{Cross\left[V_{ov}\left(20\,°\mathrm{C}\right)\right]}{Cross\left[V_{ov}\left(25\,°\mathrm{C}\right)\right]} = 1.13. \tag{5.28}$$

Concerning the gain, its relative change can be calculated with eq. (4.1):

$$\frac{G\left[V_{ov}\left(20\,°\mathrm{C}\right)\right]}{G\left[V_{ov}\left(25\,°\mathrm{C}\right)\right]} = \frac{V_{ov}\left(20\,°\mathrm{C}\right)}{V_{ov}\left(25\,°\mathrm{C}\right)} = 1.09. \tag{5.29}$$

The case of the dark count rate is more complex, as it has two dependencies, on temperature and overvoltage:

$$DCR\left(T, V_{ov}\right) = e^{a+b\cdot T} \cdot e^{c+d\cdot V_{ov}}\left[1 - \exp\left(-\frac{V_{ov}}{\alpha}\right)\right], \tag{5.30}$$

where a, b, c, d, and α are fit parameters depending on the SiPM model.

Inserting the right values in eq. (5.30), the sought variation of DCR is:

$$\frac{DCR\left[V_{ov}\left(20\,°\mathrm{C}\right)\right]}{DCR\left[V_{ov}\left(25\,°\mathrm{C}\right)\right]} = 0.57. \tag{5.31}$$

It can be noticed that, even if a higher overvoltage would tend to increase the DCR, the fact of operating the SiPM at a lower temperature has a larger net effect (a difference of $5\,°\mathrm{C}$ approximately doubles the DCR of the S13360).

5.7.2 Efficiency Variation with Temperature

The calculated changes in PDE, crosstalk, gain, and DCR, caused by operating the monitor at $20\,°\mathrm{C}$ with an overvoltage of $V_{ov} = 3.27\,\mathrm{V}$, can be used to estimate the variation of the efficiency in eq. (5.20).

A change in PDE and gain will affect the light detection and therefore the threshold settings. The distribution of detected light vary in the following way:

- The larger PDE implies more detected photons, shifting the distribution to higher MPV.

- The increase in gain enhances the charge collection, entailing an enlargement of the distribution along the x-axis, as shown in fig. 5.23. Because the threshold is set to a fixed charge value of 3.5 photons at $V_{ov} = 3\,\text{V}$, the same value at $V_{ov} = 3.27\,\text{V}$ will allow a fraction of 3-photon events to pass the threshold cut.
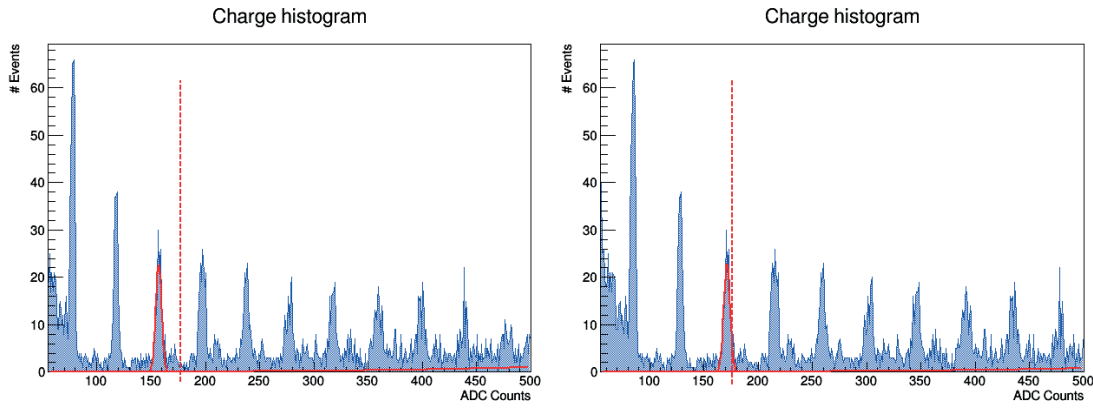
Figure 5.23 – Simulation of the SiPM charge distribution for $V_{ov} = 3\,\text{V}$ (25 °C) on the left and for $V_{ov} = 3.27\,\text{V}$ (20 °C) on the right. It can be appreciated how the photo peaks shift to higher ADC values due to the temperature variation, and the threshold (dotted vertical line) is not longer set to 3.5 photons.

These changes in PDE and gain, in fact, enhance the threshold efficiency:

$$\epsilon_{threshold}\,(20\,°\text{C}) = 0.99\%, \tag{5.32}$$

instead of 0.98% (eq. (5.22)).

Thus, the total efficiency eq. (5.20) at 20 °C becomes:

$$\epsilon_{prototype}\,(20\,°\text{C}) = 44\%. \tag{5.33}$$

Regarding the variations in crosstalk and DCR at 20 °C, the dark rate measured in Table 5.2 is reduced by half, reflecting the strong dependence of the noise on temperature.

Even if the effects of temperature described have a negligible consequence in practice, a temperature feedback system must be foreseen to guarantee the stability of future monitors. Additionally, a passive cooling system, such as a heat sink, could be employed to help maintaining a stable temperature of the SiPM.

5.8   Radiation Effects

Radiation damage is another phenomenon that influences the performance of the monitor and also its *life expectancy*. It affects principally scintillating fibres and SiPM in a dose-dependent manner (more information on the radiation damage of scintillating fibres in section 3.11, and for SiPM in section 4.2.8).

The fibres are exposed to the beam and therefore accumulate the largest dose of radiation. However, it is difficult to give an estimation of the loss of efficiency due to radiation damage during a short run. For larger accumulated doses, it is possible to make an estimation based on the literature, as done in section 6.5.

In the case of SiPM, the main source of radiation are stray particles from the beam. To investigate the effect of stray radiation in SiPM and its front-end electronics, several radiation monitor [74] were installed by the CERN group EN-STI in different strategic places of the North Area for two months. These devices did not reported accumulated doses higher to their sensitivity, 1 Gy, meaning that neither the SiPM, nor the electronics, would receive a large amount of radiation. However, as the effects of radiation are cumulative, a certain decrease in performance could be expected over the years.

Chapter 6

Beam Tests of the SciFi Prototype

The first prototype of the scintillating fibre monitor was successfully tested in the H8 beam line of the SPS North Experimental Area at CERN. It reconstructed with accuracy the profiles of secondary beams over a wide range of energies and intensities. However, the operation with lead-ion beams showed some issues, most probably related to optical crosstalk between the fibres. This issue is carefully investigated. An analysis of the absorbed dose of radiation by the monitor is also done, together with an estimation of its life expectancy.

6.1   Introduction

The SciFi prototype described in section 5.1 was installed in the experimental point P138 of H8, where it replaced one of the two planes of a FISC detector (more information on the Experimental Areas and their monitors in section 1.2 and section 1.3). In this configuration, the SciFi monitor was able to measure the vertical profile and the intensity of the beam.

6.1.1   Reference Monitors

Two of the profile monitors currently employed were standing in the vicinity: a FISC and a DWC. They also reconstructed the vertical profile, making possible a direct

comparison between them and the SciFi prototype. A scintillator paddle, was also close to the SciFi monitor and served as reference for intensity measurements. These intensity measurements are used to estimate the efficiency of the SciFi detector.

The data from all the monitors was presented and recorded in real-time in the acquisition PC (as described in section 5.4.3). Figure 6.1 is a screen capture of the data acquisition software, showing the information from the different monitors.
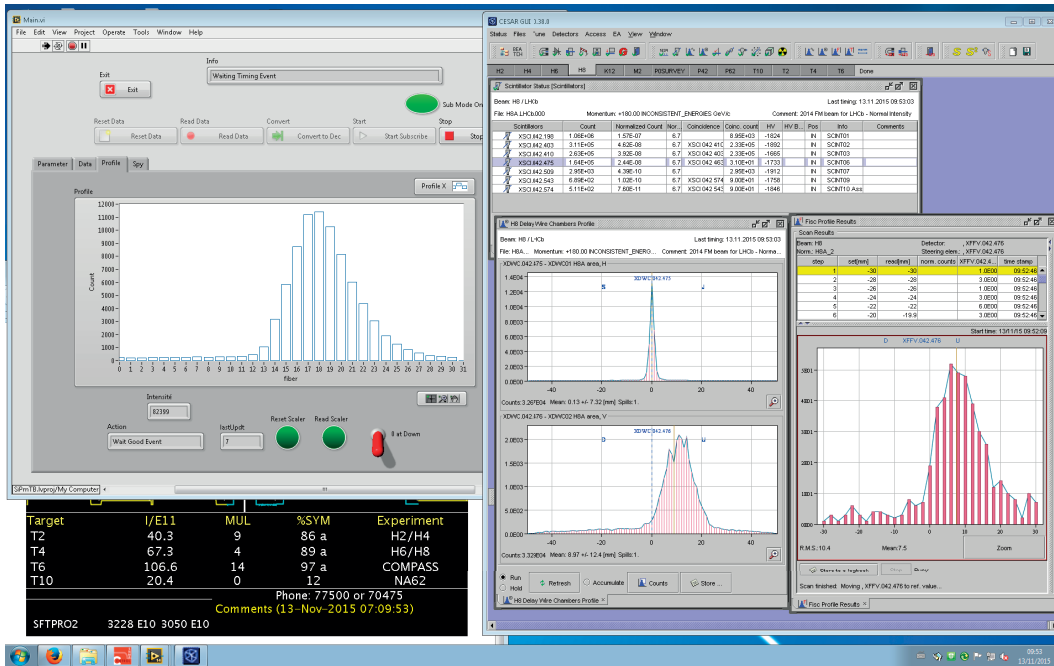
Figure 6.1 – Screen capture of the data acquisition PC showing the information from the different beam monitors.

6.1.2 Methodology of the Beam Profile Analysis

The ensemble of particles in the beam is typically Gaussian distributed [75]. For this reason, the data from the profile detectors were fitted with Gaussian curves in order to extract their characteristic parameters and establish a comparison between them.

Only the x-axis is of interest for the analysis, since it contains the information about the position of the beam (the mean of the distribution) and its spread (the standard deviation). The y-axis, which represents the number of events per spatial resolution bin, is not useful because these monitors have different spatial resolutions.

The fit of the data was done with two different analysis softwares: ROOT [76] and Mathematica [77]. The analysis of the profile shown in fig. 6.2 is illustrated for example purposes in fig. 6.3, where the best fits of the profile are superimposed. The results

are presented in Table 6.1, which shows that ROOT and Mathematica produce similar results: less than 2% difference in the standard deviation and 5% in the peak centre.
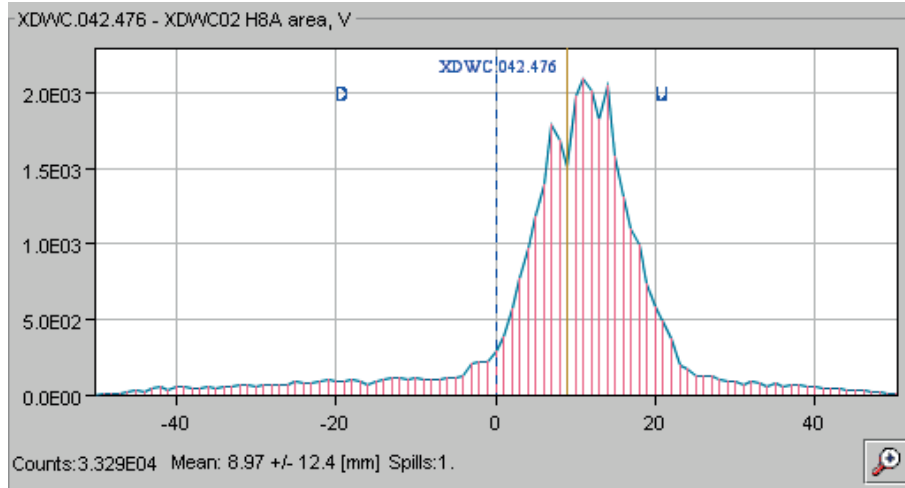
Figure 6.2 – Example of a profile from a Delay Wire Chamber
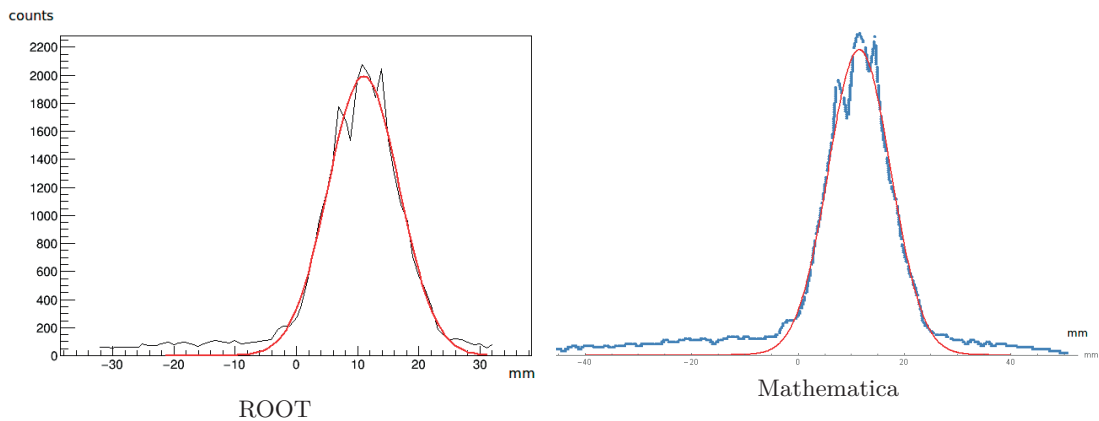
Figure 6.3 – Profile of fig. 6.2 analysed with ROOT (on the left) and Mathematica (right).

Table 6.1 – Comparison of the analysis of fig. 6.2, performed with Mathematica and ROOT.

	Mean (mm)	σ (mm)
ROOT	11.0	5.8
Mathematica	11.6	5.9

6.2   Secondary Beams

From the 26th of October to the 13th of November of 2015, the prototype took data with secondary beams. During this run, several users configured H8 to obtain beams of

diverse composition, intensity, and momentum.

From all the monitored beams, a selection of the most representative ones has been kept for analysis. This selection is summarised in Table 6.2, and the images of the profiles with their corresponding data fit are also shown in Table 6.3, Table 6.4, Table 6.5, Table 6.6, Table 6.7 and Table 6.8.

Table 6.2 – General information of the selected profiles

Profile date	Beam composition	Charge	P(GeV/c)	I(part/spill)
26/10 - 18:00	hadrons/leptons	-	60	5.0×10^4
30/10 - 15:05	pure hadrons	+	180	1.41×10^5
05/11 - 12:36	pure e^+	+	20	3.57×10^3
12/11 - 14:53	hadrons/leptons	+	180	3.14×10^6
13/11 - 09:53	hadrons/leptons	+	180	1.64×10^5
13/11 - 11:21	hadrons/leptons	+	180	3.94×10^5

Table 6.3 – Profiles on the 26th of October at 18:00.
Beam of *hadrons/leptons* at $60 \, \text{GeV/c}$ and $I = 5.0 \times 10^4$ particles/spill.

$SciFi$	DWC

$$\sigma = 2.1 \, \text{mm}$$
$$\text{centre} = -1.1 \, \text{mm}$$

$$\sigma = 2.6 \, \text{mm}$$
$$\text{centre} = -0.4 \, \text{mm}$$
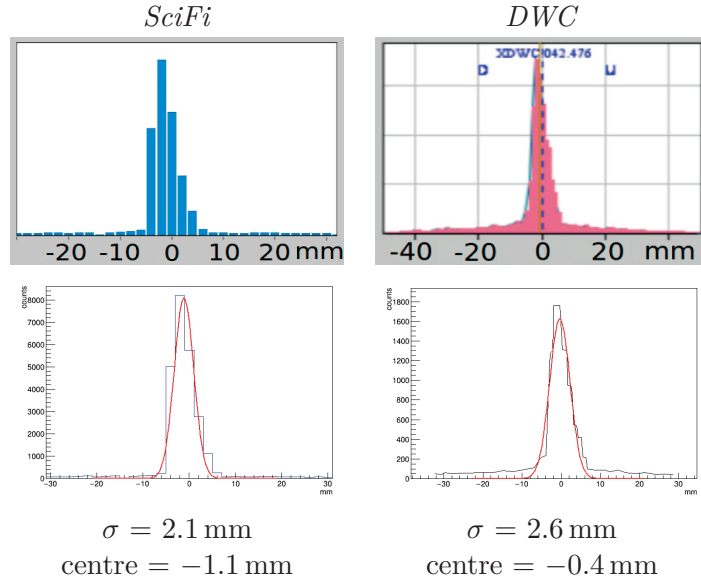
Table 6.4 – Profiles on the 30th of October at 15:05.
Beam of *pure hadrons* at $180 \, \text{GeV/c}$ and $I = 1.41 \times 10^5$ particles/spill.

$SciFi$	DWC

$$\sigma = 0.8 \, \text{mm}$$
$$\text{centre} = 1.8 \, \text{mm}$$

$$\sigma = 1.5 \, \text{mm}$$
$$\text{centre} = 1.9 \, \text{mm}$$

91
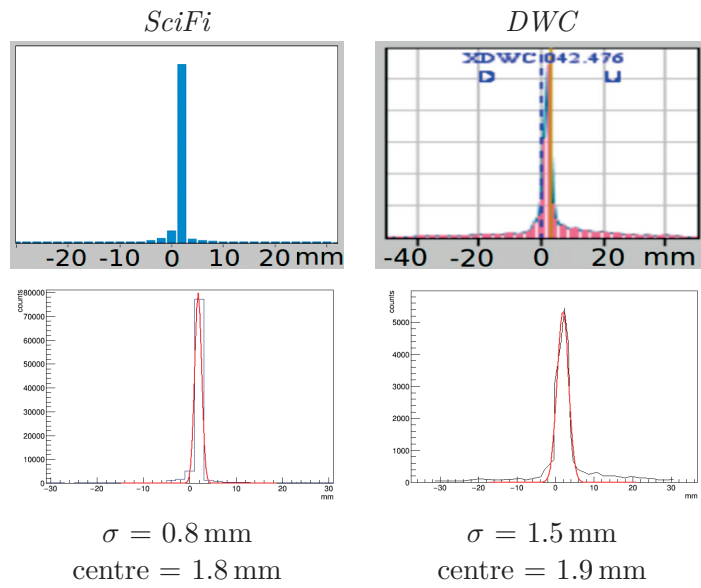
Table 6.5 – Profiles on the 5th of November at 12:36.
Beam of *pure e$^+$* at 20 GeV/c and $I = 3.57 \times 10^3$ particles/spill.

SciFi	*DWC*	*FISC*

$\sigma = 8.1\,\text{mm}$	$\sigma = 5.0\,\text{mm}$	$\sigma = 13.4\,\text{mm}$
centre $= -11.8\,\text{mm}$	centre $= -12.6\,\text{mm}$	centre $= -10.1\,\text{mm}$
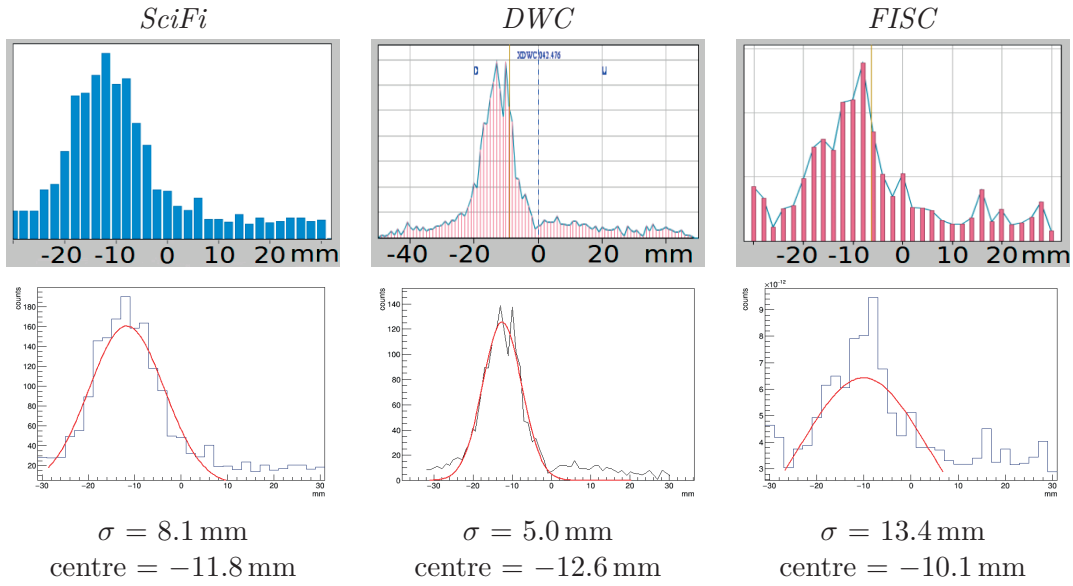
Table 6.6 – Profiles on the 12th of November at 14:53.
Beam of *hadrons/leptons* at 180 GeV/c and $I = 3.14 \times 10^6$ particles/spill.

SciFi	*DWC*	*FISC*

$\sigma = 0.9\,\text{mm}$	$\sigma = 4.0\,\text{mm}$	$\sigma = 1.1\,\text{mm}$
centre $= 1.2\,\text{mm}$	centre $= 0.8\,\text{mm}$	centre $= 1.8\,\text{mm}$
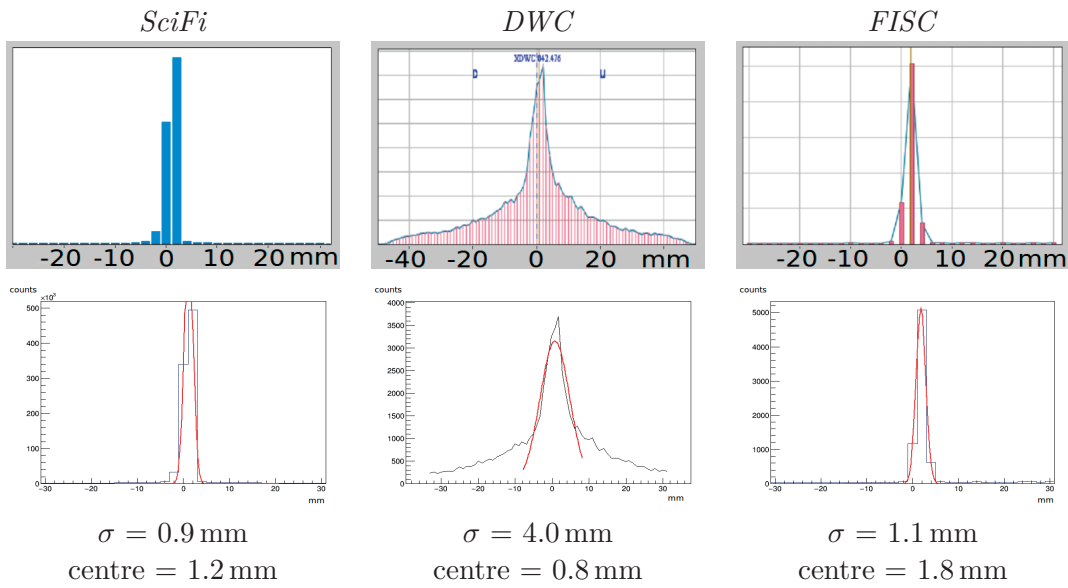
Table 6.7 – Profiles on the 13th of November at 09:53.
Beam of *hadrons/leptons* at $180\,\mathrm{GeV/c}$ and $I = 1.64 \times 10^5$ particles/spill.

SciFi	*DWC*	*FISC*

$\sigma = 5.6\,\mathrm{mm}$	$\sigma = 5.8\,\mathrm{mm}$	$\sigma = 6.6\,\mathrm{mm}$
centre $= 6.8\,\mathrm{mm}$	centre $= 11.0\,\mathrm{mm}$	centre $= 8.7\,\mathrm{mm}$
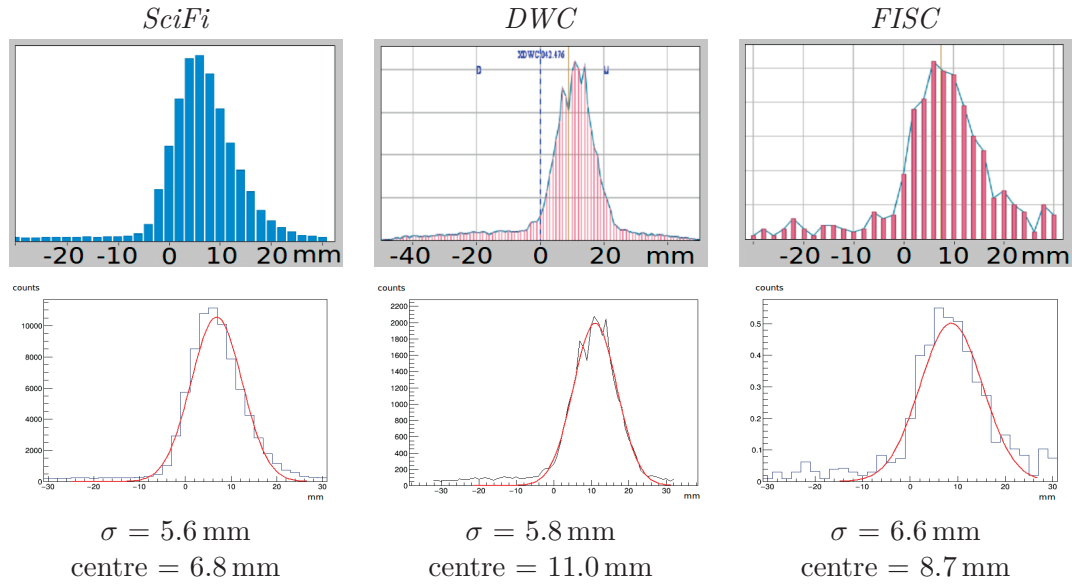
Table 6.8 – Profiles on the 13th of November at 11:21.
Beam of *hadrons/leptons* at $180\,\mathrm{GeV/c}$ and $I = 3.94 \times 10^5$ particles/spill.

SciFi	*DWC*	*FISC*

$\sigma = 5.4\,\mathrm{mm}$	$\sigma = 11.2\,\mathrm{mm}$	$\sigma = 6.2\,\mathrm{mm}$
centre $= -1.0\,\mathrm{mm}$	centre $= 2.0\,\mathrm{mm}$	centre $= 0.8\,\mathrm{mm}$

93
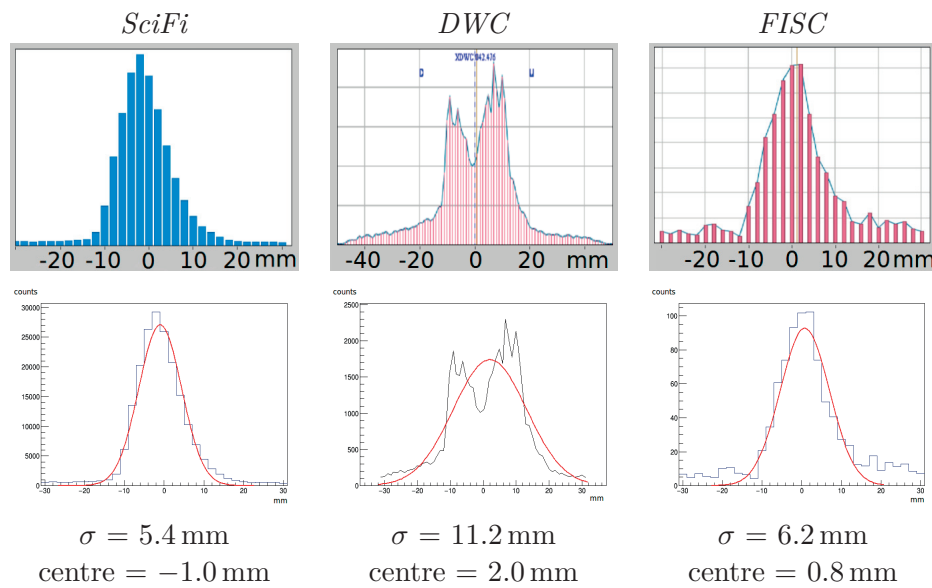
6.2.1 Analysis of the Beam Profiles

The SciFi monitor worked satisfactorily in all situations, whilst the DWC had troubles with high intensities, showing distorted profiles or artificial tails. This is a know problem of this type of detector, caused mainly by the large dead time imposed by the delay line. The FISC, on the other hand, had difficulties resolving low intensity beams, explained by its lower detection efficiency.

Table 6.9 – Standard deviation of the analysed profiles.

Profile date	SciFi (mm)	DWC (mm)	FISC (mm)[a]
26/10 - 18:00	2.1	2.6	
30/10 - 15:05	0.8	1.5	
05/11 - 12:36	8.1	5.0	13.4
12/11 - 14:53	0.9	4.0	1.1
13/11 - 09:53	5.6	5.8	6.6
13/11 - 11:21	5.4	11.2	6.2

[a] The FISC was not active during some measurements.

Table 6.10 – Peak centre of the analysed profiles.

Profile date	SciFi (mm)	DWC (mm)	FISC (mm)[a]
26/10 - 18:00	-1.1	-0.4	
30/10 - 15:05	1.8	1.9	
05/11 - 12:36	-11.8	-12.6	-10.1
12/11 - 14:53	1.2	0.8	1.8
13/11 - 09:53	6.8	11.0	8.7
13/11 - 11:21	-1.0	2.0	0.8

[a] The FISC was not active during some measurements.

From the standard deviation values in Table 6.9, it can be inferred that the SciFi monitor generally produced more accurate profiles than the DWC and the FISC. Regarding the position of the beams, Table 6.10, the three detectors show compatible results.

It should be noted that only every other fibre was read-out in the SciFi prototype, which decreases the intrinsic resolution of the device.

6.2.2 Analysis of the Beam Intensity

The intensities measured by the scintillator paddle and the SciFi monitor are presented in Table 6.11.

Table 6.11 – Comparison of the intensities registered by the scintillator paddle and the SciFi monitor.

Profile date	Scintillator[a]	SciFi[a]	SciFi/Scint.
26/10 - 18:00	$5.0 \ \times 10^4$	2.53×10^4	0.51
30/10 - 15:05	1.41×10^5	9.97×10^4	0.71
05/11 - 12:36	3.57×10^3	1.91×10^3	0.53
12/11 - 14:53	3.14×10^6	9.72×10^5	0.31
13/11 - 09:53	1.64×10^5	8.24×10^4	0.50
13/11 - 11:21	3.94×10^5	1.97×10^5	0.50

[a] The intensity is given in particles/spill.

The last column on Table 6.11 gives the ratio between the intensity measured by the SciFi monitor and the intensity scintillator. Assuming that the scintillator paddle has a 100% efficiency, that ratio corresponds therefore to the real efficiency of the prototype. However, as will be discussed in section 6.5.3, this paddle could have suffered radiation damage from previous runs and its data could not be completely reliable.

The majority of values for the efficiency in Table 6.11 lie around 0.5, with the exception of the profiles 30/11-15:05 and 12/11-14:53. These two profiles, in fact, show a noticeable different with the rest: they are very narrow and only activate one or two channels of the SciFi. In that case, it may happen that a big fraction of the particles are concentrated in one of the read-out fibres, as can be the case of 30/10-15:05, or on the contrary, be concentrated on a non read-out fibre, like the profile of 12/11-14:53 suggests.

If these two exceptional cases are discarded, the efficiency can be averaged:

$$\epsilon_{prototype} = 51 \pm 1\% \ (measured) , \tag{6.1}$$

close to the predicted value of 44% (eq. (5.33))

It is difficult to determine the origin of the small discrepancy between the two values, although the most plausible explanation is optical crosstalk between the fibres, since no particular treatment has been applied to avoid it (further information on the fibre crosstalk in section 3.5). Crosstalk could create multiple hits in several fibres for a single particle crossing the monitor, thus artificially increasing the efficiency value. This issue is discussed in detail in section 6.4.

Nevertheless, as aforementioned, the assumption of a 100% efficiency for the scintillator paddle could also be wrong, being lower in reality. No extra effort has been devoted to this issue, as it has no impact on the purpose of the device.

6.3 Lead Ion Run

In the middle of November of 2015, the SPS cycle changed to ^{208}Pb^{+82}, providing beams of these heavy particles to the North Area. During this run, the users could also configure the beam line to obtain different momenta and intensities, and even introduce secondary targets to produce diverse fragments of Pb-ions.

A saturation of light in the SiPM was observed during operation, which required lowering the bias voltage in order to reduce the PDE and be in a non-saturation regime. This large light production for Pb-ions is further explained, along with other phenomena, in section 6.4.2.

A selection of the most representative beams is presented in Table 6.12 and the profiles, together with the best fits are shown in Table 6.13, Table 6.14, Table 6.15, Table 6.16, and Table 6.17.

Note: the FISC detector was not operational during the lead ion run due to some technical issues related with saturation of the PMTs, which could not be solved.

Table 6.12 – General information of the selected profiles

Profile date	Beam composition	P(GeV/c/Z)	I(part/spill)
18/11 - 09:26	Pb	76.1	3.39×10^6
19/11 - 15:36	Pb	76.1	4.81×10^6
23/11 - 10:33	Pb / fragments	76.1 / 60	1.19×10^5
27/11 - 16:34	Pb / fragments	76.1 / 69	2.92×10^3
30/11 - 13:30	Pb	76.1	1.82×10^3

Table 6.13 – Profiles on the 18$^{\text{th}}$ of November at 09:26.
Beam of ^{208}Pb^{+82} at 76.1 GeV/c and $I = 3.39 \times 10^6$ particles/spill.

SciFi	*DWC*
$\sigma = 11.8$ mm	$\sigma = 6.0$ mm
centre $= -0.1$ mm	centre $= -0.2$ mm
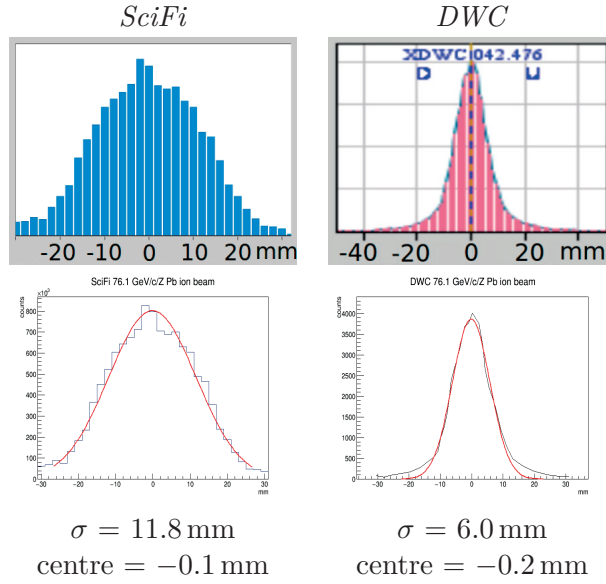
Table 6.14 – Profiles on the 19$^{\text{th}}$ of November at 15:36.
Beam of ^{208}Pb^{+82} at 76.1 GeV/c and $I = 4.81 \times 10^6$ particles/spill.

SciFi	*DWC*
$\sigma = 9.6$ mm	$\sigma = 5.1$ mm
centre $= -0.4$ mm	centre $= 0.3$ mm
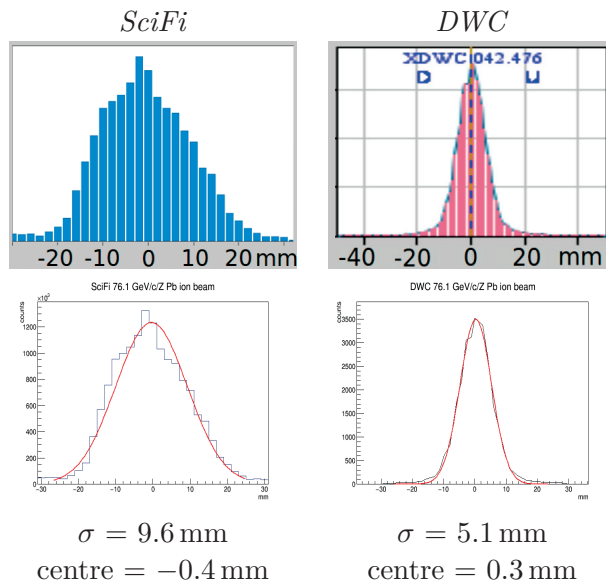
Table 6.15 – Profiles on the 23rd of November at 10:33.
Beam of ^{208}Pb^{+82}/fragments at 76.1/60 GeV/c and $I = 1.19 \times 10^5$ particles/spill.

| *SciFi* | *DWC* |

$$\sigma = 7.7\,\text{mm} \qquad \sigma = 7.0\,\text{mm}$$
$$\text{centre} = -0.3\,\text{mm} \qquad \text{centre} = -1.1\,\text{mm}$$
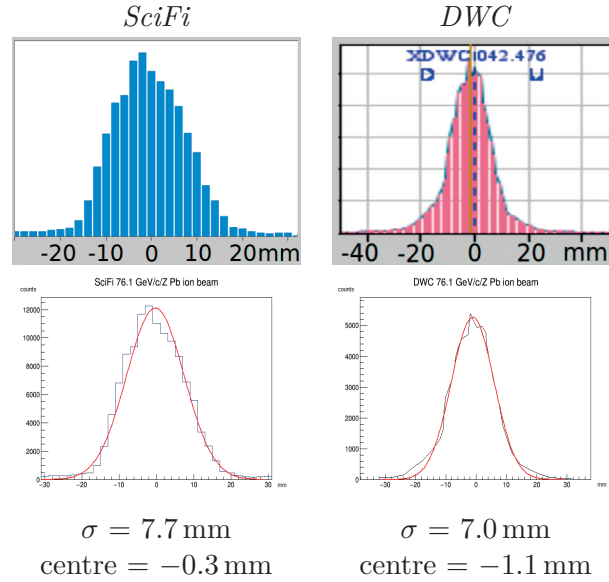
Table 6.16 – Profiles on the 27th of November at 16:34.
Beam of ^{208}Pb^{+82}/fragments at 76.1/69 GeV/c and $I = 2.92 \times 10^3$ particles/spill.

$$\sigma = 6.7\,\text{mm} \qquad \sigma = 5.1\,\text{mm}$$
$$\text{centre} = 0.9\,\text{mm} \qquad \text{centre} = 0.0\,\text{mm}$$
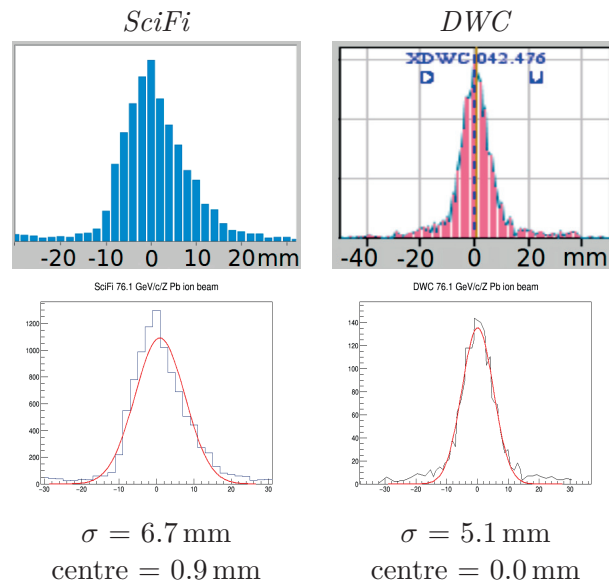
Table 6.17 – Profiles on the 30$^{\text{th}}$ of November at 13:30.
Beam of $^{208}\text{Pb}^{+82}$ at $76.1\,\text{GeV/c}$ and $I = 1.82 \times 10^3$ particles/spill.

SciFi	*DWC*

$\sigma = 5.5\,\text{mm}$ $\sigma = 4.2\,\text{mm}$
centre $= -0.5\,\text{mm}$ centre $= 0.4\,\text{mm}$
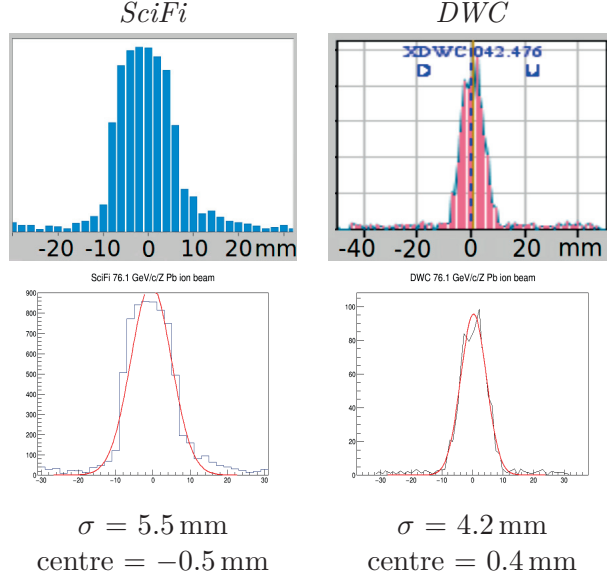
6.3.1 Analysis of the Beam Profiles

For all the measured beams, the profiles of the SciFi prototype are wider than those of the DWC (Table 6.18). The peak centre of the SciFi profiles, Table 6.19, are somehow blurred by the large sigma, although seem to be compatible with the data from the DWC.

Table 6.18 – Standard deviation of the anal-
ysed profiles.

Profile date	SciFi (mm)	DWC (mm)
18/11 - 09:26	11.8	6.0
19/11 - 15:36	9.6	5.1
23/11 - 10:33	7.7	7.0
27/11 - 16:34	6.7	5.1
30/11 - 13:30	5.5	4.2

A plausible explanation of this effect could be, as for the intensity discrepancies in section 6.2.2, optical crosstalk between the fibres. Since Pb-ions interact strongly with matter and deposit a much larger amount of energy than secondary beams, the scintillation light, and therefore the crosstalk, are expected to increase accordingly. This phenomenon could explain how the wider profiles are created by the multiplicity of fibres activated. It is further investigated in section 6.4.

Table 6.19 – Peak centre of the analysed profiles.

Profile date	SciFi (mm)	DWC (mm)
18/11 - 09:26	-0.1	-0.2
19/11 - 15:36	-0.4	0.3
23/11 - 10:33	-0.3	-1.1
27/11 - 16:34	0.9	0.0
30/11 - 13:30	-0.5	0.4

6.3.2 Analysis of the Beam Intensity

The intensities registered by the SciFi monitor (Table 6.20) are also larger compared to the scintillator paddle, indicating that there is some phenomenon creating multiple-fibre events. This observation is compatible with the hypothesis of fibre crosstalk.

Table 6.20 – Comparison of the intensities registered by the intensity monitor (scintillator) and the SciFi.

Profile date	Scintillator[a]	SciFi[a]	SciFi/Scint.
18/11 - 09:26	3.39×10^6	1.18×10^7	3.48
19/11 - 15:36	4.81×10^6	1.52×10^7	3.16
23/11 - 10:33	1.19×10^5	$1.2 \ \times 10^5$	1.0
27/11 - 16:34	2.92×10^3	9.81×10^3	3.36
30/11 - 13:30	1.82×10^3	7.21×10^3	3.96

[a] The intensity is given in particles/spill.

The profiles of 23/11 registered a lower intensity in the fibres. This could be due to the presence of different ion species in the beam that caused lower crosstalk. Unfortunately, it is not possible to assure this hypothesis, due to the lack of information on the beam composition.

6.4 Investigations on the Fibre Crosstalk

Fibre crosstalk is produced by UV primary photons that escape the fibre and excite the secondary wavelength shifter in a neighbouring fibre (this phenomenon is further described in section 3.5). It is complicated to estimate its effect, which depends on the geometry of the fibre and the detector. However, its intensity is certainly proportional to the amount of scintillation light, and thus to the energy deposited by the particles.

6.4.1 Energy Deposited by the Secondary Beams

Despite the variety of particles forming the secondary beams and their wide range of momenta, their behaviour in terms of energy deposition in the monitor is very similar. This is due to their ultra-relativistic velocities, which correspond with the minimum of the energy loss curve (more on the energy loss of particles in appendix A.3).

According to a Geant4 simulation of a scintillating fibre of the prototype (further described in appendix B.2), the distribution of energy deposited is Landau distributed, as shown in fig. 6.4, and its most probable value is:

$$E_{dep} = 140 \, \text{keV}. \tag{6.2}$$

This energy deposition yields a most probable value of detected photons by the SiPM:

$$Detected\ photons = 25 \pm 10 \ photons. \tag{6.3}$$

Energy deposited   Photons detected
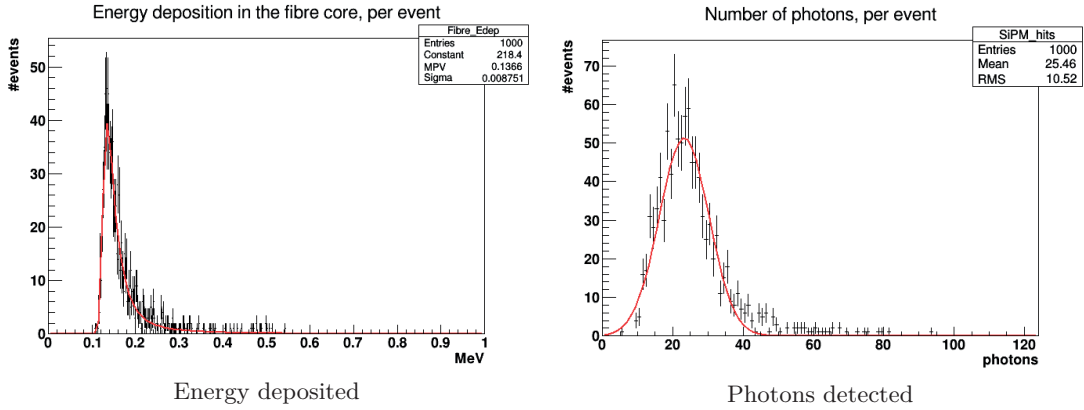
Figure 6.4 – Geant4 simulation of a scintillating fibre of the prototype that interacts with a beam of 1,000 protons of $180 \, \text{GeV/c}$. The energy deposited by the fibre is shown on the left figure and the photons detected by the SiPM on the right one.

6.4.2 Energy Deposited by Pb-ions

The interaction of $^{208}\text{Pb}^{+82}$ ions with the fibres is significantly more intense than that of secondary beams. The Geant4 simulation of a fibre of the prototype (fig. 6.5) shows that the energy deposition is approximately 10,000 times larger in this case:

$$E_{dep} = 1.2 \, \text{GeV}. \tag{6.4}$$

However, heavy particles tend to produce quenching effects in the materials which may

drain part of the ionisation energy produced. Hence, the light yield of organic scintillators does not increase linearly with the energy deposited, reaching a plateau for high values [35]. The Geant4 simulation shows, in fact, that the average number of photons detected by the SiPM is:

$$Detected\ photons = 4474 \pm 368\ photons, \tag{6.5}$$

which means that the light production is about 200 times larger than for secondary beams.

Energy deposited   Photons detected
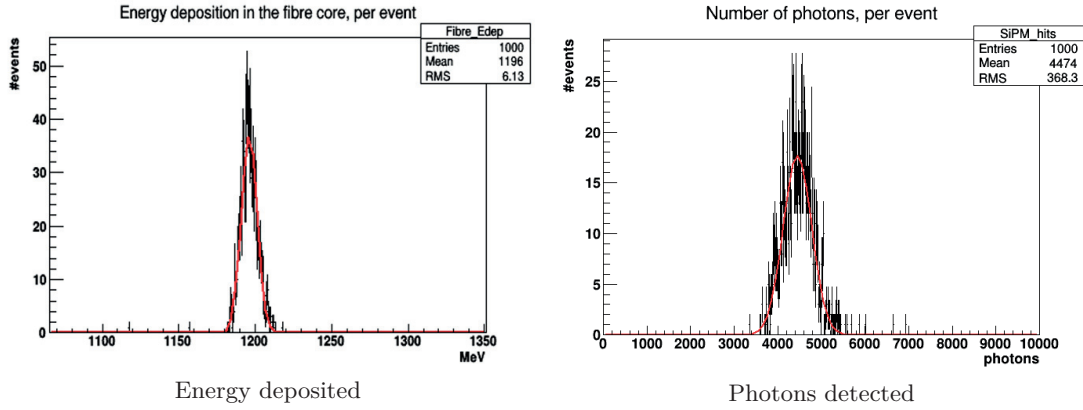
Figure 6.5 – Geant4 simulation of a scintillating fibre of the prototype that interacts with a beam of 1,000 ^{208}Pb^{+82} ions of 76 GeV/c/Z. The energy deposited by the fibre is shown on the left figure and the photons detected by the SiPM on the right one.

6.4.3 Estimation of Crosstalk

It is possible to estimate the fraction of crosstalk events from the measurements of the intensity in Table 6.11 and Table 6.20. Separating the detected events between crosstalk and no-crosstalk, the intensity registered by the SciFi monitor is:

$$I_{scifi} = I_{no-xtalk} + I_{xtalk}. \tag{6.6}$$

And the measured ratio between the SciFi intensity and the scintillator paddle intensity (I_{scifi}/I_{scint}) can be written in the following manner:

$$\frac{I_{scifi}}{I_{scint}} = \frac{I_{no-xtalk} + I_{xtalk}}{I_{scint}} = \frac{I_{no-xtalk}}{I_{scint}} + \frac{I_{xtalk}}{I_{scint}}, \tag{6.7}$$

where the fraction $I_{no-xtalk}/I_{scint}$ corresponds to the theoretical efficiency of the monitor, $\epsilon = 44\%$ (estimated in section 5.6), and I_{xtalk}/I_{scint} to the fraction of crosstalk events.

For the secondary beams, such fraction of crosstalk events is:

$$\left.\frac{I_{xtalk}}{I_{scint}}\right|_{MIP} = 0.51\,(\pm 0.01) - 0.44 \equiv 6 \pm 1\%. \tag{6.8}$$

And for lead-ions:

$$\left.\frac{I_{xtalk}}{I_{scint}}\right|_{Pb^{82}} = 3.49\,(\pm 0.29) - 0.44 \equiv 305 \pm 29\%. \tag{6.9}$$

6.4.4   Discussion

The crosstalk for lead-ions seems to be about 50 times larger than in the case of secondary beams. This calculation, even if qualitatively correct, does not fit with the increase of ~ 200 times in scintillation light found in section 6.4.2. The discrepancy could be due to the Geant4 simulation, whose accuracy for Pb-ions has not been verified. Additionally, the data from the scintillator paddle may not be reliable, as discussed in section 6.5.3.

Nevertheless, fibre crosstalk appears to have an effect in the spatial resolution and future versions of the monitor should implement a fibre treatment to avoid it.

6.5   Radiation Damage

Following the discussion of section 5.8, the lifespan of scintillating fibres is calculated based on an estimation of their accumulated dose of radiation.

6.5.1   Accumulated Dose and Lifespan for Secondary Beams

As previously seen in section 6.4.1, the most probable value of energy deposited by the secondary beams in a 1 mm thickness fibre is:

$$E_{deposited}|_{MIP} \approx 140\,\text{keV}. \tag{6.10}$$

A simple calculation taking into account the weight density of the fibres shows that the dose absorbed by the monitor, for N particles spread over an area A, can be written as:

$$D\,(N, A) = \frac{N \times 2.5 \times 10^{-10}\,\text{Gy}}{A\,(\text{cm}^2)}. \tag{6.11}$$

The absorbed dose for different beam sizes and intensities are presented in Table 6.21

and Table 6.22.

Table 6.21 – Dose absorbed by the SciFi monitor after exposure to secondary beams of different spot sizes.

Beam σ (mm)	Intensity (Particles/spill)	Absorbed dose (mGy/spill)
1	10^7	17.5
2	10^7	4.4
4	10^7	1.1
6	10^7	0.5
8	10^7	0.3

Table 6.22 – Dose absorbed by the SciFi monitor after exposure to secondary beams of different intensities.

Beam σ (mm)	Intensity (Particles/spill)	Absorbed dose (mGy/spill)
2	10^6	4.3×10^{-1}
2	10^5	4.3×10^{-2}
2	10^4	4.3×10^{-3}
2	10^3	4.3×10^{-4}

Note: the area of a Gaussian beam has been approximated by a circular spot of radius 2σ, which contains 95% of its particles.

Estimation of the Lifespan

The Saint-Gobain BCF-12 and Kuraray SCSF-78 fibres do not show symptoms of damage until doses of $1\,\text{kGy}$ have been accumulated, and preserve more than 50% of their detection efficiency after accumulated doses of $10\,\text{kGy}$ (deeper description of the radiation damage in fibres in section 3.11). Therefore, taking for example beams of $\sigma = 2\,\text{mm}$ and 10^6 particles/spill, the dose of $10\,\text{kGy}$ is reached after $\sim 2 \times 10^7$ extractions. Assuming that the beams are extracted uninterruptedly $\sim 2,000$ times per day (1 every 48 seconds), that number of extractions is reached after approximately *10,000 days*. This means that scintillating fibres can be probably employed for many years with secondary beams before showing symptoms of radiation damage.

It should be noted that this calculation has not considered any type of annealing recovery processes of the fibres.

6.5.2 Accumulated Dose and Lifespan for Pb-ion Beams

Recalling the most probable value of energy deposited by Pb-ions in a fibre, eq. (6.4):

$$E_{deposited}|_{Pb^{82}} \approx 1.2 \, \text{GeV}, \tag{6.12}$$

Similarly to eq. (6.11), the absorbed dose for different beam sizes and intensities are presented in Table 6.23 and Table 6.24.

Table 6.23 – Dose absorbed by the SciFi monitor after exposure to Pb-ion beams of different spot sizes.

Beam σ (mm)	Intensity (Particles/spill)	Absorbed dose (Gy/spill)
1	10^7	147.1
2	10^7	36.8
4	10^7	9.2
6	10^7	4.1
8	10^7	2.3

Table 6.24 – Dose absorbed by the SciFi monitor after exposure to Pb-ion beams of different intensities.

Beam σ (mm)	Intensity (Particles/spill)	Absorbed dose (Gy/spill)
2	10^6	3.7
2	10^5	3.7×10^{-1}
2	10^4	3.7×10^{-2}
2	10^3	3.7×10^{-3}

Estimation of the Lifespan

Assuming again beams of $\sigma = 2 \, \text{mm}$ and 10^6 particles/spill, the $10 \, \text{kGy}$ dose is reached after only $\sim 2,700$ extractions, due to the large energy deposition. Therefore, after a few days of data taking the fibres would show a large decrease in their performance.

Nevertheless, because the effects of radiation (a lower light yield and a worse transmission of light in the fibre) are compensated by the larger scintillation that occurs with Pb-ions. In fact, the SciFi prototype was operated during several weeks with Pb-ions.

An interesting effect that supports this hypothesis comes from an analysis of the Pb-ion profiles as a function of the date (Table 6.18), which shows a tendency towards narrower

profiles as the days pass. This fact would agree with a decrease of scintillation light and crosstalk, caused by a lower efficiency of the fibres.

The limit of functioning for the fibres with Pb-ions could be, thus, set to a larger accumulated dose of 1 MGy, where they retain 10% to 20% of their detection efficiency (fig. 3.12). With this new limit, the estimation of the life expectancy in the case of Pb ions would be rather $\sim 2.7 \times 10^5$ extractions.

It should be remarked that the fibres already exposed to Pb-ions *must* not be used with secondary beams. The high loss of efficiency due to the damage would made them unusable with secondary beams. Therefore, two versions of the monitor could exist: one for the secondary beams and another one for the lead ion beams. They should be replaced according to the run and never be mixed, otherwise they could not be employed anymore with secondary beams.

A modular design of the monitor, where the fibres are easily replaceable would facilitate such maintenance work.

6.5.3 Radiation Damage of Scintillator Paddles

Following the discussion of the previous section (6.5.2), the ratio of intensity between the scintillator paddle and the SciFi does not seem to show a reduction with the date (Table 6.20). Such decrease would be expected, since the scintillating fibres are losing efficiency due to radiation damage.

The scintillator paddles are made of a plastic scintillator, very similar to scintillating fibres, which suffers from radiation damage in a comparable way. These monitors have been used permanently for many years and with different types of beams, including Pb-ions. However, since it is not possible to evaluate their damage accumulated from past runs, their data should probably not be employed as reference. In fact, the efficiency of one of these monitors has been measured in the East Area (eq. (7.7)), showing an efficiency around 60%, far from the $\sim 100\%$ expected.

6.6 Effect of the Monitor on the Beam

The monitor can disrupt the beam in the following ways:

- Scattering of the particles.

- Variation of the energy of the particles.

- Creation of secondary particles.

An investigation of these three phenomena has been performed using a Geant4 simulation of the SciFi prototype (described in appendix B.3). It shows that for the particles and momenta of the North Area, the SciFi monitor has an effect almost negligible on scattering and energy variation of the particles. The exception are electrons and positrons, since they loss a large amount of energy in the form of Bremsstrahlung radiation (more on this phenomenon in appendix A.4), with the possibility of losing the entire energy of the particle. These light particles also suffer a noticeable scattering for momenta below 10 GeV.

Regarding the production of secondary particles, it is significant for high energy hadrons (momenta higher than 100 GeV) and particularly remarkable for Pb-ions.

The full study and the results are further discussed in appendix D.2.

Chapter 7

Beam Instrumentation for the Neutrino Platform

Two new beam lines are being built in the extension of the North Area Hall to provide very low energy beams to the protoDUNE experiments. Due to the particular requirements of these beams, special beam profile monitors based on scintillating fibres are being developed for them. These new monitors follow the design of the SciFi prototype, although incorporating many improvements, and also extending its functionality beyond the profile measurement.

7.1 Characteristics of the Beams

The two new beam lines (introduced in section 1.2.4) will deliver hadrons ($p^\pm$, $\pi\pm$ and $K\pm$) and leptons ($e\pm$, $\mu\pm$) with very low momenta (from $0.5\,\text{GeV/c}$ to $12\,\text{GeV/c}$). The maximum beam intensity expected is 500 particles/second, although the protoDUNE data acquisition system is limited to a maximum rate of $100\,\text{Hz}$. For that reason, the beam line will count with a collimator that would allow to reduce the particle flux arriving to the liquid argon detectors. The total beam spot size and its halo are expected to be large, fitting in an area of $200\,\text{mm} \times 200\,\text{mm}$. More information about the beam line characteristics can be found in [78], [79] and [80].

Both beam lines will also have a magnetic spectrometer for momentum measurement. It will be formed by a system of bending magnets and beam monitors that measure the

trajectory of the particles before and after their deflection by the magnetic field. The beam momentum will be reconstructed from the degree of deflection.

Due to the characteristics of these beams, the instrumentation has to satisfy three basic requirements: detect individual particle tracks, be in vacuum in order to minimise the material budget, and have a large area of at least $200\,\text{mm} \times 200\,\text{mm}$.

An additional constraint for the new instrumentation is the low space available, forcing the detectors to be compacted in $80\,\text{mm}$ in the longitudinal direction of the beam line.

7.2   Proposed Monitors

Scintillating fibres can fulfil all the requirements and, for this reason, it was decided to benefit from the development of the fibre monitors for the CERN experimental areas and equip the new beam lines with these instruments. In fact, the design of the new monitors has been done together with physicists from the Neutrino Platform. As a result of this collaboration, the initial functions of the monitor, profile measurement and spectrometry, have been extended to cover new functionalities. These consist in providing a trigger signal for the protoDUNE detectors and a Time-of-Flight (ToF) system for particle identification at low momenta.

Considering the various functionalities of the monitor, and the spatial constraints, the vacuum tank shown in fig. 7.1 has been proposed to host the detectors. Two independent planes of fibres can be placed inside it.

According to their function, there are two types of fibre modules that can be installed in a tank:

- XBPF: every fibre is coupled to an individual SiPM (fig. 7.2). This plane provides the spatial information of which fibre is hit. It will be used for the profile reconstruction and the spectrometry.

- XSCINT: all the fibres are read-out by one PMT (fig. 7.2). With such arrangement, only the information of the passage of the particle is obtained. This plane forms part of the trigger system, where three of these XSCINT planes are set in coincidence to generate an unambiguous signal of the passage of a beam particle. It is being investigated whether this module could be employed for ToF by using specialised readout electronics.

This modular design allows for a combination of XBPF and XSCINT planes adapted to the specific needs:
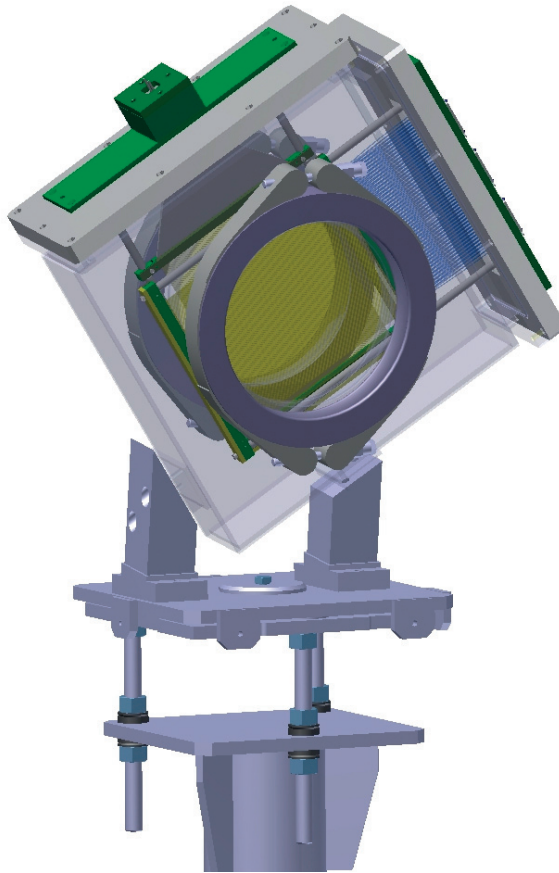
Figure 7.1 – Vacuum tank for the SciFi monitors of the Neutrino Platform. Due to its a modular design, it can equip two independent fibre detectors.

- A tank equipped with two XBPF modules can reconstruct the vertical and horizontal profile of the beam.

- The spectrometer only needs three individual XBPF planes tilted in the same direction as the magnetic field and distanced 1 m from each other. Hence, the tanks forming part of the spectrometer could equip only a XBPF in order to reduce the material budget of the beam line.

- The first and last tanks of the beam line will host two XSCINT planes, one used for triggering, and the other one for the ToF.

Image 7.3 shows the layout of H2, where the function of each module is indicated as vertical coloured lines perpendicular to the beam trajectory.
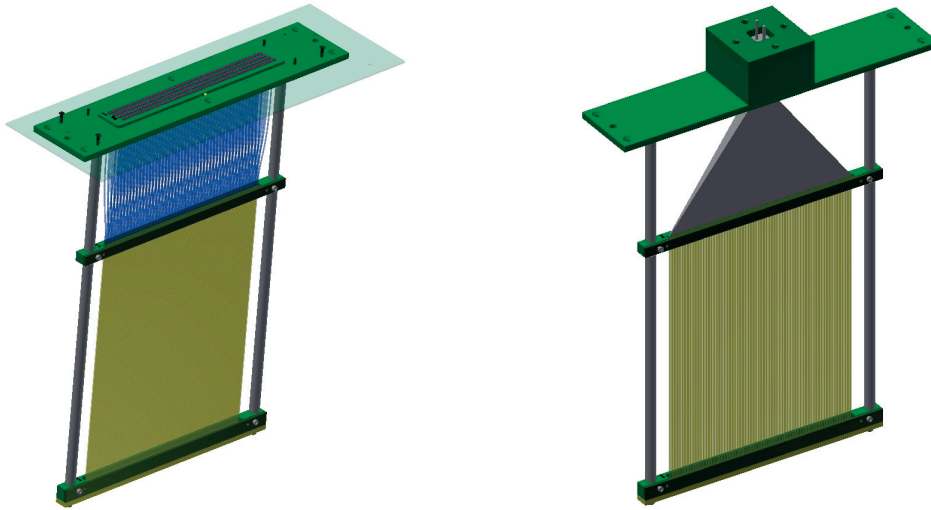
Figure 7.2 – CAD models of the XBPF (left) and the XSCINT (right), the new beam profile monitors for the Neutrino Platform.
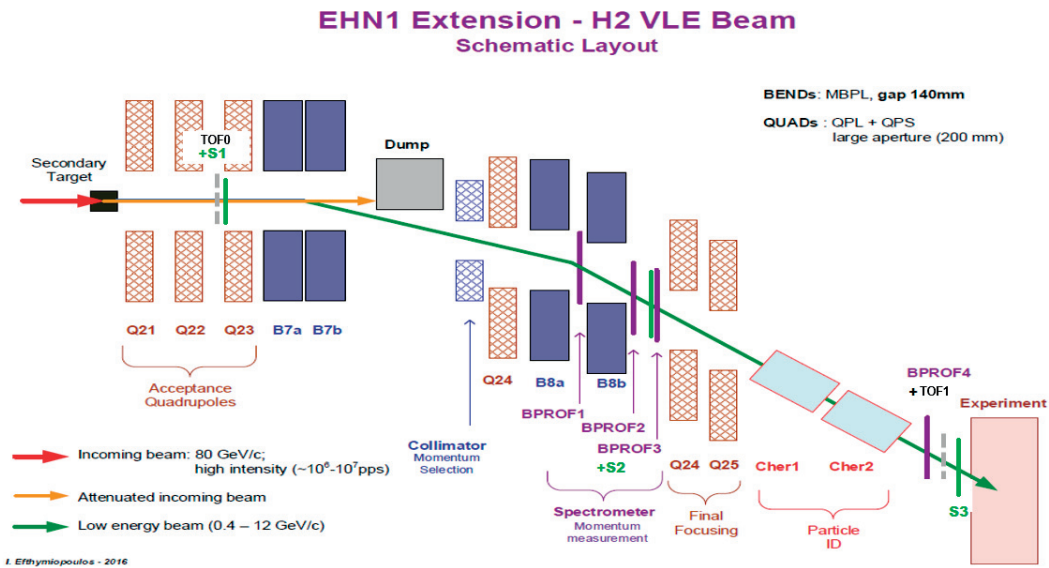
Figure 7.3 – Layout of the H2 extension, showing its main elements: Q, quadrupole magnets (orange); B, bending magnets (blue); S, the XSCINT monitors (green); BPROF, the XBPF monitors (purple); TOF, the ToF detectors (grey); Cher, Cherenkov detectors (red). Image from: [78].

7.2.1 Design Principle

The design principle of the fibre modules follows closely the pixelated readout principle of the SciFi prototype described in section 5.1:

- Square fibres of 1 mm width, tightly packed together forming a plane. The fibre model that will be used, Saint-Gobain BCF-12 MC or Kuraray SCSF-78, is still under investigation.

- A high-reflectivity aluminised Mylar mirror is glued on one end of the fibres.

- The photodetectors are placed outside vacuum and, therefore, the read-out end of the fibres must be vacuum-tight.

The production techniques are also very similar to the SciFi prototype, although two new features improve the mechanical robustness of the detector:

- An ultra-thin 25 µm Kapton foil is glued over the fibres. It guarantees a precise positioning of the fibres within the active area, without representing a significant increase of the material budget.

- A new gluing technique for the fibres in the vacuum-air interface ensures a better vacuum-tightness.

7.2.2   XBPF

Figures 7.4 7.5 and 7.6 show the first prototype of the XBPF.
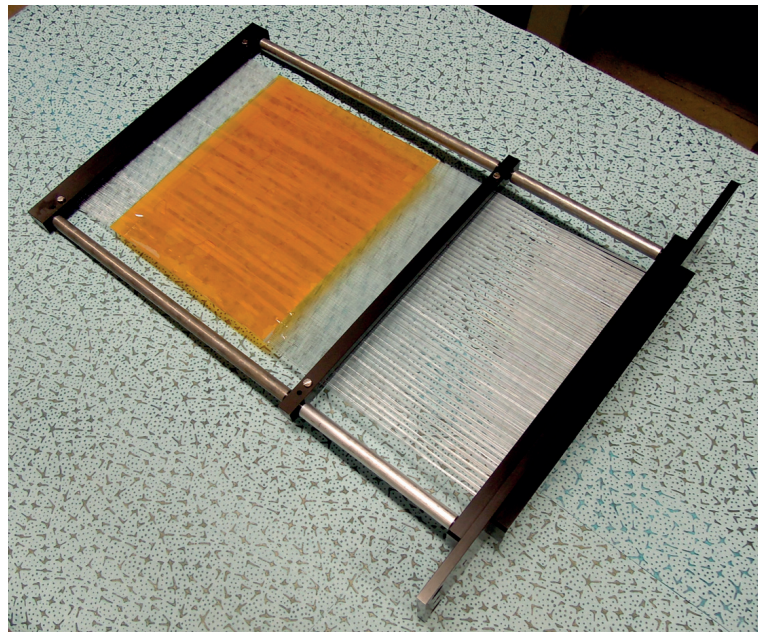
Figure 7.4 – First prototype module of the XBPF.

Figure 7.5 – Fibre connector where the scintillating fibres are coupled to the SiPM.
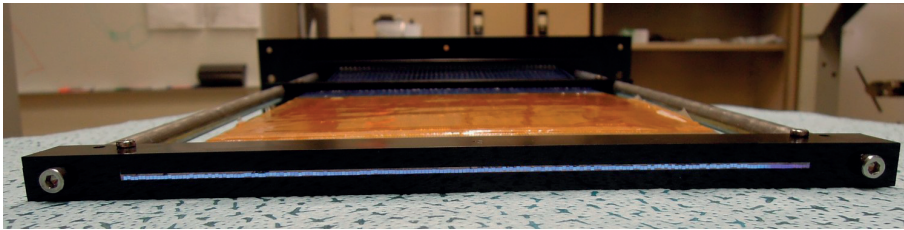
Figure 7.6 – End of the fibres where the mirror is glued.

7.2.3 XSCINT

The original design of the XSCINT has only one PMT to read-out the 192 fibres. However, as can be appreciated in fig. 7.7, the bending of the fibres creates a large transversal stress that tends to separate them from each other. Thus, there is a risk that, at a certain moment, the fibres would detach from the Kapton foil and separate within the active area. This problem has been avoided by sharing the fibres between two PMT: fig. 7.8 and fig. 7.9.

7.2.4 Photodetectors

The first prototype of the XBPF is equipped with the same model of SiPM as the SciFi prototype tested in H8: the Hamamatsu S13360-1350. However, a second revision will employ the new Hamamatsu MPPC matrix S13360-2050NS-08 [50], composed of 8×8 SiPM. This device shows two major advantages: a larger active area $2\,\text{mm} \times 2\,\text{mm}$, which improves the efficiency of the monitor, and a lower price per channel.

For the XSCINT module, the read-out of the fibres is done with the Hamamatsu PMT H11934-200 [81], which has a bi-alkali photocathode that yields a 43% quantum efficiency. Since the time response of this detector is very good, with a transit time spread of
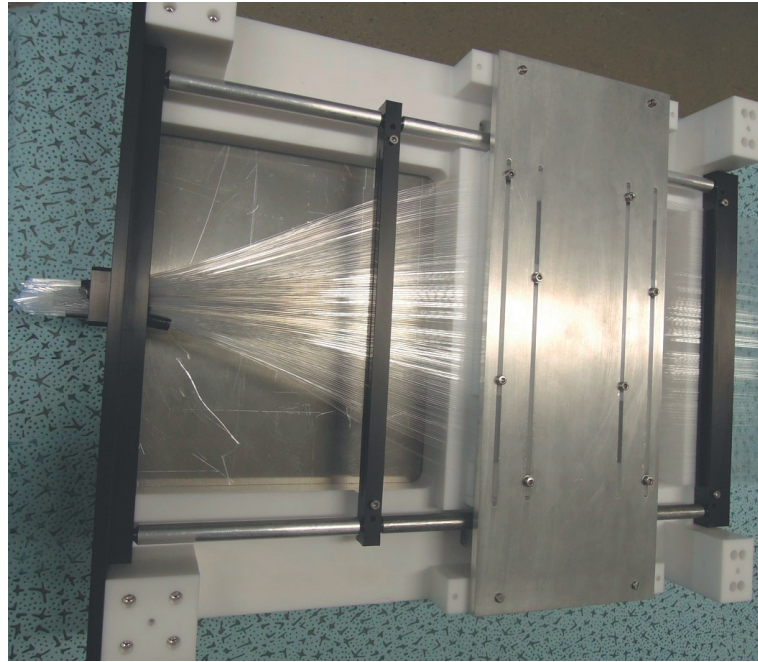
Figure 7.7 – Original design of the XSCINT with one PMT. In this design the fibres suffer from a large mechanical stress.
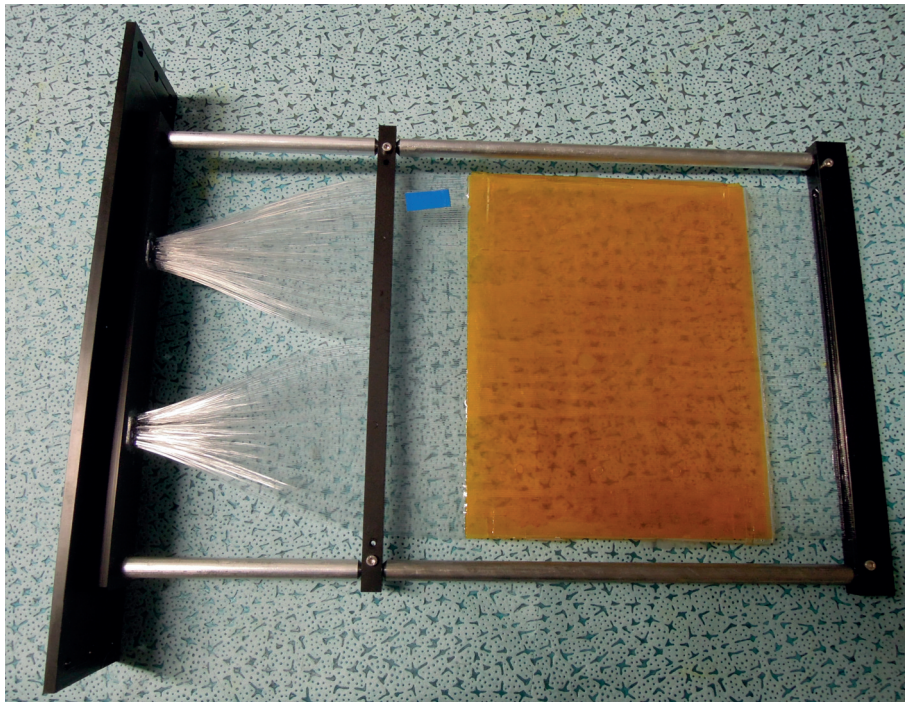
Figure 7.8 – Second version of the XSCINT with two PMT.

$\sim 300\,$ps, it has motivated the investigation of a sub-nanosecond ToF system based on the XSCINT module.

Figure 7.9 – Second version of the XSCINT with two PMT.

7.3 Readout Electronics

The architecture of the readout electronics is presented in fig. 7.10. It is divided in a front-end board containing the SiPM, which is plugged to the monitor, and a back-end board installed in a barrack 30 m away.
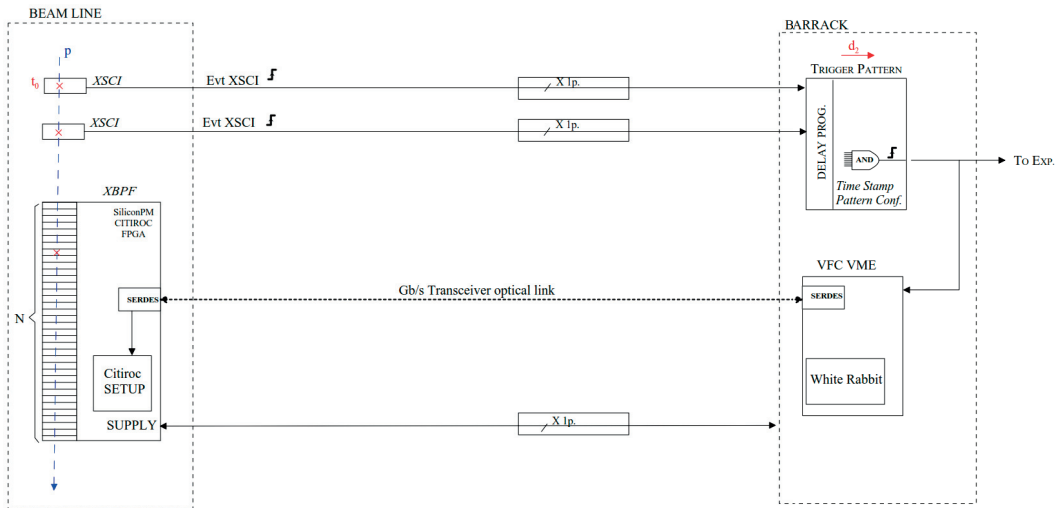
Figure 7.10 – Electronics architecture of the beam instrumentation readout.

7.3.1 Trigger Generation

The analogue signals from three XSCINT distributed along the beam line are sent to the barracks, where a programmable delay module puts them in coincidence. As a result of the three-fold coincidence, a trigger signal is generated and sent to the protoDUNE experiments and to the back-end electronics of the XBPF readout.

7.3.2 Front End Board

The front-end board of the XBPF (fig. 7.11 and fig. 7.12) has the following main components:

- 192 SiPM to detect the light generated at the fibres.

- Hamamatsu C11204 power supply for SiPM [82] with temperature compensation system.

- 6 CITIROC ASIC that process all 192 SiPM channels and produces 192 parallel digital outputs from the discrimination of the SiPM signals.

- Xilinx FPGA Artix 7 [83]: reads CITIROC output, packages data, and sends it out on Gigabit link up to 10 MHz data stream.

- SFP module with Gbit transceiver to transfer the data via optical fibre to the back-end.
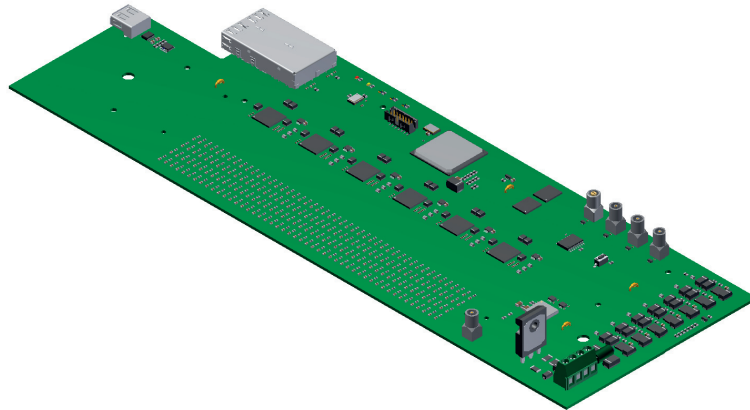
Figure 7.11 – CAD model of the Front End board (top side).

7.3.3 Back End Board

The back-end module is the VFC board, a VME general purpose digital acquisition card developed by the CERN Beam Instrumentation group [84]. This board has been chosen due to its highly configurability and the fact that is fully compatible with White Rabbit (WR).

White Rabbit is an Ethernet-based network for data transfer and high-performance time transfer [85]. This technology will be utilised by the future DUNE experiments to establish a timing distribution network among the various neutrino detectors located thousands
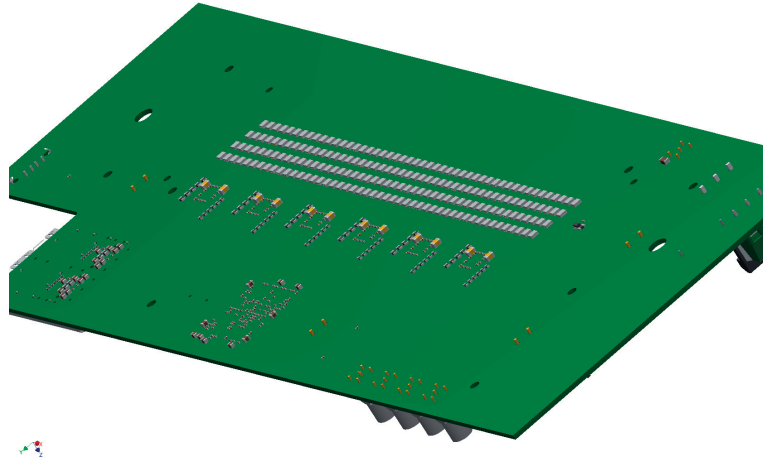
Figure 7.12 – CAD model of the Front End board (bottom side). The 192 SiPM are on this side of the board.

of kilometres away from each other. For that reason, protoDUNE will also incorporate it. The electronics of the beam instrumentation is required to time-stamp all the beam particle events with a common clock distributed over WR to both instrumentation and experiments.

The main functions of the VFC board are:

- Decode Gbit stream from front-end.

- Create event structure.

- Send control data to front-end.

The flux of data from the front-end to the VFC includes not only the real particle events, but also the noise events of SiPM. To suppress those noise events, the VFC also receives the trigger signal and only an event coinciding with that signal is recorded.

7.4   Expected Performance

7.4.1   XBPF

The beam reconstruction resolution of the XBPF would be limited by the fibre width: 1 mm. This value satisfies the required precision for the profile measurement.

For the track reconstruction performed by the three XBPF planes in the magnetic spectrometer, the spatial resolution is calculated as for a flat probability distribution

with 1 mm pitch. Such distribution yields a spatial resolution of:

$$\sigma_x = \frac{1\,\text{mm}}{\sqrt{12}} \approx 0.3\,\text{mm}. \tag{7.1}$$

According to the calculations of the protoDUNE physicists, this value would yield a momentum resolution for the spectrometer of $\delta p/p = 1.5\%$ [78], [79].

The detection efficiency of the XBPF would be mainly limited by the size of the cladding of the fibres. The Kuraray SCSF-78 only have a 4% of total cladding, while the Saint-Gobain BCF-12 MC have 12%. This would translate into a geometric efficiency of $\sim 96\%$ or $\sim 88\%$, respectively.

However, the SCSF-78 are single-clad and the BCF-12 double-clad, which represents approximately a 60% higher light yield for the BCF-12 (measurement presented in appendix C.3). Since the level of light also determines the detection efficiency, as explained in section 5.5.1, this subject is being investigated to clarify if the double cladding could really represent an improvement for this application.

Because the acquisition will be triggered by the three-fold coincidence of the XSCINT, the influence of noise events is expected to be negligible. This would allow lowering the threshold of the discriminators to a value as low as 1.5 or 2.5 photons, which would benefit the detection efficiency.

7.4.2 XSCINT

As for the case of the XBPF, the cladding of the fibres is the main factor limiting the efficiency of the detector. Therefore the maximum theoretical efficiency would be 96% or 88% depending if the fibres used are the Saint-Gobain or the Kuraray.

Since the trigger signal is formed by the three-fold coincidence of XSCINT planes, the total trigger efficiency would be:

$$\epsilon_{trigger} = \epsilon_{xscint} \times \epsilon_{xscint} \times \epsilon_{xscint}. \tag{7.2}$$

Because the trigger efficiency must be as high as possible, the SCSF-78 fibres with 4% cladding will be used for this module. Hence, the maximum theoretical efficiency of the trigger system would be:

$$\epsilon_{trigger} = (96\%)^3 = 88\%. \tag{7.3}$$

If only two XSCINT were employed to form the trigger, instead of three, the maximum

trigger efficiency would be:

$$\epsilon_{trigger} = (96\%)^2 = 92\%. \tag{7.4}$$

Two options are being investigated to further increase the efficiency of the trigger, while keeping the material budget at the same level:

- Stagger two layers of 0.5 mm fibres in order to cover the dead area of the cladding.

- Employ a 200 mm × 200 mm × 1 mm tile of plastic scintillator. However, this design is challenging regarding how to transport light outside vacuum up to the PMT.

7.5   Time-of-Flight Module

It is important for the protoDUNE experiments to identify the particles entering the liquid argon chambers. A system of Cherenkov Counters (CET) (CET introduced in section 1.3) is foreseen for particle identification, but it only works for momenta above 5 GeV/c. For low momentum beams, a Time-of-Flight (ToF) system with 1 nanosecond time resolution could complement the identification from the lowest momentum up to 4 GeV/c.

In theory, the time resolution of the XSCINT modules could be lower than 1 ns depending on the readout electronics employed. In a XSCINT ToF system, the time resolution would be an addition of the time spread of the following processes:

- Light creation in the scintillation process.

- Time jitter of the light travelling inside the fibre.

- Transit time spread of electrons in the PMT.

- Time jitter of the discriminator of the PMT signals.

- Resolution of the Time-to-Digital Converter (TDC).

Scintillating fibres are fast scintillators with short rise and decay times, which favours the time resolution. However, the number of photons trapped and their transit time jitter along the fibre can be a limiting factor to achieve a good time resolution.

As aforementioned, the 300 ps time transit spread of the H11934-200 PMT makes it good for timing measurements.

High-performance readout electronics are critical in a ToF system. For that reason, Constant Fraction Discriminators are particularly suited for timing measurements, as they do not suffer from walk jitter as other type of discriminators [86].

In the case of protoDUNE, there is the additional requirement of integrating White Rabbit for time-stamping the events in a common time reference. Fortunately, a TDC device with 700 ps time resolution and compatible with WR exist, and it is fully supported by CERN: the SVEC FMC-TDC [87]. It consists in a VME carrier board (the SVEC), which incorporates a FMC mezzanine board with the TDC.

Therefore it is being investigated if the XSCINT module, read-out by the proper electronics, could achieve a sub-ns time resolution.

7.6 Preliminary Results From Beam Tests in the East Area

From the 20th of November to the 4th of December of 2017 (the two weeks before the defence of this manuscript), there was the possibility of testing the first prototypes of the XBPF and the XSCINT in the T10 beam line of the East Area (section 1.2). This line provides low energy beams with a maximum momentum of 6 GeV/c, and a maximum intensity of 10^5 particles/spill. The collimators of the beam line can be closed to reduce the beam intensity, approaching the conditions to the Neutrino Platform.

7.6.1 Description of the Setup

Two XBPF and two XSCINT modules were ready for the tests, along with their respective readout electronics and vacuum tanks. The tanks hosting the detectors were placed 14 m far away from each other, making use of the maximum available space in the beam line. A long distance is particularly important for the Time-of-Flight, since it facilitates the differentiation the particle species present in the beam.

The upstream tank contained a XBPF plane, which reconstructed the horizontal profile of the beam, and a XSCINT module. The downstream tank was equipped with a XBPF plane to measure the vertical profile and the other XSCINT module. These four detectors replicated a similar setup to the Neutrino Platform, but in a smaller scale: the coincidence of the two XSCINT modules created a signal that triggered the acquisition event-by-event of the XBPF modules. A schematic of the beam setup can be seen in fig. 7.13.

The fibres used in both XBPF and XSCINT were the Kuraray SCSF-78, square cross section, single-clad, and 1 mm thickness. The cladding represents a total of 4% in this fibre model. In the XBPF modules, half of the fibres (the first 96 fibres) were coated with an ultra-thin evaporation of 100 nm of aluminium, in order to avoid fibre crosstalk.

Figure 7.14 shows two pictures of the installation of a XSCINT module and the front-end board of the XBPF in the downstream tank. Figure 7.15 shows the upstream monitor ready for data taking. A DWC and a Scintillator Paddle were placed close to the upstream tank in order to make a comparison with the new equipment.

The data from all the equipments (XBPF, XSCINT, DWC, and Scintillator Paddle) has been stored in a long-term storage database at CERN [88] with open access to CERN users.
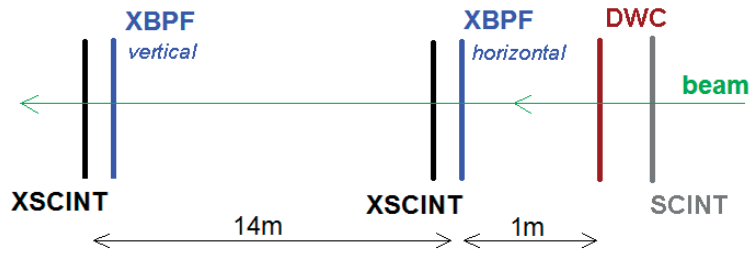
Figure 7.13 – Schematic diagram of the setup in the East Area showing the relative position of the XBPF, the XSCINT, the DWC, and the Scintillator Paddle.
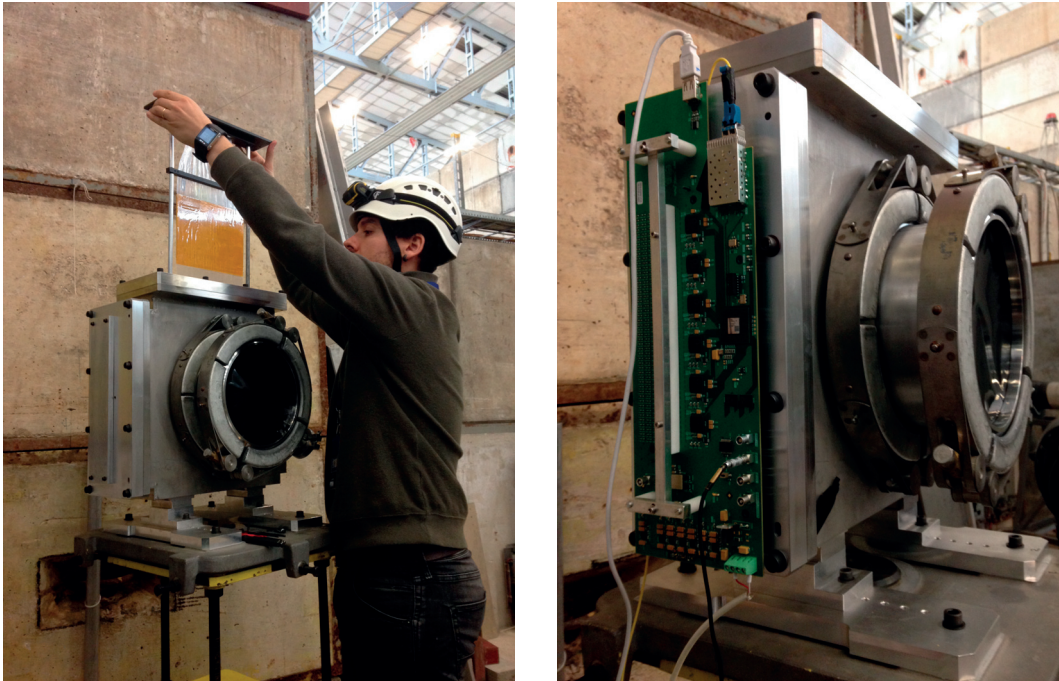
Figure 7.14 – Left: the author installing a XSCINT in the downstream tank. Right: XBPF front-end board plugged to the fibre connector during the installation.

The vacuum tanks containing the XBPF and the XSCINT were successfully tested for vacuum prior to the beam tests in the East Area. However, they were not put into vacuum for the East Area tests.

Figure 7.15 – Upstream vacuum tank, installed close to a DWC and a Scintillator Paddle.

7.6.2 Architecture of the Readout Electronics

Trigger Generation

The signals from the upstream and downstream XSCINT planes travelled to a Constant Fraction Discriminator (CFD) CAEN N842 [89], which was mounted in a NIM crate installed in the beam area, approximately in the middle of the two detectors. This kind of discriminator is particularly suited for timing measurements, as it minimises the jitter due to differences in signal amplitude [86]. The digital pulses pulses from the CFD had 200 ns width and travelled to a coincidence module connected to the same NIM crate. This latter module produced the trigger signal from the coincidence of two simultaneous XSCINT signals. After a conversion to TTL logic level, the trigger signal was sent to the VFC board.

XBPF Data

The XBPF data could be recovered in parallel by two mechanisms: connecting locally from a PC to the front-end board via USB, and remotely by reading the VFC board with a Java application developed within the CERN FESA framework [90]. In order to get the data locally, a computer was installed close to every XBPF and connected via USB to the front-end board. Those PC run a LabView acquisition software that displayed in real time the profile of the beam. The data transferred via USB contained exclusively the profile of the beam integrated for every spill.

The VFC board was installed in a VME crate placed in the control room of T10 and connected to the front-end board via an optical link. The data from the VFC contained event-by-event information, with the status of the 192 fibres in every event (hit, no-hit) and a time stamp in the White Rabbit format. The WR time reference was provided by a WR switch installed in the same rack as the VME crate and connected to the VFC

through an optical link. Figure 7.16 shows the VME crate with the VFC board (second board from the left) and the TDC for the Time-of-Flight (fourth board). The rest of the modules are a MEN A20 VME controller (first board) and an accelerator-timing board (third one). The WR switch can be seen in the same figure standing on top of the VME crate.
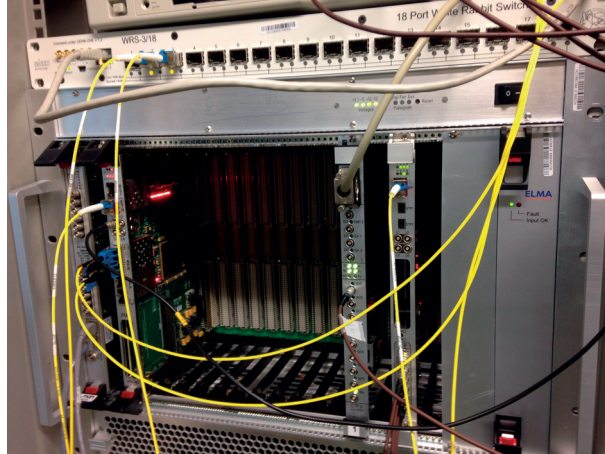
Figure 7.16 – VME crate in the control room hosting the VFC board for the XBPF event acquisition (second module from the left) and the TDC for the Time-of-Flight measurements (fourth module from the left). The White Rabbit switch that provides a common reference clock is standing on top of the crate.

Due to the specification of beam intensity for the Neutrino Platform (maximum of 500 particles per spill), the VFC firmware uses a buffer that can only accumulate a maximum of 3276 events per extraction. Therefore, in spills with a higher number of events, the buffer is filled in with the first 3276 events and the rest of events in the spill are lost. This limitation does not prevent the reconstruction of the profile with the VFC, neither the measurement of the the performance of the XBPF.

7.6.3 Measured Performance of the XSCINT

The setup of the East Area allowed to measure the detection efficiency of the XSCINT. This magnitude is defined as follows: for a certain number of particles crossing the monitor, N_t, the efficiency is given the fraction of those particles actually detected, N_x:

$$\epsilon = \frac{N_x}{N_t}. \tag{7.5}$$

For the upstream XSCINT, it is certainly true that a particle has crossed the monitor, detected or not, when there is a coincidence between the Scintillator Paddle and the downstream XSCINT. In the case where the particle is detected, the coincidence of

the three monitors (Scintillator Paddle, downstream XSCINT, and upstream XSCINT) should be true. Therefore, counting during a spill the number of simultaneous events between the Scintillator Paddle and the downstream XSCINT gives N_t, and the number of simultaneous events in the three monitors provides N_x. Such logical operations were done with a coincidence logic module in the NIM crate and stored along the rest of the data for subsequent analysis. Figure 7.17 shows a diagram of the coincidence logic and fig. 7.18 shows a real time measurement.

It should be noted that in order to measure the efficiency, it is not necessary to know the absolute number of particles crossing the monitor, but just to be certain of the fraction of particles detected.
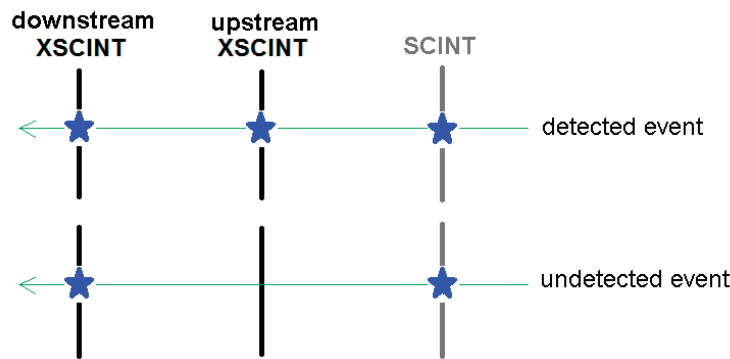
Figure 7.17 – Diagram of the logic used to measure the efficiency of the upstream XSCINT. *Note: all other combinations of hits are ignored.*

Figure 7.18 – Real time measurement of the scintillators logic. The red circle highlights the beam intensity measured by the Scintillator Paddle. Similarly, the blue circle shows the coincidence of the downstream XSCINT and the Scintillator Paddle, and the green the coincidence of the three detectors. *Note: due to divergence of the beam, the number of particles arriving to the downstream monitor is typically much lower.*

The efficiency of the XSCINT strongly depends on the voltage of the PMT and the threshold level of the CFD discriminator. After tuning these two parameters, a maximum efficiency of 94% was obtained for the maximum recommended voltage of the PMT, $-1000\,\mathrm{V}$, and a threshold value of $-20\,\mathrm{mV}$:

$$\epsilon_{xscint} = 94.0 \pm 0.1\%. \tag{7.6}$$

125

The same coincidence technique can be used to analyse the detection efficiency of the Scintillator Paddle. In that case, N_t is given by the coincidence of the two XSCINT. Such analysis yields a lower limit in the efficiency of this monitor of:

$$\epsilon_{scint} = 59 \pm 1\%. \tag{7.7}$$

However, the real efficiency of the Paddle is probably higher, since the area of the XSCINT is four times larger and some particles could actually cross the two XSCINT, but not the Paddle.

It should be noted that the efficiency of the downstream XSCINT cannot be measured using this coincidence technique, due to the fact that it is placed 14 m away and part of the beam is diverging. In such case, the coincidence of the upstream XSCINT and the Scintillator Paddle would not guarantee that the particle is also crossing the downstream XSCINT.

7.6.4 Measured Performance of the XBPF

A visual comparison between the profiles of the XBPF (obtained locally via USB) and the DWC shows that the new monitor produces more accurate profiles than the old gaseous chamber. This is clearly seen, for example, in the profile of a -6 GeV/c pion beam of $I = 1.5 \times 10^5$ particles. An image from the acquisition software of the DWC and the XBPF is shown in fig. 7.19, which shows the horizontal profile of both monitors. Since the horizontal XBPF is around 1 m away from the DWC, their profiles can be qualitatively compared. The corresponding vertical profiles are shown in fig. 7.20. However, the vertical XBPF is placed 14 m away from the DWC and, therefore, they are not equiparable due to the divergence of the beam.

The measurement of a 1 GeV/c pion beam of $I = 9.4 \times 10^4$ particles also shows a smoother profile in the XBPF compared to the DWC (fig. 7.21). The vertical profiles are also shown in fig. 7.22.

For every event, the data from the VFC contains the hit information of the 192 fibres. This information allows to calculate the detection efficiency and the hit multiplicity of the monitor. The preliminary analysis of a focused beam of -6 GeV/c pions of $I = 1.5 \times 10^5$ particles is shown in histograms fig. 7.23 and fig. 7.24, which show the number of fibres hit per event. The profile of this beam, as reconstructed by the VFC, is shown in fig. 7.25 and fig. 7.26.

The detection inefficiency is easily calculated from these histograms (fig. 7.23 and fig. 7.24), since it is equal to the number of events with no fibres hit, divided by the total number of events. Similarly, the multiplicity of the monitor is given by the ratio between the
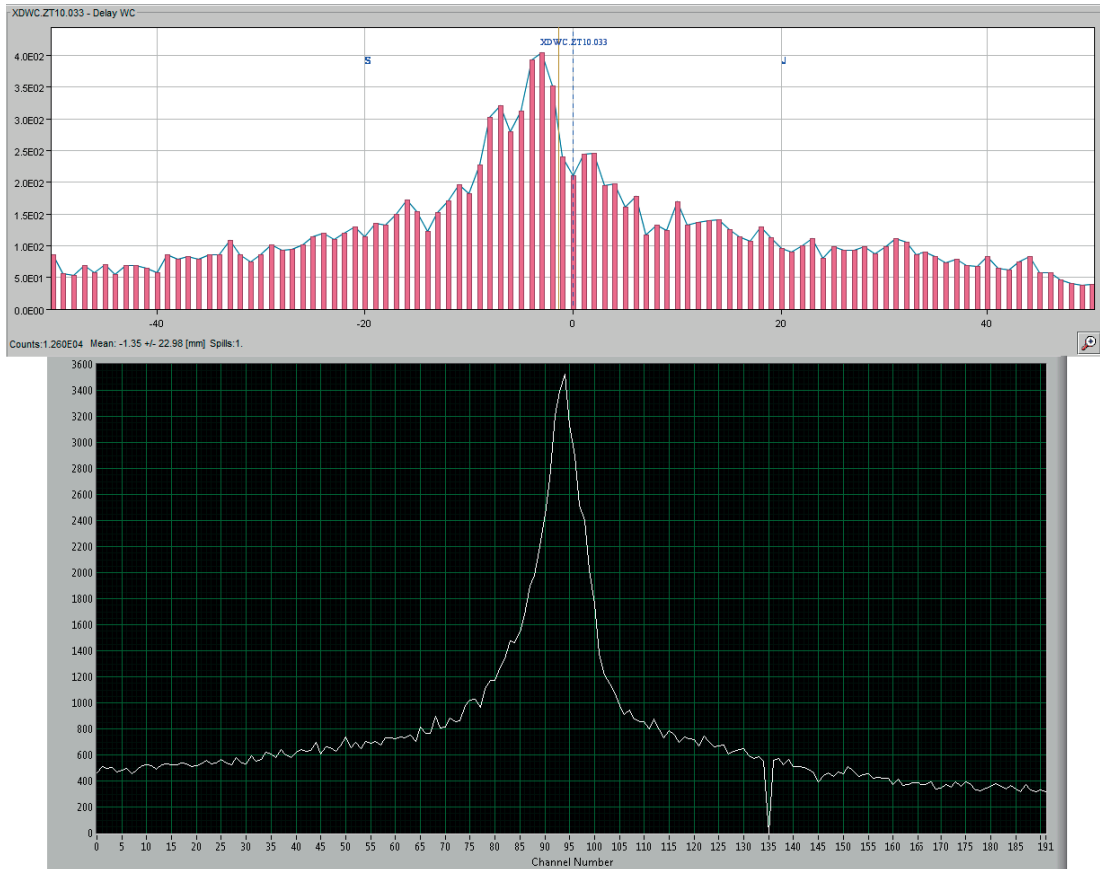
Figure 7.19 – Horizontal profile of a $-6\,\text{GeV}/\text{c}$ pion beam of $I = 1.5 \times 10^5$ particles measured by the DWC (above) and the XBPF (below). *Note: channel 135 of the horizontal XBPF was not working, probably due to a faulty SiPM.*

number of events with more than one fibre hit and the total number of events. The multiplicity can be used to quantify the optical crosstalk between the fibres.

These prototypes of the XBPF have half of the fibres covered with a $\sim 100\,\text{nm}$ aluminium coating to avoid optical crosstalk: fibres 1 to 96 are coated, while fibres 97 to 192 have no treatment. The motivation for this layout is to investigate the impact of crosstalk in the monitor and the effectiveness of the aluminium coating. For this reason, the fibre-hit histograms in fig. 7.23 and fig. 7.24 are analysed for the totality of fibres (Total Multiplicity) and the two halves (Multiplicity A and Multiplicity C). However, this analysis by halves is still under development and no data has been yet extracted from it.

Another interesting figure that can be extracted from the fibre-hit information is the distance between hit fibres in an event with multiplicity higher than 1. It could be useful to identify optical crosstalk events, which can only happen between adjacent fibres, and multiple particles acquired during the sampling time of the electronics, which is $100\,\text{ns}$. Figure 7.27 shows such fibre-span analysis for the same beam of $-6\,\text{GeV}/\text{c}$ pions
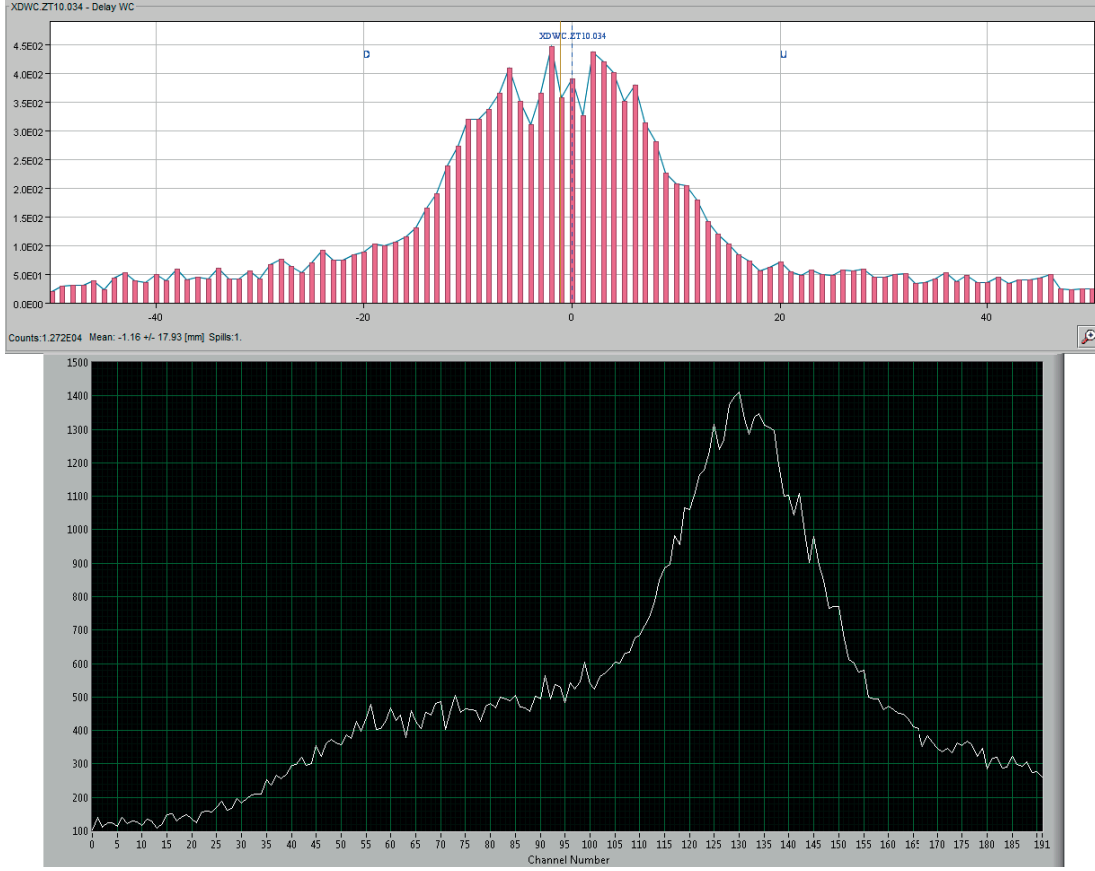
Figure 7.20 – Vertical profile of a $-6\,\mathrm{GeV/c}$ pion beam of $I = 1.5 \times 10^5$ particles measured by the DWC (above) and the XBPF (below). *Note: the vertical XBPF is 14m away from the DWC, therefore their profiles are not equiparable.*

of $I = 1.5 \times 10^5$ particles.

The preliminary analysis of a focused beam of $-6\,\mathrm{GeV/c}$ pions with $I = 1.5 \times 10^5$ particles yields an efficiency of 96.1% for the upstream XBPF and 89.6% for the downstream one.

$$\epsilon_{upstream\ xbpf} = 96.1\%, \tag{7.8}$$

$$\epsilon_{downstream\ xbpf} = 89.6\%. \tag{7.9}$$

The origin of that discrepancy is still under investigation and whether it is dependent on the beam conditions.

It should be noted that the efficiency is strongly dependent on the bias voltage of the SiPM and the threshold of the CITIROC discriminators. The measurements above described were done with a bias voltage of $55.7\,\mathrm{V}$ ($3\,\mathrm{V}$ of overvoltage, as compensated for a temperature of $\sim 33\,^\circ\mathrm{C}$). The threshold of the CITIROC discriminators was set to 290 DAC value. An analysis of the dark count rate of the SiPM versus the CITIROC
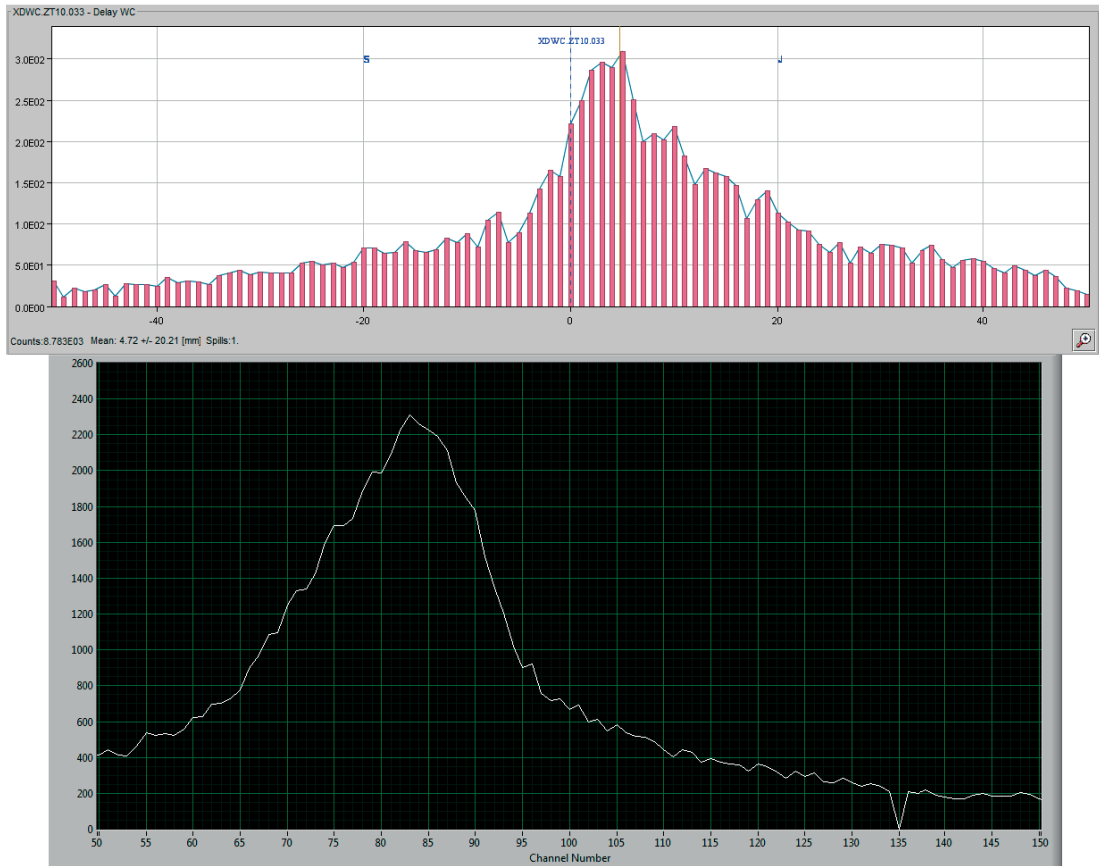
Figure 7.21 – Horizontal profile of a $1\,\mathrm{GeV/c}$ pion beam of $I = 9.4\times10^4$ particles measured by the DWC (above) and the XBPF (below). *Note 1: the profile of the horizontal XBPF is inverted with regard to the DWC. Note 2: in this particular chart, the horizontal scale of the XBPF has been zoomed to* $100\,\mathrm{mm}$ *to make it equal to the DWC.*

threshold reveals that such value (290 DAC) approximately corresponds to a level of 4.5 photons, as can be seen in fig. 7.28.

Lowering the CITIROC discriminators to a lower value, such as 1.5 or 2.5 photons would certainly increase the detection efficiency. The rise in noise that would involve a lower threshold should not be a problem, since the acquisition of the events is triggered by the XSCINT, which makes the probability of acquiring noise almost negligible. Unfortunately, there was not time to do a rigorous analysis of the light production of the monitor in the laboratory prior to the beam test. Such procedure would have allowed to know the efficiency as a function of the discriminators value.
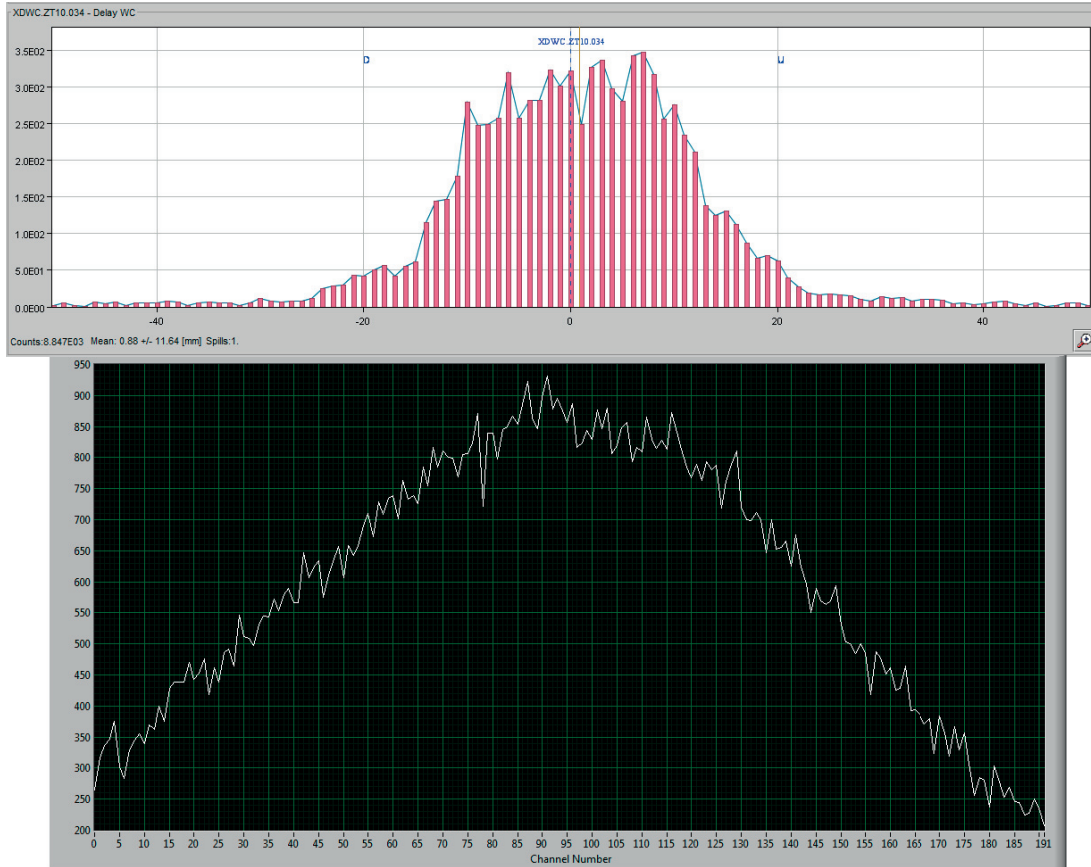
Figure 7.22 – Vertical profile of a 1 GeV/c pion beam of $I = 9.4 \times 10^4$ particles measured by the DWC (above) and the XBPF (below). *Note: the vertical XBPF is 14m away from the DWC, therefore their profiles are not equiparable.*

7.6.5   Measured Performance of the ToF

It was also possible to do a measurement of the time of flight of the beam particles by reading-out the XSCINT signals with the SVEC FMC-TDC. This TDC used the reference clock provided by the WR switch to put a time stamp of picosecond precision to the XSCINT events. The preliminary analysis shows a time resolution of the ToF system of:

$$\sigma_t \approx 900\,\text{ps}. \tag{7.10}$$

This value allows to differentiate, in a distance of 14 m, pions and protons with 4σ, from the lowest momenta up to 2.5 GeV. A plot with the ToF analysis of this beam is shown in fig. 7.29.

With this time resolution, it would be possible to differentiate protons from pions up to 4 GeV in the 39 m available in the Neutrino Platform. Similarly, kaons and protons
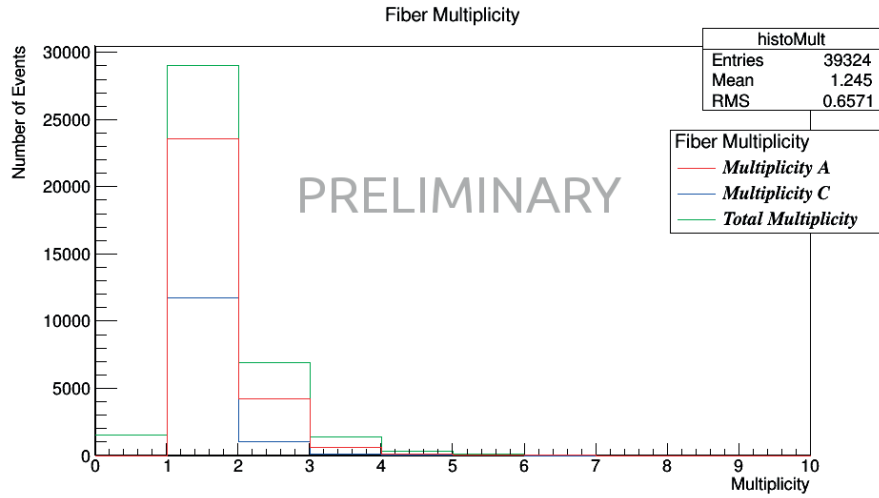
Figure 7.23 – Fibre hit analysis of a focused beam of $-6\,\mathrm{GeV/c}$ pions of $I = 1.5 \times 10^5$ particles, for the upstream XBPF.
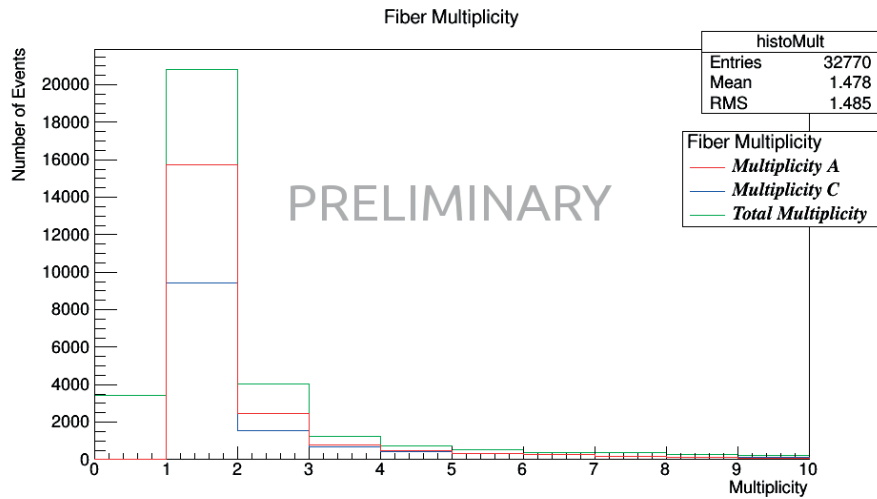
Figure 7.24 – Fibre hit analysis of a focused beam of $-6\,\mathrm{GeV/c}$ pions of $I = 1.5 \times 10^5$ particles, for the downstream XBPF.

could be identified up to $3.5\,\mathrm{GeV}$.
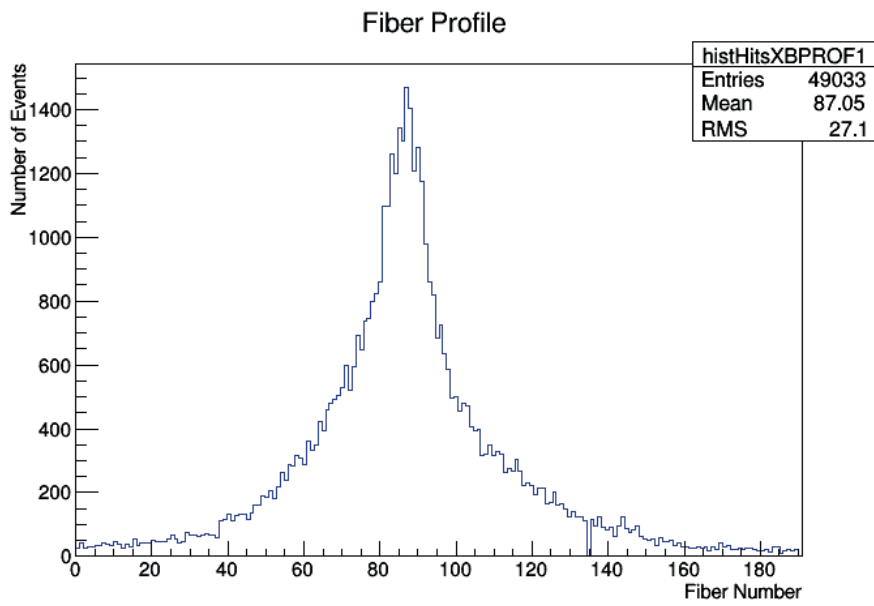
Figure 7.25 – Profile of the upstream monitor (horizontal) of the beam analysed in fig. 7.23, as reconstructed by the VFC.
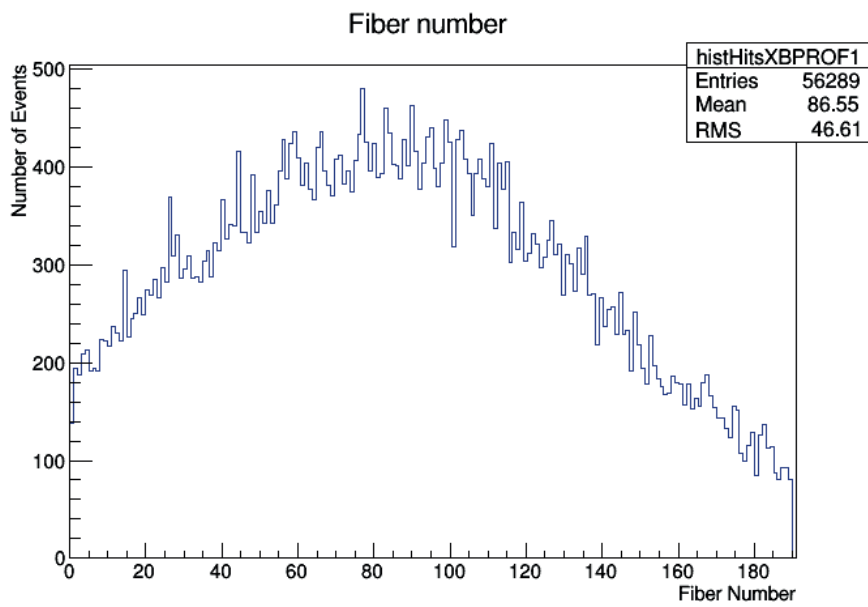
Figure 7.26 – Profile of the downstream monitor (vertical) of the beam analysed in fig. 7.24, as reconstructed by the VFC.
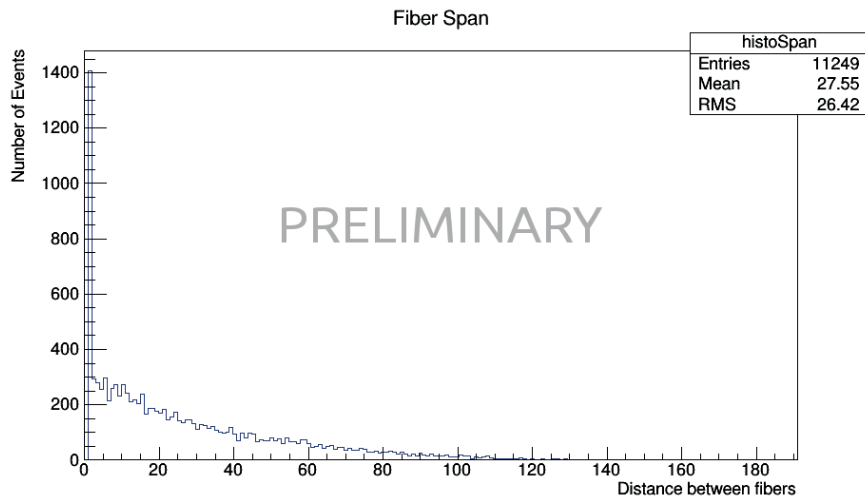
Figure 7.27 – Distance between hit fibres in events with multiplicity higher than 1, for the upstream XBPF and the beam of $-6\,\mathrm{GeV/c}$ pions of $I = 1.5 \times 10^5$ particles.
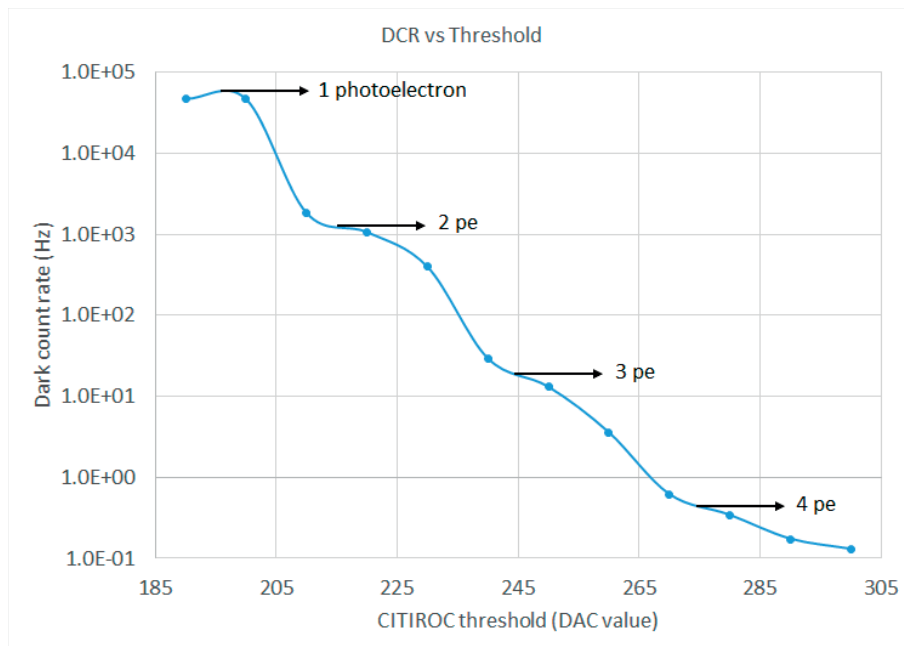
Figure 7.28 – Characterisation of the dark count rate of the SiPM versus the CITIROC threshold, performed in the East Area during the absence of beam. The levels of 1, 2, 3, and 4 photoelectrons are estimated from the shape of the curve and the drop in DCR.
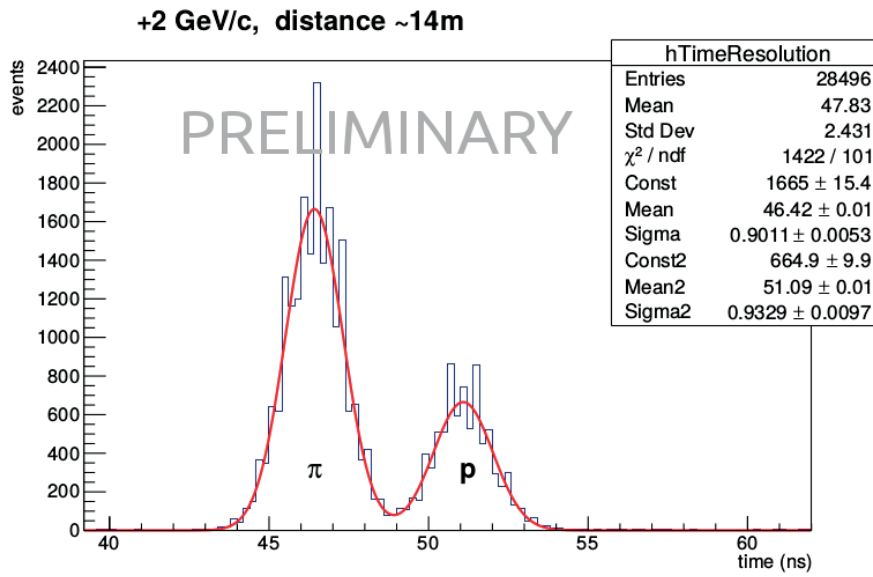
Figure 7.29 – Time of flight measured with the XSCINT and the SVEC FMC-TDC for a 2.5 GeV/c pion-proton beam in a distance of 14 m. The time resolution of the system is 900 ps.

Chapter 8

Conclusions and Outlook

Two prototypes of the SciFi monitor have proven that scintillating fibres can replace the existing profile monitors and extend their functionalities. They have produced more accurate profiles over a wider range of intensities, while representing a similar material budget. In addition to that, they have been completely built in workshops of the CERN Beam Instrumentation group and for a low price. During their construction and operation, several issues that could affect the performance were found. These are presented hereafter, along with solutions to improve future versions of the monitor.

8.1   Conclusions

The first SciFi monitor prototype worked satisfactorily with all secondary beams, whilst the DWC had troubles with high intensities, showing distorted profiles or artificial tails; the FISC on the other hand was unable to resolve profiles properly at intensities lower than 10^3 particles/s (full discussion in section 6.2.1).

Additionally, the intensity measured by the SciFi agreed within a few percent with the intensity from the scintillator paddles. The origin of this discrepancy is believed to be optical crosstalk between the fibres (section 6.4) or unreliable data from the scintillator paddles (section 6.5.3).

For lead ions, however, the profiles from the SciFi were seen to be wider than those from the DWC (complete study in section 6.3.1). The origin of these wider profiles is also believed to be crosstalk between the fibres, which could be avoided by applying one of the treatments discussed in section section 3.5.

The preliminary data from the beam tests of the second prototype, the XBPF (section 7.6), shows an excellent performance in the profile reconstruction and the intensity measurement. Furthermore, just with the addition of a suitable TDC, this device measured the time of flight of the beam particles with a time resolution of 900 ps, which allowed to identify the different particle species at low momenta. Therefore, this device has proven that it can perform, with good precision, all the functions required by the new beam lines of the Neutrino Platform: profile measurement, intensity measurement, trigger generation, and time-of-flight measurement.

The radiation damage of the fibres with secondary beams is believed to be very low, which would allow its use for many years (section 6.5). By contrast, the damage from Pb-ions would be orders of magnitude higher. Despite of this damage, the fibres could also work for years, provided that they are only used with Pb-ions.

Therefore, two versions of the monitor, one for secondary beams and another one for Pb-ions, could have a lifespan of many years. For this purpose, a modular design of the monitor, in which the fibres are easily exchanged, would facilitate having a set of fibres for every type of run. Nevertheless, even if radiation damage occurs, since the cost of scintillating fibres is relatively low, the replacement of the fibres would be a simple and effective solution.

Most of the monitors in the EA have a motorisation that allows moving them out from the beam line when they are not being used. This simple strategy avoids unnecessary beam perturbation and ageing of the detectors. Therefore, this feature should be incorporated to future versions of the monitor for the North and East Area.

8.2 Future Improvements

The following list summarises all the ideas gathered to improve future versions of the monitor:

- Mirror: use a better combination of reflective foil and glue.

- Polishing: create a design that allows diamond milling on both fibre ends.

- Fresnel reflections: employ a suitable optical grease to improve light transmission at the boundary fibre-SiPM.

- Light collection by SiPM: use a photodetector with a larger active area and a thinner window to optimise light collection (section 5.3.3). Hamamatsu has released a new version of the MPPC of the prototype, the S13360-2050VE [50], with an active area of $2\,mm \times 2\,mm$ and a thinner window of $100\,\mu m$.

- Threshold configuration: make a full characterisation of the light collection by the SiPM, as described in appendix C.2. It could be done in a beam line test with MIP or in the laboratory with a ^{90}Sr electron monochromator [91].

- Readout electronics: develop dedicated electronics that record the information of which fibre is hit, time-stamp the events, and measure the charge of the SiPM pulses. With a time-stamp it would be possible to extend the applications of the monitor, while the integrated charge is necessary to study the light collection by the SiPM. Developing custom electronics is also a more efficient solution in terms of cost for a series production of the detector.

- Efficiency at high rates: smaller pixel SiPM and dedicated readout electronics would decrease the dead time per channel (section 5.6.4). The use of thinner fibres would spread the beam spot amongst a larger number of fibres, reducing also the intensity per channel.

- Acceptance: staggering layers of fibres could be investigated in applications where a higher detection efficiency and better spatial resolution are required.

- Temperature effects: install a temperature sensor close to the SiPM, along with a bias voltage control system. Hamamatsu has developed a MPPC power supply, the C11204-02 [82], that features an autonomous temperature compensation function. A passive cooling system, such as a heat sink, would help maintaining a stable temperature in the SiPM.

- Noise suppression: an auxiliary detector installed in the beam line could anticipate the arrival of a particle and generate a signal that triggers the acquisition of the fibre monitor. Such technique would practically suppress the noise, allowing also to improve the detection efficiency. Besides an auxiliary detector, two planes of fibres whose signals are put in coincidence would produce a similar effect.

- Efficiency measurement: perform a measurement of the efficiency of the monitor with the help of well calibrated scintillator paddles.

- Radiation damage and general maintenance: a modular design of the monitor where the fibres, the SiPM, and the electronics are easily exchanged would allow an easy maintenance and a cost effective solution for eventual radiation damage.

- Motorisation: investigate a motorisation of the monitor in order to set it apart from the beam line when it is not being used.

8.3   Final Note

A scintillating fibre-SiPM detector based on the designed described in this work can be used to track charged particles up to intensities of 10^8 particles per second over a

wide range of energies. Its design follows a simple and cost effective production principle that allows a spatial resolution equal to the fibre thickness and a detection efficiency above 90%. In addition, SiPM show the advantage of having a compact size, a low power consumption, and being simple to operate, with no high voltage required. Therefore, the fibre monitor here presented could perhaps extend its application field beyond particle physics, and be adapted to industrial applications, such as medicine, homeland security, or radio-protection, for example.

Appendix A

Passage of Particles Through Matter

This annex presents a reminder of the fundamental physics of the interaction of radiation with matter, which is the basis of particle detection. Even though the reader most probably knows these principles, some of the concepts exposed will be often employed during the manuscript. The exposition begins with basic notions, such as the cross section and the types of interactions, to subsequently introduce essential magnitudes for the design of particle detectors, like the stopping power or multiple scattering. For simplicity, the discussion is restricted to charged particles and photons.

A.1 Basic Concepts

The microscopic processes involved in the interaction of particles with matter are governed by probabilistic laws. For this reason, the concepts of *cross section probability* and *mean free path* are necessary in this description:

- The cross section measures the probability for a certain reaction between two particles to occur (or a particle and a medium).

- The mean free path represents the average path that a particle can travel freely inside a medium before suffering an interaction.

The cross section is commonly used in its differential form, the *differential cross section*, which is defined in the classical formalism as the scattering distribution of a beam of

particles by a fixed target (fig. A.1). Calling Φ the flux of incident particles with energy E, and dN the number of scattered particles per differential solid angle $(d\Omega)$, the differential cross section is:

$$\frac{d\sigma}{d\Omega}(E, \Omega) = \frac{1}{\Phi}\frac{dN}{d\Omega}. \tag{A.1}$$

When the physics of the interaction are understood, it is possible to deduce an analytical formula of the cross section.

The equation (A.1) can also be interpreted in the formalism of quantum mechanics. In that context, N represents the scattered probability current and Φ the total incident probability.
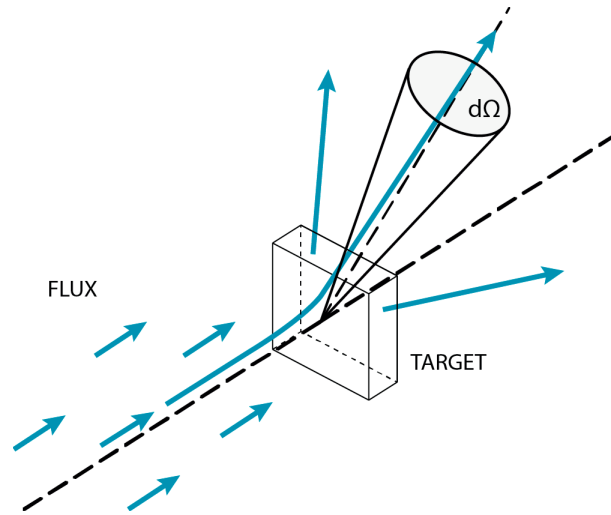
Figure A.1 – Definition of cross section as the scattering distribution of a beam of particles by a fixed target.

The differential cross section eq. (A.1) can be integrated over all solid angles to eliminate the spatial dependency. Such integration yields the cross section:

$$\sigma(E) = \int \frac{d\sigma}{d\Omega}d\Omega. \tag{A.2}$$

Particles travelling in a medium typically undergo different reactions, each one described by its own cross section probability. The addition of all of them yields the *total cross section*, which gives a full description of be interaction of the particle with the medium.

Intuitively, the cross section and the mean free path (λ) must be related. For thin

materials this relation takes the form:

$$\lambda = \frac{A}{N_A \rho} \frac{1}{\sigma},$$

(A.3)

where A is the atomic weight of the material, ρ its density, and N_A is Avogadro's number.

For an interaction with mean free path λ, the probability for the particle to penetrate into the medium a depth x without suffering any interaction is:

$$P(x) = e^{-\frac{x}{\lambda}}.$$

(A.4)

And the probability of having suffered n interactions after travelling a distance x is Poisson distributed with a mean x/λ:

$$P(n\ interactions\ in\ x) = \frac{1}{n!} \left(\frac{x}{\lambda}\right)^n e^{-\frac{x}{\lambda}},$$

(A.5)

A.2 Interaction of Charged Particles with Matter

Charged particles travelling through a medium interact with the electrons and nuclei from atoms. Some of the physical processes that can occur in those interactions are:

- Elastic collisions

- Inelastic collisions

- Emission of Bremsstrahlung radiation

- Emission of Cherenkov radiation

- Emission of transition radiation

- Annihilation

- Direct pair creation

- Nuclear reactions

For the beams of the EA, given the type of particles and range of energies, the most frequent and significant reactions are the emission of Bremsstrahlung and the collisions with atomic electrons and nuclei.

A.2.1   Inelastic Collisions

Charged particles travelling through a medium will experience, above all, inelastic collisions with atomic electrons. During these collisions, part of the energy of the particle is transferred to the atom, causing its ionisation, excitation, or even producing collective atomic excitations. Although the fraction of energy transferred per collision is low, when the number of collisions per unit path length is large, as frequently occurs, the overall energy lost by the particle can be considerable. In addition to the energy loss, the particle suffers a change in momentum that produces a deviation from its initial trajectory.

A.2.2   Elastic Collisions

Elastic scattering of particles by nuclei, caused by Coulomb forces, is also very frequent. The energy transfer in this case is negligible, due to the difference in masses of particles and nuclei, but the deflection of the particle can be considerable. The cross section of this process is well described by the classical Rutherford formula:

$$\frac{d\sigma}{d\Omega} \propto \frac{z^2 Z^2}{m^2 v^4} \frac{1}{sin^4(\theta/2)}, \tag{A.6}$$

with z, m and v, the charge, mass and velocity of the incident particle, respectively, Z the atomic number of the target material, and θ the deflection angle of the particle. This cross section describes a symmetric scattering distribution, very populated at low deflection angles and with progressively decreasing tails for larger angles.

A.2.3   Bremsstrahlung

Bremsstrahlung radiation is emitted by a particle when it is decelerated or deflected by the electromagnetic field of a nucleus. Since the energy of the emitted photons varies inversely with the square of the mass of the particle $(1/m^2)$, this reaction is important for particles with small masses, notably the electron and the positron. The cross section probability of this process can be calculated using quantum mechanics:

$$\frac{d\sigma(E,\nu)}{d\nu} \propto z^4 Z^2 \frac{1}{h\nu} f(E, E'). \tag{A.7}$$

Where:
E and E' are the initial and final energy of the particle after the emission of the Bremsstrahlung photon.
$h\nu = E - E'$ is the energy of the emitted photon.
z is the charge of the projectile particle.
Z is the atomic number of the target material.

$f(E, E')$ is a function accounting for screening effects produced by atomic electrons.

This formula shows that the emission of very high energetic photons carrying all the energy of the particle, although being possible, is highly suppressed; it also shows the strong dependency of the emission probability on the particle charge and the medium.

A.2.4 Other reactions

Cherenkov radiation is emitted when a charged particle travels through a dielectric medium with a velocity larger than the speed of light in that medium. The photons are distributed over a cone with angle $\theta = \cos^{-1}(1/\beta n)$, being n the refractive index of the material and $\beta = v/c$ the speed of the particle.

Transition radiation is produced when a charged particle crosses the boundary between two dielectric media with different indices of refraction. It is emitted in a narrow cone in the direction of the trajectory of the particle and its intensity is proportional to the mass and the velocity of the particle: $I \propto m\sqrt{1-\beta^2}$.

The cross section and intensity of Cherenkov and transition radiations are low, making them rare reactions. Nevertheless, due to the fact that both depend on the velocity of the particle, they are often employed in applications for particle identification.

The *annihilation* of a particle by its antiparticle has a large cross section at low energies, but small at high energies. Therefore, it is a major reaction for low energy beams of antiparticles such as antiprotons or positrons.

Both *direct pair creation* and *nuclear reactions* are particle-nucleus interactions. In direct pair creation, a new particle-antiparticle pair is created from the energy of the incident particle; this process is important for very energetic particles. In nuclear reactions, the collision of a particle with a nucleus can break the latter into smaller nuclide.

A.3 Energy Loss of Heavy Charged Particles

As aforementioned, the main mechanism of energy loss for charged particles are inelastic collisions with electrons, which can lead to ionisation or excitation of the atoms of the medium. For light particles, like the electron and the positron, Bremsstrahlung can become a larger source of loss than collisions. For this reason, the energy loss of light particles is studied separately.

The amount of energy transferred during inelastic collisions fluctuates from event to event, due to the statistical nature of the process. Nevertheless, when the number of collisions

per unit path length is large, it is meaningful to employ the average of the energy lost by a particle in a material. This quantity is called the *stopping power*, or $\langle dE/dx \rangle$, which can be experimentally measured. An analytical formula was also calculated, first by H.Bethe, based on quantum mechanics and special relativity, and subsequently corrected by F.Bloch, W.Barkas and H.H.Andersen. It is commonly known as the Bethe formula:

$$-\left\langle \frac{dE}{dx} \right\rangle = 2\pi N_a r_e^2 m_e c^2 \rho \frac{Z}{A} \frac{z^2}{\beta^2} \left[\ln \left(\frac{2m_e c^2 \beta^2 \gamma^2 T_{max}}{I^2} \right) - 2\beta^2 - \delta - 2\frac{C}{Z} \right], \quad \text{(A.8)}$$

where:

N_A is Avogadro's number.

r_e is the classical radius of the electron

m_e is the rest mass of the electron.

ρ is the density of the material.

z is the charge of the projectile particle.

Z is the atomic number of the target material.

A is the atomic weight of the material.

γ is the Lorentz factor of the particle.

T_{max} is the maximum possible energy transferred in a collision.

I is the *mean excitation energy* of the material.

δ is the *density effect* correction.

C is the *shell* correction.

The mean excitation energy of the material reflects the dependency of the stopping power on the binding energy of the atomic electrons. The density effect and shell corrections terms are necessary to increase the accuracy of the formula at high and low energies respectively. Further corrections can be applied to refine the precision; these take into account radiative effects, ultra-relativistic velocities, spin effects, electron capture, or higher-order quantum electrodynamics processes, among others.

Figure A.2 illustrates a graph of the Bethe formula for muons on copper; fig. A.3 shows a graph of the stopping power of protons in polystyrene, indicating the contribution from electronic collisions to the total energy loss.

An important feature of the Bethe formula is that, for a given material, it is only dependent on the velocity of the particle within the region $0.1 < \beta\gamma < 1,000$. The formula has a minimum at $\beta = 0.96$ and for this reason all particles travelling at this velocity are also called *minimum ionising particles* (MIP). Practically all the particles in the EA are MIP.

Another important characteristic of the stopping power is that when it is divided by the density, it is almost independent of the material. This is clearly seen when the Bethe
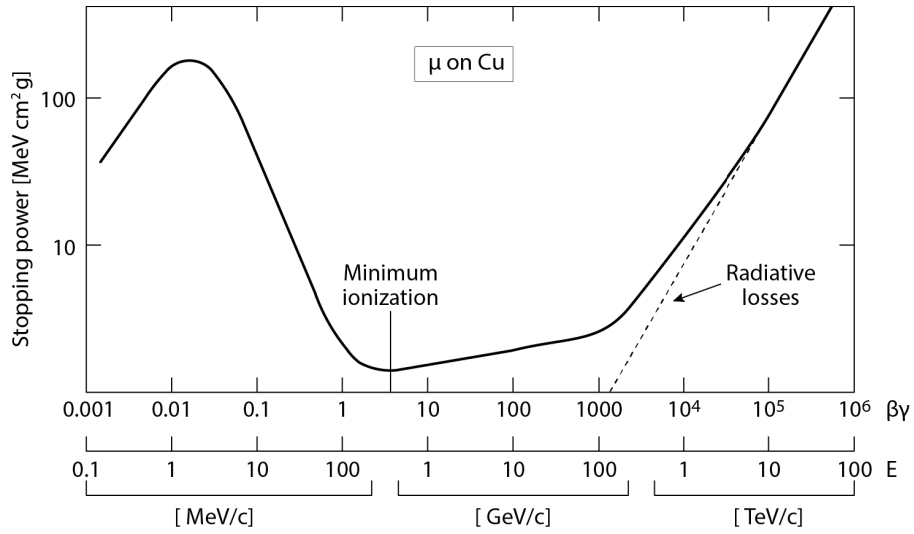
Figure A.2 – Graph of the Bethe formula calculated for muons on copper.
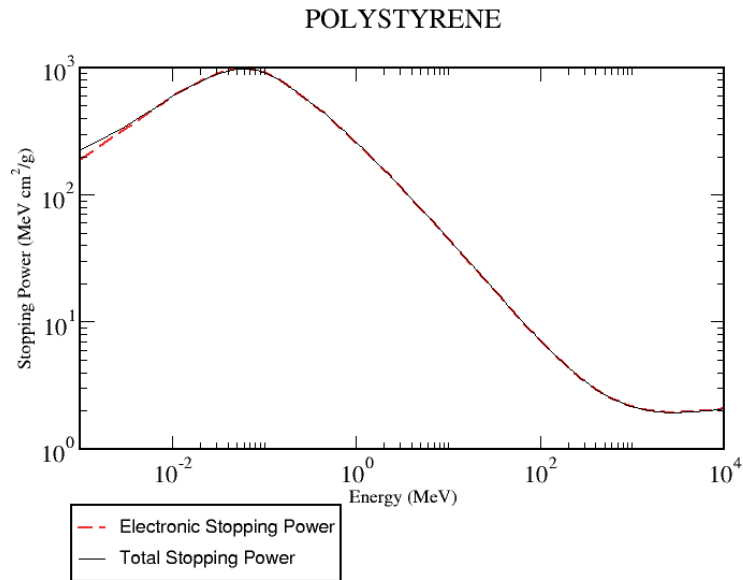
Figure A.3 – Stopping power of polystyrene for protons of different kinetic energy. The specific contribution of collisions with atomic electrons is shown with a red-dotted curve. Chart calculated with the PSTAR computer program, courtesy of NIST [92].

formula is rewritten as:

$$\frac{1}{\rho}\left\langle\frac{dE}{dx}\right\rangle = z^2\frac{Z}{A}f\left(\beta, I\right). \tag{A.9}$$

For most of mid-Z materials, the fraction Z/A and the function $f\left(\beta, I\right)$ vary very little.

Regarding the incident particle, the Bethe formula is accurate within a few percent for

projectiles with masses larger than the electron but lower than alfa particles. For heavier particles, like ions, the addition of further correction terms is needed.

A.4 Energy Loss of Electrons and Positrons

In the case of electrons and positrons, due to their lower mass, Bremsstrahlung radiation (described in appendix A.2.3) becomes also an important source of energy loss. The stopping power for these particles is usually separated into two contributions for collisions and Bremsstrahlung:

$$
\left\langle \frac{dE}{dx} \right\rangle_{total} = \left\langle \frac{dE}{dx} \right\rangle_{collision} + \left\langle \frac{dE}{dx} \right\rangle_{radiation} .
\tag{A.10}
$$

The collision stopping power is slightly different than for heavy particles. This is mainly due to the fact that two electrons are indistinguishable particles during a collision. Therefore, a modification accounting for this phenomenon is necessary to eq. (A.8), which becomes:

$$
- \left\langle \frac{dE}{dx} \right\rangle_{coll} = 2\pi N_a r_e^2 m_e c^2 \rho \frac{Z}{A} \frac{z^2}{\beta^2} \left[\ln \frac{T_{kin}^2 (T_{kin} + 2)}{2 (m_e c^2)^{-2} I^2} - f(T_{kin}) - \delta - 2\frac{C}{Z} \right],
\tag{A.11}
$$

where T_{kin} is the kinetic energy of the electron or positron, and $f(T_{kin})$ is a function that has a different form for electrons and positrons.

The radiative term in eq. (A.10) can be calculated by integration of the Bremsstrahlung cross section, eq. (A.7), over all the possible energies:

$$
- \left\langle \frac{dE}{dx} \right\rangle_{rad} = \frac{N_A \rho}{A} \int_0^E h\nu \frac{d\sigma}{d\nu} d\nu \propto E Z^2 .
\tag{A.12}
$$

Thus, the radiative term is proportional to the energy of the particle and the square of the atomic number of the material.

Figure A.4 shows the stopping power of polystyrene for electrons, calculated over a wide range of energies, and indicating the contributions from Bremsstrahlung and collisions. The energy at which the losses by radiation and collisions are equal is commonly called the critical energy of the material.
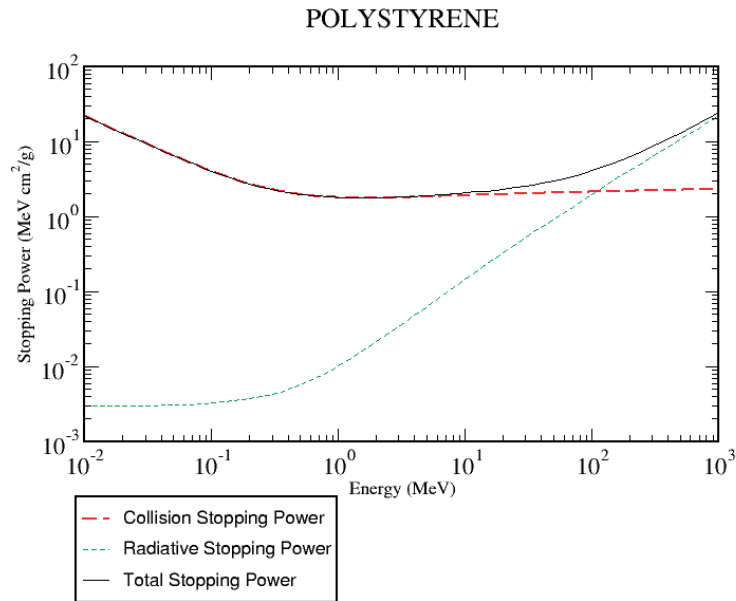
POLYSTYRENE

Figure A.4 – Stopping power of polystyrene for electrons of different kinetic energy. The specific contributions from electronic collisions and Bremsstrahlung are shown with red-dotted and green-dotted curves, respectively. Chart calculated with the ESTAR computer program, courtesy of NIST [92].

A.5 The Energy Loss Distribution

The stopping power gives the average energy lost per unit path length of material crossed. Nevertheless, it should be noted that this average is weighted with single rare events in which the particle can loss a large amount of energy, such as head-on collisions or highly energetic Bremsstrahlung photons.

For thick materials the number of interactions is large and it can be shown that the energy loss is Gaussian distributed. However, the case of thin materials is rather different, since the number of interactions is smaller and has a larger fluctuation. Thus, due to the possibility of large energy losses in single events, the energy-loss distribution for thin materials is rather skewed and asymmetric, showing a long tail to infinity. Such distribution is commonly known as the *Landau distribution* (fig. A.5), which is characterised by its *Most Probable Value* (MPV). The MPV is, by definition, smaller than the mean energy loss.

A.6 Multiple Scattering

During the passage of a particle through a medium, it experiences multiple deflections as a result of their mutual interaction. Most of these deflections can be described by the
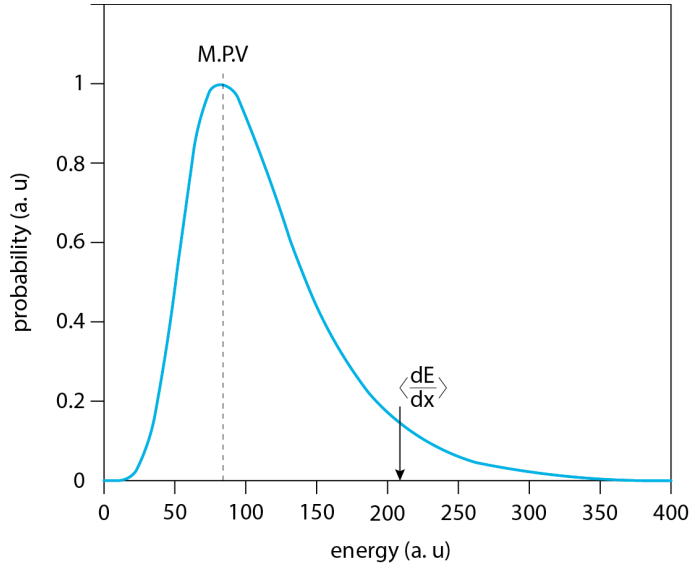
Figure A.5 – The Landau distribution describes the energy loss in thin absorbers. It is a skewed and asymmetric distribution, having a long tail to infinity.

Rutherford differential cross section, eq. (A.6), by which small deflection angles are more probable than large angles. Thus, the trajectory of a particle inside a medium is rather a zigzag than a straight line (fig. A.6).
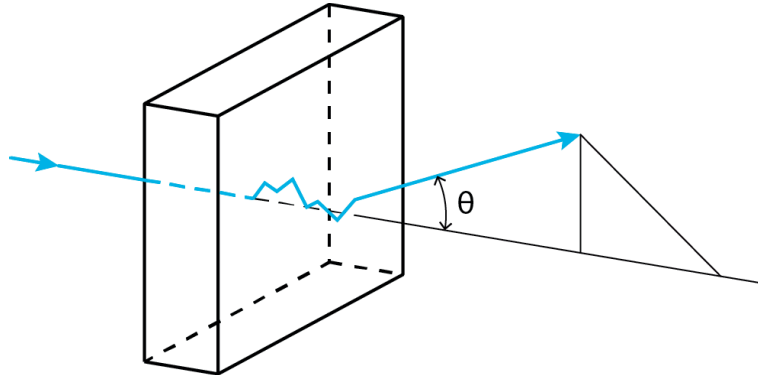
Figure A.6 – Effect of multiple scattering on a particle trajectory.

Multiple scattering is a complex phenomenon, very difficult to analyse. The theory of Molière gives an approximation for small angles, in which the scattering distribution is Gaussian distributed, with *r.m.s.*:

$$\theta_0 = \frac{13.6\,\text{MeV}}{\beta c p} z \sqrt{\frac{x}{X_0}} \left[1 + 0.038 \ln \left(\frac{x}{X_0}\right)\right], \tag{A.13}$$

being βc, p and z, the velocity of the particle, momentum and charge, respectively; x the thickness of the material and X_0 is a magnitude called the radiation length. Sometimes, the quantity x/X_0, is also known by the name *radiation thickness*.

The *radiation length* is formally defined as the distance at which the energy of an electron has been reduced by $1/e$, due only to radiation losses. The appearance of X_0 in the multiple scattering formula is just a writing simplification that does not limit its application to electrons.

Scattering angles larger than a few θ_0 are usually due to single scattering events and they are, therefore, well described by the Rutherford formula.

For compound materials, the total radiation length can be calculated via the weighted sum:

$$\frac{1}{X_0} = \sum \frac{w_i}{X_i}, \tag{A.14}$$

where w_i and X_i are the fraction by weight and the radiation length of the ith element of the compound.

In the slang of particle detectors, is common to talk about the *material budget* of the detector, to refer to the X_0 of the ensemble.

A.7   Interaction of Photons with Matter

Photons are massless and chargeless particles that interact with matter in a very different way than charged particles. The most common reactions occurring during the interaction of photons with matter are:

- Photoelectric effect

- Compton scattering

- Thomson and Rayleigh scattering

- Pair production

A.7.1   Photoelectric Effect

In the *photoelectric effect*, the incident photon is absorbed by an atomic electron, providing the latter with the necessary energy to escape the atom. The maximum kinetic energy of the ejected electron is:

$$T_{max} = h\nu - \phi, \tag{A.15}$$

where h is the Planck constant, ν the frequency of the photon and ϕ is the *work function* of the material, which is related to the binding energy of the electrons. The cross section of this process is strongly related to the atomic orbital structure, being its probability larger for photon energies close to the binding energy of the electrons. The cross section also shows a dependency on the atomic number of the material, being $\sigma \propto Z^4$ for low energy photons and $\sigma \propto Z^5$ for high energy photons.

A.7.2   Compton Scattering

Compton scattering describes the scattering process of photons by electrons. During this process, part of the energy of the photon is transferred to the atomic electron, which can escape the atom and further interact with the medium. The maximum energy transferred allowed is:

$$T_{max} = h\nu - \frac{h\nu}{1 + 2\frac{h\nu}{m_e c^2}}, \tag{A.16}$$

which is commonly called the Compton edge. The cross section of Compton scattering is proportional to the Z of the material, $\sigma \propto Z$.

A.7.3   Thomson and Rayleigh Scattering

Thomson scattering refers to the elastic scattering of a photon by an electron. It can be seen as the classical, low energy limit, of Compton scattering, where no energy is transferred to the electron and the only effect is the deflection of the photon.

Rayleigh scattering, also called *coherent scattering*, describes the elastic scattering of a photon by an atom, which occurs when the wavelength of the photon is larger than the size of the atom. Its cross section shows a dependency with the inverse square of the wavelength $\sigma \propto 1/\lambda^2$. This scattering phenomenon has an important effect on the propagation of light in optical fibres.

A.7.4   Pair Production

When a photon has the required energy, it may create a particle-antiparticle pair in the presence of the electromagnetic field of the nucleus, or of the atomic electrons. The most common type of pair produced is an electron-positron, and the average energy transferred to each particle is:

$$\langle T \rangle = \frac{1}{2}\left(h\nu - 2m_e c^2\right). \tag{A.17}$$

The cross section of this process is large for high energy photons, rapidly decreasing at low energies. It also has a dependency on the square of the atomic number of the material, $\sigma \propto Z^2$.

A.7.5 Total Cross Section and Attenuation Length

The total cross section of photons in matter is calculated by adding the cross section of all the aforementioned reactions. Figure A.7 shows the measured total cross section of silicon and polystyrene for a wide range of photon energies, indicating the contribution from every reaction.
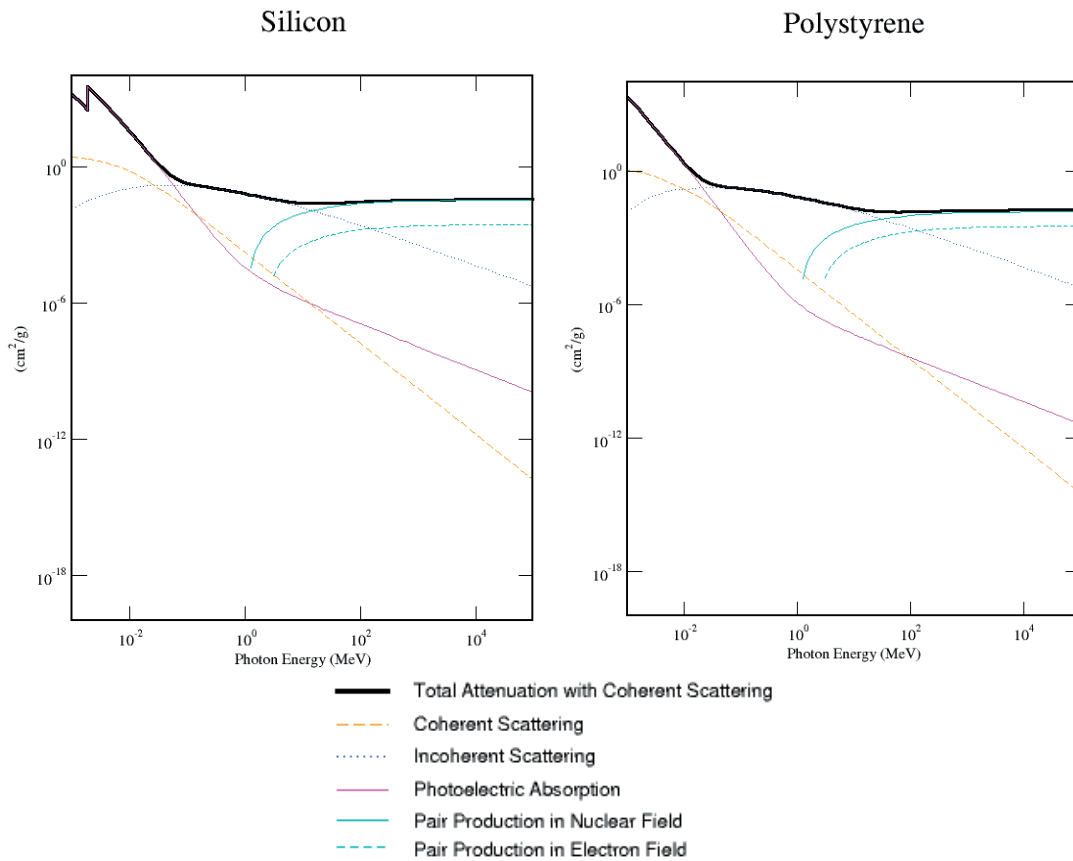
Figure A.7 – Total cross section of photons in silicon and polystyrene (left and right respectively), showing the contribution from each photon process. Compton scattering is called *incoherent scattering*, in contrast to Thomson scattering, also known as *coherent scattering*. Charts from the XCOM database, courtesy of NIST [93].

Beams of photons and beams of charged particles behave very differently with matter. The overall cross section of photons is significantly lower than the cross section of charged particles, meaning that photons undergo far less interactions per unit path length. Another difference is that a beam of photons is always attenuated in intensity,

but not in energy, as opposed to charged particles. The reason is that photons disappear from the beam after an interaction, either by absorption or scattering. Therefore, a beam of photons of initial intensity I_0, after a distance x will have an intensity:

$$I\left(x\right) = I_0 e^{-\frac{x}{\Lambda}}, \tag{A.18}$$

where Λ is called the *attenuation length* of the medium, which is an equivalent of the mean free path, eq. (A.3).

A.8   References

The following bibliography has been the main reference for the elaboration of this chapter: [34], [94], [95], [96], [97], [98], [99], [100], [92] and [93].

Appendix B

Geant4 Simulations

A Geant4 simulation of a scintillating fibre is presented. It covers all the physical phenomena, from the energy deposition of the particle, to the scintillation and light propagation inside the fibre. A second simulation of a full SciFi monitor that investigates the impact of the monitor on the beam is also described. The results of both simulations are not presented in this annex, but employed when it is necessary in other sections of this manuscript.

B.1   Geant4

Geant4 is a software toolkit for the simulation of the interaction of particles with matter based on Monte Carlo methods [101] [102]. It is the reference simulation software in high-energy physics, although its areas of application also include medicine, space radiation physics, microelectronics design, solid-state physics, accelerator physics, and nuclear physics, among others. It is developed and maintained by a large worldwide collaboration of physicists and software engineers; the numerous physics models contained in Geant4 are updated and verified with experimental measurements by many contributing sources. Thus, Geant4 acts also as a repository of the present knowledge about the interaction of radiation with matter. The source code is written in C++, it is object-oriented, and is freely available under the Geant4 copyright.

A simulation typically requires from the user:

  - Definition of the geometry and the main components.

- Description of the employed materials.

- Selection of the physical processes and particles involved.

- Selection of the physical quantities to be measured and recorded.

- Generation of the primary events that begin the simulation.

Almost every aspect and variable of the simulation process are accessible, from the track of every individual particle, to the generation of secondary particles, or the response of sensitive detector components. Therefore, the possibilities of customisation are very high, although at the expense of a very steep learning curve.

B.1.1 Scintillating Fibre Simulations

Two simulations have been done for the fibre monitor:

- A single scintillating fibre coupled to a SiPM on one end and a mirror on the other end (fig. B.1). This simulation covers the energy deposition, the scintillation, and all the optical phenomena that transport light up to the SiPM.

- An array of fibres that interacts with a particle beam of Gaussian shape (fig. B.2). This simulation studies the beam scattering processes and the production of secondary particles. Optical processes are not taken into account to save computation time.

B.2 Individual Fibre

The simulated fibre is the modelling of a fibre from the prototype: it has a core, cladding (or claddings), a mirror coupled on one end, and a SiPM on the other. Its geometric properties, length, thickness, and shape (round or square), can be easily varied.

The following physical properties of the fibre are specified:

- Material composition of core and claddings, from which Geant4 obtains the density and other physical properties.

- Refractive index of core and cladding as a function of the light wavelength.

- Attenuation length spectra of core and cladding.

- Scintillation light spectra.
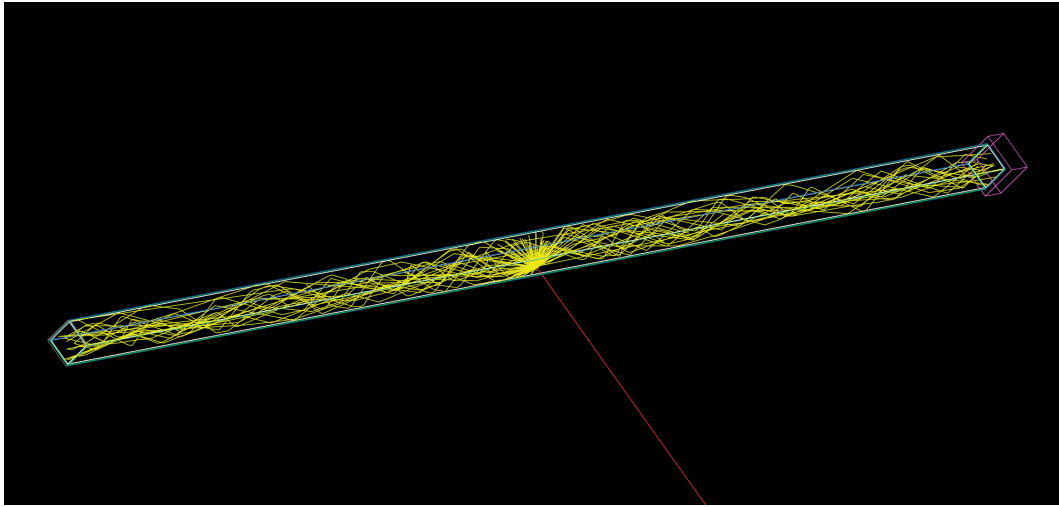
Figure B.1 – Simulation of a scintillating fibre BCF-12 MC, identical to those of the SciFi prototype, interacting with an 80 keV electron (in red); the mirror is coloured in grey (left end) and the SiPM in magenta (right end). The photons (in yellow) are generated at the interaction point and travel by total internal reflection inside the fibre. The photons escaping the fibre are not shown for clarity.
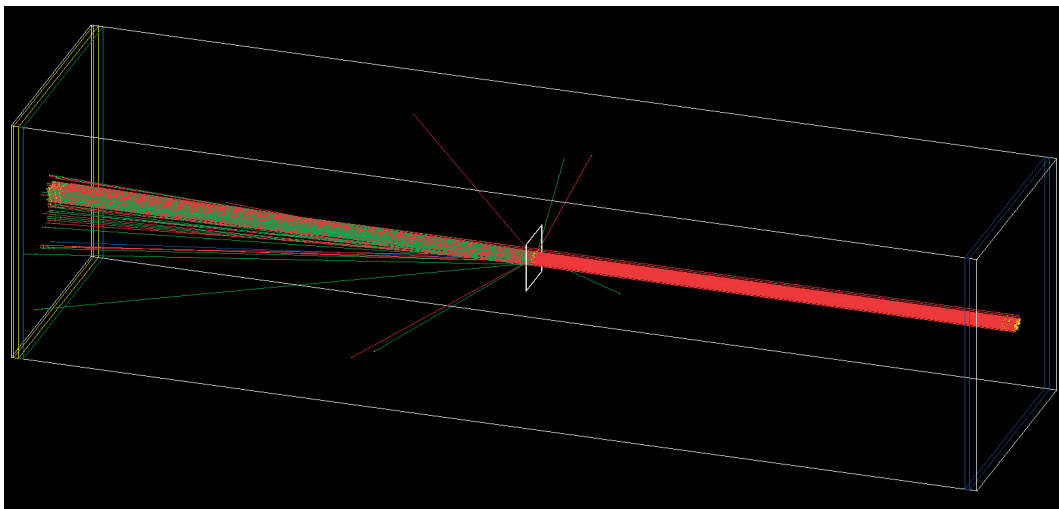
Figure B.2 – Simulation of a SciFi monitor (white tile in the middle), interacting with a Gaussian beam of 0.5 MeV electrons (red). The beam blown-up and the creation of secondary particles (tracks of different colours) can be appreciated.

- Scintillation yield and its resolution.

- Scintillation decay times, fast and slow, and its relative strength.

- Birk's constant.

- Rayleigh scattering interaction length (described in appendix A.7.3).

- Polishing degree of the surfaces.

- Quality of the adherence of core and cladding (and internal cladding-outer cladding for multi-clad fibres).

For the mirror, its material material composition and reflectivity are also defined. Regarding the SiPM, the window geometry of a Hamamatsu S13361 is recreated with the proper refractive index and reflectivity. Its photo detection efficiency as a function of the wavelength is also specified in the simulation.

Due to its versatility, the simulation can describe both Kuraray SCSF-78 and Saint-Gobain BCF-12 fibres. Most of their properties are obtained from the manufacturers and the scientific literature, but others had to be adjusted with the feedback from the laboratory measurements described in appendix C.3. Some of the latter are: the fluctuations of the scintillation yield (resolution), the Rayleigh scattering, the reflectivity of the mirror, the degree of polishing, the degree of imperfection in the contact between surfaces, and the PDE of the SiPM.

The physics models used in the simulation are based on a Geant4 modular list that includes all the common electromagnetic processes, interactions of hadrons (FTFP BERT model), and optical physics. More information can be found in [103].

Every aspect of the simulation can be potentially measured. However, this simulation only registers the "hit information" (time, position and energy) of the interactions at the fibre, cladding, and SiPM. The data is recorded in ROOT NTuples [76], from which several interesting plots can be generated:

- Number of photons detected by the SiPM.

- Time of arrival of photons to the SiPM.

- Wavelength spectra of photons detected by the SiPM.

- 2D map of the hits in the SiPM (fig. B.3).

- Energy deposited in the fibre by the incident particle.

- Distance travelled inside the fibre by the incident particle.

- Number of photons escaping the fibre.

- Energy deposited in the cladding by the incident particle.
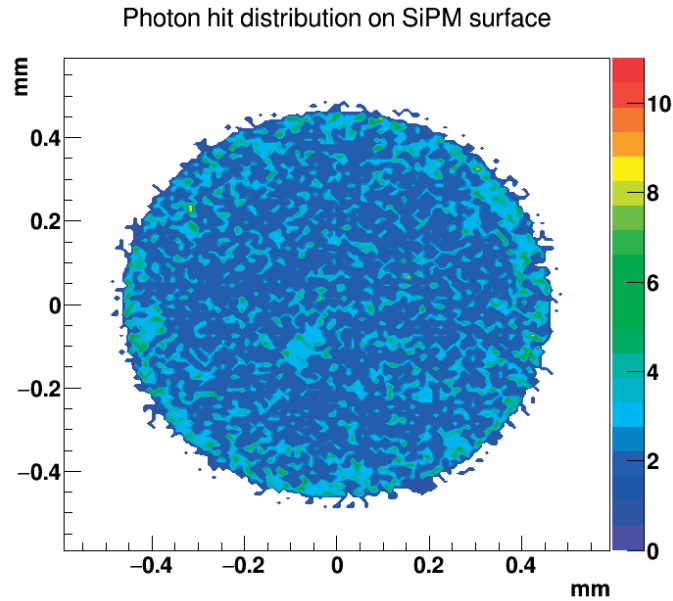
Figure B.3 – Hit distribution on a SiPM of photons generated in a round fibre of 0.5 mm diameter.

B.3   Fibre Array

This second simulation recreates a beam monitor with hundred fibres, although instead of modelling them one by one, it uses a scintillator tile of $100\,\mathrm{mm} \times 100\,\mathrm{mm} \times 1\,\mathrm{mm}$ for simplicity. Such simplification does not affect its precision, since the objective of this simulation is to measure the effect of the monitor on a particle beam.

The physics list is the same as for the individual fibre, with the exception that the optical photons have been deactivated to save computing time.

In order to study the scattering and the creation of secondaries, the tracks of the particles are measured at four points: $0.5\,\mathrm{m}$ before the monitor, at the monitor, and $0.5\,\mathrm{m}$ and $1\,\mathrm{m}$ after it. The beams shot to the monitor have Gaussian shape, are monoenergetic, and they contain only one type of particle.

Appendix C

Small Fibre Setups

Several small setups of fibres coupled to SiPM were built as an exercise to learn the procedure of building a scintillating fibre detector and detecting particles with it. A measurement of the light yield of different type of fibres was carried with these small setups, which helped to choose a model of fibre for the first prototype and also to tune the Geant4 simulations. The process of analysing the distribution of light collected by a fibre-SiPM setup is described in detail.

C.1   Small Fibre Setups

Each unit consists in a plastic mechanical structure that holds a fibre and precisely aligns a SiPM for its read-out (fig. C.1 and fig. C.2). The plastic structures have a hole pierced on them, in which the fibres are inserted, glued, and polished to guarantee a good optical coupling with the SiPM. Two types of square section fibres were employed: Saint-Gobain BCF-12, multi-clad, 1 mm thickness; and Kuraray SCSF-78, single-clad, 0.5 mm thickness. Regarding the SiPM, three models from different brands could be coupled to the fibres: Hamamatsu S13360-1350, Ketek PM1150NS and SensL MicroFC-SMTPA-10050.

C.2   Light Yield Measurements

The small experimental setups served to measure the light yield of the fibres. For that purpose, the fibres were excited approximately at their centre with 1 MeV electrons

Figure C.1 – Small experimental setups built to study scintillating fibres.
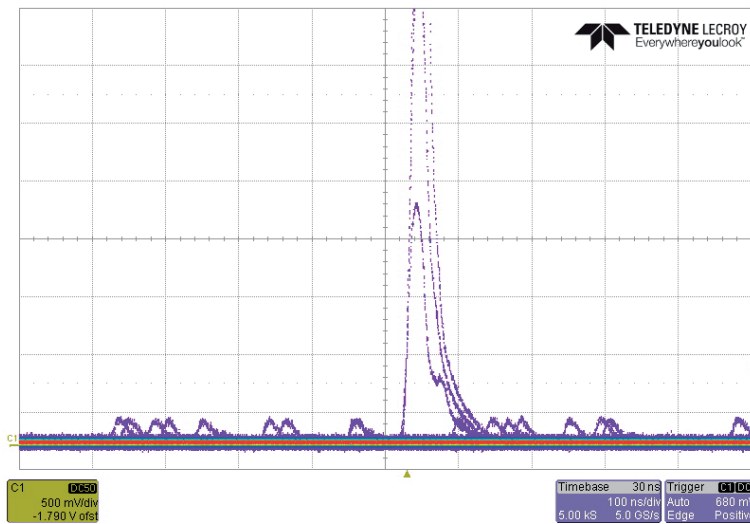
Figure C.2 – Persistence image of a LeCroy WaveRunner $1\,\mathrm{GHz}$ oscilloscope showing cosmic rays detected with a small fibre setup (large signals). The small signals correspond to one-photoelectron dark counts of the SiPM.

generated by a $^{90}\mathrm{Sr}$ electron monochromator [91]. These particles are convenient for a light yield characterisation, since their energy deposition is identical to that of the MIPs of the secondary beams.

Two different setups of fibres were employed: a BCF-12 fibre of $1\,\mathrm{mm}$ thickness and $24\,\mathrm{cm}$ long, and a SCSF-78 of $0.5\,\mathrm{mm}$ and $13\,\mathrm{cm}$ long. A mirror was glued on one end of the fibres to increase the total light collection at the SiPM side; that mirror could be easily removed to allow the measurement of light yield with and without mirror.

The light from the fibres was detected with a Hamamatsu S13360-1350, operated at the recommended operating voltage and corrected for temperature effects. The charge from the SiPM was integrated by a VATA64 ASIC.

The histograms with the collected charge from the SiPM (which is proportional to the number of photons), are shown in fig. C.3 and fig. C.4.
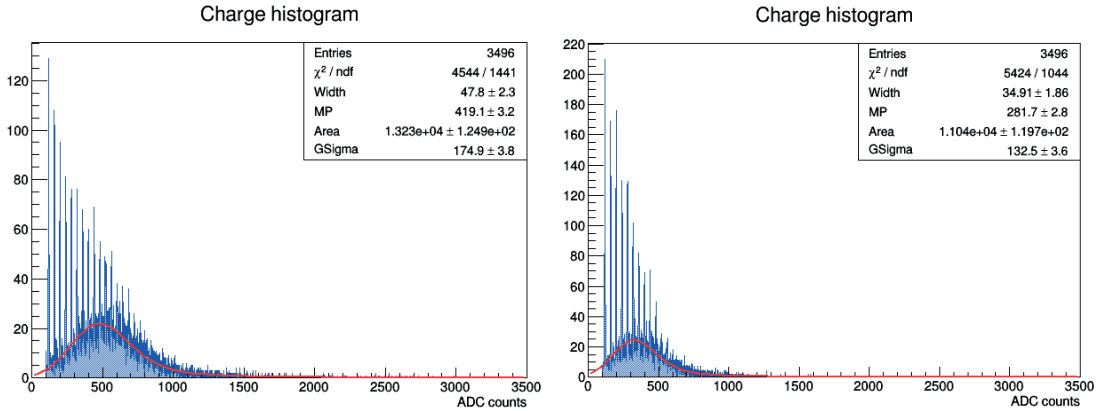
Figure C.3 – Charge histograms for the SCSF-78, square, 0.5 mm, 13 cm length, with mirror on one end (left) and without mirror (right).
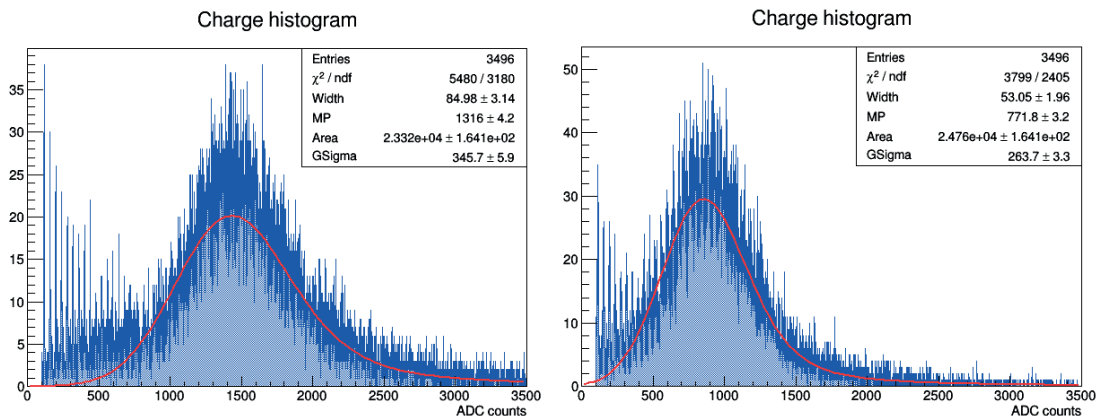
Figure C.4 – Charge histograms for the BCF-12, square, multi-clad, 1 mm, 24 cm length, with mirror on one end (left) and without mirror (right).

C.3   Detected Light Distribution

The charge histograms in fig. C.3 and fig. C.4 contain all the information about the number of photons detected. In fact, due to the discrete nature of SiPM, the individual photopeaks can be distinguished as sharp lines in the histograms. The effect is more evident in the lowest part of the histogram, since for larger signals the energy resolution is degraded, due to gain fluctuations, and the photopeaks are no longer distinguishable [104] (hence, from a certain number of photons, the distribution looks continuous rather than discrete). The possibility of distinguishing individual photons serves to calibrate the x-axis (ADC counts) with the number of detected photons.

The amount of primary scintillation photons created is proportional to the energy deposited by the particle in the fibre, which is well described by a Landau distribution (more on the energy deposition of particles in appendix A.5). Therefore, the light detected by the SiPM could be expected to be Landau distributed as well. However, light undergoes several phenomena in a fibre before being detected:

- Absorption and conversion of the primary photons.

- Absorption or scattering within the fibre.

- Reflections or refractions in the boundary fibre-SiPM.

- Creation of a signal in the SiPM.

All the aforementioned processes are stochastic and their fluctuations are Gaussian distributed [105]. Therefore, it can be shown that the distribution that fits better the charge histograms (fig. C.3 and fig. C.4) is, in fact, a Landau convoluted with a Gaussian,

$$[Landau * Gauss](t) = \int_{-\infty}^{\infty} L(\tau) G(t - \tau) d\tau. \tag{C.1}$$

Such convolution is characterised by the Most Probable Value (MPV) of the Landau, which gives the most probable number of detected photons, and the sigma (σ) of the convoluted Gaussian, which gives the spread of the latter. The best fit of fig. C.3 and fig. C.4 is shown as a red line superposed to the histograms; the statistical information of the fitted variables is also shown in a legend. Table C.1 summarises the findings of the light yield measurement.

Table C.1 – Light yield of SCSF-78 and BCF-12 fibres measured with the small fibre setups.

Fibre type	Thickness (mm)	Length (cm)	Mirror on one end	*MPV* (photons)	*Sigma* (photons)
SCSF-78	0.5	13	yes	10.5	4.4
SCSF-78	0.5	13	no	7.1	3.3
BCF-12 MC	1	24	yes	32.9	8.6
BCF-12 MC	1	24	no	19.3	6.5

The 1 mm fibres generate a significantly larger amount of light, which cannot be only explained by the larger energy deposition in a thicker fibre. In fact, the double cladding has an effect of increasing the light collection by $\sim 60\%$, in comparison with a single cladding. The impact of the mirror is an increase of 70% in the light collection for the 1 mm fibre and $\sim 48\%$ for the 0.5 mm one.

Appendix D

Impact of the SciFi Prototype on a Particle Beam

This annex studies the impact of a scintillating fibre monitor on a particle beam. In the first part, the material budget of the MWPC, the DWC, and the SciFi monitor are calculated and compared between them. Then, in the second part, a Geant4 simulation of the SciFi monitor is employed to quantify the beam scattering, the production of secondary particles, and the energy loss of the beam.

D.1   Calculation of Material Budget

The radiation thickness has been calculated analytically using eq. (A.14). The material budget of every detector is itemised in Table D.1, Table D.2, Table D.3, and Table D.4. All the material properties have been obtained from *The Review of Particle Physics* [94].

The MWPC and the DWC are not directly connected to the beam pipe; they are placed in open segments of the line, which requires the use of windows to keep the vacuum. These windows, made of Mylar, and the section of open air are also added to the material budget.

The results are summarised in Table D.6. Furthermore, the material budget of a SciFi monitor of 0.5 mm fibres, placed in air, is also calculated in Table D.5. The increase due to the vacuum windows and air is about 0.19%.

Table D.1 – Material budget of a MWPC.

Material	X_0 (g/cm^2)	ρ (g/cm^3)	Thickness (mm)	x/X_0 (%)
Mylar [1]	39.95	1.39	0.39	0.136
Air	36.66	$1.29 \cdot 10^{-3}$	200	0.070
Gas [2]	25.79	$1.88 \cdot 10^{-3}$	40	0.029
Aluminium [3]	24.01	2.7	0.08	0.090
Tungsten [4]	6.76	19.25		0.036
TOTAL				**0.36**

[1] Detector windows (25 μm) and beam pipe windows (170 μm).
[2] CO_2 + Ar (50%/50%).
[3] Four Al cathode foils of 20 μm.
[4] Two anode planes, each with 100 tungsten wires of 20 μm diameter.

Table D.2 – Material budget of a DWC.

Material	X_0 (g/cm^2)	ρ (g/cm^3)	Thickness (mm)	x/X_0 (%)
Mylar [1]	39.95	1.39	0.34	0.118
Kapton [2]	40.56	1.42	0.05	0.018
Air	36.66	$1.29 \cdot 10^{-3}$	200	0.070
Gas [3]	25.79	$1.88 \cdot 10^{-3}$	40	0.029
Beryllium [4]	65.19	1.85		0.020
Tungsten [5]	6.76	19.25		0.020
TOTAL				**0.28**

[1] Beam pipe windows (170 μm).
[2] Detector windows (25 μm).
[3] CO_2 + Ar (50%/50%).
[4] Four cathode planes, each with 55 beryllium wires of 100 μm diameter.
[5] Two anode planes, each with 28 tungsten wires of 20 μm diameter.

Table D.3 – Material budget of a two-plane 0.5 mm square fibre detector (for the horizontal and vertical reconstruction of the profile), placed in vacuum.

Material	X_0 (g/cm^2)	ρ (g/cm^3)	Thickness (mm)	x/X_0 (%)
Polystyrene	43.72	1.03	1	0.24
TOTAL				**0.24**

D.2 Geant4 Simulations

The Geant4 simulation described in appendix B.3 recreates the effect of the fibre monitor on the beam scattering, the energy loss, and the production of secondary particles. The simulated beams consist on 1,000 particles randomly distributed inside a Gaussian

Table D.4 – Material budget of a two-plane 1 mm square fibre detector (for the horizontal and vertical reconstruction of the profile), placed in vacuum.

Material	X_0 (g/cm^2)	ρ (g/cm^3)	Thickness (mm)	x/X_0 (%)
Polystyrene	43.72	1.03	2	0.48
TOTAL				**0.48**

Table D.5 – Material budget of a two-plane 0.5 mm square fibre detector (for the horizontal and vertical reconstruction of the profile), placed in air.

Material	X_0 (g/cm^2)	ρ (g/cm^3)	Thickness (mm)	x/X_0 (%)
Polystyrene	43.72	1.03	1	0.24
Mylar [1]	39.95	1.39	0.34	0.118
Air	36.66	$1.29 \cdot 10^{-3}$	200	0.070
TOTAL				**0.43**

Table D.6 – Comparison of the material budget of the different detectors.

Detector	x/X_0 (%)
MWPC	0.36
DWC	0.28
SciFi 0.5 mm	0.24
SciFi 1 mm	0.48
SciFi 0.5 mm air	0.43

envelope with $\sigma_{horizontal} = 1$ cm and $\sigma_{vertical} = 0.5$ cm. The beam profile is measured before and 1 m after the interaction by a set of transparent detectors that register the passage of every individual particle.

The simulation has been run for three types of particles: electrons, protons, and $^{+82}$Pb^{208} ions; and three momenta: 1 GeV/c, 10 GeV/c, and 100 GeV/c. This selection is representative of the EA beams: electrons, because due to their small mass produce more Bremsstrahlung radiation and suffer more scattering, particularly at low energies; protons, which behave like MIPs at those momenta (further information MIP in appendix A.3), similarly to pions and kaons; lead ions, whose behaviour is significantly different, since these heavy particles interact strongly with matter.

D.2.1 Beam scattering

The calculated scattering for electrons (fig. D.1, fig. D.2, fig. D.3 and fig. D.4) is presented in Table D.7, which shows some beam blow-up at very low momenta, although it practically vanishes above $10\,\mathrm{GeV/c}$. The $0.5\,\mathrm{GeV/c}$ momentum has been added, since it is the lowest achieved by the new low energy beams of EHN1.

Table D.7 – Scattering of electron beams of different momenta by a SciFi monitor of $1\,\mathrm{mm}$ thickness.

P (GeV/c)	σ_x (mrad)	σ_y (mrad)
0.5	4.26	5.25
1	3.51	2.69
10	0.11	0.38
100	0.03	0.01

Protons (fig. D.5, fig. D.6 and fig. D.7) suffer less scattering than electrons at very low energies, becoming statically negligible above $10\,\mathrm{GeV}$: Table D.8.

Table D.8 – Scattering of proton beams of different momenta by a SciFi monitor of $1\,\mathrm{mm}$ thickness.

P (GeV/c/Z)	σ_x (mrad)	σ_y (mrad)
1	1.24	2.55
10	-0.02	0.03
100	0.01	-0.01

Heavy lead ions (fig. D.8 and fig. D.9) show no significant scattering: Table D.9.

Table D.9 – Scattering of $^{+82}\mathrm{Pb}^{208}$ beams of different momenta by a SciFi monitor of $1\,\mathrm{mm}$ thickness.

P (GeV/c)	σ_x (mrad)	σ_y (mrad)
10	0.03	0
100	-0.06	-0.02

D.2.2 Secondary production

Charged and neutral particles can be produced from the interaction of the beam with the material from the detector. In this discussion, Bremsstrahlung gamma photons are also considered secondary particles.

The findings about secondary production for electron beams (fig. D.10, fig. D.11, fig. D.12 and fig. D.13) is summarised in Table D.10. Bremsstrahlung gammas are the most abundant, with an energy spectrum that peaks at some MeV and spreads up to the energy of the electron beam (thus indicating that some gammas can carry almost the totality of energy of the electron, although it is less probable).

Table D.10 – Production of secondary particles by a SciFi monitor of 1 mm thickness, for electron beams of different momenta.

P (GeV/c)	Type of secondary	Relative production[a]
0.5	γ	1.7
	$e^{\pm}$	0.01
1	γ	1.8
	$e^{\pm}$	0.02
10	γ	1.9
	$e^{\pm}$	0.06
100	γ	1.6
	$e^{\pm}$	0.1

[a] Number of secondary particles produced per incident electron.

The production of secondaries for protons is rare at low energies, increasing slowly at momenta higher than 100 GeV/c (fig. D.14, fig. D.15 and fig. D.16). The results are summarised in Table D.11.

Table D.11 – Production of secondary particles by a SciFi monitor of 1 mm thickness, for proton beams of different momenta.

P (GeV/c)	Type of secondary	Relative production[a]
1	γ, e^{-}, n	10^{-3}
10	γ, e^{-}, n	10^{-3}
100	γ	0.1
	$\pi^{\pm}$,	0.05
	n, e^{-}	0.01

[a] Number of secondary particles produced per incident proton.

Heavy lead ions produce a large amount of secondaries (fig. D.18 and fig. D.19) of very diverse energy. The most abundant are presented in Table D.12.

Table D.12 – Production of secondary particles by a SciFi monitor of 1 mm thickness, for Pb-ion beams of different momenta.

P (GeV/c)	Type of secondaries	Relative production[a]
10	γ, e^-	20
	p, n, $\pi\pm$	1
	e^+	0.05
100	γ, e^-	30
	p, n, $\pi\pm$	2
	e^+	0.3

[a] Number of secondary particles produced per incident Pb-ion.

D.2.3   Beam Energy Loss

The simulation also provides the energy of the beam after its passage through the detector. It can be seen that the energy loss for electron beams is high, particularly due to the emission of high-energy Bremsstrahlung gammas, which in some cases can carry almost the full energy of the electron (fig. D.10, fig. D.11, fig. D.12 and fig. D.13).

The energy loss for protons (fig. D.14, fig. D.15 and fig. D.16) is only relevant at low energies, although it just represents $\sim 0.1\%$ of the energy of the particle.

The losses of Pb-ions are not significant relative to their extreme energies in the TeV scale (fig. D.17).

D.2.4   Figures
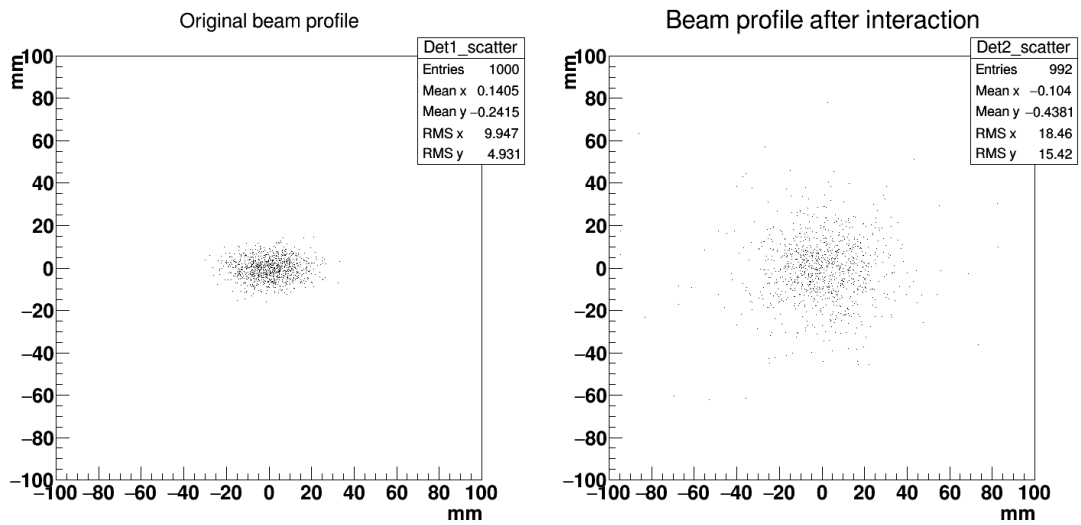
Figure D.1 – Profile of a beam composed of 1,000 electrons of 0.5 GeV/c before interacting with the fibre plane (left) and 1 m after the interaction (right).
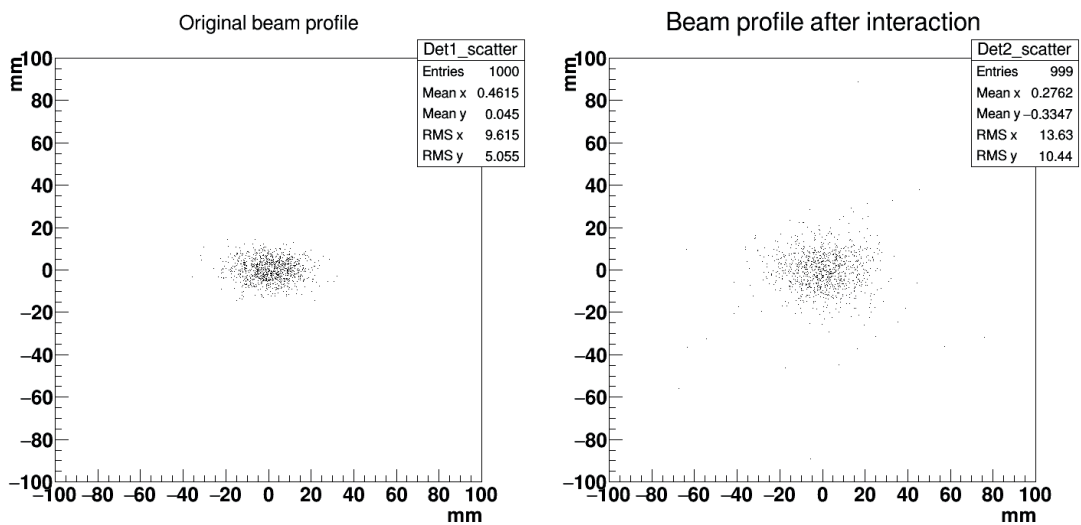
Figure D.2 – Profile of a beam composed of 1,000 electrons of 1 GeV/c before interacting with the fibre plane (left) and 1 m after the interaction (right).
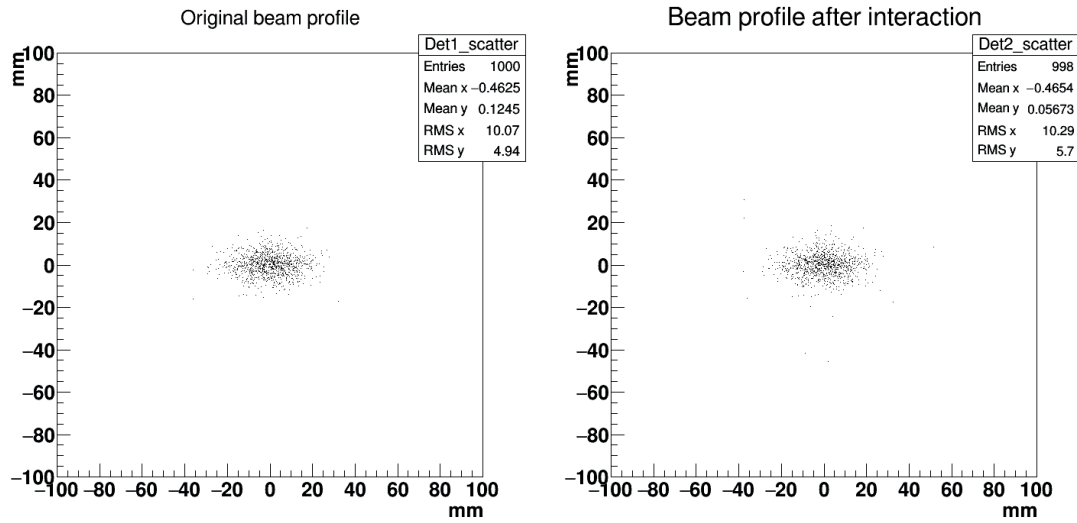
Figure D.3 – Profile of a beam composed of 1,000 electrons of $10\,\mathrm{GeV/c}$ before interacting with the fibre plane (left) and $1\,\mathrm{m}$ after the interaction (right).
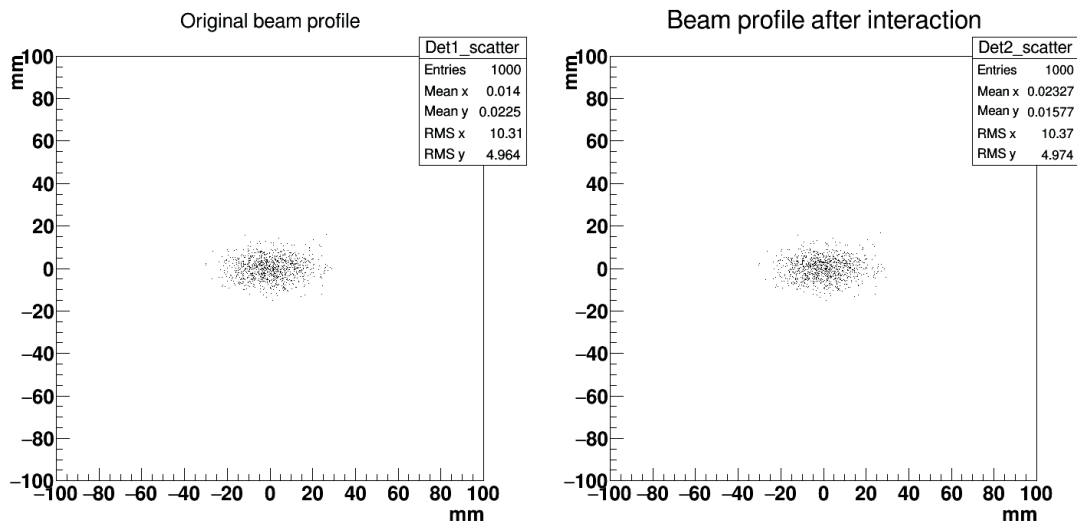
Figure D.4 – Profile of a beam composed of 1,000 electrons of $100\,\mathrm{GeV/c}$ before interacting with the fibre plane (left) and $1\,\mathrm{m}$ after the interaction (right).
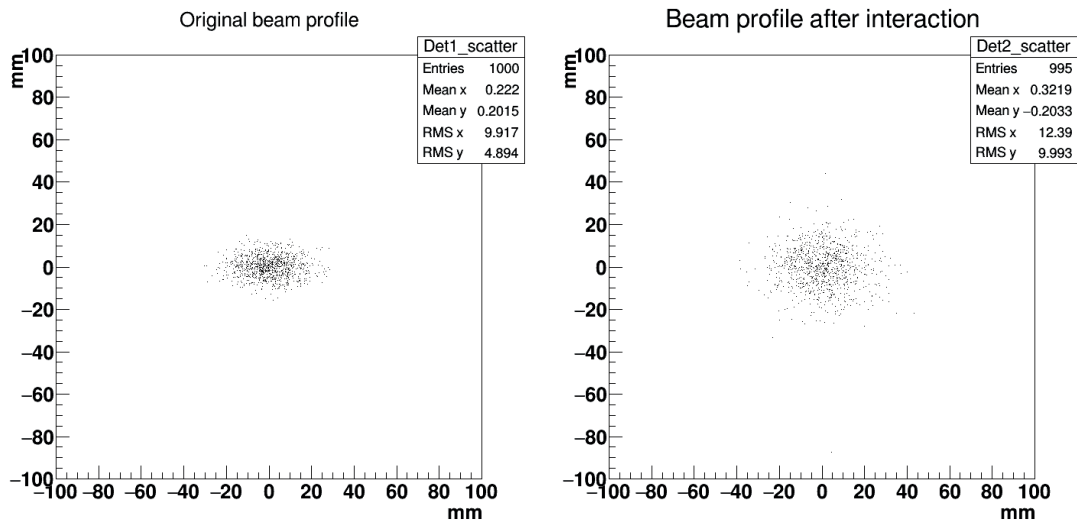
Figure D.5 – Profile of a beam composed of 1,000 protons of $1\,\mathrm{GeV/c}$ before interacting with the fibre plane (left) and $1\,\mathrm{m}$ after the interaction (right).
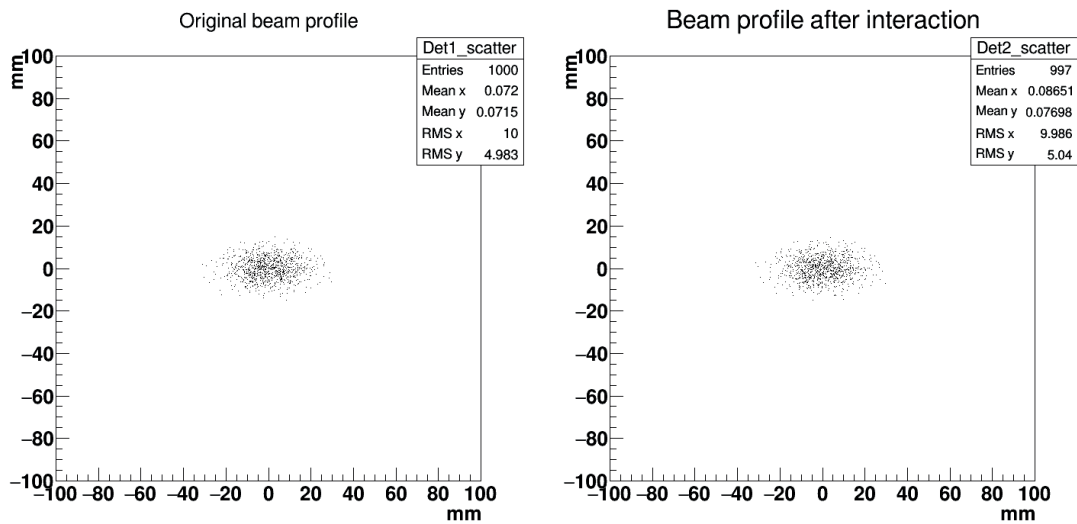
Figure D.6 – Profile of a beam composed of 1,000 protons of $10\,\mathrm{GeV/c}$ before interacting with the fibre plane (left) and $1\,\mathrm{m}$ after the interaction (right).
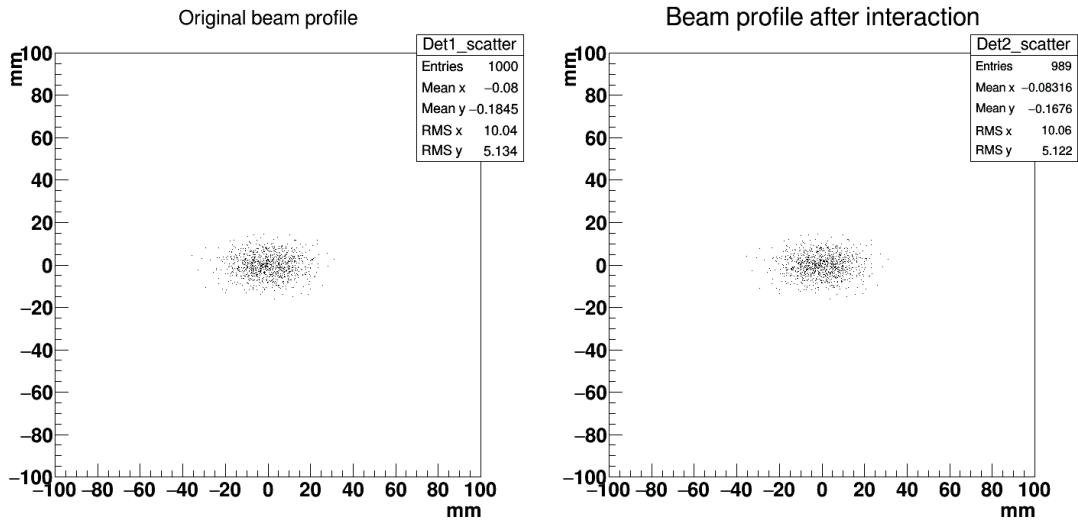
Figure D.7 – Profile of a beam composed of 1,000 protons of 100 GeV/c before interacting with the fibre plane (left) and 1 m after the interaction (right).
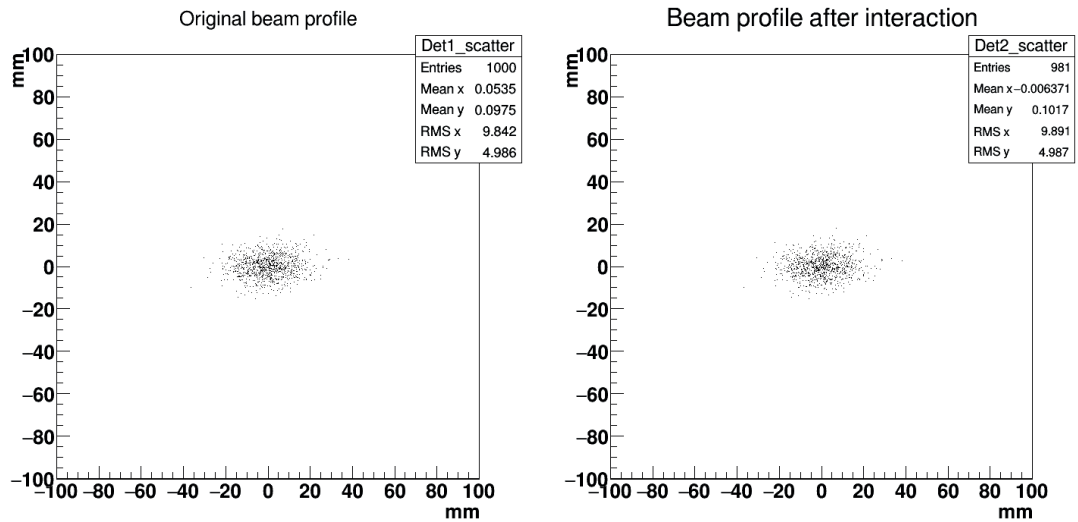
Figure D.8 – Profile of a beam composed of 1,000 Pb-ions of 10 GeV/c/Z before interacting with the fibre plane (left) and 1 m after the interaction (right).
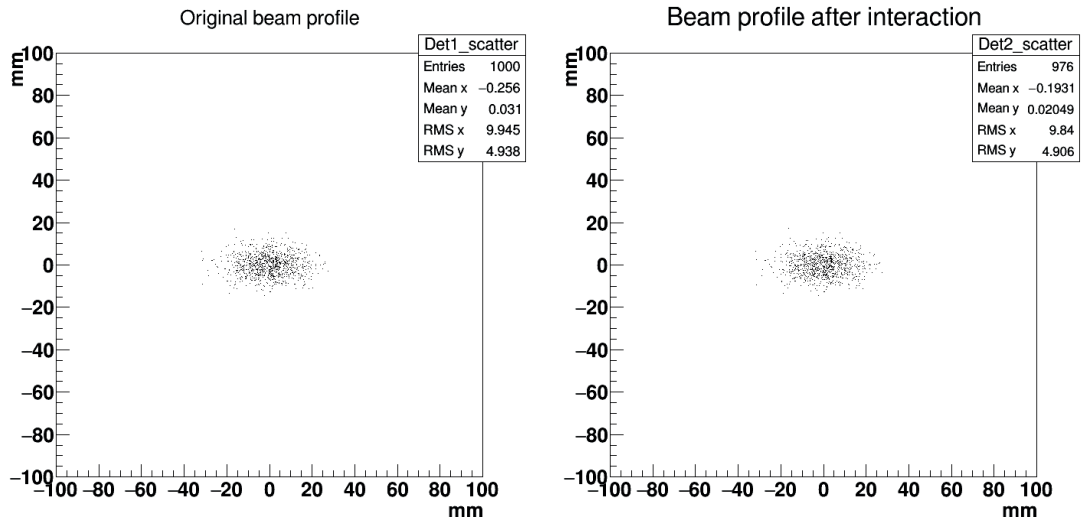
Figure D.9 – Profile of a beam composed of 1,000 Pb-ions of 100 GeV/c/Z before interacting with the fibre plane (left) and 1 m after the interaction (right).
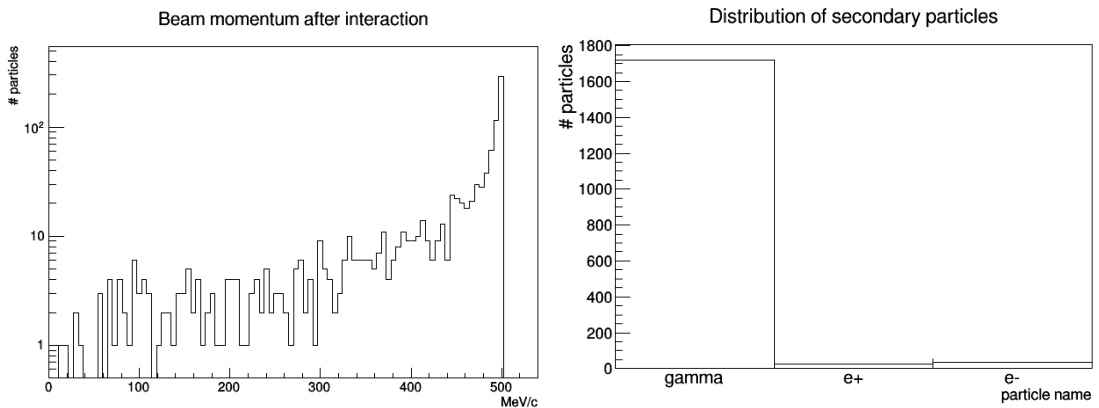
Figure D.10 – Energy distribution of a beam of 1,000 electrons of 0.5 GeV/c after crossing the monitor (left), and distribution of secondary particles created (right).
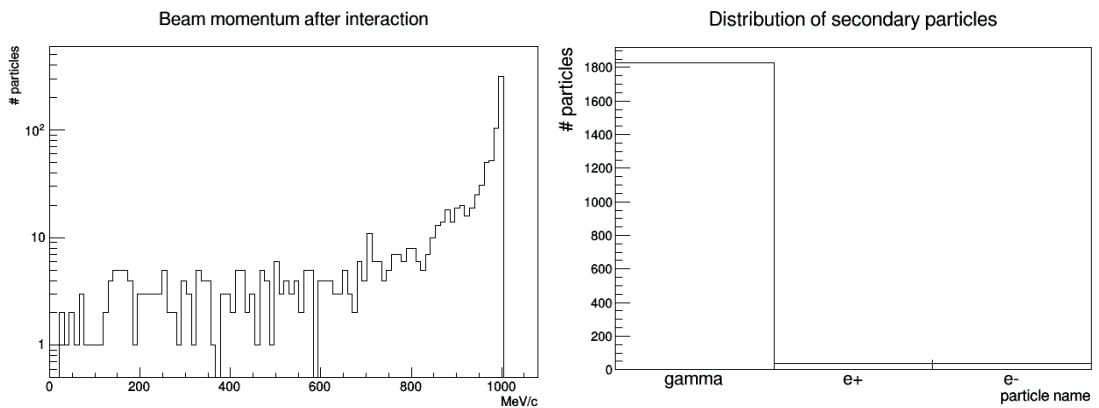
Figure D.11 – Energy distribution of a beam of 1,000 electrons of 1 GeV/c after crossing the monitor (left), and distribution of secondary particles created (right).

173
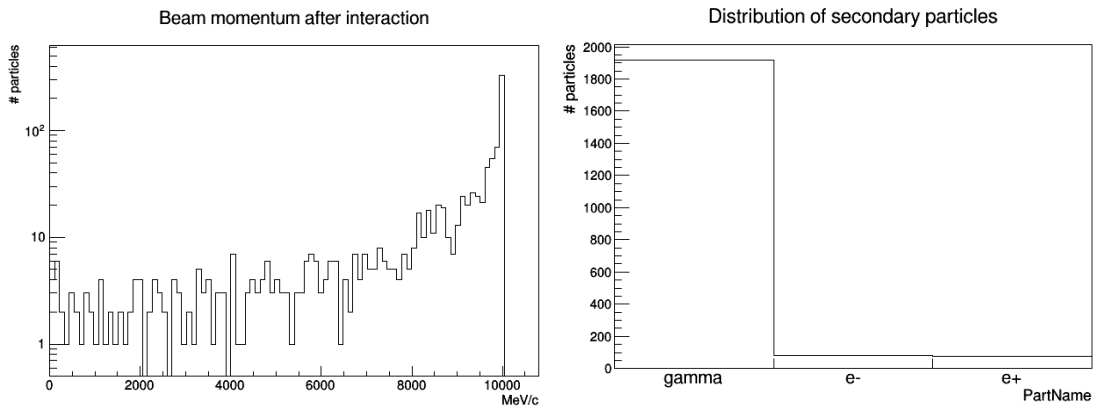
Figure D.12 – Energy distribution of a beam of 1,000 electrons of 10 GeV/c after crossing the monitor (left), and distribution of secondary particles created (right).
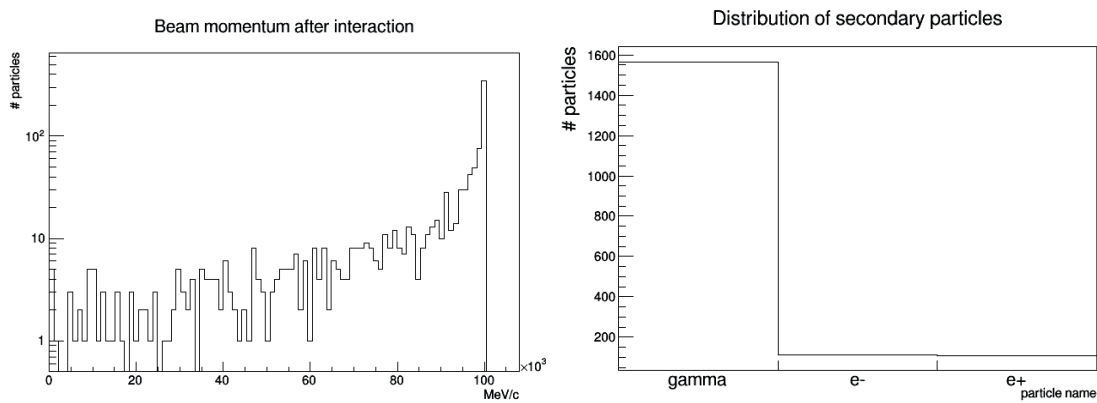
Figure D.13 – Energy distribution of a beam of 1,000 electrons of 100 GeV/c after crossing the monitor (left), and distribution of secondary particles created (right).
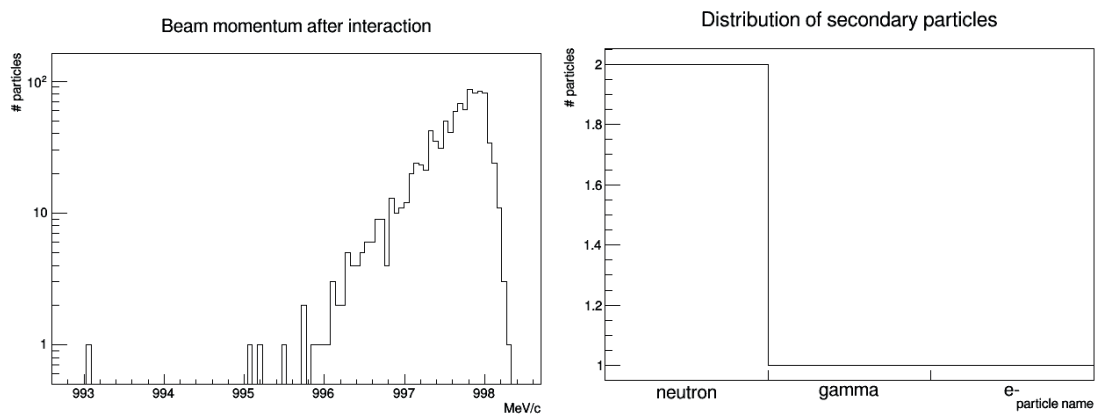
Figure D.14 – Energy distribution of a beam of 1,000 protons of 1 GeV/c after crossing the monitor (left), and distribution of secondary particles created (right).
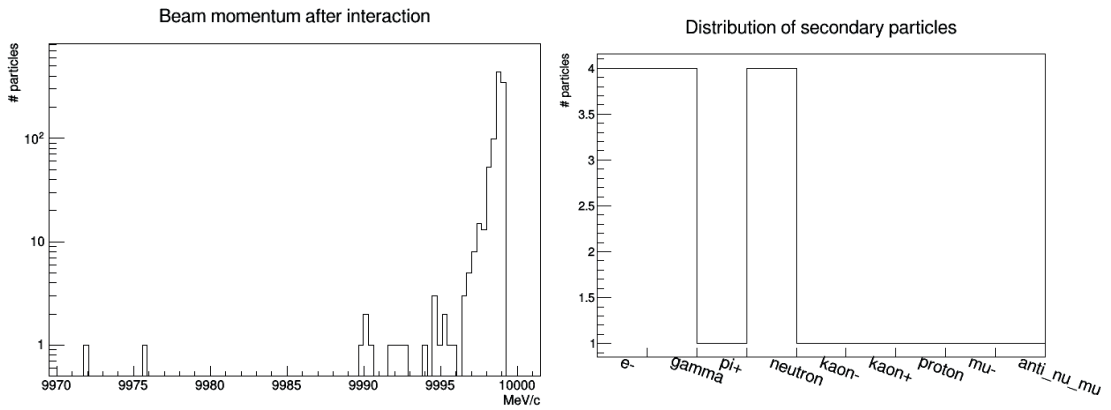
Figure D.15 – Energy distribution of a beam of 1,000 protons of 10 GeV/c after crossing the monitor (left), and distribution of secondary particles created (right).
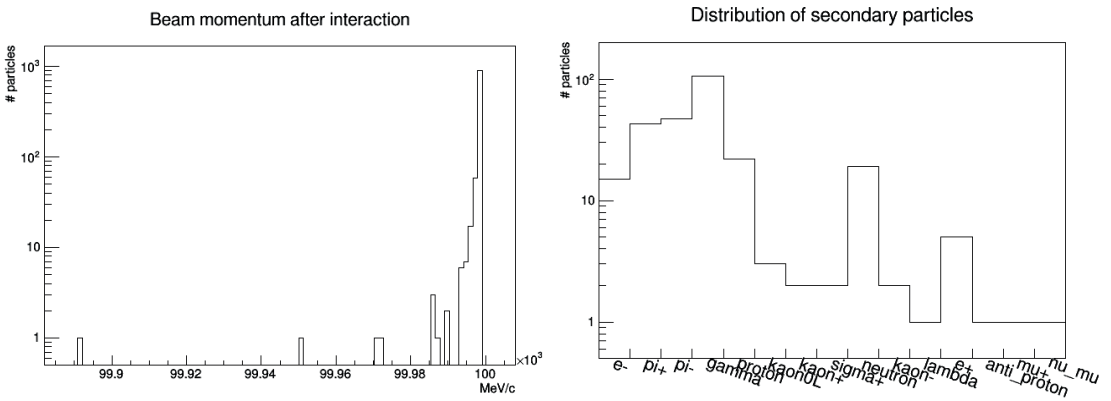
Figure D.16 – Energy distribution of a beam of 1,000 protons of 100 GeV/c after crossing the monitor (left), and distribution of secondary particles created (right).
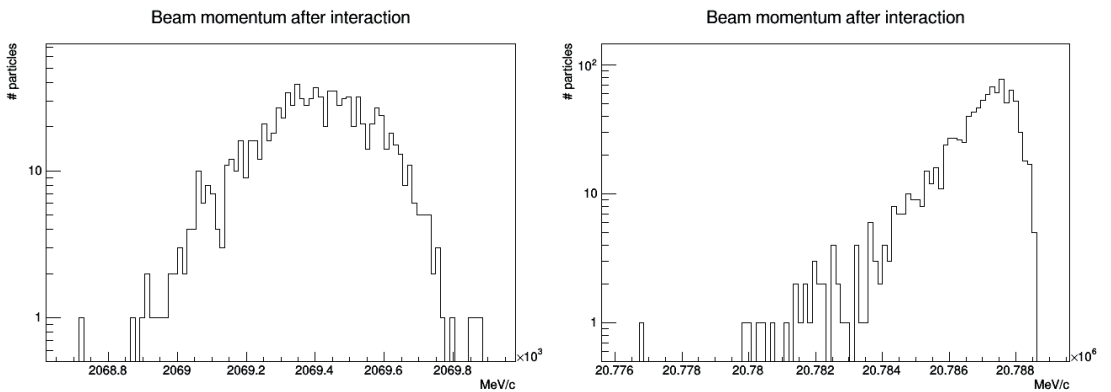
Figure D.17 – Left: energy distribution of a beam of 1,000 Pb-ions of 10 GeV/c/Z after crossing the monitor. Right: energy distribution of a beam of 1,000 Pb-ions of 100 GeV/c/Z after crossing the monitor.
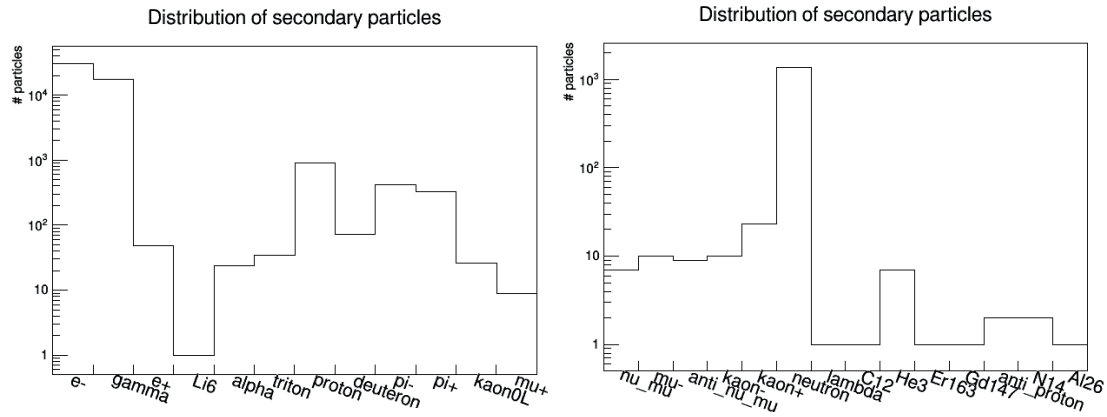
Figure D.18 – Distribution of secondary particles created by a beam of 1,000 Pb-ions of 10 GeV/c/Z after interacting with the monitor.
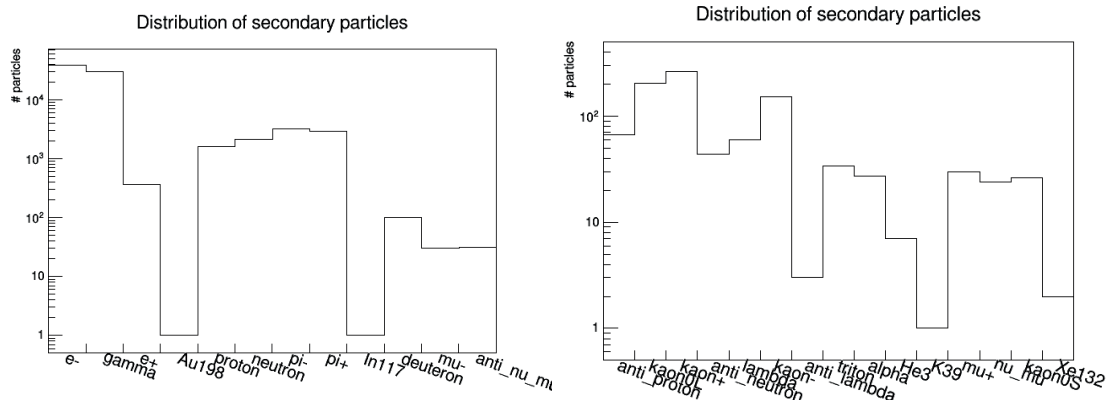
Figure D.19 – Distribution of secondary particles created by a beam of 1,000 Pb-ions of 100 GeV/c/Z after interacting with the monitor.

Bibliography

[1] Secondary beams & areas. URL http://sba.web.cern.ch/sba/. Home Webpage.

[2] The compass experiment. URL http://wwwcompass.cern.ch/. Home Webpage.

[3] Henry W Atherton, G Von Holtey, L Piemontese, Edouard Rossa, Claude Bovet, David E Plane, Alfredo Placci, Niels T Doble, Max Reinharz, and Massimo Placidi. Precise measurements of particle production by 400 gev/c protons on beryllium targets. Technical report, CERN, 1980.

[4] Laura Manenti. Protodunes. *arXiv preprint arXiv:1705.05669*, 2017.

[5] Dune. URL http://www.dunescience.org/. Home webpage.

[6] Georges Charpak, R Bouclier, T Bressani, J Favier, and Č Zupančič. The use of multiwire proportional counters to select and localize charged particles. *Nuclear Instruments and Methods*, 62(3):262–268, 1968.

[7] J Spanggaard. Delay wire chambers-a users guide. Technical report, CERN-SL-Note-98-023-BI, 1998.

[8] Fabio Sauli. The gas electron multiplier (gem): Operating principles and applications. *Nuclear Inst. and Methods in Physics Research, A*, (805):2–24, 2016.

[9] C Altunbas, M Capéans, K Dehmelt, J Ehlers, J Friedrich, I Konorov, A Gandi, S Kappler, B Ketzer, R De Oliveira, et al. Construction, test and commissioning of the triple-gem tracking detector for compass. *Nuclear Instruments and Methods in Physics Research Section A: Accelerators, Spectrometers, Detectors and Associated Equipment*, 490(1):177–203, 2002.

[10] D Thers, Ph Abbon, J Ball, Y Bedfer, C Bernet, C Carasco, E Delagnes, D Durand, J-C Faivre, H Fonvieille, et al. Micromegas as a large microstrip detector for the compass experiment. *Nuclear Instruments and Methods in Physics Research Section A: Accelerators, Spectrometers, Detectors and Associated Equipment*, 469 (2):133–146, 2001.

[11] M Benoit, J Bilbao De Mendizabal, FA Di Bello, D Ferrere, T Golling, S Gonzalez-Sevilla, G Iacobucci, M Kocian, D Muenstermann, B Ristic, et al. The fe-i4

telescope for particle tracking in testbeam experiments. *Journal of Instrumentation*, 11(07):P07003, 2016.

[12] F. Anghinolfi et al. Alfa forward detectors for measurement of elastic scattering and luminosity. Technical report, ATLAS-TDR-18, CERN-LHCC-2008-004, CERN, Geneva., 2008.

[13] Christian Joram, Ulrich Uwer, Thomas Kirn, Blake Dean Leverington, Sebastian Bachmann, Robert Jan Ekelhof, and Janine Müller. Lhcb scintillating fibre tracker engineering design review report: Fibres, mats and modules. Technical report, CERN, 2015.

[14] S. Jakobsen. *Commissioning of the absolute luminosity for ATLAS detector at the LHC*. PhD thesis, The Niels Bohr Institute, Faculty of Science, University of Copenhagen, 2013.

[15] A Gorin, S Horikawa, K-I Kuroda, T Maki, I Manuilov, A Riazantsev, F Takeutchi, T Toeda, and K Okada. Scintillating fiber hodoscopes for dirac and compass experiments. *Czechoslovak journal of physics*, 49(2):173–182, 1999.

[16] S Horikawa, I Daito, N Doshita, A Gorin, T Hasegawa, N Horikawa, T Iwata, K Kondo, K Kuroda, I Manuilov, et al. A scintillating fiber tracker with high time resolution for high-rate experiments. *IEEE Transactions on Nuclear Science*, 49 (3):950–956, 2002.

[17] J Spanggaard, P Carriere, S Duarte Pinto, and G Tranquille. Gem detectors for the transverse profile measurement of low energy antiprotons and high energy hadrons. Technical report, CERN, 2012.

[18] Rainer E Ansorge, C Anrouet, P Bareyre, P Bonamy, CN Booth, M Bouchard, M Bourdinaud, M Cordier, J Crittenden, RS Dewolf, et al. The ua2 scintillating fibre detector. *Nuclear Instruments and Methods in Physics Research Section A: Accelerators, Spectrometers, Detectors and Associated Equipment*, 273(2-3):826–832, 1988.

[19] Patrio Annis, S Aoki, G Brooijmans, J Brunner, J Dupraz, J Dupont, J-P Fabre, D Favart, W Flegel, D Frekers, et al. The chorus scintillating fiber tracker and opto-electronic readout system. *Nuclear Instruments and Methods in Physics Research Section A: Accelerators, Spectrometers, Detectors and Associated Equipment*, 412 (1):19–37, 1998.

[20] D Adams, M Adams, B Baumbaugh, I Bertram, A Bross, D Casey, S Chang, M Chung, C Cooper, C Cretsinger, et al. Performance of a large scale scintillating fiber tracker using vlpc readout. *IEEE transactions on nuclear science*, 42(4): 401–406, 1995.

[21] Niklaus Berger, Mu3e Collaboration, et al. The mu3e experiment. *Nuclear Physics B-Proceedings Supplements*, 248:35–40, 2014.

[22] D Nakajima, B Özel-Tashenov, S Bianchin, O Borodina, V Bozkurt, B Göküzüm, M Kavatsyuk, S Minami, C Rappold, TR Saito, et al. Scintillating fiber detectors for the hyphi project at gsi. *Nuclear Instruments and Methods in Physics Research Section A: Accelerators, Spectrometers, Detectors and Associated Equipment*, 608 (2):287–290, 2009.

[23] Hiroyuki Sako, Tomofumi Maruta, and Akihiko Miura. Measurement of beam loss tracks by scintillating fibers at j-parc linac. *IPAC11, San Sebastian, Spain*, page 1251, 2011.

[24] Anthony Clarkson, David J Hamilton, Matthias Hoek, David G Ireland, JR Johnstone, Ralf Kaiser, Tibor Keri, Scott Lumsden, David F Mahon, Bryan McKinnon, et al. The design and performance of a scintillating-fibre tracker for the cosmic-ray muon tomography of legacy nuclear waste containers. *Nuclear Instruments and Methods in Physics Research Section A: Accelerators, Spectrometers, Detectors and Associated Equipment*, 745:138–149, 2014.

[25] A Fernandez Fernandez, B Brichard, S O'Keeffe, C Fitzpatrick, E Lewis, J-R Vaille, L Dusseau, DA Jackson, F Ravotti, M Glaser, et al. Real-time fibre optic radiation dosimeters for nuclear environment monitoring around thermonuclear reactors. *Fusion Engineering and Design*, 83(1):50–59, 2008.

[26] Andreas Bachlechner, Bastian Beischer, Roman Greim, Thomas Kirn, Carsten Mai, Gregorio Roper Yearwood, Stefan Schael, David Schug, Heiner Tholen, and Jens Wienkenhöver. The perdaix detector. *Nuclear Instruments and Methods in Physics Research Section A: Accelerators, Spectrometers, Detectors and Associated Equipment*, 695:91–95, 2012.

[27] Stefan Diehl, Rainer W Novotny, Nicolas Aubry, Sara Faraj, and Gabriel Ferro. Development and characterization of inorganic scintillating fibers made of luag: Ce and lyso: Ce. *IEEE Transactions on Nuclear Science*, 61(1):353–361, 2014.

[28] Alessandro Mapelli, B Gorini, M Haguenauer, Sébastien Jiguet, G Lehmann Miotto, W Vandelli, N Vico Trivino, and Philippe Renaud. Scintillation particle detection based on microfluidics. *Sensors and Actuators A: Physical*, 162(2):272–275, 2010.

[29] TO White. Scintillating fibres. *Nuclear Instruments and Methods in Physics Research Section A: Accelerators, Spectrometers, Detectors and Associated Equipment*, 273(2-3):820–825, 1988.

[30] Heinrich Leutz. Scintillating fibres. *Nuclear Instruments and Methods in Physics Research Section A: Accelerators, Spectrometers, Detectors and Associated Equipment*, 364(3):422–448, 1995.

[31] R Ruchti. Tracking with scintillating fibers. *Nuclear Physics B-Proceedings Supplements*, 44(1-3):308–319, 1995.

[32] AD Bross, A Pla-Dalmau, and CW Spangler. New fluorescent compounds for plastic scintillator applications. *Nuclear Instruments and Methods in Physics Research Section A: Accelerators, Spectrometers, Detectors and Associated Equipment*, 325 (1-2):168–175, 1993.

[33] Alan D Bross and Anna Pla-Dalmau. Radiation effects in intrinsic 3hf scintillator. *Nuclear Instruments and Methods in Physics Research Section A: Accelerators, Spectrometers, Detectors and Associated Equipment*, 327(2-3):337–345, 1993.

[34] W.R.Leo. *Techniques for Nuclear and Particle Physics Experiments.* Springer-Verlag, second revised edition edition, 1993.

[35] John B Birks. *The theory and practice of scintillation counting Vol. 27, International series of monographs on electronics and instrumentation.* Macmillian, New York, 1964.

[36] *Scintillating Optical Fibers.* Saint-Gobain Crystals, 2016. URL `http://www.crystals.saint-gobain.com/sites/imdf.crystals.com/files/documents/fiber-brochure.pdf`. Product Catalogue.

[37] Ph Rebourgeard, F Rondeaux, JP Baton, G Besnard, H Blumenfeld, M Bourdinaud, J Calvet, J-C Cavan, R Chipaux, A Giganon, et al. Fabrication and measurements of plastic scintillating fibers. *Nuclear Instruments and Methods in Physics Research Section A: Accelerators, Spectrometers, Detectors and Associated Equipment*, 427 (3):543–567, 1999.

[38] Richard RA Syms and John Ritchie Cozens. *Optical guided waves and devices.* McGraw-Hill, 1992.

[39] Carsten Patrick Achenbach. Active optical fibres in modern particle physics experiments. *arXiv preprint nucl-ex/0404008*, 2004.

[40] Norman A Amos, AD Bross, and MC Lundin. Optical attenuation length measurements of scintillating fibers. *Nuclear Instruments and Methods in Physics Research Section A: Accelerators, Spectrometers, Detectors and Associated Equipment*, 297 (3):396–403, 1990.

[41] CM Hawkes, M Kuhlen, B Milliken, R Stroynowski, E Wicklund, T Shimizu, and O Shinji. Decay time and light yield measurements for plastic scintillating fibers. *Nuclear Instruments and Methods in Physics Research Section A: Accelerators, Spectrometers, Detectors and Associated Equipment*, 292(2):329–336, 1990.

[42] Mirco Deckenhoff. *Scintillating Fibre and Silicon Photomultiplier Studies for the LHCb upgrade.* PhD thesis, Dortmund U., 2016.

[43] *Plastic scintillating fibres.* Kuraray Co., Ltd., 2016. URL `http://kuraraypsf.jp/pdf/all.pdf`. Product Catalogue.

[44] S Bruggisser. Literature study on the radiation damage on kuraray fibers, 2012.

[45] Alessandro Mapelli. *Scintillation Particle Detectors Based on Plastic Optical Fibres and Microfluidics.* PhD thesis, Ecole Polytechnique, Lausanne, 2011.

[46] Sergei A Ponomarenko, Nikolay M Surin, Oleg V Borshchev, Yuriy N Luponosov, Dmitry Y Akimov, Ivan S Alexandrov, Alexander A Burenkov, Alexey G Kovalenko, Viktor N Stekhanov, Elena A Kleymyuk, et al. Nanostructured organosilicon luminophores and their application in highly efficient plastic scintillators. *Scientific reports*, 4, 2014.

[47] O Borshchev, ABR Cavalcante, L Gavardi, L Gruber, C Joram, S Ponomarenko, O Shinji, and N Surin. Development of a new class of scintillating fibres with very short decay time and high light yield. *Journal of Instrumentation*, 12(05):P05013, 2017.

[48] André Braem, A Folley, L Kottelat, and C Joram. Characterization studies on scintillating fibres. Technical report, CERN, 2006.

[49] KK Hamamatsu Photonics. Photomultiplier tubes: Basics and applications. *Edition 3a*, 310, 2007.

[50] *MPPC (multi-pixel photon counter) S13360-2050VE.* Hamamatsu K. K., 2016. URL `http://www.hamamatsu.com/eu/en/product/new/S13360-2050VE/index.html`. Datasheet.

[51] PK Lightfoot, Gary John Barker, K Mavrokoridis, YA Ramachers, and NJC Spooner. Characterisation of a silicon photomultiplier device for applications in liquid argon based neutrino physics and dark matter searches. *Journal of Instrumentation*, 3(10):P10001, 2008.

[52] P Bohn, A Clough, E Hazen, A Heering, J Rohlf, J Freeman, S Los, E Cascio, S Kuleshov, Y Musienko, et al. Radiation damage studies of silicon photomultipliers. *Nuclear Instruments and Methods in Physics Research Section A: Accelerators, Spectrometers, Detectors and Associated Equipment*, 598(3):722–736, 2009.

[53] Yi Qiang, Carl Zorn, Fernando Barbosa, and Elton Smith. Radiation hardness tests of sipms for the jlab hall d barrel calorimeter. *Nuclear Instruments and Methods in Physics Research Section A: Accelerators, Spectrometers, Detectors and Associated Equipment*, 698:234–241, 2013.

[54] T. Harion, K. Briggl, H. Chen, P. Fischer, A. Gil, V. Kiworra, M. Ritzert, H. C. Schultz-Coulon, W. Shen, and V. Stankova. Stic – a mixed mode silicon photomultiplier readout asic for time-of-flight applications. *J. Instrum.*, 9, 2014.

Bibliography

[55] J. Fleury, S. Callier, C. de La Taille, N. Seguin, D. Thienpont, F. Dulucq, S. Ahmad, and G. Martin. Petiroc and citiroc: front-end asics for sipm read-out and tof applications. *J. Instrum.*, 9, 2014.

[56] D Impiombato, S Giarrusso, T Mineo, O Catalano, C Gargano, G La Rosa, F Russo, G Sottile, S Billotta, G Bonanno, et al. Characterization and performance of the asic (citiroc) front-end of the astri camera. *Nuclear Instruments and Methods in Physics Research Section A: Accelerators, Spectrometers, Detectors and Associated Equipment*, 794:185–192, 2015.

[57] *Dow Corning silicon adhesive.* Dow Corning, 2015. URL `http://www.dowcorning.com/DataFiles/090276fe801f97f8.pdf`. Datasheet.

[58] A. B. Cavalcante, L. Gavardi, C. Joram, F. Ravotti, and T. Schneider. Irradiation test of mirror samples for the lhcb scifi tracker. Technical report, CERN, 2016. LHCb-PUB-2016-006.

[59] *Araldite Standard.* Huntsman Advanced Materials, 2011. URL `http://www.chemcenters.com/images/suppliers/169257/Araldite%Standard.pdf`. Datasheet.

[60] Helmut Schönbacher and Marc Tavlet. Radiation effects on structural materials for high-energy particle accelerators and detectors. Technical report, CERN, 1994.

[61] Epotek. Removing bubbles from epoxy. Technical report, Epotek Technology Inc., 2009. URL `http://www.jpkummer.com/sites/default/files/Tech%20Tip%204%20-%20Removing%20Bubbles.pdf`.

[62] Ticona Engineering Polymers. *POM*, 2007. URL `http://www.b2bpolymers.com/TDS/Ticona_Hostaform_C9021.pdf`. Datasheet.

[63] Eljen. Machining and polishing of plastic scintillators. Technical report, Eljen Technology, 2015. URL `http://www.eljentechnology.com/images/technical_library/Machine_Polish_Plastics_2015.pdf`.

[64] Burnus GmbH. *Acrylglas Polier & Repair Paste*, 2015. URL `http://www.igefa.de/mediadatenNeu/pdf_dinblaetter/1391771.pdf`. Datasheet.

[65] *MPPC (multi-pixel photon counter) S13360-1350.* Hamamatsu Photonics K.K., 2016. URL `http://www.hamamatsu.com/resources/pdf/ssd/s13360_series_kapd1052e.pdf`. Datasheet.

[66] Christian Joram. Transmission curves of plexiglass (pmma) and optical grease. Technical report, CERN, 2009. PH-EP-Tech-Note-2009-003.

[67] *CAEN N89 NIM - TTL - NIM Adapter.* CAEN, 2010. URL `http://www.caen.it/csite/CaenProd.jsp?idmod=100&parent=12`.

[68] *V560 16 Channel Scaler.* CAEN, 2002. URL `http://www.tunl.duke.edu/documents/public/electronics/CAEN/caen_v560.pdf`.

[69] *iSeg EHS high precision HV module.* iseg Spezialelektronik GmbH, 2012. URL `http://productspice.iseg-hv.com/media/production/MAN_EHS_82x_F_EN-20140116.pdf`. Manual.

[70] *MPOD Crate.* W-IE-NE-R Power Electronics GmbH, 2013. URL `http://www.wiener-d.com/sc/power-supplies/mpod--lvhv/mpod-crate.html`. Datasheet.

[71] Chance Elliott, Vipin Vijayakumar, Wesley Zink, and Richard Hansen. National instruments labview: a programming environment for laboratory automation and measurement. *JALA: Journal of the Association for Laboratory Automation*, 12(1): 17–24, 2007.

[72] Landon Wootton and Sam Beddar. Temperature dependence of bcf plastic scintillation detectors. *Physics in medicine and biology*, 58(9):2955, 2013.

[73] Adam Nepomuk Otte, Distefano Garcia, Thanh Nguyen, and Dhruv Purushotham. Characterization of three high efficiency and blue sensitive silicon photomultipliers. *Nuclear Instruments and Methods in Physics Research Section A: Accelerators, Spectrometers, Detectors and Associated Equipment*, 2016.

[74] CERN EN-STI. *RadMon monitoring system to asses the radiation levels of LHC and other accelerators.*, 2016. URL `https://wikis.web.cern.ch/wikis/display/ECE/Projects+-+RadMon`.

[75] E Bravin. Transverse beam profiles. *CAS - CERN Accelerator School*, 2009. doi: 10.5170/CERN-2009-005.377.

[76] Rene Brun and Fons Rademakers. Root—an object oriented data analysis framework. *Nuclear Instruments and Methods in Physics Research Section A: Accelerators, Spectrometers, Detectors and Associated Equipment*, 389(1-2):81–86, 1997.

[77] Inc. Wolfram Research. Mathematica. software, Wolfram Research, Inc., Champaign, Illinois, 2016.

[78] Nikolaos Charitonidis, Ilias Efthymiopoulos, and Yannis Karyotakis. Beam performance and instrumentation studies for the protodune-dp experiment of cenf. *arXiv preprint arXiv:1607.07612*, 2016.

[79] Nikolaos Charitonidis, Ilias Efthymiopoulos, and Yannis Karyotakis. Addendum to ats note cern-acc-note-2016-0052. Technical report, CERN, 2016.

[80] Nikolaos Charitonidis, Markus Brugger, Ilias Efthymiopoulos, Laurent Gatignon, Yannis Karyotakis, PR Sala, E Nowak, and I Ortega-Ruiz. The beam lines design for the cern neutrino platform in the cern north area and an outlook on their

Bibliography

expected performance. In *8th Int. Particle Accelerator Conf.(IPAC'17), Copenhagen, Denmark, 14â 19 May, 2017*, pages 2382–2384. JACOW, Geneva, Switzerland, 2017.

[81] *Photomultiplier tube H11934.* Hamamatsu K. K., 2016. URL `https://www.hamamatsu.com/resources/pdf/etd/R11265U_H11934_TPMH1336E.pdf`. Datasheet.

[82] *Power supply for MPPC.* Hamamatsu K. K., 2017. URL `https://www.hamamatsu.com/eu/en/product/category/3100/4004/4149/C11204-02/index.html`. Datasheet.

[83] Brent Przybus. Xilinx fpga families: Virtex-7, kintex-7, and artix-7. *Xilinx White Paper*, 2010.

[84] Andrea Boccardi, Manoel Barros Marin, Thomas Levens, Balint Szuk, William Viganò, and Christos Zamantzas. A modular approach to acquisition systems for future cern beam instrumentation developments. *CERN*, 2015.

[85] Javier Serrano, M Lipinski, T Wlostowski, E Gousiou, Erik van der Bij, M Cattin, and G Daniluk. The white rabbit project. *CERN*, 2013.

[86] DA Gedcke and WJ McDonald. Design of the constant fraction of pulse height trigger for optimum time resolution. *Nuclear Instruments and Methods*, 58(2): 253–260, 1968.

[87] Fmc time to digital converter. URL `https://www.ohwr.org/projects/fmc-tdc/wiki`. Home webpage.

[88] Timber, 2012. URL `http://cern.ch/timber`. Javascript program.

[89] *Constant Fraction Discriminator N842.* CAEN, 2016. URL `www.caen.it/servlet/checkCaenManualFile?Id=7720`. Manual.

[90] A Guerrero, JJ Gras, S Jackson, JL Nougaret, M Arruat, and M Ludwig. Cern front-end software architecture for accelerator controls. Technical report, 2003.

[91] S Arfaoui, C Joram, C Casella, and E van der Kraaij. Characterisation of a 90sr based electron monochromator, 2015.

[92] M.J.Berger, J.S.Coursey, M.A.Zucker, and J.Chang. Estar, pstar, and astar: Computer programs for calculating stopping-power and range tables for electrons, protons, and helium ions (version 1.2.3). Technical report, National Institute of Standards and Technology, Gaithersburg, MD., 2005. URL `http://physics.nist.gov/Star`.

184

[93] M.J.Berger, J.H.Hubbell adn S.M.Seltzer, J.S.Coursey, M.A.Zucker, J.Chang, R.Sukumar, and K.Olsen. Xcom: Photon cross section database (version 1.5). Technical report, National Institute of Standards and Technology, Gaithersburg, MD., 2010. URL `http://physics.nist.gov/xcom`.

[94] C. Patrignani et al. (Particle Data Group). *The Review of Particle Physics*, volume 40. Chinese Physics C, 2016.

[95] Claude Leroy and Pier-Giorgio Rancoita. *Principles of radiation interaction in matter and detection*. World Scientific, 2011.

[96] Glenn F. Knoll. *Radiation Detection and Measurement*. John Wiley & Sons, Inc., fourth edition edition, 2010.

[97] Claus Grupen and Boris Schwartz. *Particle Detectors*. Cambridge University Press, second edition edition, 2008.

[98] Syed Naeem Ahmed. *Physics and Engineering of Radiation Detection*. Elsevier, 2007.

[99] H Hirayama. Lecture note on photon interactions and cross sections. *KEK, High Energy Accelerator Research Organization Ibaraki, Japan*, 2000.

[100] Rudolf K. Bock and Angela Vasilescu. *The Particle Detector BriefBook*. Springer, 1998.

[101] S. Agostinelli et al. Geant4-a simulation toolkit. *Nucl. Instr. Meth. Phys. Res. Sect. A*, 506:250–303, 2003.

[102] Makoto Asai, Gabriele Cosmo, Andrea Dotti, Laurent Garnier, Ivana Hrivnácová, Sebastien Incerti, Vladimir Ivantchenko, Alberto Ribon, Marc Verderi, and Dennis H Wright. Geant4 version 10 series. In *Joint International Conference on Mathematics and Computation, Supercomputing in Nuclear Applications and the Monte Carlo Methods*, 2015.

[103] J Apostolakis, G Folger, V Grichine, A Howard, V Ivanchenko, M Kosov, A Ribon, V Uzhinsky, and DH Wright. Geant4 physics lists for hep. In *Nuclear Science Symposium Conference Record, 2008. NSS'08. IEEE*, pages 833–836. IEEE, 2008.

[104] Antonin Vacheret, Gary John Barker, Michal Dziewiecki, P Guzowski, Martin David Haigh, B Hartfiel, Alexander Izmaylov, W Johnston, M Khabibullin, Alexei Khotjantsev, et al. Characterization and simulation of the response of multi-pixel photon counters to low light levels. *Nuclear Instruments and Methods in Physics Research Section A: Accelerators, Spectrometers, Detectors and Associated Equipment*, 656 (1):69–83, 2011.

[105] T Davidek and R Leitner. Parametrization of the muon response in the tile calorimeter. Technical report, CERN-ATL-TILECAL-97-114, 1997.

Ortega Ruiz, Inaki

Address:	Rue des Pâquis 3, 1201 Geneva, Switzerland.
Telephone:	+41 762 142 682
E-mail:	inaki_ortega@hotmail.com
Date of birth:	14$^{\text{th}}$ March 1982
Nationality:	Spanish

WORK EXPERIENCE

Senior Fellow Physicist at CERN
August 2017 - Present

Design, development, and series production of a multipurpose scintillating fibre beam monitor for the secondary beams of the CERN experimental areas and the CERN Neutrino Platform.

Doctoral Student at CERN / Ecole Polytechnique Fédérale de Lausanne
May 2014 - July 2017

Thesis title: *"Accurate profile measurement of the low intensity secondary beams in the CERN experimental areas."*
Development of the prototype of a particle detector, based on scintillating fibres and silicon photomultipliers, for the diagnosis of the secondary beams in the CERN experimental areas.

Physics Trainee at CERN / Universidad de Zaragoza
March 2012 - April 2014

Participation in the operation and upgrades of the CAST experiment at CERN: particle detector R&D (implementation and commissioning of Micromegas and silicon drift diode detectors); analysis of experimental data; finite elements simulations of superconducting magnets.

EDUCATION

Licenciatura in Physics. University of Zaragoza, Spain	·	2005 - 2011
Erasmus Scholarship. Università Federico II, Naples, Italy	·	2009 - 2010

FURTHER TRAINING

- Comprehensive VHDL for FPGA design. CERN, 2017.
- CERN Accelerator School: Basics of accelerator technology. CERN, 2017.
- International School on Trigger and Data Acquisition. Nikhef, 2017.
- Introduction to VHDL. CERN, 2016.
- Project Management for Research. University of Geneva, 2015.
- GEANT4 International School and ROOT Analysis Concepts. INFN, 2014.

Personal Skills

- Team work: participation in different international collaborations.

- Communication: frequent presentations in conferences. Official CERN guide.

- Programming/computing: C, C++, Python, Git, Linux, and LabView.

- Physics simulations and data analysis: Geant4, Comsol, Root, Mathematica, SPSS, and Matlab.

- Teaching: exercise assistant for general physics courses at EPFL.

- Other skills (basic level): Altium Designer, VHDL programming, and Autodesk Inventor.

Languages

English	Full professional proficiency (C1).
French	Professional working proficiency (B2). Certificate CERN/SuperComm, Geneva.
Italian	Professional working proficiency (B2).
Spanish	Mother tongue.

Awards

- "Subprograma especialización OOII 2011." Spanish government grant to be trained at CERN.

- Gold and bronze medals in the National Olympiad of Chemistry of Spain, 2000.

Publications

- CAST Collaboration. "New CAST limit on the axion-photon interaction." *Nature Physics* 13.6 (2017): 584-90.

- Ortega, I., *et al.* "A scintillating fibre beam profile monitor for the experimental areas of the SPS at CERN." *Journal of Physics: Conference Series.* Vol. 763. No. 1. IOP Publishing, 2016.

- A complete list of published papers can be found at:
  `http://inspirehep.net/author/profile/I.Ortega.1`

References

Prof. Aurelio Bay, Ecole Polytechnique Fédérale de Lausanne.　　　　aurelio.bay@epfl.ch
Dr. Gerard Tranquille, CERN.　　　　gerard.tranquille@cern.ch

Others

- Science speaker for schools and science clubs. Volunteer for the CERN open days.

- Interests: hiking, running, cycling, piano, guitar, chess, literature and cinema.

- Car driving license.